2007-08-16

Two-Dimensional Modeling of AP/HTPB Utilizing a Vorticity Formulation and One-Dimensional Modeling of AP and ADN

Matthew L. Gross
Brigham Young University - Provo

TWO-DIMENSIONAL MODELING OF AP/HTPB UTILIZING A VORTICITY FORMULATION AND ONE-DIMENSIONAL MODELING OF AP AND ADN

by

Matthew L. Gross

A dissertation submitted to the faculty of

Brigham Young University

in partial fulfillment of the requirements for the degree of

Doctor of Philosophy

Department of Chemical Engineering

Brigham Young University

December 2007

BRIGHAM YOUNG UNIVERSITY

GRADUATE COMMITTEE APPROVAL

of a dissertation submitted by

Matthew L. Gross

This dissertation has been read by each member of the following graduate committee and by majority vote has been found to be satisfactory.

Date	Merrill W. Beckstead, Chair
Date	Thomas H. Fletcher
Date	Larry L. Baxter
Date	Calvin H. Bartholomew
Date	William C. Hecker

BRIGHAM YOUNG UNIVERSITY

As chair of the candidate's graduate committee, I have read the dissertation of Matthew L. Gross in its final form and have found that (1) its format, citations, and bibliographical style are consistent and acceptable and fulfill university and department style requirements; (2) its illustrative materials including figures, tables, and charts are in place; and (3) the final manuscript is satisfactory to the graduate committee and is ready for submission to the university library.

Date

Merrill W. Beckstead
Chair, Graduate Committee

Accepted for the Department

Larry L. Baxter
Graduate Coordinator

Accepted for the College

Alan R. Parkinson
Dean, Ira A. Fulton College of Engineering and Technology

ABSTRACT

TWO-DIMENSIONAL MODELING OF AP/HTPB UTILIZING A VORTICITY FORMULATION AND ONE-DIMENSIONAL MODELING OF AP AND ADN

Matthew L. Gross

Department of Chemical Engineering

Doctor of Philosophy

This document details original numerical studies performed by the author pertaining to the propellant oxidizer, ammonium perchlorate (AP). Detailed kinetic mechanisms have been utilized to model the combustion of the monopropellants AP and ADN, and a two-dimensional diffusion flame model has been developed to examine the flame structure above an AP/HTPB composite propellant. This work was part of an ongoing effort to develop theoretically based, *a priori* combustion models.

The improved numerical model for AP combustion utilizes a "universal" gas-phase kinetic mechanism previously applied to combustion models of HMX, RDX, GAP, GAP/RDX, GAP/HMX, NG, BTTN, TMETN, GAP/BTTN, and GAP/RDX/BTTN. The universal kinetic mechanism has been expanded to include chlorine reactions, thus

allowing the numerical modeling of AP. This is seen as a further step in developing a gas-phase kinetic mechanism capable of modeling various practical propellants. The new universal kinetic mechanism consists of 106 species and 611 reactions. Numerical results using this new mechanism provide excellent agreement with AP's burning rate, temperature sensitivity, and final species data.

An extensive literature review has been conducted to extract experimental data and qualitative theories concerning ADN combustion. Based on the literature review, the first numerical model has also been developed for ADN that links the condensed and gas phases. The ADN model accurately predicts burning rates, temperature and species profiles, and other combustion characteristics of ADN at pressures below 20 atm. Proposed future work and modifications to the present model are suggested to account for ADN's unstable combustion at pressures between 20 and 100 atm.

A two-dimensional model has been developed to study diffusion in composite propellant flames utilizing a vorticity formulation of the transport equations. This formulation allows for a more stable, robust, accurate, and faster solution method compared to the Navier-Stokes formulations of the equations. The model uses a detailed gas-phase kinetic mechanism consisting of 37 species and 127 reactions. Numerical studies have been performed to examine particle size, pressure, and formulation effects on the flame structure above an AP/HTPB propellant. The modeled flame structure was found to be qualitatively similar to the BDP model. Results were consistent with experimental observations. Three different combustion zones, based on particle size and pressure, were predicted: the AP monopropellant limit, the diffusion flame, and a premixed limit. Mechanistic insights are given into AP's unique combustion properties.

ACKNOWLEGMENTS

I would like to thank the faculty and staff in the Chemical Engineering Department for their guidance during my years at BYU. Their doors were always open whenever I had questions or concerns. I would especially like to thank my advisor, Dr. Merrill Beckstead for his invaluable guidance and counsel throughout my years at BYU. If not for him, I would not have undertaken the challenges of graduate study at BYU.

I am grateful to those students who have gone before me so that I could stand on their shoulders to continue the research. I would like to thank my fellow students for the time and association we have had together. Ben Hardy, Matt Tanner, Dan Smyth, Mike Hawkins, Karthik Puduppakkam, and many others have greatly contributed to my work. I would like to thank Scott Felt for his many sleepless nights in developing the initial diffusion flame model. Lastly, I would like to thank Ephraim Washburn for helping me, as a new employee, gain the vision of this work.

I am very blessed to have a wonderful wife and son. Missy has been my greatest support throughout our life together and I would not be the happy man I am without her. Preston has brought such a great joy into my life and his wonderful smile can brighten any day. I am grateful to my parents and siblings for their love and support. The loving home I grew up in has shaped my life. Lastly, I am grateful to my Heavenly Father and His son Jesus Christ and the many blessing they have bestowed upon me.

TABLE OF CONTENTS

LIST OF TABLES

LIST OF FIGURES

NOMENCLATURE

A	rate constant pre-exponential	
b	constant in burning rate correlation	
c_p	heat capacity	[erg/g/K]
D	diffusivity	[cm^2/sec]
E_A	activation energy	[cal/mole]
$\mathbf{g}$	gravity vector	[cm/sec^2]
h	specific enthalpy	[erg/g]
K	total number of species	
M	Mach number	
n	pressure exponent	
P	pressure	[$dyne/cm^2$]
Q	condensed-phase heat release	[cal/g]
r	radial distance	[cm]
r_b	burning rate	[cm/sec]
R	universal gas constant	[erg/mole/K]
R_p	overall particle radius	[cm]
t	time	[sec]
Y	mass fraction	
$\mathbf{v}$	velocity vector	[cm/sec]
$\hat{v}$	diffusion velocity	[cm/sec]
$\dot{w}$	chemical production rate	[g/cm^3/sec]
W	molecular weight	[g/mol]
x	distance	[cm]

X	mole fraction	
z	axial distance	[cm]

Greek

δ	distance between nodes	[cm]
ϕ	dependent variable	
γ	generic transport property	
λ	thermal conductivity	[erg/sec/cm/K]
μ	viscosity	[poise]
ρ	density	[g/cm^3]
σ_p	temperature sensitivity	[1/K]
$\boldsymbol{\tau}$	viscous stress tensor	[g/sec^2/cm]
ω	nonzero vorticity component	[1/sec]
$\boldsymbol{\omega}$	vorticity vector	[1/sec]

Subscript

c	correction factor
i	species index
j	species index
m	mixture
r	radial direction
z	axial direction

Superscript

–	average
^	unit vector

GLOSSARY

AN – Ammonium nitrate (NH_4NO_3), oxidizer

ADN – Ammonium dinitramide ($NH_4N(NO_2)_2$), oxidizer

AP – Ammonium perchlorate (NH_4ClO_4), oxidizer

Binder – Energetic or non-energetic material used to hold crystalline oxidizer together

BTTN – 1,2,4-butane triol trinitrate ($C_4H_7N_3O_9$), an energetic plasticizer

CFL – Courant-Friedrichs-Lewy stability criterion

Composite Propellant – Propellant containing a mixture of both oxidizer and binder

CTPB – Carboxy-terminated polybutadiene, a binder

Dark Zone – Spatial region before luminous portion of the flame with relatively constant temperature, attributed to slow nitrogen chemistry

Diffusion Flame – Flame in which fuel and oxidizer must diffuse together for combustion to proceed (i.e. candles)

Doped Binder – Binder containing very small oxidizer particles (~<10 μm)

GAP – Glycidyl azide polymer [$(C_4H_7N_3O_9)_n$], energetic binder

HMX – Cyclotetramethylenetetranitramine ($C_4H_8N_8O_8$), an oxidizer

HTPB – Hydroxy-terminated Polybutadiene, binder

I_{sp} – Specific impulse (sec), impulse per unit weight

Monopropellant – A single, unmixed ingredient

PBAN – Polybutadiene-acrylic acid acrylonitrile, a binder

pdl – Pressure deflagration limit, pressure below which unassisted combustion will not take place

PETSc – Portable, Extensible Toolkit for Scientific Computation

PHASE3 – Numerical code capable of modeling monopropellant combustion

Premixed Flame – Flame in which fuel and oxidizer are intimately mixed before combustion (i.e. gas ranges and Bunsen burners)

RDX – Cyclotrimethylenetrinitramine ($C_3H_6N_6O_6$), an oxidizer

SEM – Scanning electron microscope

1 Introduction

Rocketry is a very well established field of science that has developed rapidly since World War II. The scientific community has established immense understanding in fields such as aerodynamics, supersonic flow, and propulsion. However, whereas the areas of aerodynamics and supersonic flow have become very theoretically based, the science of propulsion is still a very empirical science. Empiricism is present in all aspects of rocketry, but it is especially evident in propulsion. Combustion properties of new solid propellant mixtures cannot be determined without experimentation. Theoretical understanding of propulsion is limited due to the rapidity of solid propellant combustion and the extremely small scale in which combustion takes place, a matter of microns. Decomposition and the subsequent combustion of solid propellants involve extremely complex kinetics, which are difficult to resolve experimentally. Further, as ingredients are mixed together to form a composite propellant, the gas-phase kinetics change due to the introduction of multi-dimensional diffusion. These difficulties require the continued use of large experimental data sets to understand composite propellant combustion properties.

There is a great desire to develop theoretical models capable of predicting combustion properties of solid propellants to move away from the large expenses of empirical studies. In the past, simplifying assumptions, such as global kinetics, have been

used to model propellant combustion, but the resulting models are only valid over a very small range of conditions and based largely on empirical studies. Advances in computers are now making it possible to model these complex systems without the many simplifying assumptions in hopes of developing more predictive combustion models. Great steps have been taken in modeling the combustion behavior of individual solid monopropellants over the last decade with the development of one-dimensional detailed gas-phase kinetic models. However, these combustion models are unable to predict the behavior of actual propellants due to the inherent two- and three-dimensional interactions between ingredients. Therefore, current and future work is beginning to expand into multi-dimensional modeling.

Ammonium perchlorate (AP) has been in use as a major propellant ingredient for decades. AP is the standard ingredient in solid rocket propellants and is used in many applications: ballistic missiles, military attack missiles, space applications, etc. Two major reasons for AP's widespread use are, its stability, resulting in safe munitions, and its ability to control a propellant's burning rate. By varying the AP particle size distribution it is possible to achieve vastly different overall propellant burning rates. No other current oxidizer has the capacity to control a propellant's burning rate in this manner. This unique behavior of AP has not been accurately calculated using detailed *a priori* numerical models, and thus empirical studies are still relied upon heavily to characterize AP containing propellants.

AP has been the subject of numerous experimental and theoretical studies in an attempt to explain its unique properties. The most widely accepted theoretical picture was developed in 1970 and is known as the BDP Model.[1,2] The BDP physical picture is

presented in Figure 1-1. This model proposes that the combustion region above the surface of AP and the corresponding binder/fuel is composed of three unique flames: a primary diffusion flame, a monopropellant flame, and a final diffusion flame. The impact of these three flames on the propellant burning rate varies with particle size and pressure. A numerical model was developed analogous to the proposed BDP flame structure and was able to accurately predict many of the unique properties of AP composite propellants. However, due to the numerical constraints of the time, many simplifying assumptions were made in the numerical model, and therefore, there is still debate today as to the accuracy of the BDP Model.

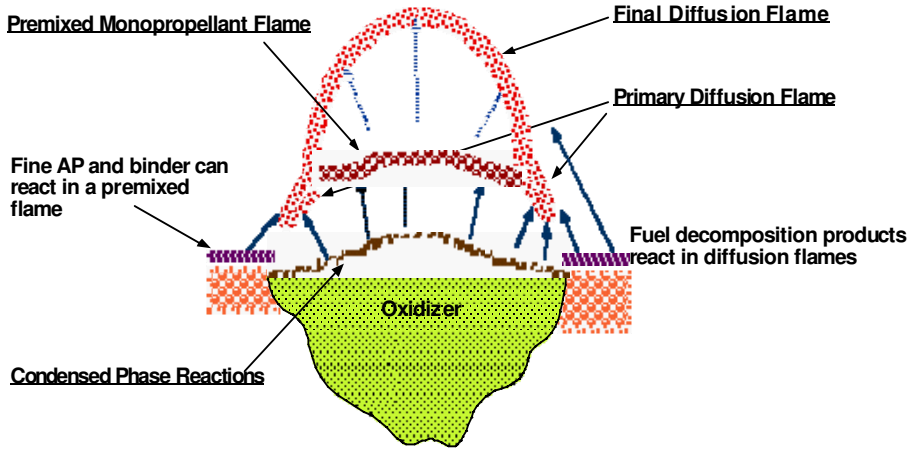

Figure 1-1: Proposed BDP flame structure above an AP/HTPB composite propellant.

To examine AP composite propellant flames in more detail, Felt[3] developed a two-dimensional combustion model, using detailed gas-phase kinetics. Felt's model was the first attempt to apply a detailed gas-phase kinetic mechanism to capture the structure of an AP composite propellant flame, thereby eliminating many of the assumptions used in previous models. Calculations appeared to support the proposed BDP flame structure;

however, only preliminary results were obtained due to the computationally time-intensive nature of the numerical model.

Despite AP's beneficial combustion characteristics, there is one major drawback to its use: the vast amount of hydrochloric acid (HCl) produced during combustion. For example, every time the space shuttle is launched, roughly 240 tons of HCl are released to the atmosphere. To prevent damage to the inland crops and natural habitat, the wind must be blowing out to sea at the time of the launch. Therefore, there is great interest in finding possible replacements for AP in propellants. One such alternative may be ammonium dinitramide (ADN). ADN is oxygen rich, similar to AP, but does not contain chlorine.

1.1 Project Objectives

This study focused on developing theoretical models to further the understanding of solid propellant combustion. The study was split into three main tasks:

- Update the mechanisms for AP monopropellant combustion.
- Determine condensed- and gas-phase mechanisms to simulate ADN combustion using PHASE3.
- Develop a two-dimensional diffusion flame model to examine the flame structure above an AP/HTPB composite propellant.

1.1.1 Update AP Monopropellant Model

The previous gas-phase mechanism used for AP monopropellant combustion was largely developed in the 1980s; therefore the accuracy of many of the kinetic parameters

used in the mechanism are suspect. BYU is in the process of developing a comprehensive gas-phase mechanism capable of modeling most propellant ingredients. At the start of this study, the comprehensive mechanism did not include chlorine-containing species. Therefore, AP needed an updated mechanism which could be incorporated into the comprehensive mechanism. The objectives of this task were:

1. Incorporate Cl-containing reactions into the comprehensive mechanism and address any short comings of the mechanism to model AP.
2. Determine a compatible, global AP condensed-phase mechanism.
3. Calculate AP monopropellant combustion characteristics in conjunction with the numerical model PHASE3.

1.1.2 Development of an ADN Monopropellant Model

As a possible substitute for AP, an ADN model was desired that could accurately calculate ADN combustion properties. Previously, detailed ADN models were developed for gas-phase calculations only. Those models were unable to predict combustion properties such as burning rate and temperature sensitivity, and therefore, a more detailed ADN model was desired. The objectives for this task were:

1. Gather physical and chemical properties of ADN.
2. Determine gas- and condensed-phase mechanisms for ADN combustion.
3. Incorporate the mechanisms into the combustion model PHASE3 and predict ADN combustion properties such as burning rate, temperature and species profiles, and temperature sensitivity.

1.1.3 Two-Dimensional AP/HTPB Model

The primary focus of the current study was to use the two-dimensional model developed by Felt to further examine the complex flame structure above an AP/HTPB composite propellant. The Felt model was relatively unstable and very time consuming. Model calculations took weeks to months to reach a final solution, and the accuracy of the final solution was questionable. The objectives for this task were:

1. Increase the convergence speed, stability, accuracy, and robustness of the model using a vorticity formulation of the governing equations.
2. Examine the flame structure above a composite propellant varying particle size, pressure, and propellant formulation.

1.2 Document Outline

Chapter 2 gives a background overview of solid propellant combustion. Specifics of AP monopropellant combustion, ADN monopropellant combustion, and AP/HTPB composite propellant combustion are then given. Chapter 3 outlines the work performed in developing a new AP mechanism and incorporating AP related reactions into the comprehensive mechanism. Results and future recommendations are included. Chapter 4 presents the work performed in developing an ADN mechanism, and Chapter 5 presents the results and future recommendations of the ADN model. Chapter 6 details the theoretical model used for two-dimensional modeling of AP/HTPB, including the vorticity formulation of the governing equations. Chapter 7 presents the results of the diffusion flame calculations varying particle size, pressure, and propellant formulation. Chapter 8 summarizes the work performed and gives recommendations for future work.

2 Background

Solid propellants fall into two general categories, composite and double base propellants. One of the major differences between the two categories is the type of binder used in the propellant mixture. Composite propellants use a non-energetic hydrocarbon binder; the hydrocarbon binder acts as fuel when combined with the (hopefully) oxygen-rich oxidizer. Double base propellants, on the other hand, use an energetic binder such as nitroglycerin and a cross-linking agent, typically nitrocellulose. The double base propellants typically result in a greater specific impulse (I_{sp}), but at the cost of increased safety hazards. Double base propellants are far more likely to accidentally ignite, whereas composite propellants are very safe to handle and store. The relative safety of composite propellants is the reason they are used for the space shuttle launch, whereas the higher energy content of double base propellants makes them ideal for use as ballistic missiles in submarines where space is limited. The primary focus of this study is composite propellants, and therefore, double base propellants will not be discussed further.

2.1 Solid Propellant Combustion

Composite propellants typically consist of three major ingredients: an energetic oxidizer, a polymeric binder, and a metal. The oxidizer is most often AP and multiple size distributions (modes) are generally included in the propellant. The multiple oxidizer

modes maximize the solids loading in the propellant mixture. Modes range from large 400 μm particle size distributions to very small 1-2 μm particle size distributions. The binder is a polymer that is cured to solidify the mixture. The space shuttle boosters use PBAN, but the more common binder in use today is HTPB. Both are essentially a type of rubber. Often a metal, typically aluminum, is added to the propellant. Usually the metal does not directly influence the propellant burning rate, but it greatly enhances the overall energy in the system and thus increases the I_{sp}. An example of an idealized slice of a solid propellant mixture appears in Figure 2-1. The image was created using a particle packing code developed at ATK Thiokol. The calculation used monodisperse spherical particles. The apparent differences in size arise from cross sectioning monodisperse spheres at different radial distances. In an actual mixture the particles would be slightly aspherical and each mode would have a distribution of particle sizes. Figure 2-1 illustrates two AP modes, the large grey particles and the small red particles, corresponding to 400 and 20 μm modes respectively. The small blue particles represent aluminum, and the remaining empty space represents the binder.

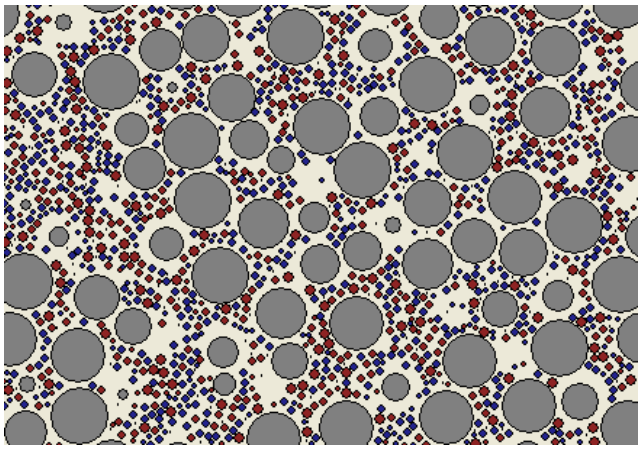

Figure 2-1: Calculated particle pack for a bimodal, aluminized composite propellant.

2.1.1 Decomposition and Combustion

Propellant decomposition and combustion are generally divided into three different phases: solid, condensed (a liquid/gas region), and gas. A schematic of these three phases is presented in Figure 2-2 for a homogeneous monopropellant. The scale of the system is very small with each phase being only microns thick. Combustion of a heterogeneous composite propellant would be very similar to that presented in Figure 2-2. However the condensed-phase regions of the individual ingredients may mix at their interface, and there would be gas-phase diffusion that can greatly influence the overall combustion.

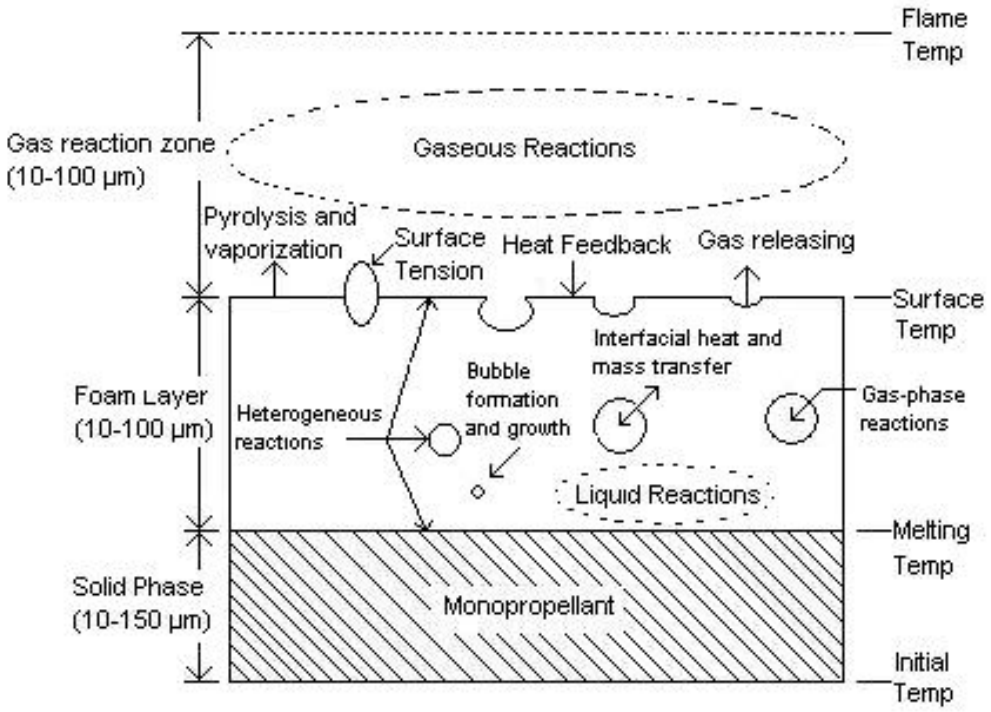

Figure 2-2: Physical picture for monopropellant combustion.

2.1.1.1 Solid Phase

Solid-phase decomposition and/or sublimation may take place during combustion, but it is generally assumed to be negligible compared to the rapid condensed-phase decomposition. One notable exception is AP, which decomposes up to 30% in the solid phase. For the crystalline oxidizers, it is common for solid-solid phase transitions to take place as the temperature rises from the initial temperature to the melt temperature. AP, HMX, ADN, and AN all undergo solid-solid phase changes. Solid propellant acts as a good insulator and thermal penetration is limited to the micron scale and the bulk of the solid phase remains at the initial temperature.

2.1.1.2 Condensed Phase

Once the propellant melts, decomposition and evaporation begin to take place rapidly. This results in a frothy layer containing bubbles of decomposition products and evaporated material, as well as the melted propellant. The decomposition may be endothermic or exothermic depending upon the material being burned. Kinetic parameters and physical properties are difficult to obtain experimentally for the condensed phase due to its small scale. Mixing between ingredients can occur as well, adding to the complexity of modeling multiple ingredients. Lack of understanding of the condensed phase is the greatest hindrance to combustion modeling. Typically only global or semi-global reactions can be determined for the condensed phase due to its complexity and the lack of fundamental understanding.

2.1.1.3 Gas Phase

The products leaving the surface quickly react in the gas phase producing high heat feedback to the condensed phase, which along with the condensed-phase heat

release, drives the combustion process. The flame stand-off distance, and thus the heat flux to the surface, varies with pressure. As pressure increases, the gas-phase reaction rates increase, drawing the flame closer to the surface and increasing the gas-phase heat flux. It is possible for "dark zones" to form in the gas phase. A dark zone is a region of essentially unchanging temperature before the final flame temperature is reached. The relatively slow nitrogen chemistry causes dark non-reactive zones.

For monopropellant combustion the gas phase is premixed, and therefore, radial diffusion is negligible. However, when ingredients are mixed to form an actual propellant, radial diffusion can become a very dominant factor and must be considered when modeling composite propellant combustion. The intricacies of the gas phase are easier to examine both theoretically and experimentally compared to the condensed phase. Therefore, detailed kinetic mechanisms are the standard in use today to simulate the gas phase. Finally, equilibrium calculations are used as a reference point for gas-phase calculations to verify that the gas-phase mechanisms predict the correct final species.

2.1.2 Numerical Models

Due to the cost and safety factors involved in experimental evaluations of rocket ingredients, it is desirable to develop numerical models capable of modeling propellant combustion. Accurate numerical models will then be able to limit the amount of experimentation necessary by focusing studies in critical areas. As computer power has increased over the years, so has the complexity of numerical models. The evolution of steady-state propellant combustion models can be divided into three general categories: 1) models based on global kinetics; 2) semi-global models based on some finite-rate

kinetic mechanisms in either, or in both, the gas and condensed phases; 3) multi-phase models with detailed kinetic mechanisms. An advantage of the detailed models is that, in addition to calculating the burning rate and pressure exponent, the models provide the capability to calculate the temperature sensitivity, the temperature and species profiles, and the surface and flame temperatures. Experimental data for the temperature and species profiles are not often available, but if available, they provide a more comprehensive validation of the models and a more comprehensive view of the combustion process.[4] The first two categories are typical of modeling efforts of the 60s, 70s, and 80s. The primary focus of this study is the further refinement and development of combustion models in the third category. To this end, there are two general areas of interest: a monopropellant premixed model, and a two-dimensional diffusion flame model.

2.1.2.1 Homogeneous Premixed Combustion Model

Work at BYU over the last decade has focused on the development of a one-dimensional detailed kinetic combustion model. This model, known as PHASE3,[5] is capable of predicting monopropellant properties such as burning rate, temperature and species profiles, temperature sensitivity, and other steady-state combustion properties. The model has been used to successfully model numerous ingredients including RDX, HMX, AP, etc., and is described elsewhere.[5,6,7,8,9] In general, the model is capable of modeling all three phases present during monopropellant combustion. A solid-phase decomposition scheme can be included in the model. Condensed-phase decomposition is modeled using the energy and species equations, and by keeping track of a void fraction created by the reactions. A detailed kinetic mechanism can also be included in the

condensed phase. The gas phase is modeled by solving the continuity, energy, and species equations and utilizes the solver package CHEMKIN[10] to determine chemical properties. The monopropellant burning rate is calculated by iterating between the condensed and gas phases until the respective heat fluxes are equal at the condensed/gas interface, the propellant surface.

A comprehensive gas-phase mechanism has been developed by Puduppakkam[11] at BYU for use with the PHASE3 combustion model. This comprehensive gas-phase mechanism successfully describes one-dimensional, steady-state monopropellant combustion of HMX, RDX, GAP, GAP/RDX, GAP/HMX, NG, BTTN, TMETN, GAP/BTTN, and GAP/RDX/BTTN. Burning rate calculations for some of these ingredients are presented in Figure 2-3. The corresponding data points have not been included, as they would obscure the graph. The comprehensive mechanism is based on several other detailed kinetic mechanisms developed independently. These include

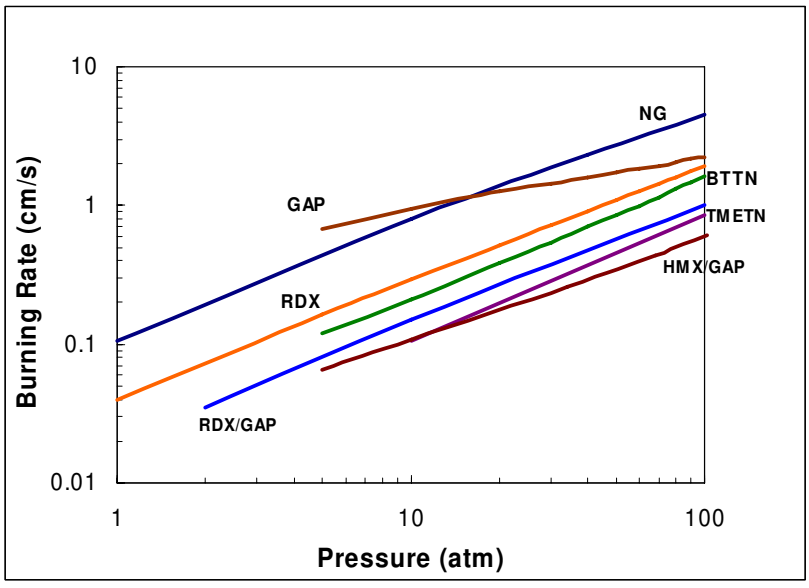

Figure 2-3: Burning rate calculations using Puduppakkam's comprehensive gas-phase mechanism.

Yetter's RDX mechanism[12] (default mechanism), the GRI mechanism for natural gas combustion[13] (limited use), Miller's mechanism for nitroglycerine combustion,[14] and other sources. Extensive *ab initio* calculations of kinetic pathways relative to propellant combustion have also been performed by Lin et al.[15] at Emory University, and have been included in the comprehensive mechanism. Available kinetic data were then combined; identical reactions dropped, keeping the most theoretically based reactions. Modification of the reaction parameters was not permitted. The desire is to have a gas-phase mechanism as theoretically-based as possible.

2.1.2.2 Heterogeneous Diffusion Flame Model

When multiple ingredients are mixed to form a propellant, gas-phase diffusion can become significant, especially for AP propellants. A two-dimensional model was developed at BYU by Felt,[3] capable of modeling two-dimensional diffusion. The model utilizes the one-dimensional PHASE3 model for condensed-phase calculations, and then solves the two-dimensional gas-phase equations to allow for gas-phase diffusion and reaction effects. Additional details of the diffusion model will be given in later chapters due to further model development performed in this work.

2.2 AP Monopropellant Combustion

2.2.1 Experimental Studies

Ammonium perchlorate burns as a monopropellant at pressures above 20 atmospheres, and is characterized by a unique relationship between burning rate and pressure. Experimental data obtained by Atwood et al.[16] are provided in Figure 2-4. The data are characterized by a "U-shaped" curve at pressures above 2000 psi. This non-linear

behavior is uncommon among oxidizers and illustrates the complexity of AP combustion. Boggs et al.[17,18] separated the burning rate versus pressure relationship into four regions as illustrated in Figure 2-4.

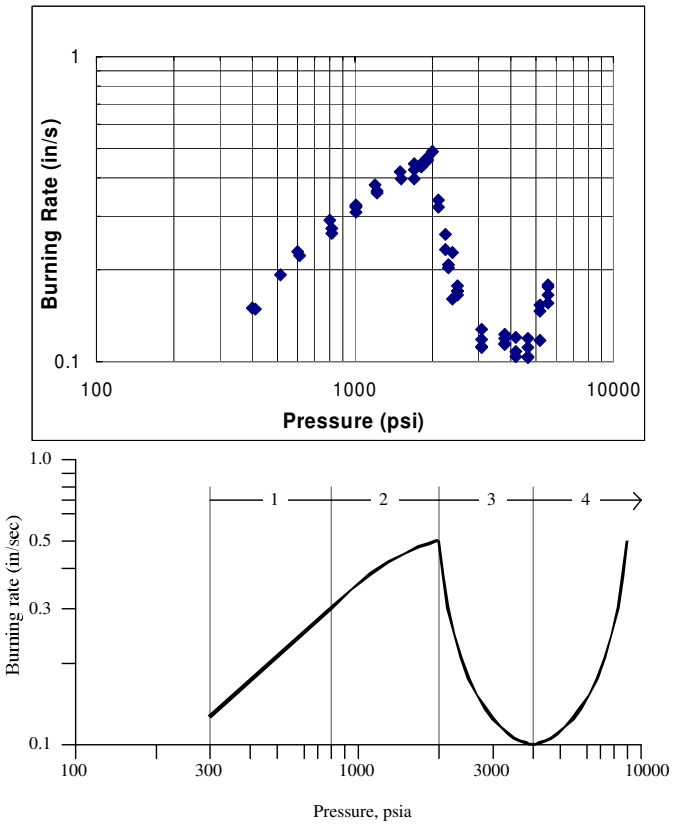

Figure 2-4: Experimental data for AP from Atwood (top) and the four AP burning rate regions proposed by Boggs (bottom).

The first region is characterized by a linear burning rate described by the standard $r_b \sim bP^n$. Boggs observed a two-phase zone (condensed phase) in which liquid AP traps gas bubbles, creating a melt layer between 1 and 5 μm thick. The second regime is characterized by a decreasing positive value of dr_b/dP, in which experimental data begin to deviate from $r_b \sim bP^n$. The third regime is characterized by a decrease in

burning rate as pressure increases. The exact reason for this behavior is unknown, but Boggs proposed that it could be due to a lack of significant energy contribution from either the gas or condensed phases. Finally, the fourth regime is characterized once again by an increase in burning rate as pressure increases. The details of the condensed phase have not been observed in the second, third, or fourth regions because experimental methods are incapable of resolving such a small scale, ~1 μm.

In addition to its unique burning rate versus pressure behavior, ammonium perchlorate also possesses unique solid-phase behaviors. At temperatures from about 500 K up to 723 K, and for isothermal heating rates, AP decomposes up to ~30% in the solid phase, after which decomposition ceases regardless of the heating rate.[19,20] Other oxidizers such as HMX, RDX, and ADN are observed to have negligible solid-phase decomposition; with significant decomposition occurring only after melting has occurred. AP also undergoes an abrupt solid-phase transition from orthorhombic crystal to cubic crystal at 513 K. This transition is so violent that embedded thermocouples break, making it virtually impossible to measure the surface temperature of pure AP. Due to this abrupt phase change and the relatively high pressure deflagration limit (pdl) of 20 atm, very little experimental data are available concerning the surface temperature, gas-phase temperature profiles, or the species profiles for AP combustion.

To circumvent these problems, Ermolin et al.[21] obtained species and temperature profiles for an AP flame by preheating the propellant to 530 K at a pressure of 0.6 atm. Quantitative data were obtained below the monopropellant's pdl by increasing the energy in the sample via preheating. The low pressure of 0.6 atm allowed for a more spread out flame, making gas-phase measurements easier to obtain. Ermolin's results indicated large

amounts of final products (H_2O, HCl, and O_2) leaving the surface and a final flame temperature 300 K lower than the adiabatic flame temperature. The low final flame temperature was probably due to pre-heating the sample to 530 K, in which case the 30% decomposition would have already occurred. These data represent the only quantitative data available on species and temperature profiles in an AP flame.

Other condensed-phase studies have also been performed on AP to examine products leaving the surface. Using his T-jump experiment, Brill et al.[22] reported an AP aerosol in the gas phase during a condensed-phase study. The AP aerosol was attributed to the recombination of NH_3 and $HClO_4$ upon entering a cool gas-phase environment. Brill stated that the appearance of AP aerosol supports a commonly held theory that dissociative sublimation, Equation (2-1), is an initial decomposition step for AP.

$$AP(s) \rightarrow NH_3(g) + HClO_4(g) \tag{2-1}$$

Behrens et al.[20] and many others[23] have proposed (based on experimental data) that AP condensed-phase decomposition takes place in two steps. The first step is the AP solid-phase decomposition as described above accounting for 30% of the decomposition, and the second proposed step is dissociative sublimation of AP to form NH_3 and $HClO_4$, Equation (2-1).

Determining condensed-phase reactions and corresponding kinetic parameters for any ingredient is still a major experimental and numerical limitation facing combustion modeling. This is due to the complexity of the reactions, the small scale of the condensed-phase region, and the high operating pressures of typical propellants.[24] The

above studies give insight into possible decomposition pathways for AP's condensed phase, but give no concrete answers.

2.2.2 Numerical Studies

Numerous models have been developed to study AP combustion. Early models used global kinetics and empirical relations to achieve satisfactory results. A number of summaries on this early work are available.[25,26,27,28,29] Models then shifted to using more detailed gas-phase kinetic mechanisms in an attempt to develop more theoretically-based models. A summary of detailed AP kinetic models is provided in Table 2-1.

Table 2-1: Summary of AP monopropellant models using detailed gas-phase kinetics.

Author	Year	Mechanism	Description
Guirao et al.[28]	1971	19 Species 14 Reactions	Created 1 global reaction based on 14 steps; Assumed 70% heat release in condensed phase
Beckstead et al.[29]	1971	1 Reaction	Modeled AP & HMX using global kinetics and BDP-type model; Based on fundamental eqs.
Ermolin et al. [30]	1982	24 Species 80 Reactions	Based mechanism on experimental data collected by Ermolin et al. ; Identified important gas phase species; Mechanism served as bases for ingredients
Naharahi et al.[31]	1984	17 Species 14 Reactions	Predictions slightly off experimental data; Shortcomings attributed to deficiencies in gas phase kinetic mechanism
Ermolin[32]	1995	30 Species 79 Reactions	Refined original mechanism to more closely match experimental data
Jing et al.[7]	1998	30 Species 79 Reactions	Used Ermolin's 1995 mechanism with slight modifications; Included solid phase decomp

Ermolin et al.[30] produced the first detailed gas-phase kinetic reaction mechanism for AP combustion in 1982, consisting of 80 reactions and 24 species. Using his

experimental data[21] (section 2.2.1), Ermolin identified important gas-phase species and created a mechanism that included each observed species. One-dimensional transport equations were solved neglecting thermal conductivity and diffusion. The reaction mechanism was able to calculate temperature and species profiles within ~30% of the experimental values. Results of Ermolin's work are presented in Figure 2-5.

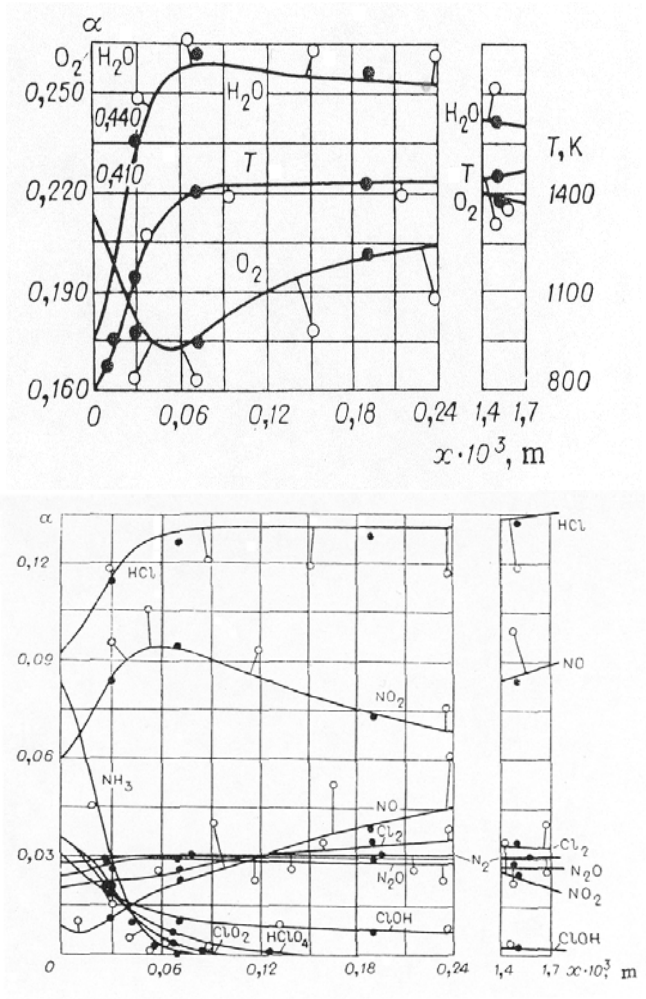

Figure 2-5: Comparison of Ermolin numerical results (solid circles) with Ermolin experimental results (open circles) for AP, mole fractions (α) versus axial distance.

The Ermolin mechanism served as the basis for a mechanism developed by Jing in the late 1990's to simulate AP combustion. Jing utilized the PHASE3 code and was able to accurately calculate burning rate, temperature and species profiles, and temperature sensitivity.

The accuracy of many of the Ermolin reaction rate expressions has been questioned in recent years, raising questions about the Jing mechanism. Previous attempts to incorporate the Jing mechanism into the BYU comprehensive mechanism have failed. Results produced extremely low burning rates and final temperatures compared to the experimental data. Lin[15] has performed numerous *ab initio* calculations pertaining to the chlorine reactions specific to AP that were not included in the Jing mechanism. The Lin reactions have a more theoretically sound basis than Ermolin's reactions and needed to be incorporated into the comprehensive mechanism.

2.2.3 Summary and Shortcomings of Previous Work

Despite being studied extensively for decades, the combustion characteristics of AP still pose many challenges experimentally and numerically. Experimental difficulties have resulted in minimal experimental data pertaining to species and temperatures in the condensed and gas phases of AP. Numerically studies have been changing from empirically-based to theoretically-based models. The PHASE3 model at BYU has a solid theoretical background, but the previous AP gas-phase mechanism developed by Jing appears suspect. That mechanism was based on the work of Ermolin, and many of the reactions were proposed in the early 1980's. Theoretical calculations are now available that enable calculation of gas-phase reactions and the corresponding kinetic parameters, such as the work performed by Lin. To develop a truly comprehensive mechanism, AP

reactions need to be included in the comprehensive mechanism. The latest work by Lin provides a basis to include more realistic AP reactions into the comprehensive gas-phase mechanism.

2.3 ADN Monopropellant Combustion

The search for "green" propellants to replace AP has led to great interest in ammonium dinitramide (ADN), a chlorine free oxidizer. The former Soviet Union has used ADN as a primary oxidizer in one of its engine stages, thus demonstrating the feasibility of ADN as a practical solid propellant ingredient. Theoretical work had been conducted to model ADN combustion, but no detailed numerical models were developed that coupled the condensed and gas phases to calculate a burning rate. Previous detailed kinetic studies focused on simulating the gas phase only with the burning rate as an input parameter.

2.3.1 Chemical and Physical Characteristics

ADN possesses a number of unique physical properties when compared to other propellant oxidizers. The melt temperature of ADN is 366 K,[33] significantly lower than propellants such as HMX (551 K), RDX (477 K),[34] or AP (~865 K).[35] ADN also has a high condensed-phase heat capacity, 0.59 cal/g/K,[36] whereas a more traditional value for oxidizer heat capacities is between 0.3 and 0.4 cal/g/K. Further, the burning rate of ADN is extremely high. At 6.8 atm, ADN has a burning rate of ~2 cm/s, whereas RDX burns at 0.19 cm/s, HMX at 0.17 cm/s, and both AP and AN are well below their pressure deflagration limits (pdl) at this pressure.[16] Table 2-2 contains a list of solid and condensed-phase properties of ADN.

ADN not only has a high burning rate, but it also has a unique burning rate versus pressure behavior. This can be seen in Figure 2-6,[16,37,38,39,42] where the burning rate can

Table 2-2: Chemical and physical properties of ADN at 298 K.

Chemical Formula	$NH_4N(NO_2)_2$
Molecular Weight (g/mol)	124.1
Heat of Formation (kcal/mol)	-31.8 [33] to -35.0 [40]
Density of Solid (g/cm^3)	1.82 to 1.84 [33]
Thermal Conductivity of Solid (cal/cm/s/K)	0.001 [41]
Heat Capacity of Solid (cal/g/K)	0.3 [42] to 0.43 [43]
Thermal Diffusivity (m^2/s)	1.78x10^{-7} [36]
Melting Temperature (K)	365.7 [33]
Enthalpy of Phase Change Solid to Liquid (kcal/mol)	3.4 [36] to 3.97 [42]
Heat Capacity of Condensed Phase (cal/g/K)	0.59 [36]
Density of Liquid (g/cm^3)	~1.55 [44]
Thermal Conductivity of Condensed Phase (cal/cm/s/K)	0.00193 [36]
Heat of Vaporization (kcal/mol)	35.1 to 37.1 [45]

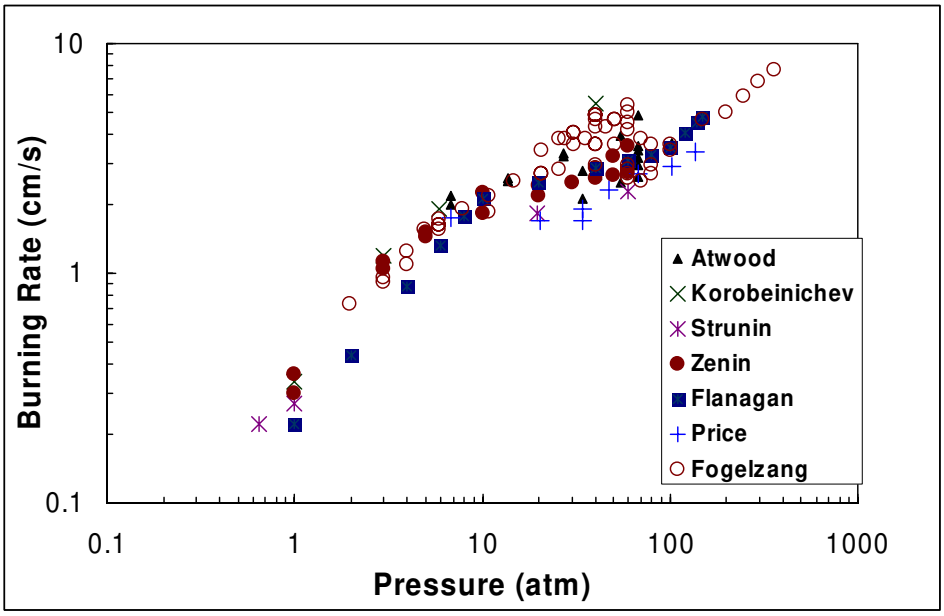

Figure 2-6: Burning rate versus pressure for ADN monopropellant.

be divided into three distinct regions. The first region ranges from low pressures to about 20 atm and exhibits typical oxidizer behavior with a linear fit of $r_b \sim bP^n$ and a pressure exponent of 0.67. The second region ranges from 20 to 100 atm and is marked by combustion instability and a large variation in burning rates. Burning rate measurements at the same conditions and by the same experimentalist have been recorded to change by up to a factor of 2 between 20 and 100 atm.[16,36] The final region, above 100 atm, is once again characteristic of a typical oxidizer with a stable combustion region and a pressure exponent of 0.63. Also, ADN has a pdl of approximately 2 atm.[36,46] Therefore, all data presented in Figure 2-6 below 2 atm must have been augmented in some way (preheated, catalyzed, or laser assisted) to generate a burning rate.

Sinditskii et al.[46,47] proposed a qualitative theory for the three segments on ADN's burning rate versus pressure curve. He noted that ADN combustion is marked by a large exothermic condensed-phase heat release. Also, Sinditskii measured little temperature gradient above the surface of ADN at low pressures, and therefore, assumed that there is no heat feedback from the gas phase in the first region (<~20 atm). Therefore, Sinditskii proposed that condensed-phase decomposition controls the first region of combustion; the gas-phase flame having virtually no impact. Also, due to the high burning rate, he assumed that condensed-phase material (i.e. liquid droplets) is dispersed into the gas phase and decomposes there. Dispersion of condensed material has been observed for substances in which condensed-phase decomposition dominates combustion;[48,49] supporting the claim that ADN has a large condensed-phase heat release. According to Sinditskii, the temperature at which ADN dissociation takes place increases with pressure, as well as the energy required for dissociation. However, the

condensed-phase heat release does not increase with pressure in this region, and the gas phase still does not contribute significantly. This results in a growing deficiency of energy that is required to heat up and evaporate the condensed-phase material. To remove all of the condensed-phase material as pressure increases, the dispersion rate increases and this causes a large scatter in the burning rate data. Finally, at about 100 atm, stable combustion is once again achieved as the flame is now close enough to the surface to provide significant heat feedback and support combustion by augmenting the condensed-phase heat release. This theory by Sinditskii appears to provide the most rational explanation for ADN's erratic combustion behavior.

2.3.2 Condensed-Phase Decomposition

The unique burning rate behavior of ADN has not been modeled satisfactorily to date. The main reason for the difficulty is the complex condensed-phase chemistry. The condensed-phase decomposition process is very exothermic, and experimental results give heat release values varying between -100 cal/g and -460 cal/g[50] (see Table 2-3).

Table 2-3: Experimentally calculated condensed-phase heat release at atmospheric conditions.

Author	Heat Release (cal/g)
Zenin et al.	104
Brill et al.	217
Strunin et al.	280
Fetherolf at al.[51]	300
Sinditskii et al.	400
Oxley et al.[52]	406
Vyazovkin et al.[53]	460

This wide variation in experimentally determined heat release illustrates the difficulty in examining propellant decomposition. There is also a wide range in reported activation energy for the decomposition of ADN, ±15 kcal/mole. Table 2-4 contains reported global reaction rates for the decomposition of ADN.

Table 2-4: Experimental values for the overall ADN decomposition rate.

Author	**A (s^{-1})**	**E_A (kcal/mol)**
Kraeutle & Atwood (13.5 psi)[54]	$5.5x10^{13}$	32.8
Kraeutle & Atwood (200 psi)	$9.9x10^{11}$	29.6
Wight et al.	$1.0x10^{21}$	47.8
Strunin et al.	$2.5x10^{14}$	35.5
Vyazovkin et al.	$1.0x10^{20}$	30.0 - 41.8
Oxley et al.	$1.4x10^{15}$ to $8.8x10^{16}$	36.0 - 40.0
Korobeinichev et al.[55]	$3.5x10^{15}$	32.0
Sinditskii et al.	$1.3x10^{15}$	35.5
Sinditskii et al.	$1.46x10^{16}$	38.5

The highly exothermic condensed-phase decomposition is believed to be the key as to why ADN has a burning rate an order of magnitude higher than AN, and why there is erratic combustion instability for ADN over the pressure range of 20 to 100 atm. However, due to experimental constraints it is still not possible to precisely determine the elementary condensed-phase reactions and their corresponding kinetics. Numerous experimental studies have been performed to examine the condensed phase, and these studies have resulted in two main schools of thought concerning ADN condensed-phase decomposition.

2.3.2.1 Decomposition Theory #1

One theory of ADN decomposition is proton transfer resulting in the production of ammonia and dinitramic acid (DA).[37,40,51,56] This initial decomposition step is presented in Equation (2-2).

$$ADN(l) \rightarrow NH_3(g) + HN(NO_2)_2(g) \tag{2-2}$$

Proton transfer as the initial step in decomposition is supported by experimental work conducted by Brill et al.[40] Brill analyzed ADN condensed-phase decomposition using the T-jump/FTIR technique. Tests were performed using a high heating rate with the goal of heating the sample to its assumed monopropellant surface temperature of ~573 K at a pressure of 1 atm. Two different condensed-phase schemes were then proposed based on the experimental results, one for slow pyrolysis and one for fast pyrolysis, with the fast pyrolysis path assumed to be the dominant path. The slow pyrolysis path is represented by Equation (2-3) and appears to indicate that AN is a precursor in the decomposition process, but this path was largely discounted by Brill as not being important under actual combustion conditions.

$$ADN \rightarrow NH_3 + HNO_3 + N_2O \tag{2-3}$$

The first step in the fast pyrolysis scheme proposed by Brill is Equation (2-2). This is then followed by the decomposition of $HN(NO_2)_2$, dinitramic acid (DA), through an additional seven reactions. The sum of the reactions, which form and then destroy DA,

result in Equation (2-4), with a heat of reaction of -49 kcal/mol, or -73 cal/g heat release in the condensed phase.

However, Equation (2-4) does not account for the large heat release detected experimentally, and therefore, Brill also proposed Equation (2-5). Brill postulated that this is the path of the major heat release seen during ADN combustion and occurs either in the condensed region or near the surface in the gas phase. Summing Equations (2-3), (2-4), and (2-5) leads to Equation (2-6), Brill's proposed global reaction. Equation (2-6) has a heat of reaction of -323 kcal/mol, or -217 cal/g condensed-phase heat release. Unfortunately, no kinetic data are known for the proposed reaction scheme.

$$9ADN \rightarrow 6NH_3 + 7N_2O + 10NO_2 + 9H_2O + 3N_2 \tag{2-4}$$

$$4NH_3 + 4NO_2 \rightarrow 3N_2 + 2NO + 6H_2O \tag{2-5}$$

$$12ADN \rightarrow 9NH_3 + 10N_2O + 10NO_2 + 9H_2O + 3N_2 + 3HNO_3 \tag{2-6}$$

Russell et al.,[56] Fetherolf and Litzinger,[51,57] and Korobeinichev et al.[37] also performed experimental analyses on ADN, and concluded that their results support the conclusions drawn by Brill. Russell also noted a slow pyrolysis decomposition path, but claimed it is only important at temperatures below 393 K. Fetherolf proposed, unlike Brill, that Equation (2-5) does not occur in the condensed phase or near-surface region, but rather takes place in the luminous region of the flame. He still concluded that the first step in decomposition is proton transfer and predicted a condensed-phase heat release of

-300 cal/g; however no mechanism was proposed to account for this large heat release. Korobeinichev estimated the activation energy for Equation (2-2) to be between 50-52 kcal/mole. A comparison of the surface mole fractions measured by Brill and Fetherolf is presented in Table 2-5. The data are fairly consistent, both report large amounts of H_2O and N_2O leaving the surface and similar minor product mole fractions. The major difference is Fetherolf reports three times more AN(s) than reported by Brill.

Table 2-5: Comparison of experimental surface species mole fractions for ADN pyrolysis.

Species	Brill et al.	Fetherolf et al.
NH_3	0.07	0.03
H_2O	0.33	0.31
N_2	0.13	0.13
NO	0.05	0.01
N_2O	0.22	0.29
NO_2	0.13	0.08
HNO_3	0.02	0.0
AN(s)	0.05	0.15

2.3.2.2 Decomposition Theory #2

Brill,[40] Russell,[56] and Fetherolf[51] all observed the same phenomena at low pressures, the emission of a solid aerosol of AN. Brill noted a white cloud of AN particles leaving the surface of ADN during his pyrolysis studies, but attributed its appearance to the recombination of NH_3 and HNO_3 upon entering the cool gas phase. He postulated that AN would not be present if combustion were taking place because NH_3 and HNO_3 would decompose to other species instead of recombining to AN. Russell agreed with Brill's conclusions. Fetherolf also observed the white particles leaving the surface, but noted once a luminous flame was established at 3 atm virtually no particles were seen leaving

the surface. The appearance of an AN aerosol is not unique to these authors, but other authors have developed a different theory as to why these white particles are present. This leads to a second theory on ADN decomposition.

Instead of proton transfer being the first step, the second theory proposes that AN forms by the removal of a N_2O group as represented by Equation (2-7).[36,38,41,52]

$$ADN(l) = AN(l) + N_2O(g) \tag{2-7}$$

Sinditskii[36,58] observed profuse amounts of white vapor that condensed as a fine white powder inside his experimental apparatus, and at the cold surfaces of his constant pressure window bomb. After examining the white powder, he noted that it consisted of not only AN, but also ADN. To be able to test at 1 atm, he used a 0.2% paraffin doped ADN sample. He then determined that ADN accounted for about 6% of the white residual at 1 atm. He observed that the ADN content decreases as pressure increases. Sinditskii attributed the presence of AN and ADN aerosols to the dispersion of some of the molten surface into the gas phase. Due to the high combustion rate and low heat feedback from the gas flame, gases apparently blow off of the surface, and take condensed material with them, resulting in an aerosol zone above the condensed phase. The dispersion causes the reaction layer and adjacent gas-phase region to be heterogeneous. Sinditskii attributed the aerosol zone to the physical impossibility of evaporating all of the condensed-phase substance without significant heat feedback from the flame. Thus, the condensed-phase material is carried off of the surface and reacts in the gas phase. Further, as pressure increases, the flame standoff distance decreases,

causing an increase in the condensed-phase decomposition rate, this results in the disappearance of condensed-phase material in the gas flow. Sinditskii believes the aerosol zone exists up to at least 20 atm and probably higher. Based upon the presence of ADN and AN as aerosols, Sinditskii proposed that the first step in ADN decomposition is the conversion of ADN to AN via Equation (2-7).

Using work performed by Feick[59] in the 1950's, Sinditskii calculated that the surface temperature of ADN corresponds to the dissociation temperature of AN via Equation (2-8). He theorized that, in general, the condensed species with the lowest dissociation temperature controls the surface temperature of a reacting substance. In the case of ADN and AN, AN has the lower dissociation temperature and should control the surface temperature. Sinditskii stated that this idea is similar to a thermodynamic phase change where the temperature remains constant until the entire change is complete. Therefore, he proposed that AN dissociation controls the surface temperature and ADN dissociation controls the aerosol zone temperature via Equation (2-2).

$$AN(l) \rightarrow NH_3(g) + HNO_3(g) \tag{2-8}$$

Sinditskii also noted that the surface temperature of atmospheric ADN combustion did not change with initial temperature. This supports the hypothesis that ADN surface temperature is controlled by a thermodynamic event such as boiling or dissociation. Figure 2-7 shows Sinditskii's proposed gas-phase temperature profile. However, Sinditskii noted that the heat release from the conversion of ADN to AN is not sufficient to warm-up, melt, and dissociate all of the condensed-phase material, therefore

other exothermic reactions must proceed simultaneously. He proposed that decomposition also follows the path outlined as theory #1. He stated that analysis of the condensed-phase products shows that about 60% of the ADN is converted to AN at atmospheric pressure. As pressure increases the conversion to AN decreases, but still remains significant. Therefore, all of the energy released from the reaction in Equation (2-7), (-33 kcal/mol), is consumed during dissociation of AN, (39 to 40 kcal/mol) and the net heat release from the conversion of ADN to AN is slightly endothermic in the condensed phase. This would require the reaction path based on theory #1, which Sinditskii believes accounts for only 40% of the decomposition, to be responsible for all of the condensed-phase heat release during ADN decomposition.

Theory #2 is also supported by Strunin et al.,[38] Oxley et al.,[52] and Vyazovkin and Wight.[41,53] Vyazovkin and Wight discounted theory #1 because they did not detect NH_3 until late in the decomposition of ADN, whereas according to theory #1 it would be evident in the early stages of decomposition. Vyazovkin and Wight stated that the experimental method used by Brill[40] favors a gas-phase decomposition path and not a condensed-phase path, and that is why Brill detected large amounts of NH_3. They also proposed a parallel path leading to the formation of ammonium nitrite, but Sinditskii[36] stated that ammonium nitrite's dissociation temperature is lower than that of ADN or AN, and ammonium nitrite dissociation would control the surface temperature of ADN. Since, the surface temperature of ADN is higher than the dissociation temperature of ammonium nitrite, Sinditskii discounted the formation of ammonium nitrite in any significant amount. Sinditskii is the only author that supported aspects of both theories #1 and #2.

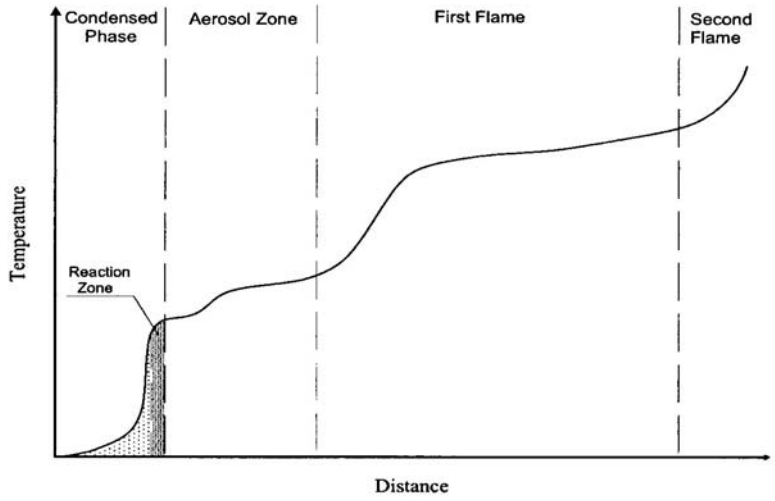

Figure 2-7: Gas-phase temperature profile proposed by Sinditskii for ADN.

2.3.2.3 Evaporation vs. Dissociation

Two schools of thought exist concerning ADN evaporation: some believe ADN evaporates to form ADN(v),[37,45,60,64] and others believe that it dissociates upon evaporation[36,52,61] via Equation (2-2). Theoretical work performed by Mebel et al.[60] examined three major configurations of ADN(v) using various *ab initio* methods; the ionic form $[NH_4]^+N(NO_2)_2]^-$, the isomer $[NH_3][HN(NO_2)_2]$, and the isomer $[NH_3][HON(O)NNO_2]$. He concluded that the molecular complex $[NH_3][HN(NO_2)_2]$ is the most stable form, and therefore, ADN(l) would most likely evaporate to $[NH_3][HN(NO_2)_2]$. Using this information, Mebel proposed a mechanism for ADN decomposition that is consistent with theory #1 and included ADN evaporation.

Korobeinichev et al.[37] and Shmakov et al.[45] performed experimental work that supports the view that ADN(l) evaporates to ADN(v). Using a two stage reactor they determined vapor pressure correlations for ADN, presented in Table 2-6 in Arrhenius form.

Table 2-6: Experimental values for ADN vapor pressure.

Author	A (dyne/cm^2)	E_A (kcal/mol)
Korobeinichev et al.	5.07×10^{22}	40.1
Shamakov et al.	2.75×10^{21}	37.0

The view that ADN dissociates upon evaporation is supported by Sinditskii,[36] Vyazovkin,[52,53] and Ermolin.[61] Sinditskii discounted the experimental evidence that ADN(v) exists. He found no evidence in his work to support the formation of ADN(v) and further stated that the theory used by Mebel to calculate enthalpies for molecular ADN complexes was appropriate for salts such as LiCl, but not for onium salts such as ADN. Sinditskii predicted a heat of vaporization of 22.5 kcal/mole based on experimental data, whereas Mebel calculated a value of 35.2 kcal/mole, further "proof" that Mebel's calculation is incorrect. Ermolin performed a numerical study of ADN evaporation in a flow reactor. He was unable to accurately simulate the experimental data when he assumed that ADN(v) was formed, but could simulate the data assuming ADN dissociates. Therefore, based on experimental and numerical data, Ermolin concluded that ADN dissociates upon evaporation.

2.3.3 Gas Phase Combustion

ADN has an interesting gas-phase behavior. At low pressures, the final flame temperature is hundreds of degrees below the adiabatic flame temperature (~2100 K). This observation has been reported by Fetherolf,[51] Korobeinichev,[37] Sinditskii,[36] Zenin,[42] and others. ADN also has numerous dark zones (see glossary) with the length and

number of the dark zones decreasing as pressure increases. Such trends have been observed both experimentally and theoretically.

2.3.3.1 Experimental Studies

Experimental work has been performed by a number of experimentalists concerning ADN's gas phase, and in general their results are consistent. One of the most comprehensive data sets was obtained by Zenin. He recorded temperature profiles for the gas-phase region of ADN for pressures ranging from 1 to 70 atm and for four different initial temperatures. He also measured or calculated burning rate, heat flux at the surface, condensed-phase heat release, surface temperature, dark zone lengths, and a number of other properties. However, no species concentrations were reported. The temperature profiles determined by Zenin are presented in Figure 2-8 for an initial temperature of 293 K and pressures from 1 to 60 atm. Note that the adiabatic flame temperature is not reached until 60 atm.

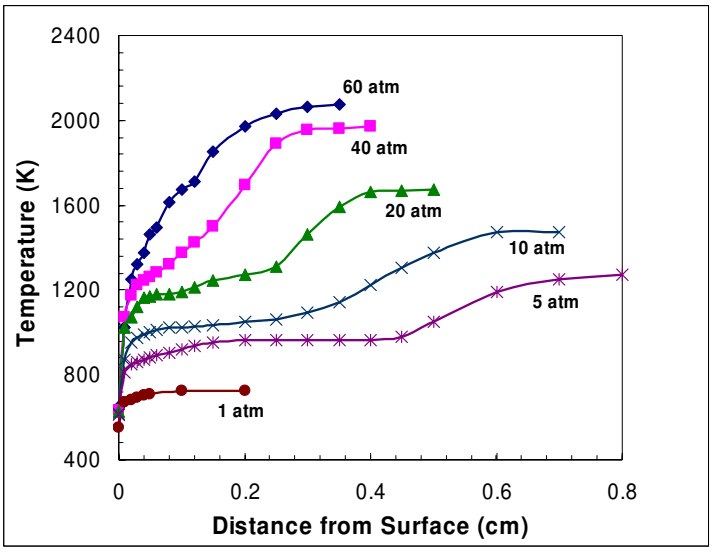

Figure 2-8: ADN gas-phase temperature profiles measured by Zenin.

Korobeinichev[45,37,55] has conducted numerous experimental and numerical studies of ADN combustion. Korobeinichev performed experimental studies of the gas phase of ADN for pressures of 1, 3, and 6 atm. He determined surface temperatures, burning rates, and species and temperature profiles in the gas phase. Due to experimental limitations, measurements were not taken at a distance closer than 4 mm to the propellant surface. He noted that a visible flame was not present at 1 atm or 3 atm and the final temperature did not approach the adiabatically predicted temperature. Species and temperature profiles are presented in Figure 2-9 for a pressure of 6 atm; note that the measurements began 4 mm from the surface.

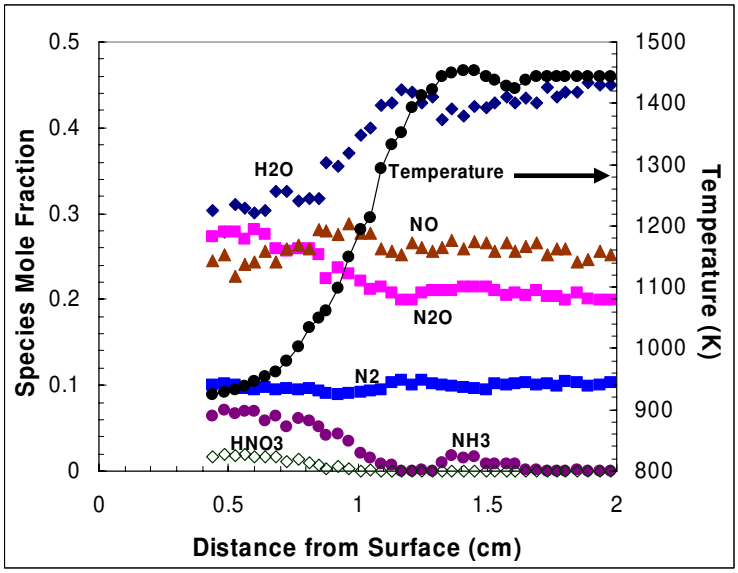

Figure 2-9: Species and temperature profiles measured by Korobeinichev for ADN at 6 atm.

Korobeinichev also determined the final species for the flameless combustion at 1 atm and 3 atm. These results are presented in Table 2-7. Table 2-8 presents the thermodynamically predicted products at 1 atm using the Edwards Equilibrium Code.

Calculations at higher pressures using the equilibrium code vary only slightly from the calculation at 1 atm. Comparing the two tables illustrates that a number of gas-phase reactions are not taking place at these pressures because equilibrium is not reached.

Sinditskii[36] measured temperature profiles in the gas phase of reacting ADN. He concluded that three different flame zones exist in the gas phase as presented above in Figure 2-7. Sinditskii proposed that AN(l) dissociation controls the condensed phase, and therefore, the initial temperature in the aerosol zone is that of AN dissociation. Once AN dissociates, ADN(l) then decomposes, determing the temperature leaving the aerosol zone. The aerosol zone was named because Sinditskii postulated that liquid material is dispersed into the gas phase due to ADN's high burning rate. In Figure 2-8, Zenin's work, it appears that the aerosol zone and first flame zone are present at 5 atm supporting the idea of an aerosol zone. The second flame zone appears at higher pressures and could be present at lower pressures if heat losses could be minimized.

Table 2-7: Final species mole fractions, temperature, and burning rate for ADN determined by Korobeinichev.

P(atm)	NH_3	H_2O	NO	N_2O	NO_2	HNO_3	N_2	b_r(cm/s)	T_{final} (K)
1	0.18	0.17	0.01	0.16	0.38	0.07	0.03	0.344	~625
3	0.08	0.27	0.23	0.23	0.07	0.035	0.08	1.2	~825

Table 2-8: Adiabatically predicted final species and temperature for ADN.

P(atm)	NH_3	H_2O	NO	N_2O	NO_2	HNO_3	N_2	O_2	T_{final} (K)
1	0	0.4	0.006	0	0	0	0.4	0.2	2057

2.3.3.2 Theoretical Studies

Ermolin[62] developed one of the first detailed ADN gas-phase mechanisms in the mid 1990's. One of the primary focuses of the study was to predict the formation of AN aerosol during ADN combustion at pressures below 3 atm. Comparison with temperature and species data gives varying results, and no burning rates were predicted for monopropellant combustion. In 2004 Ermolin[61] presented a new mechanism containing 218 reactions for ADN combustion. The primary focus of Ermolin's study was examining the vaporization of ADN. Calculations were performed to determine if ADN(l) evaporated to ADN(v) or if it dissociates upon evaporation to NH_3 and DA instead. Numerical calculations best matched experimental data if ADN(l) was assumed to undergo dissociative evaporation.

Lin and various collaborators[60,63] have performed a large amount of work to determine reactions and kinetics for gas-phase reaction mechanisms using *ab initio* methods. Their work has been used to successfully model numerous other oxidizers and binders such as HMX, RDX, and GAP.[8] The gas-phase structure of ADN(v) was studied by Mebel and Lin.[60] Their study determined that the molecular salt complex is not the most stable form of ADN(v); instead they determined that the $[NH_3][HN(NO_2)_2]$ complex had the lowest local minima on the potential energy curve, and thus is the most stable form of ADN(v). This form has a hydrogen bond between the NH_3 and $N(NO_2)_2$ molecules. These findings give credence to the existence of dinitramic acid ($HN(NO_2)_2$), and support the theory that the first step in ADN decomposition is NH_3 + $HN(NO_2)_2$. Other useful parameters were also calculated by Mebel, such as activation energies and

enthalpies of formation for molecules unique to ADN, formed in the first steps of decomposition.

The work by Lin and others formed the basis of a study published by Liau et al.[64] in which a gas-phase mechanism was developed for ADN. The study used experimental species, temperature, and burning rate data determined by Korobeinichev[37] as the initial conditions for the gas-phase calculations. Good agreement was achieved with the experimental temperature and species profiles. Calculations started 4 mm from the surface, where the data were collected, and no burning rate was determined; rather burning rate was an input to the model. Liau stated that if ADN dissociated to NH_3, DA, N_2O and HNO_3 at the surface, then he was unable to accurately predict the gas-phase flame structure. In a second study, he concluded that the proposed condensed-phase mechanisms are inconsistent with the measured gas-phase species.[65] Liau suggested further investigation into the initial decomposition of the condensed and gas phases.

Korobeinichev[45,66] has also presented a number of papers containing results of modeling ADN's gas phase using detailed gas-phase kinetics. His reaction mechanism was similar to Liau's. Korobeinichev used the same data set and initial conditions to model the gas phase and obtained similar results to those of Liau. He also estimated the activation energy for ADN gas-phase decomposition, Equation (2-2), as 12 kcal/mol. This value was used in both the Korobeinichev and Liau mechanisms. Korobeinichev asserted that ADN(c) evaporates to ADN(v) and then decomposes in the gas phase.

A summary of the gas-phase mechanisms developed to study ADN combustion is presented in Table 2-9. However, none of the studies attempted to link the condensed and

gas phases to determine a burning rate for ADN. They were all purely gas phase studies, with burning rate as an input parameter.

Table 2-9: Detailed gas-phase mechanisms developed to date for ADN combustion.

Author	# of Species	# of Reactions
Ermolin (1996)	26	256
Liau et al. (1998)	33	180
Korobeinichev (2001)	33	172
Ermolin (2004)	34	218

2.3.4 Summary and Shortcomings of Previous Work

Experimental data are far more plentiful for ADN than for AP. The data give insight into the condensed-phase decomposition and have resulted in a number of proposed condensed-phase decomposition mechanisms. Over the last ten years much work has been devoted to developing detailed gas-phase mechanisms, and as a result, four mechanisms have been developed for ADN combustion. However, no previous work has combined both the condensed and gas phases of ADN to predict a burning rate. All numerical studies have only focused on the gas phase, with burning rate as a boundary condition. Given the large amount of experimental data, a coupled condensed/gas phase model of ADN could be developed.

2.4 AP/HTPB Composite Propellant Combustion

Ammonium perchlorate based composite propellants typically consist of multi-modal distributions of AP and aluminum particles in a polymeric binder such as HTPB. One of the desirable characteristics of AP composite propellants is the dependence of

their burning rates on the size distribution of AP particles used. In general, as the amount of fine AP particles increases in a propellant, so does the overall burning rate. A predicted particle-size dependence of an AP/HTPB propellant's burning rate is illustrated graphically in Figure 2-10.[2] Note that large particles (>100 μm) begin to approach the monopropellant burning rate of AP, whereas increasingly smaller particles increase the burning rate of the propellant until a premixed limit is reached. The shape of the curve presented in Figure 2-10 varies with propellant formulation and pressure.

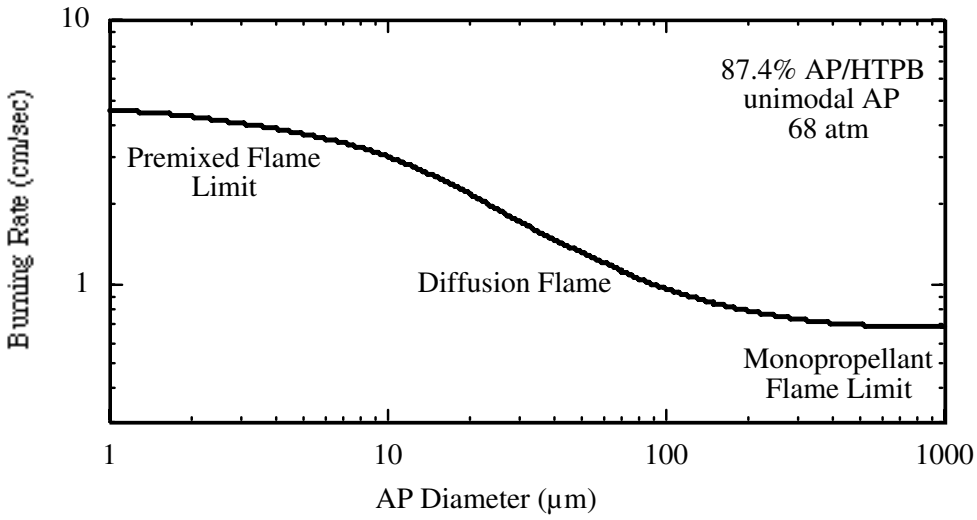

Figure 2-10: Predicted particle-size dependence of AP burning rate at 68 atm.

Determine burning rate versus particle size curves and understanding the reasons for AP's particle size effects is a very daunting task both experimentally and theoretically. Numerous studies have been dedicated to understanding AP combustion over the last half century.

2.4.1 Experimental Studies

Combustion of composite propellants is a very complicated process and is influenced by particle size distribution, weight percent of additives, initial temperature, pressure, interactions between ingredients, and other variables. Such a complicated process is extremely difficult to evaluate experimentally. Experimental procedures have been developed that attempt to isolate the effects that an individual parameter has on composite propellant combustion.

2.4.1.1 Particle Size and Particle-Size Distribution Effects

Foster et al.[67] studied the effects of AP particle size on propellant burning rate. In the study, monomodal propellants were created using 12 μm AP particles and HTPB with three different oxidizer weight fractions: 75%, 77.5% and 80 %. The burning rate for each propellant was measured, and the results are presented in Figure 2-11 (solid lines). Foster reported that as the weight fraction of oxidizer increased, so did the propellant's burning rate, a typical result for AP. Foster then included 400 μm AP particles with the 12 μm AP particles creating a bimodal distribution. The fine AP to binder ratio was kept the same as in the monomodal propellants with only the amount of coarse AP varying. A summary of the composite propellant formulations used by Foster is given in Table 2-10 and burning rate results for the bimodal propellants are presented in Figure 2-11 (dashed lines).

Experimental results show that the inclusion of coarse AP particles decreases the burning rate for all propellants when compared to the combustion of monomodal fine AP propellants. Therefore, Foster concluded that combustion properties of AP composite

Table 2-10: Foster's oxidizer weight distributions for monomodal and bimodal composite propellants.

Monomodal Propellants		Bimodal Propellants			Fine AP/Binder ratio
12 µm AP %	Binder %	400 µm AP %	12 µm AP %	Binder %	
75.0	25.0	44.0	42.0	14.0	3/1
77.5	22.5	37.8	48.2	14.0	3.44/1
80.0	20.0	30.0	56.0	14.0	4/1

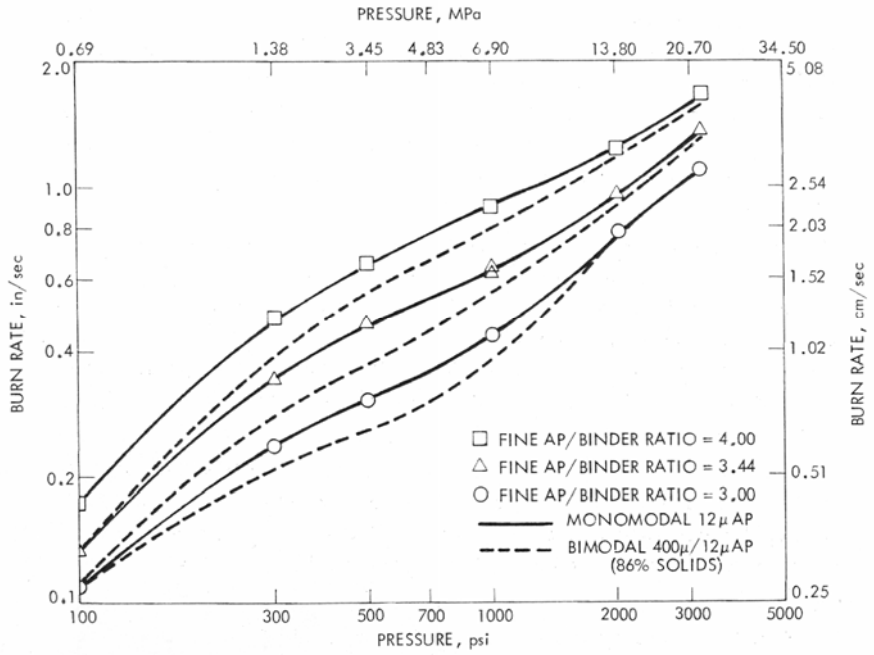

Figure 2-11: Burning rate versus pressure for Foster propellants reported in Table 2-10.

propellants are controlled by fine AP/binder interactions. He further stated that the effect of coarse AP particles on burning rate is to absorb the energy required to ignite the fine AP-binder mixture and thus slow combustion. Foster then replaced the 400 µm AP particles with 200 µm particles. This had only a minor effect, slightly increasing the burning rate above that of the 400 µm formulation. Also, coarse RDX was substituted for coarse AP and the RDX propellants were seen to behave identically as those with coarse AP. Therefore, as fine AP is replaced by coarse particles (AP or RDX) the burning rate of

the propellant decreases. These results further support Foster's conclusion that the fine AP-binder mixture dominates propellant combustion.

Miller et al.[68] performed a systematic experiment in the mid 1970's varying only the oxidizer size distribution in a series of 25 composite propellant formulations consisting of only AP and HTPB, all at the same AP loading fraction. Miller observed that as the width of the particle size distribution increased, so did the value of the burning rate pressure exponent. He concluded that it was possible to have the same propellant burning rate with a different pressure exponent based solely on the width of the particle size distribution. Miller also noted that the burning rate increased as the weight fraction of fine AP increased. In a second study, Miller et al.[69] proposed that individual AP particle flames interact, and therefore, particles cannot be assumed to burn independently of each other, as assumed by some models.

2.4.1.2 Sandwich Propellants

Combustion of a composite propellant is an inherently complex, three-dimensional problem. Although condensed-phase decomposition for each ingredient is believed to occur as it does in the monopropellant, the gas-phase reactions are very complicated as species interact between ingredients in the form of diffusion flames. Sandwich experiments are an attempt to evaluate solid propellant diffusion flames in two-dimensional space. A sandwich is created by "gluing" two rectangular pieces of oxidizer together with a piece of binder.

Boggs and Zurn[70] conducted sandwich propellant studies using sample sizes of 25, 127, and 250 μm thick binder slices sandwiched between two 750 μm thick slices of AP, simulating extremely large AP particles. Tests were conducted at pressures from 100

to 1000 psi. They observed three main trends. First, the binder became liquid and could flow onto the oxidizer; however, for HTPB the flow was quite viscous, and therefore, mixing with the oxidizer was limited. Secondly, the maximum regression rate occurred in the AP slices. As pressure increased, AP regressed much more rapidly than the binder, leaving the binder protruding above the oxidizer in a "Christmas Tree" configuration. Finally, no evidence for interfacial interactions was observed between the binder and the AP.

Price et al.[71,72] systematically examined the effects of binder thickness, with an emphasis placed on attempting to achieve actual propellant scales. Results were similar to those reported by Boggs and Zurn for binder thicknesses above 70 μm. However, at binder thicknesses below 70 μm, the binder became recessed below the oxidizer instead of protruding above the surface. Binder thicknesses well below 70 μm are far more typical in standard propellants. Chorpening et al.[73] reported that the binder thickness became important below 100 μm in their sandwich propellant studies. Also, Price observed an individual AP flame, diffusion "flamelets" along the interface, and a smooth melt band at the interface of the sandwiches. He further noted that binder protrusion or recession varies with pressure as well as binder thickness. The pressure deflagration limit of AP is substantially lowered with the inclusion of binder as compared to AP monopropellant. Price observed that below 10 MPa the burning rate of an AP/binder composite propellant with "optimal" binder thickness is faster than the AP monopropellant rate. Above 10 MPa the burning rate is approximately equal to the AP monopropellant rate, and no high pressure "U" shape trend is observed in the propellant burning rate curve as seen in Figure 2-4 for the monopropellant.

2.4.1.3 Pressure Effects

Particle size effects are also influenced by pressure, and the impact of pressure on the flame structure above an AP/HTPB propellant is not fully understood. General trends are known for both premixed and diffusion flames, separately. Combustion of premixed flames is controlled by chemical kinetics, which are proportional to pressure. Therefore, an increase in pressure is expected to increase reaction rates, thus shortening the flame stand-off distances for premixed flames. On the other hand, diffusion flames are relatively pressure independent due to the dominance of diffusion over kinetics. Diffusion is proportional to ρD_{iff}, where density (ρ) is proportional to pressure, and diffusivity (D_{iff}) is inversely proportional to pressure. Therefore, the pressure dependence essentially cancels out and pressure should have little impact on the location of a diffusion flame. However, the flame structure above the AP/HTPB system is a combination of both premixed and diffusion flames and, therefore, is far more complex. An increase in pressure should still draw the premixed monopropellant flame closer to the surface. This will greatly impact the diffusion flames due to higher temperatures closer to the surface and different species densities throughout the flame structure.

Boggs et al.[74] performed qualitative work examining the effect of AP particle size and pressure. Samples of composite propellants consisting of AP and a binder were burned at pressures ranging from 15 to 800 psi. Once the sample reached steady-state combustion, the chamber was rapidly depressurized, thus quenching the sample. Using SEM to examine the quenched samples, Boggs observed that AP particles protruded above the binder at low pressures (~<400 psi) and were recessed at higher pressures (~800 psi). The results indicate that the regression rate of the homogenized binder

containing fine AP particles is greater than the regression rate of AP at low pressure, but as pressure increases, the regression rate of the AP particle overtakes the rate of the homogenized binder. Lee et al.[75] also observed that at sub-atmospheric conditions, 400 μm AP particles protrude above the surface of the propellant, but are recessed at pressures above ~450 psi. These results indicate a changing flame structure above the propellant as pressure changes, analogous to the change in flame structure observed in the sandwich propellant data.

2.4.2 Numerical Studies

Ammonium perchlorate composite propellants have been the subject of numerous numerical studies for the last half century. Various numerical models have been developed in an attempt to predict the effects of changing propellant formulation and operating conditions on the complex combustion of composite propellants. These models have progressed through various levels of complexity, from one-dimensional to multi-dimensional models, and from global or semi-global gas-phase kinetics to detailed reaction mechanisms with tens of species and hundreds of reactions.

The BDP Model[1,2] represents the most widely accepted theory as to AP's unique combustion properties when mixed with a binder. The model is based on the physical picture illustrated in Figure 2-12, and proposes that three distinct flames exist above the surface of composite propellant: 1) A primary diffusion flame between the AP decomposition products and the binder decomposition products, 2) A premixed flame due to the combustion of the AP monopropellant, and 3) A final diffusion flame between the AP monopropellant flame products and the binder products (mixed with the primary

diffusion flame products). The primary diffusion flame is assumed to be a dominant driving force in AP composite propellant combustion.

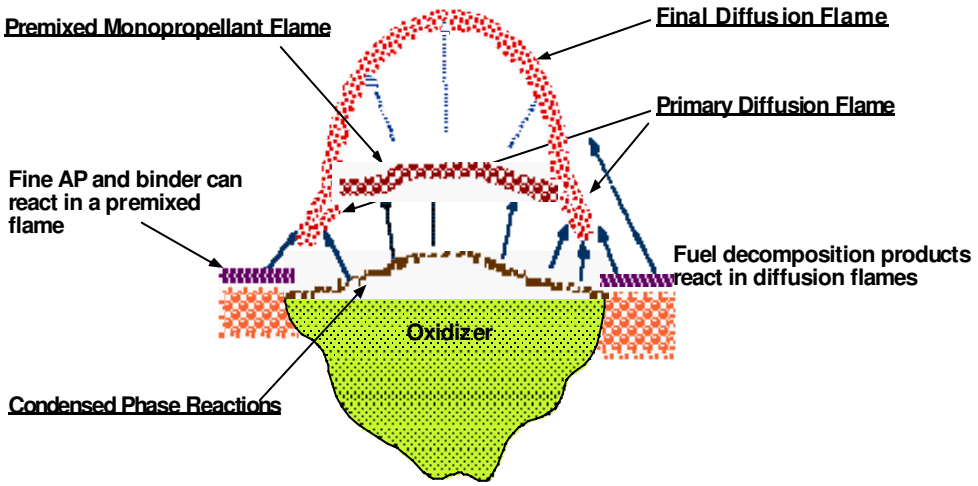

Figure 2-12: BDP Model physical picture.

In the BDP model, the flame structure above the surface is dynamic, varying within the lifetime of a particle and with pressure. Large AP crystals burn more slowly than small particles, being driven primarily by the relatively cool premixed self-deflagration AP flame above their surface. The decomposition products from very small particles in the binder matrix are able to mix intimately with binder pyrolysis products, resulting in an approximately one-dimensional hot premixed flame over the binder. Combustion of particles of intermediate diameter is driven by a combination of these effects, with hot diffusion flames near the particle edges competing with the self-deflagration flame for AP decomposition products. This flame structure provides spatially-varying heat feedback to the surface and a single particle could be controlled by all three different flame structures during its lifetime.

The BDP flame structure also varies with pressure. This is because a premixed flame is pressure dependent (due to its dependence on gas-phase reaction rates), whereas a diffusion flame is relatively pressure independent (based on diffusivity, ρD, in which pressure dependencies are mutually exclusive). Therefore, as pressure changes so does the importance of the various flames in the model. At low pressure the monopropellant flame is relatively far from the surface, and therefore, combustion is dominated by the kinetic aspects of the primary diffusion flame. As pressure increases the monopropellant flame standoff distance decreases, and eventually contributes more to the surface heat flux, competing with the primary diffusion flame. At even higher pressures, the monopropellant flame becomes the dominant mechanism. At all pressures, the final diffusion flame is assumed to be too far from the surface to contribute significantly to the decomposition rate.

2.4.2.1 Premixed Flame Assumption

If a composite propellant consists of fine AP particles only, then it may be possible to assume that the decomposition products from the oxidizer and binder are all virtually premixed. Such an assumption allows one-dimensional models to be developed to represent the composite propellant. To this end, Korobeinichev et al.[76,77] created what they assumed to be a homogeneous composite propellant consisting of 77% AP (<50 μm) and 23% polybutadiene rubber. The gas flame was then studied with a mass-spectrometer, and a detailed kinetic mechanism was developed to model the results. The mechanism consisted of 49 species and 243 reactions. Results were reported to be "satisfactory," however; wide deviations were present between the experimental and

calculated final flame temperature (20% deviation) and oxygen concentration profile (off by a factor of 2).

Jeppson[9] also developed a model to examine the premixed combustion of fine AP/HTPB propellants. AP particles were assumed to be small enough to simulate a homogeneous propellant. The model was intended to be valid for low to moderate pressures and was based on a detailed gas-phase mechanism consisting of 44 species and 157 reactions. Figure 2-13 presents some of the results obtained by Jeppson compared against data from Foster[67] (see Figure 2-11). The model appears to be valid up to a

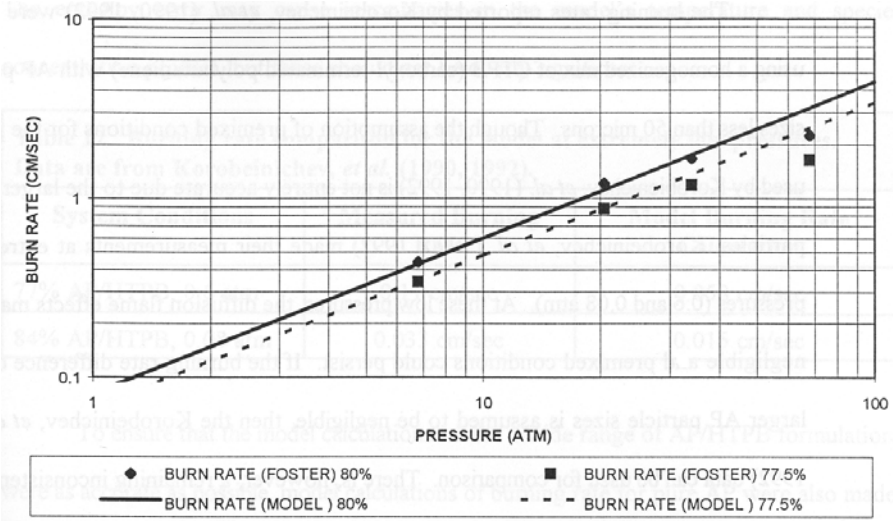

Figure 2-13: Comparison of Jeppson AP/HTPB model to Foster data.

pressure of ~35 atm, but at higher pressures the premixed assumption is apparently no longer valid, and the model over predicts burning rate.

2.4.2.2 Diffusion Flame Studies

The premixed assumption is only valid for small AP particles, and the size at which the assumption is valid varies with pressure. Due to the importance of diffusion flames in AP combustion, according to the BDP model, a number of numerical models have been developed to take into account multi-dimensional diffusion.

A classical problem of combustion modeling is that of the two-dimensional diffusion flame as depicted in Figure 2-14[3] and outlined by Williams.[78] Two typical configurations are illustrated. The first configuration is an overventilated flame where the amount of oxidizer exceeds the amount of fuel resulting in a candle-like flame. The second flame is underventilated. There is excess fuel resulting in a disconnected flame. The earliest theoretical description of the laminar diffusion flame was by Burke and Schumann, published in 1928.[79] Their analytical solution was one of the initial methods utilized to examine diffusion in AP composite propellants.

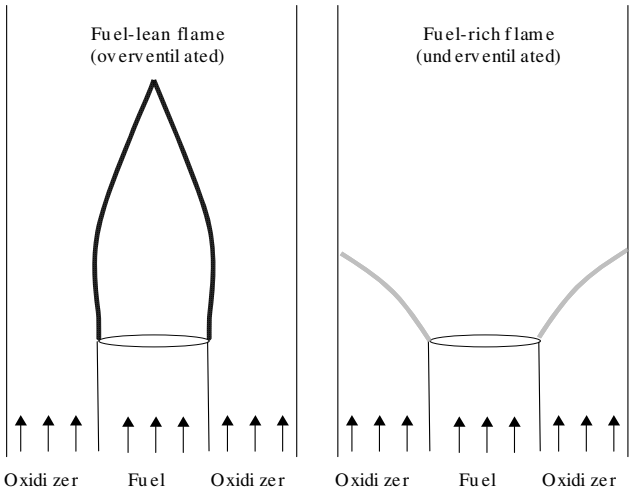

Figure 2-14: Typical setup of a confined diffusion flame in axisymmetric ports.

Numerous models were proposed during the 1950's and 60's to try to explain the unique interaction of AP and binder with varying results. Hermance[80] proposed a heterogeneous reaction between the gas-phase oxidizer species and solid binder. He also proposed the idea of a final diffusion flame; however numerical calculations produced mixed results.

The BDP[1] computer model was developed in the 1960s and early 1970s and was a one-dimensional mathematical representation of the BDP flame structure (outlined in section 2.4.2). Three different global reactions were used to describe each flame. The locations of the primary and final diffusion flames were determined using a modified Burke-Schumann solution. This allowed for the heat feedback from each flame to the surface to be calculated. A spatial averaging method was then used to determine an overall propellant burning rate with particle size effects. The model predicted pressure, particle size, temperature, and concentration effects more accurately than previous models.

The BDP model has since served as the basis for a number of models. Cohen and Strand[81] added a separate energy equation for the binder to allow for different surface temperatures between AP and the binder. Ermolin[82] developed a methodology for predicting kinetic parameters for global reactions to be used in a BDP-type model. Beckstead[83] modified the method to allow for separate surface temperatures between the binder and oxidizer. Also, instead of determining the composite propellant burn rate based on spatial distributions, a time averaging approach was developed. This approach, in effect, determined burning rates at different locations in the propellant, and used those burning rates to determine an average overall burning rate. Numerous reviews have been

undertaken concerning combustion models of composite propellants throughout the years.[84,85,86,87,88]

Determining burning rate from composite propellant models is of great importance. The BDP model has used two different methods, spatial and time averaging. Miller[89] evaluated these two methods and concluded that the spatial average method is unsatisfactory because all particles of a given size are assumed to be in a common plane and the surface is presumed to be flat. He also concluded that time averaging is unsatisfactory because it makes no allowance for the possibility that the fastest burning path through the propellant may zigzag. Instead, he proposed a statistical method in which it is possible for the fastest path to transition between rays or paths to find the fastest rate of combustion. He used a Monte Carlo technique to determine the fastest propagation rate assuming transition could take place during binder pyrolysis or particle ignition. However, the model requires six empirical correlations for each pressure. Miller et al.[90] further refined this methodology and developed a computerized model based on percolation theory to find the fastest path.

A more theoretically based composite propellant model was presented by Tanner et al.[91] The model uses a three-dimensional, multi-modal particle packing code to better simulate the geometry of an actual composite propellant. The fastest path is then chosen based on individual burning rates of binder and oxidizer particles. Burning rates are determined using PHASE3. Use of PHASE3 eliminates the need for empirical relations for monopropellant combustion properties. All properties are calculated by PHASE3. GAP/RDX heterogeneous mixtures were examined using this method and were found to

be in agreement with high pressure data. However, the model did not account for two-dimensional diffusion between ingredients.

Concurrent with the advancements in propellant modeling has been development of detailed kinetic mechanisms to describe the gas-phase combustion reactions. Beginning with the 14-step chain reaction mechanism of Guirao and Williams,[28] there have been several mechanisms proposed for the combustion of pure AP.[92,93,94] Mechanisms have also been developed for homogeneous AP composite systems.[76,95] These detailed mechanisms have been applied in one-dimensional propellant models, for both premixed and counterflow[96,97] geometries, as well as a limited number of two-dimensional models using simple gaseous hydrocarbons rather than polymeric binders.[98,99] While there are little detailed species and temperature profile data for flames above AP and AP composite propellants with which to compare,[21] the counterflow and coflow modeling with gaseous hydrocarbons has shown good agreement with available experimental results.[96,99,100]

Extensive work has been performed at the University of Illinois by Buckmaster, Jackson, and co-workers to develop a two- and three-dimensional methodology to describe the geometric effects within solid propellants.[101,102,103,104,105] The complex unsteady heat transfer and propellant surface regression through oxidizer/binder sandwiches, and two- and three-dimensional random packs of propellant particles has been modeled using two- and three-step reaction mechanisms to describe the gas-phase heat release. The major focus of the work is to accurately simulate the propellant surface and predict the heterogeneous combustion rate. However, computational limitations and their chosen kinetics limit their progress. Their latest combustion model assumes a three

flame model similar to the BDP model. However, their validation calculations have been limited to four propellant formulations with 20-30% error for three data sets and 100% error for the fourth. Considering the fact that there are 11 constants in their kinetic model, and they treat them as arbitrary constants, their validation is not impressive.[4] As part of the work, a methodology was employed to capture the complexity of the three-dimensional surface and track its regression, i.e. the level set method.[106,107]

Felt[3] developed a two-dimensional, steady-state model with a detailed gas-phase kinetic mechanism to examine the flame structure above an AP particle and AP/HTPB binder. The model simulates the combustion of an AP particle surrounded by AP doped HTPB binder. Boundary conditions at the surface are based on previously published one-dimensional models for AP[7] and AP/HTPB.[9] Results agreed qualitatively with the general concepts of the BDP model[1] of composite propellant combustion. However, only preliminary results were obtained and the code takes well over a week to converge, running on multiple processors, and must be restarted numerous times.

2.4.3 Summary and Shortcomings of Previous Work

The BDP model gives insight into the structure of the AP/HTPB gas-phase flame, but to date only one model has been developed to examine the flame structure of a heterogeneous mixture of AP/HTPB using detailed kinetics, the Felt model.[3] However, only preliminary results were obtained. All other AP/HTPB composite propellant models assume global kinetics or one-dimensional flames, so they are unable to predict the details of the gas-phase flame structure. The work by Jackson[101,102,103] has been very in depth pertaining to the propellant's solid phase and surface structure, but has trivialized the gas phase reaction kinetics. Only recently have they switched from using two

reactions, which account for the monopropellant flame and the final diffusion flame, to three reactions to include a primary flame. Such an approach assumes the make up of the gas phase and cannot predict its actual flame structure *a priori*. The work by Jackson focuses on the geometric surface effects and trivializes the gas-phase reaction kinetics. The work by Felt focuses on the gas-phase and trivializes the propellant geometry. The method developed by Tanner[91] to determine a composite propellant burning rate does not take into account the influences of diffusion flames between particles. Therefore, it cannot correctly model AP containing propellants. Also, initial results by Tanner et al. indicate that diffusion flames may affect the combustion of GAP/RDX mixtures, but no two-dimensional gas-phase flame structure studies have been performed on such mixtures.

2.5 Summary and Objectives

The previous gas-phase mechanism used for AP monopropellant combustion was largely developed in the 1980s; therefore, many of the reactions used in the mechanism are suspect as to their accuracy. Extensive theoretical work has been performed by Lin in the last 10 years to develop elementary gas-phase reactions pertinent to AP monopropellant combustion. The BYU gas-phase comprehensive mechanism has been successfully applied to non-chlorine containing ingredient, but needs to be expanded to include AP. Expansion of the comprehensive mechanism to include AP gives further credence to the validity of the mechanism and also utilizes the most up to date work pertaining to AP combustion.

As a possible substitute for AP, an ADN model is desired which can accurately calculate ADN combustion properties. Previously, ADN models used detailed gas-phase kinetics for gas-phase calculations only. Those models were unable to predict combustion properties such as burning rate and temperature sensitivity, and therefore, a more detailed ADN model is desired.

The flame structure above an AP/HTPB composite propellant needs to be examined in detail. The diffusion flame model developed by Felt allows for two-dimensional calculations using detailed gas-phase kinetics. However, the Felt model suffers from long runtimes, and problems with stability, accuracy, and robustness. These shortcomings must be addressed to obtain any sizeable study on the AP/HTPB flame structure. The flame structure needs to be examined in relation to particle size, pressure, and formulation in such a way that the calculations can then be applied to actual propellants.

3 Development of an AP Monopropellant Combustion Model

Ammonium perchlorate is a key ingredient in many solid propellant formulations because AP has the unique ability to greatly influence solid propellant burning rates by varying only the particle size. Detailed numerical models are a key aspect to gaining an understanding of AP's unique properties. Previously, a one-dimensional model had been developed for AP monopropellant combustion by Jing[7] at BYU utilizing PHASE3.[5] The detailed gas-phase kinetic mechanism was based largely on the work of Ermolin[30,32,76] and was coupled with a semi-global condensed-phase mechanism. The AP model accurately predicted combustion properties, including burning rate and final species. However, the gas-phase kinetic mechanism was unique to AP, and attempts to incorporate part or all of the AP kinetic mechanism into other ingredient mechanisms have yielded poor results when modeling non-chlorine containing ingredients. Also, attempts to utilize the Puduppakkam comprehensive mechanism[11] to model AP have resulted in poor burning rate and final species calculations.

To develop a new AP mechanism that was consistent with the comprehensive mechanism, it was necessary to review available experimental and numerical studies to gain understanding into the combustion of AP. It was also necessary to investigate the condensed-phase mechanism developed by Jing[7] and determine its accuracy when used with the new comprehensive mechanism. The methodology involved in developing a new

condensed-phase mechanism and the necessary additions to the comprehensive mechanism to model AP are presented. Results are presented using the new model. Attention is also given to deficiencies of the current gas-phase kinetics available to model chlorine reactions.

3.1 Methodology to Develop New AP Model

The basis for the calculations in this work is the Puduppakkam[8] comprehensive mechanism for C, H, O, N and the 57 Lin[15] reactions for Cl species. Hereafter the combination of the two reaction sets will be referred to as the universal mechanism. Modifications to this universal mechanism will be outlined with the corresponding effects to the numerical solution. This methodology section is provided to illustrate the deficiencies of the universal mechanism in an attempt to focus future work on developing better combustion mechanisms.

3.1.1 Jing Condensed-Phase Mechanism

The condensed-phase mechanism developed by Jing consists of four high-temperature condensed-phase reactions which account for 70% of the decomposition (see Table 3-1) and one low-temperature reaction which accounts for the experimentally observed 30% solid-phase decomposition. The model includes two separate phase transitions: the solid-solid phase transition at 513 K and the melting phase transition at 825 K. This condensed-phase model results in a very endothermic condensed-phase heat release of 173 cal/g. There is disagreement in the scientific community as to whether heat is consumed or released in the condensed phase during AP combustion,[22] and therefore, such a large endothermic heat release seems unreasonable. Also, at 0.6 atm, the surface

species calculated with the Jing condensed-phase mechanism differ greatly from the experimental data of Ermolin.[21] The Jing mechanism calculates far more NH_3 and $HClO_4$ than is measured experimentally (see Figure 3-1), which results in the very endothermic condensed phase.

Table 3-1: Previous AP condensed-phase mechanism developed by Jing.

Reaction	A (1/s)	E_A (cal/mol)
AP(C) → NH_3 + $HClO_4$	$4.0x10^{12}$	28,000
AP(C) → H_2O + O_2 + HCl +HNO	$1.0x10^{8}$	22,000
AP(C) → $2H_2O$ + Cl + NO_2	$5.0x10^{7}$	22,000
AP(C) → ClO_3 + NH_3 + OH	$1.0x10^{9}$	22,000

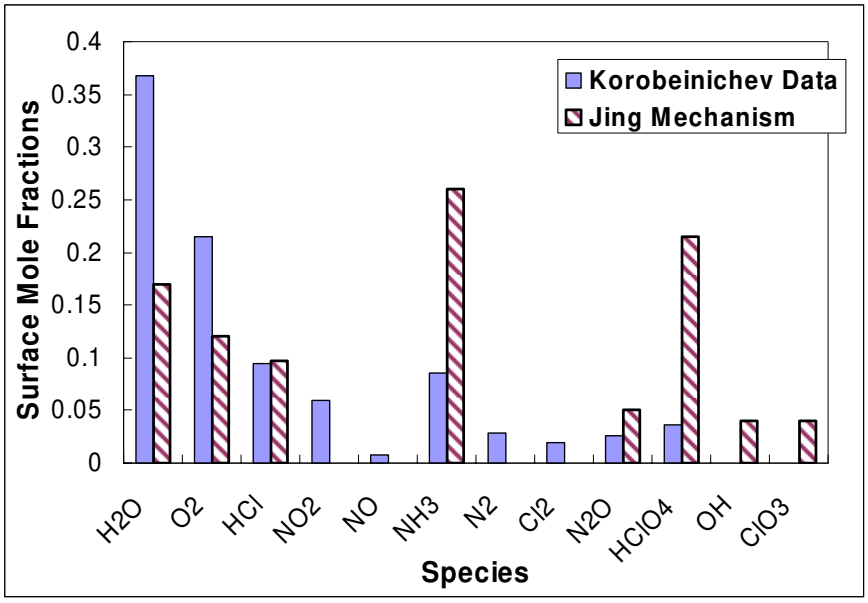

Figure 3-1: Comparison of Ermolin's AP surface species data and the calculated surface species using the Jing condensed-phase mechanism.

To evaluate the new universal gas-phase mechanism, calculations were performed combining the Jing condensed-phase mechanism and the universal gas-phase mechanism.

To fully examine the Jing condensed-phase mechanism, various permutations of the condensed-phase mechanism were evaluated. These include the unmodified version of the Jing mechanism, slightly modified condensed-phase reaction parameters; and inclusion of only some of the condensed-phase reactions proposed by Jing. Agreement with experimental data was found to be poor in all cases (see Figure 3-2); in fact, agreement with experimental burning rates and final flame temperatures appeared to be mutually exclusive goals. Generally, when good burning rates resulted, the final temperatures were found to be low by 200 K or more, and the final mole fractions of NO,

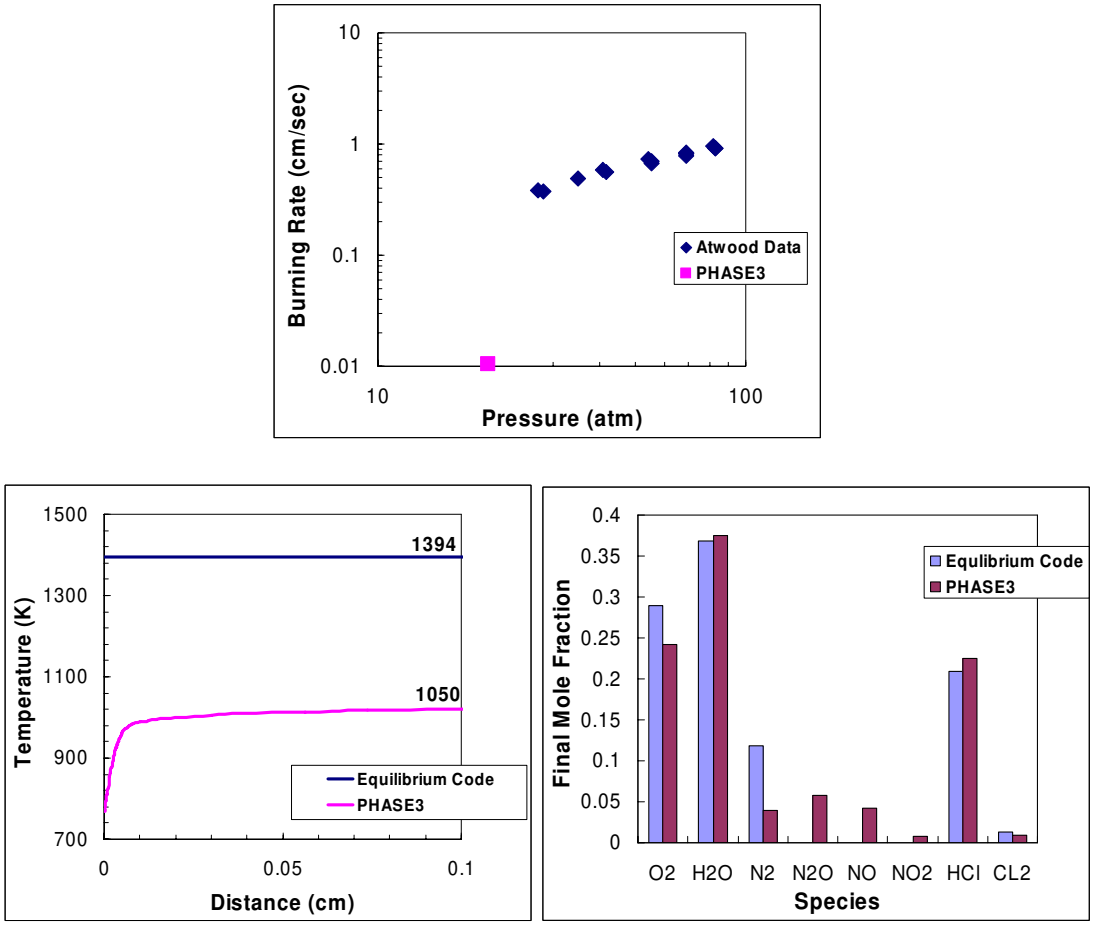

Figure 3-2: Results using the unmodified Jing condensed-phase mechanism and the universal gas-phase mechanism.

N_2O, and NO_2 were found to be very high. When the final flame temperature was within 100 K of the calculated adiabatic flame temperature (1394 K at 20 atm), the burning rate was found to be low by an order of magnitude. Therefore, it was concluded that the condensed-phase mechanism of Jing is incompatible with the universal gas-phase mechanism, although Jing's condensed-phase mechanism had worked well with Ermolin's gas-phase mechanism. The Jing condensed-phase mechanism is highly endothermic, and therefore, it relied on the inaccurate gas-phase kinetics in the Ermolin mechanism to achieve a large near-surface heat release. The same reactions are not present in the universal mechanism and thus, the gas-phase is unable to break down the initial species leaving the surface and combustion stalls. Numerical results using the unmodified Jing condensed-phase mechanism combined with the universal gas-phase mechanism are presented in Figure 3-2. As seen in the figure, the flame temperature is low by 350 K and the burning rate is low by an order of magnitude.

3.1.2 New Condensed-Phase Mechanism #1

The inaccuracies of the Jing condensed-phase mechanism, when used with the universal mechanism, led to the need to develop a new condensed-phase mechanism for AP. The approach taken has been to start from a single global reaction designed to initially match the Ermolin experimental data.[21] Note that use of a global reaction is seen as a first step and a more detailed condensed-phase mechanism can be investigated once any gas-phase mechanistic issues have been resolved. Using the Ermolin data as initial conditions yields poor results; therefore the global condensed-phase reaction was modified in an attempt to match the burning rate, final temperature, final species concentrations, etc, while still being fairly consistent with the Ermolin data. The

condensed-phase heat release is assumed to be exothermic on the order of -100 cal/g. Literature sources including works by Brill[22] and Behrens[20] were consulted to find reasonable species and concentrations for use in the condensed-phase mechanism. After dozens of iterations, Equation (3-1) was determined to satisfactorily represent the condensed-phase species leaving the surface and give a reasonable condensed-phase heat release.

$$16AP(c) \rightarrow 14O_2 + 18H_2O + 6N_2 + 4NH_3 + 7HCl + 3HClO_4 + 2H_2 + 2OH + ClO + ClO_3 + 4Cl \quad (3\text{-}1)$$

Equation (3-1) results in an exothermic condensed-phase heat release of -62 cal/g. The greater heat release is due to the assumption that far less $HClO_4$ and NH_3 are present at the surface as compared to the Jing mechanism. A comparison of the Ermolin[21] experimental data, the calculated surface species using the Jing mechanism, and Equation (3-1) is presented in Figure 3-3. The new mechanism agrees with the experimental surface species data far better than the Jing mechanism.

Calculations using the new condensed-phase mechanism/global reaction produced mixed results initially. At 20 atm, a burning rate of 0.24 cm/s is calculated, compared to the experimental value of 0.31 cm/s. The flame profile displays an unexpected slight peak in the temperature profile and a low final flame temperature. Figure 3-4 presents gas-phase calculations using the new condensed-phase mechanism and the universal gas-phase mechanism.

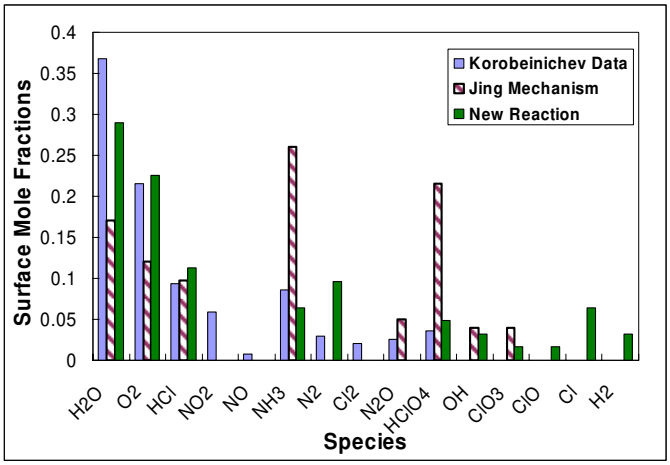

Figure 3-3: Comparison of Ermolin's AP surface species data to the unmodified Jing condensed-phase mechanism and the new condensed-phase mechanism (Equation (3-1)).

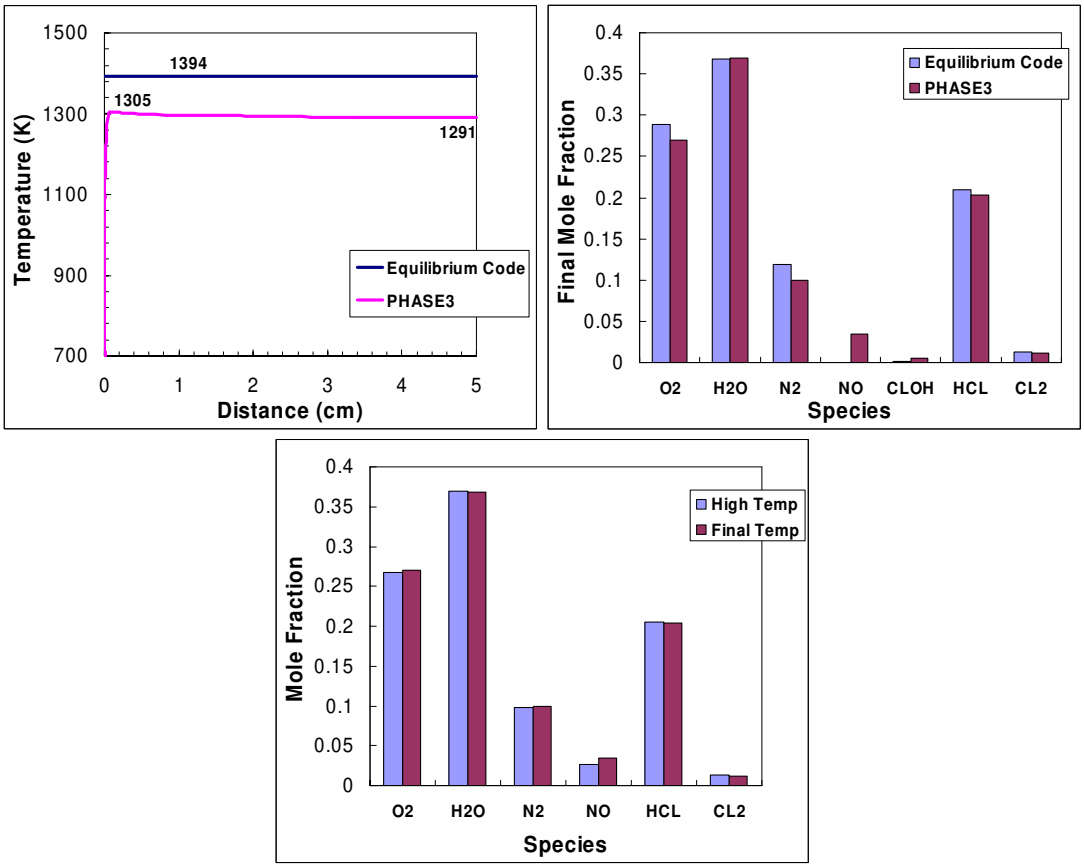

Figure 3-4: Gas-phase calculations using Equation (3-1): gas-phase temperature profile (top left), final species (top right), and comparison of mole fractions at the peak temperature and final temperature (bottom).

Figure 3-4 illustrates that the mole fractions at the temperature peak are closer to the equilibrium code calculations than the final mole fractions. The amount of NO increases from the peak temperature of 1305 K to the final temperature, and thus lowers the final temperature to 1291 K. Such a result indicates either a deficiency in the condensed or gas-phase mechanisms. Equation (3-1) was developed after a number of previous attempts, all of which produced similar or worse gas-phase results. Therefore, it is assumed that a deficiency is present in the gas-phase universal mechanism, specifically pertaining to chlorine reactions because the mechanism has previously been used successfully to model non-chlorine containing ingredients.

The universal mechanism has previously predicted the final temperature very closely for ingredients such as HMX, RDX, GAP, etc. Therefore, it was postulated that there was a deficiency in the chlorine reactions. Through personal communication with Lin[15] at Emory University, it was apparent that the work was not yet finished on Cl-containing reactions, specifically HCl, Cl_2, NOCl, ClOH, Cl + NH_x (x=1-3), and ClO_x + NH_y (x=1-4;y=2,3). Therefore, additional Cl-containing reactions had to be found elsewhere. It was noted that the Ermolin mechanism contains the species NOCl, which is currently not included in the Cl reactions produced by Lin. Brill[22] noted the appearance of NOCl during AP decomposition using his T-Jump/FTIR method. Due to these reasons, all five reactions containing NOCl used in the old Ermolin based gas-phase mechanism were added to the universal mechanism. The five NOCl reactions are presented in Table 3-2.

Table 3-2: NOCl reactions added to the universal mechanism.

Reaction	A (1/s)	b	E_A (cal/mol)
NOCL+M=CL+NO+M	$2.0x10^{17}$	0	37,700
CL_2+NO=CL+NOCL	$2.7x10^{12}$	0	19,900
CLOH+HNO=H_2O+NOCL	$3.0x10^{12}$	0	0
CLO+NOCL=CL_2+NO_2	$1.5x10^{12}$	0	0
CLOH+NH=H_2+NOCL	$1.0x10^{13}$	0	0

Inclusion of these five reactions eliminated the slight peak in the temperature profile and slightly raised the burning rate to 0.25 cm/s, but the final species were still not in sufficient agreement with the equilibrium calculations. These results are presented in Figure 3-5. As can be seen, there is still far too much NO as a final product and there is also a slight excess of Cl_2 remaining.

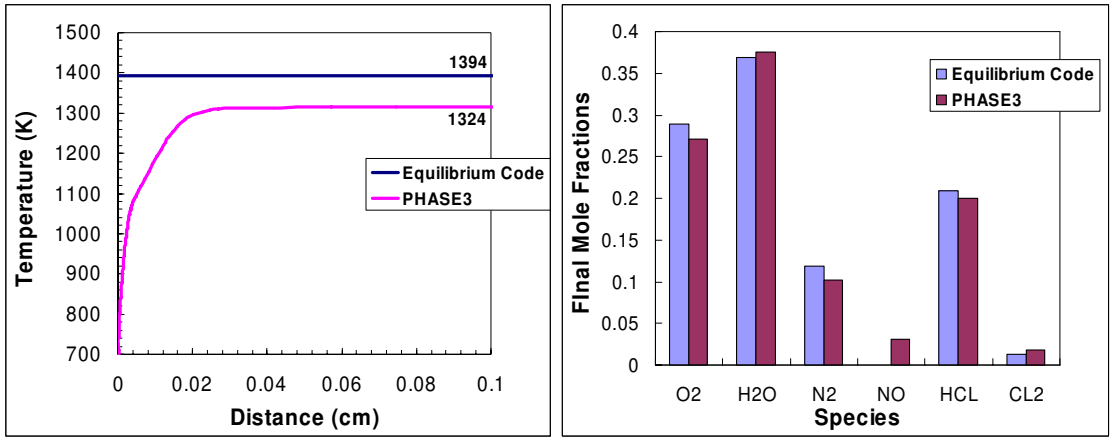

Figure 3-5: Results using the universal mechanism plus 5 NOCl reactions.

In an attempt to predict less Cl_2 and more HCl, reactions that produce HCl were investigated. Five HCl reactions were taken from the Jing mechanism and 4 HCl reactions from the IUPAC[108] mechanism. These reactions are presented in Table 3-3.

The inclusion of these nine HCl reactions and the five NOCl reactions yielded the same burning rate (0.24 cm/s), but better agreement with the equilibrium final species. The final temperature was still low by 80 K, and there was still excess NO. The results with the addition of both the NOCl and HCl reactions are presented in Figure 3-6.

Table 3-3: Additional HCl reactions added to the universal mechanism.

Reaction	A (1/s)	b	E_A (cal/mol)	Source
$CL+HO_2=HCL+O_2$	$1.08x10^{13}$	0	-340	Jing*
$CLOH+O=HCL+O_2$	$1.2x10^{12}$	0	0	Jing
$CLOH+HCL=CL_2+H_2O$	$4.0x10^{12}$	0	10,000	Jing
$CL_2+H=HCL+CL$	$8.4x10^{13}$	0	1,150	Jing
$HCL+O=CL+OH$	$2.3x10^{11}$	0.64	900	Jing
$OH+HCL=H_2O+CL$	$1.08x10^{12}$	0	477	IUPAC
$CLO+HO_2=HCL+O_3$	$1.32x10^{12}$	0	-676	IUPAC
$CL+H_2=HCL+H$	$2.35x10^{13}$	0	4,590	IUPAC
$CL+H_2O_2=HCL+HO_2$	$6.62x10^{12}$	0	1,947	IUPAC

*NIST Database reaction parameters[109]

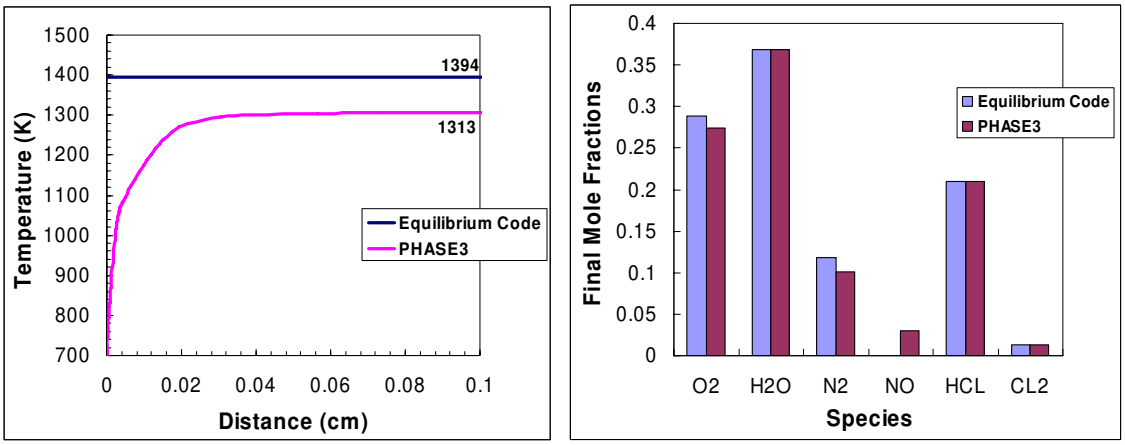

Figure 3-6: Results using the universal mechanism with 5 NOCl reactions and 9 HCl reactions.

An ammonium dinitramide (ADN) mechanism was published by Liau[64] and modified by Korobeinichev[66] as discussed in section 2.3.3.2. This mechanism was also examined in relation to AP to investigate reaction paths to reduce the amount of NO in the final products. A comparison of the ADN mechanism with the universal mechanism identified 11 more N, H, O reactions from the ADN mechanism not included in the universal mechanism. These reactions from the ADN mechanism were added to the universal mechanism. Table 3-4 contains the additional 11 reactions.

Table 3-4: Additional reactions added from the ADN mechanism to the universal mechanism.

Reaction	A	b	E_A (cal/mol)
$NH+NO=N_2O+H$	$2.16x10^{13}$	-0.2	0
$NO_2+HO_2=HONO+O_2$	$4.64x10^{11}$	0.0	479
$NH_3+NO_2=NH_2+HONO$	$2.45x10^{11}$	0.0	25,029
$NO+NO=N_2+O_2$	$1.3x10^{14}$	0.0	75,506
$NH_3+O=H_2+HNO$	$1.1x10^{10}$	0.0	500
$NH_2+NO=N_2+OH+H$	$1.08x10^{11}$	0.0	-1,300
$NH+H_2O=HNO+H_2$	$1.0x10^{11}$	0.5	3,000
$NO+N_2H_2=HNO+NNH$	$5.0x10^{12}$	0.0	10,000
$HNNO_2+NH_2=>N_2H_2+HONO$	$2.5x10^{12}$	0.0	0
$N_2H_3+M=N_2H_2+H+M$	$3.5x10^{12}$	0.0	46,000
$NNH=N_2+H$	$1.0x10^{6}$	0.0	0

The inclusion of the 11 ADN reactions, 5 NOCl reactions, and 9 HCl reactions gave the correct burning rate and improved the final temperature to 1365 K, about 30 K below the adiabatic temperature. Figure 3-7 presents the results using the universal mechanism and the 25 additional reactions. As shown in Figure 3-7, there was still a very slight excess of NO and N_2O present in the final products. The failure of the nitrogen species to go to equilibrium is attributed to missing Cl-N interactions, and results in the slightly low final flame temperature.

Despite the low flame temperature, these results are very close to matching experimental rate data. There is excellent agreement with the calculated and measured AP burning rates. The next step was to investigate the temperature sensitivity (σ_p) predicted by the model. Results are presented in Figure 3-8; the calculated σ_p values more than double the experimental values. Temperature sensitivity is very dependent on the condensed-phase mechanism (i.e., a larger energy release close to the surface results in a higher dependence of the burning rate on the initial temperature), and such poor agreement casts doubt on the validity of the condensed-phase reaction. As a result, it was deemed necessary to further investigate the condensed-phase mechanism.

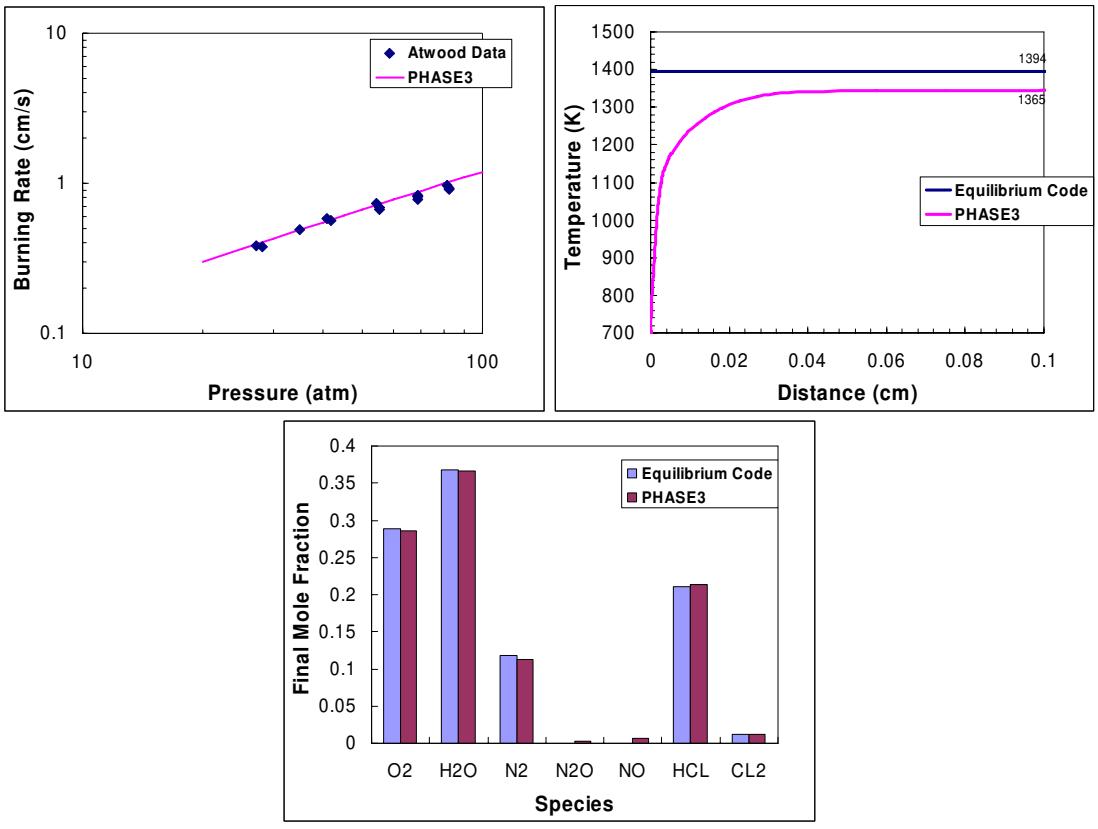

Figure 3-7: Results using the universal mechanism, 25 additional reactions, and Equation (3-1) for the condensed phase.

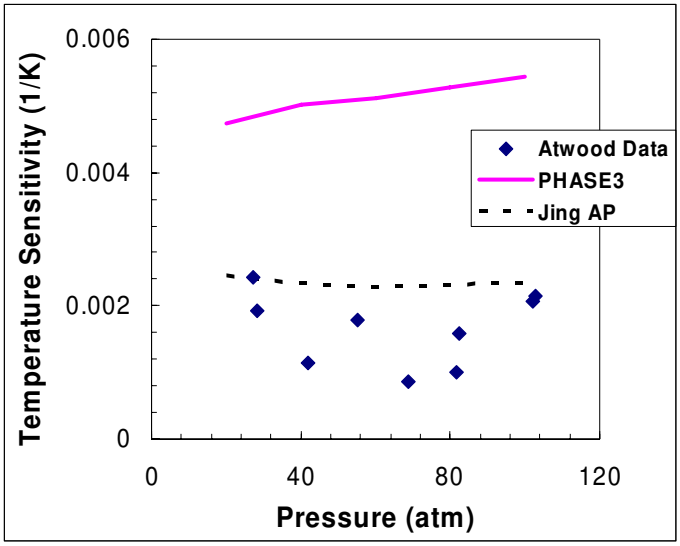

Figure 3-8: Temperature sensitivity (298K vs. 373K) for AP, experimental and numerical values.

3.1.3 New Condensed-Phase Mechanism #2

An accurate condensed-phase mechanism should: introduce correct species into the gas phase, predict a reasonable condensed-phase heat release, and allow for the calculation of correct temperature sensitivity. From the work to date, the necessary species to be introduced into the gas phase have been determined both experimentally and numerically, therefore it is a matter of obtaining a correct heat release (Q) and temperature sensitivity (σ_p). Various permutations of the condensed-phase reaction were tried, calculating the effect on both Q and σ_p. This was a trial and error method based on the available surface species data. Figure 3-9 presents the results of this study for both Q and σ_p with lines representing the desired σ_p and the estimated Q values.

As can be seen, there does not appear to be a specific correlation between Q and σ_p. Therefore, an educated trial and error method was necessary to obtain both a

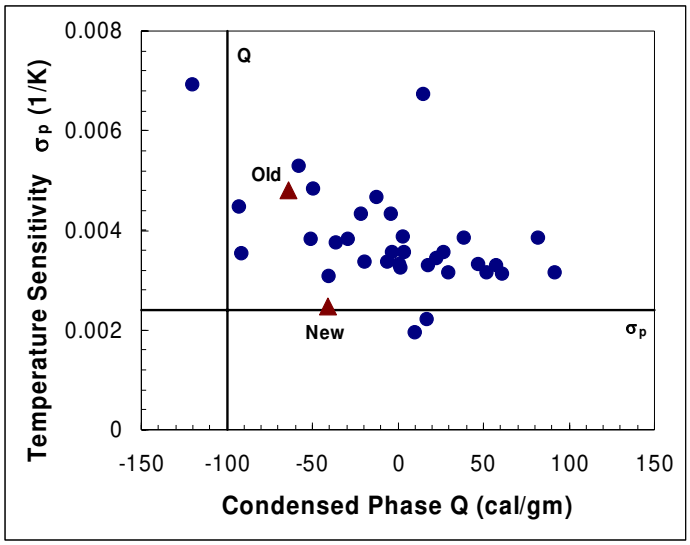

Figure 3-9: Tradeoff between temperature sensitivity and condensed-phase heat release for AP at 20 atm, including values for the old and new condensed-phase reactions.

reasonable heat release and temperature sensitivity. The surface species generated by the new condensed-phase reaction, Equation (3-2), are compared to the previously calculated surface species in Figure 3-10. There is reasonable agreement between the old and new reactions, and the new condensed-phase reaction also agrees reasonably well with the Ermolin surface species data.

Old Condensed-Phase Reaction:

$$16AP(c) \rightarrow 14O_2 + 18H_2O + 6N_2 + 4NH_3 + 7HCl + 3HClO_4 + 2H_2 + 2OH + ClO + ClO_3 + 4Cl \quad (3\text{-}1)$$

New Condensed-Phase Reaction:

$$10AP(c) \rightarrow 7O_2 + 13H_2O + 3N_2 + 4NH_3 + HCl + HClO_4 + Cl_2 + 3ClO_3 + 3Cl \quad (3\text{-}2)$$

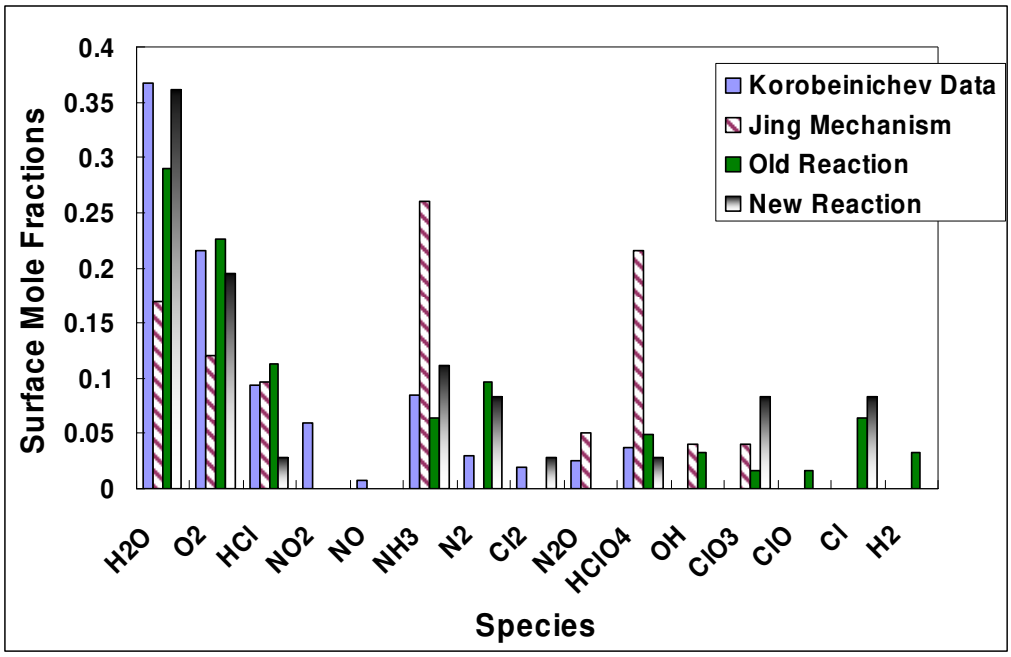

Figure 3-10: Comparison of Ermolin's AP surface species data to the unmodified Jing condensed-phase mechanism, Equation (3-1), and Equation (3-2).

The results that follow are based on the condensed-phase mechanism consisting of Equation (3-2). Since work began on the AP gas-phase mechanism four more reactions became available from Lin, and therefore, the gas-phase mechanism outlined above was modified. Thirteen of the 25 additional reactions added to the universal mechanism from sources other than Lin were removed. These 13 reactions were removed because they were either directly replaced with the new Lin reactions, became insignificant, or Lin recommended their removal. Therefore, the latest gas-phase mechanism consists of the comprehensive mechanism plus 61 Lin reactions and only 12 of the 25 additional reactions outlined above, totaling 106 species and 611 reactions. The 12 additional reactions from sources other than Lin are presented in Table 3-5.

Table 3-5: Reactions added to the comprehensive mechanism from sources other than Lin.

Reaction	A (1/s)	b	E_A (cal/mol)	Source
$NO+NO=N_2+O_2$	$1.3x10^{14}$	0.0	75,506	ADN
NOCL+M=CL+NO+M	$2.0x10^{17}$	0	37,700	Ermolin
$CL_2+NO=CL+NOCL$	$2.7x10^{12}$	0	19,900	Ermolin
$CLOH+HNO=H_2O+NOCL$	$3.0x10^{12}$	0	0	Ermolin
$CLO+NOCL=CL_2+NO_2$	$1.5x10^{12}$	0	0	Ermolin
$CL+HO_2=HCL+O_2$	$1.08x10^{13}$	0	-340	Jing
$CLOH+O=HCL+O_2$	$1.2x10^{12}$	0	0	Jing
$CLOH+HCL=CL_2+H_2O$	$4.0x10^{12}$	0	10,000	Jing
$CL_2+H=HCL+CL$	$8.4x10^{13}$	0	1,150	Jing
$OH+HCL=H_2O+CL$	$1.08x10^{12}$	0	477	IUPAC
$CL+H_2=HCL+H$	$2.35x10^{13}$	0	4,590	IUPAC
$CL+H_2O_2=HCL+HO_2$	$6.62x10^{12}$	0	1,947	IUPAC

Due to the inability of the gas-phase mechanism to achieve the adiabatically predicted final species, a gas-phase reaction prefactor was changed. Changing gas-phase kinetic parameters is not typically done at BYU. Such a procedure biases the mechanism to a specific ingredient and if not included in the write-up causes deception as to the accuracy of the mechanism. In general it is not good scientific practice. The goal of the universal mechanism is to create a mechanism that is valid for as many ingredients as possible without having to be tailored for each or any monopropellant. Therefore, theoretically-based kinetic values are preferred because, hopefully, they have not been tampered with to fit the data. That being said, there are obvious shortcomings in the universal mechanism related to the chlorine chemistry, and to obtain reasonable results, one rate was changed. The pre-exponential factor for the reaction $2NO = O_2 + N_2$ was increased 6 orders of magnitude to force NO to N_2 and O_2 at equilibrium. This rate increase had no effect on the burning rate, due to the typically slow nitrogen chemistry, but only affected the far field temperature profile. The effect of the modifications to the

reaction $2NO = N_2 + O_2$ on final mole fractions is shown in Figure 3-11. Further, as more data for Cl-related reactions become available, this reaction should be removed because it is not an elementary reaction; it is only included to achieve the correct final species.

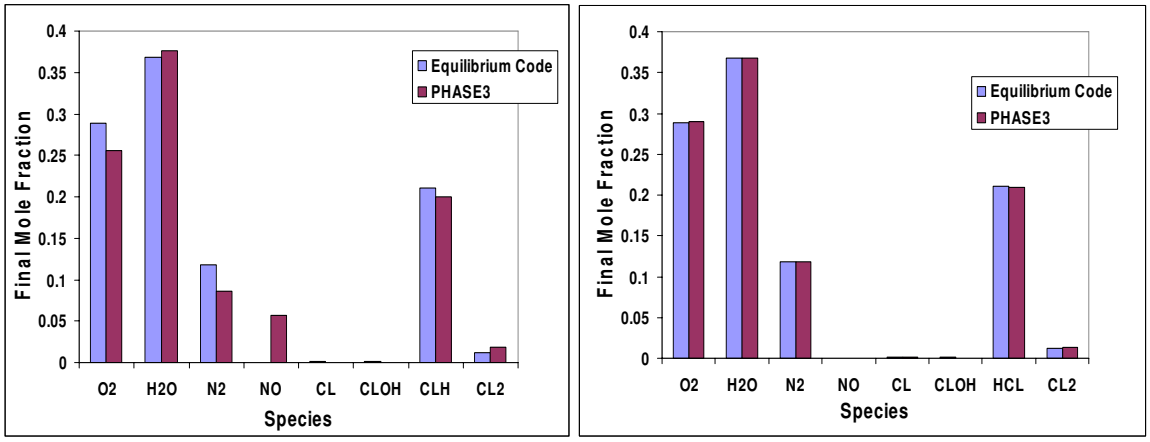

Figure 3-11: Final mole fractions without modification (left) and with modification (right) to the reaction rate of $2NO = N_2 + O_2$.

3.1.4 Final Note Concerning the Gas-Phase Mechanism

As a final note, any attempts to include NO_x species evolution from the condensed-phase produced very poor results. The gas-phase kinetic mechanism is unable to eliminate the extra NO, N_2O, and NO_2 from the gas phase. This can be seen in Figure 3-12 where there is an excess of all three species. The only modification to Equation (3-1) was to convert a single mole of O_2 and N_2 into 2NO. This modification greatly increased the amount of NO in the final products. The poor final mole fractions are attributed to missing chlorine-nitrogen chemistry. This problem is not unique to the current mechanism. Jeppson,[9] a co-author with Jing, noted that the former AP mechanism also failed to reach equilibrium products for N_2 in his AP modeling work. Therefore, this

problem is not unique to the current mechanism, but seems to be a general problem with modeling AP.

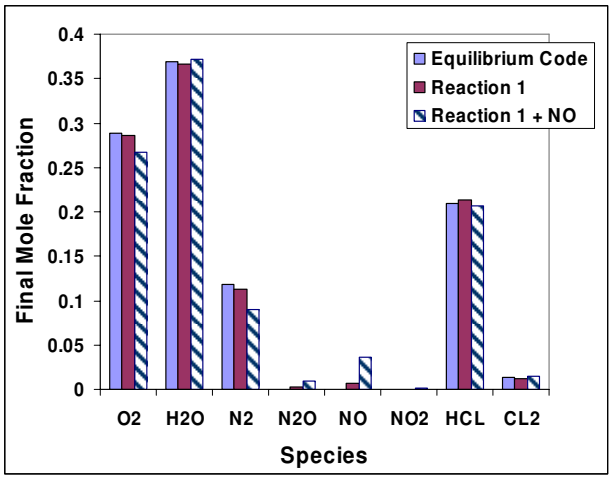

Figure 3-12: Change in final species when a small amount of NO leaves the surface.

Work is underway at BYU for a pseudo-propellant model of fine AP particles and HTPB. The same gas-phase mechanism is being used in that work. However, no modification has been made to the reaction rate of $2NO = O_2 + N_2$. The pre-exponential has not been increased by 6 orders of magnitude to obtain a reasonable final temperature, as was necessary for pure AP. The model accurately predicts the final mole fractions for the AP/HTPB mixture without the modification to the reaction rate. With the inclusion of carbon, the NO_x problem is no longer evident, as can be seen in Figure 3-13. The path to convert NO_x to N_2 is apparently present for carbon containing ingredients, but absent for non-carbon ingredients.

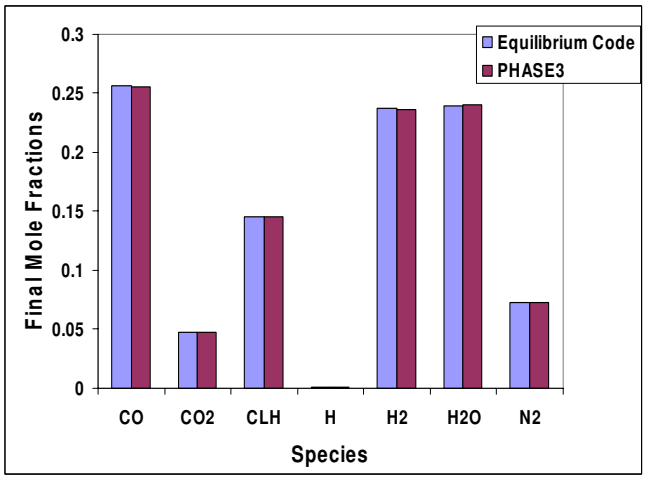

Figure 3-13: AP/HTPB final mole fractions.

3.2 Results and Discussion

Very good results are obtained for AP using the universal mechanism (Appendix A) and the global condensed-phase reaction (Equation (3-2)). Burning rate predictions are presented in Figure 3-14 and agree with the Atwood[16] experimental data. Model calculations predict a pressure exponent of 0.8 compared to a pressure exponent of 0.76 for the experimental data. Also presented in Figure 3-14 are the final species calculated by the model compared to those thermodynamically predicted by an equilibrium code. Again the agreement is excellent.

Gas-phase heat flux to the surface of a burning propellant is a dominant factor in determining burning rate. The previous AP monopropellant model by Jing[7] predicted a very high heat flux to the surface, especially compared to AP's relatively slow burning rate. At 20 atm, the previous model predicted a heat flux of 1100 W/cm^2, a value higher than that predicted for faster burning monopropellants such as HMX and RDX. The new

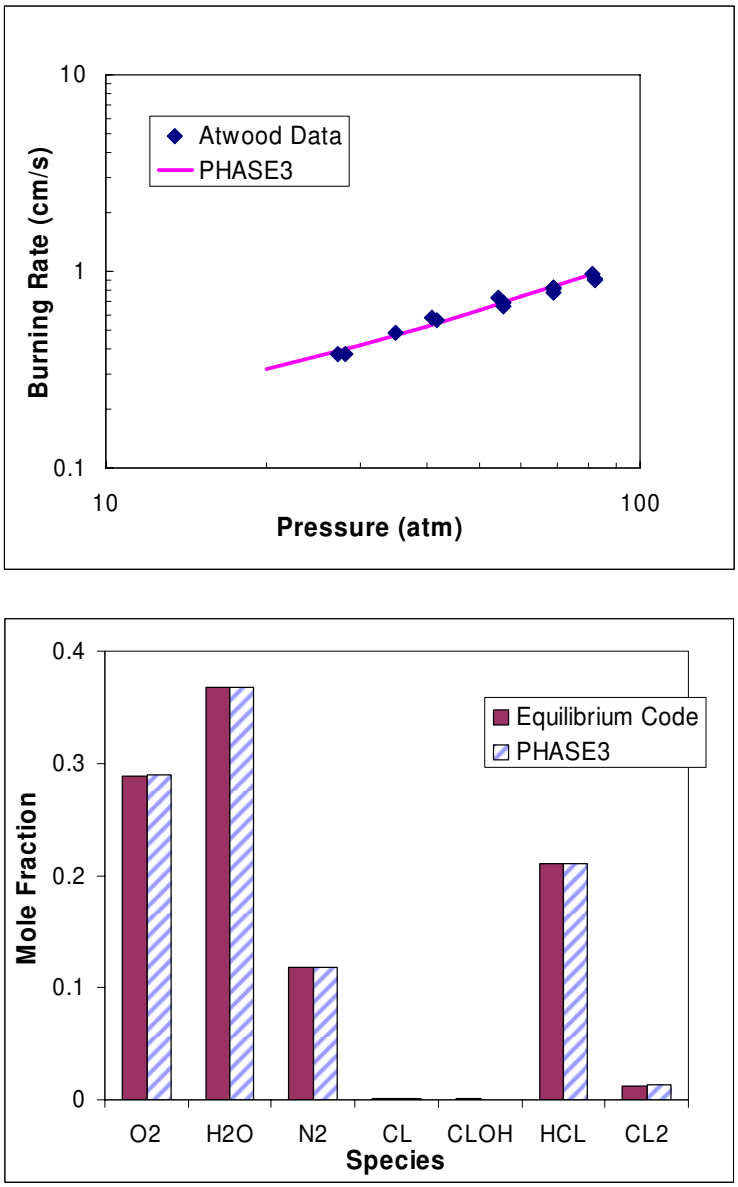

Figure 3-14: Predicted AP monopropellant burning rate and final species.

model predicts a more reasonable value of 435 W/cm^2 at 20 atm. Figure 3-15 compares the old and new values predicted for AP's surface heat flux with values for other ingredients currently modeled with the universal mechanism. The figure also includes experimental burning rates as reported by Atwood to allow a comparison between heat

flux and burning rate for various ingredients. The new AP heat flux value is more reasonable considering its burning rate.

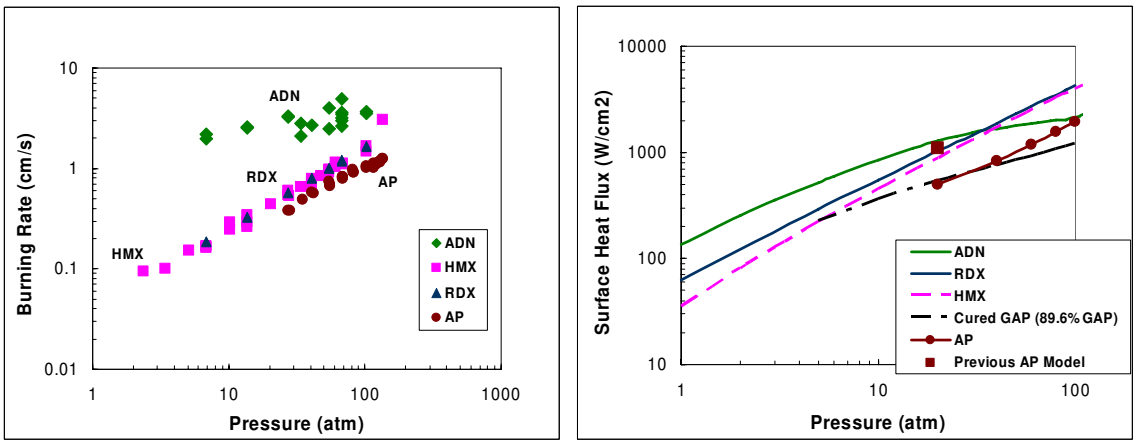

Figure 3-15: Experimental burning rate by Atwood (left) and calculated heat fluxes (right) for various ingredients.

As previously mentioned, there is disagreement as to whether heat is consumed or released in the condensed phase during AP combustion.[22] The previous model predicted a very endothermic condensed phase reaction, 173 cal/g at 20 atm. The new model predicts an exothermic condensed-phase reaction of -42 cal/g, as experimental data seem to indicate. Figure 3-16 contains numerical comparisons of the old and new values of condensed-phase heat release for AP, along with other ingredients calculated using the universal mechanism.

Temperature sensitivity calculations give acceptable agreement with experimental data. As can be seen in Figure 3-17, the calculations fall within the data scatter at pressures below 40 and then increase with pressure. The old model calculations by Jing

fell at the upper limit of the data. The temperature sensitivity data and calculations are for initial temperatures of 298 K and 373 K.

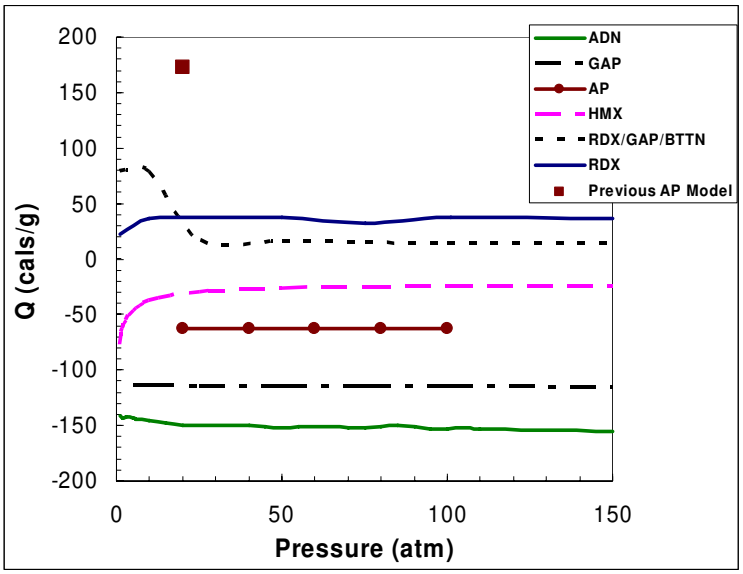

Figure 3-16: Calculated condensed-phase heat release for various ingredients.

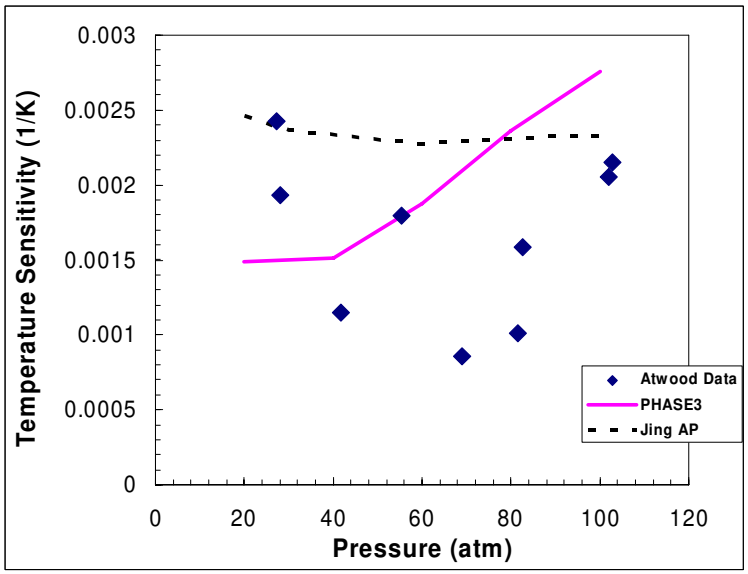

Figure 3-17: AP monopropellant temperature sensitivity.

3.3 Summary and Conclusions

An improved model has been developed for AP monopropellant that utilizes the newest reaction kinetics available. A comprehensive gas-phase mechanism was previously developed by Puduppakkam[8] and had been used to successfully model HMX, RDX, GAP, BTTN, NG and combinations of these ingredients. To expand this mechanism to include AP, chlorine-containing reactions were added. Extensive theoretical work performed by Lin[15] resulted in kinetic parameters for a number of Cl-containing reactions, which were added to the Puduppakkam gas-phase kinetic mechanism. However, results using the Puduppakkam mechanism and the Lin reactions produced poor agreement with experimental data. It was therefore necessary to include an additional 4 NOCl and 7 HCl-containing reactions proposed by Ermolin[7] and IUPAC,[108] as well as one additional reaction from the Korobeinichev[66] ADN gas-phase kinetic mechanism. The new expanded mechanism results in excellent agreement with experimental burning rate. However, the final temperature and species are still slightly off, and an arbitrary modification to the reaction rate of $2NO=N_2+O_2$ was made to obtain the correct equilibrium final species. The low final temperature is attributed to deficiencies in the chlorine-nitrogen chemistry of the gas-phase mechanism. Suggestions and work are necessary to address this shortcoming in future detailed kinetic studies.

3.4 Future Work

Work is currently underway at BYU to create a more detailed condensed-phase mechanism. The global reaction, Equation (3-2), has been divided into two reactions. The first reaction is the assumed initial decomposition step previously presented as Equation

(2-1) and the second reaction is a semi-global to achieve similar surface species to the experimental data. Also, solid-phase decomposition will be included in the model in a similar manner to the Jing mechanism.[7] Solid-phase decomposition products are introduced into the condensed-phase as gas species, and the decomposition accounts for 30% of the overall decomposition, as observed experimentally. Table 3-6 contains the mass fractions of the solid-phase decomposition products which account for 30% of the overall decomposition and Equations (3-3) and (3-4) list the two-step condensed-phase mechanism accounting for 70% of the overall decomposition.

Table 3-6: Proposed AP solid-phase decomposition mass fraction of major species as determined from an equilibrium code, accounts for 30% of the overall AP decomposition products.

Species	O_2	H_2O	N_2	HCl	Cl_2
Mass Frac.	0.328	0.243	0.119	0.257	0.005

$$AP(c) \rightarrow NH_3 + HClO_4$$
$$A = 6.0 \times 10^{10} \quad E_A = 28{,}000 \tag{3-3}$$

$$7AP(c) \rightarrow 3O_2 + 9H_2O + 2N_2 + 3NH_3 + 4ClO_3 + Cl_2 + ClOH$$
$$A = 3.0 \times 10^{10} \quad E_A = 28{,}000 \tag{3-4}$$

4 Development Methodology for ADN Numerical Model

The number of theories concerning ADN condensed-phase decomposition is evidence of the difficulties in examining condensed-phase processes in all monopropellants. Based on the literature review in Chapter 2, this project developed a methodology to describe condensed and gas-phase mechanisms for ADN combustion. Initially, available gas-phase kinetic mechanisms were evaluated to determine the mechanism most capable of matching available experimental data. Once a suitable mechanism was determined, a global condensed-phase reaction was determined based on available experimental surface species data. Use of a global condensed-phase reaction hides many of the intricacies of the condensed-phase decomposition, but does allow for more complex theories to be incorporated into the model at a later time. Evaporation and dissociation were then examined to complete the condensed-phase mechanism.

4.1 Determination of a Detailed Kinetic Mechanism

The available detailed kinetic mechanisms, Table 2-9, were examined using PHASE3. Since no condensed-phase mechanisms had yet been developed, these were gas-phase calculations only. Initial conditions (burning rate, initial temperature, and initial species) were taken from the Korobeinichev[45] experimental data, Table 4-1. Note that the experimental data were collected 4.19 mm into the gas-phase, so calculations did

not begin at the propellant surface, but at the location of these initial conditions. The following evaluations for each available mechanism were performed with the same initial conditions to allow for a direct comparison between the mechanisms. Korobeinichev also recorded species and temperature profiles that correspond to the initial conditions, and all models were compared to these data. Korobeinichev's data were chosen for comparison based on the extensive use of the data in the literature and the quality of his previous work regarding propellant combustion.

Table 4-1: Initial conditions used for the ADN gas-phase calculations.

Pressure	m_{dot}	x_{start}	T_{start}	NH_3	H_2O	NO	N_2O	N_2	HNO_3
6 atm	3.4 g/sec	4.19 mm	919 K	0.07	0.3	0.23	0.28	0.1	0.02

4.1.1 Evaluation of the Liau Mechanism

The Liau[64] mechanism was incorporated into the PHASE3 numerical model with the values from Table 4-1 as initial conditions. Temperature and species calculations resulted in very poor agreement with the Korobeinichev data; the calculated final temperature was low by 500 K. Upon further evaluation of the Liau work, it was discovered that an area expansion of five was included in his gas-phase calculation. An area expansion can be included into one-dimensional models to account for two-dimensional gas-phase expansions. Such expansions have been observed for HMX and RDX laser induced ignition. Liau gave no reason for the use of an area expansion or why the value of five was chosen. After performing an extensive literature review, no experimental justification was found to support the inclusion of an area expansion for

ADN. Through personal correspondence with Liau's coauther Yang, he stated that experimental results showed that an area expansion of five is valid for certain RDX combustion conditions, but no such experimental data were given for ADN combustion. The area expansion was used to obtain "more reasonable results" for the temperature and species profiles when compared to the Korobeinichev data.

In the current study it was found that inclusion of an area expansion was necessary to match the Korobeinichev data and obtain results similar to those of Liau; this can be seen in Figure 4-1. No area expansion (AE = 1) caused the solution to undershoot the experimental data by 500 K. Then, as the area expansion was increased, the calculated temperature profile approached the experimental data, with an optimal value of five.

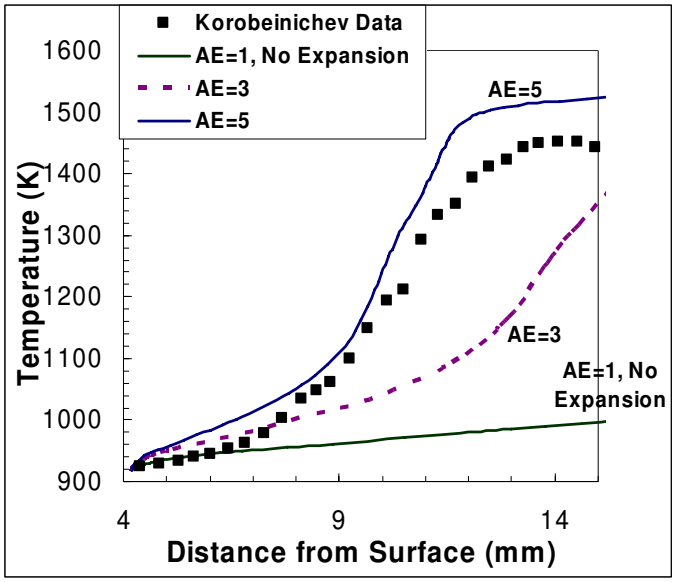

Figure 4-1: ADN area expansion (AE) study using the Liau mechanism compared to the Korobeinichev data.

Using an area expansion of 5, the species and temperature profile predictions of Liau were reproduced as illustrated in Figure 4-2.

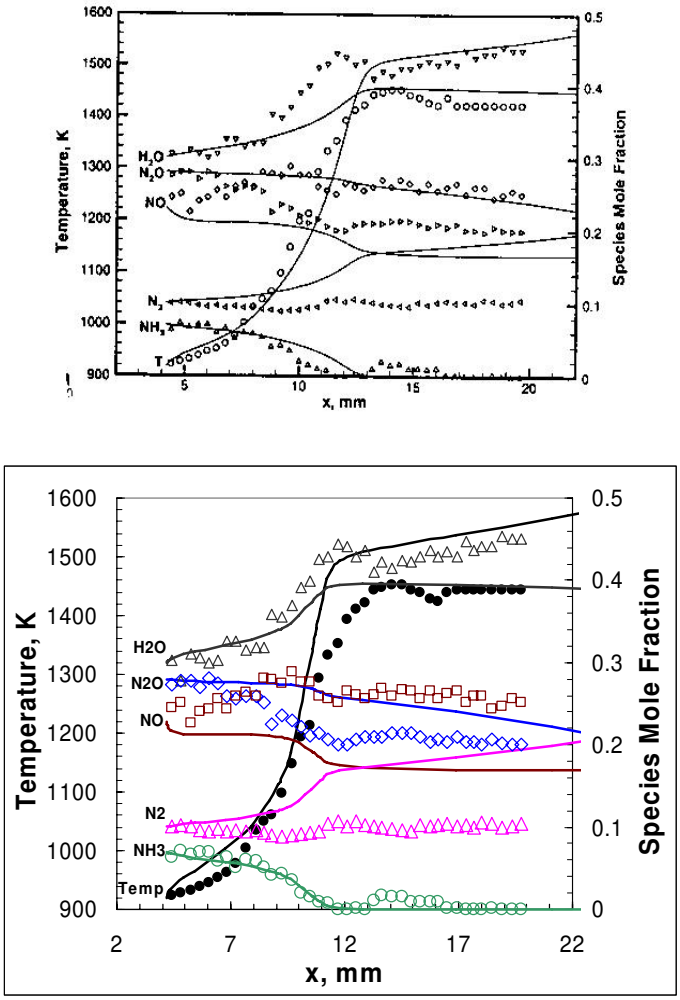

Figure 4-2: Comparison of numerical results between Liau (top) and the current study (bottom) including the Korobeinichev data for ADN combustion at 6 atm.

4.1.2 Evaluation of the Korobeinichev Mechanism

The Korobeinichev[45] mechanism was based largely on the Liau mechanism. As with Liau's work, it was necessary to include an arbitrary area expansion to obtain satisfactory results. Korobeinichev did not mention the use of an area expansion, but this

investigator suggests one was used. Results are presented in Figure 4-3 and Figure 4-4 where an area expansion of 2.5 was found to be optimal.

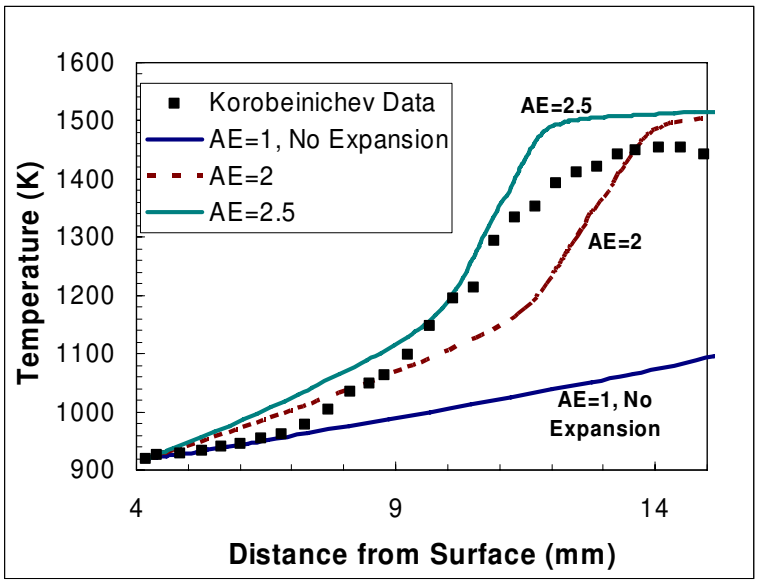

Figure 4-3: ADN area expansion (AE) study at 6 atm using Korobeinichev's gas-phase mechanism in PHASE3 compared to the Korobeinichev data.

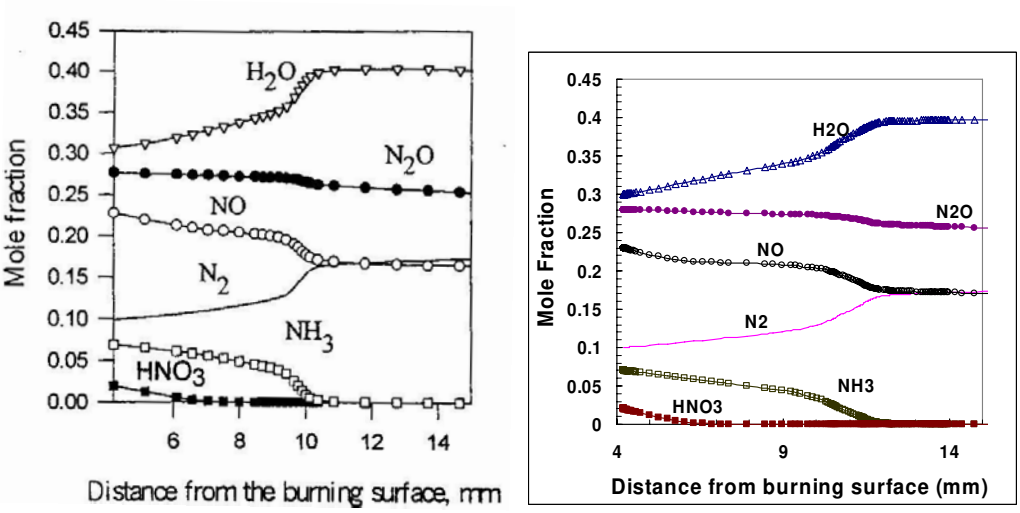

Figure 4-4: ADN species profile comparisons at 6 atm between Korobeinichev (left) and the current study (right) with an area expansion of 2.5.

4.1.3 Evaluation of the Ermolin Mechanism

A gas-phase mechanism was published in 2004 by Ermolin[61] for ADN combustion. Ermolin did not use data in Table 4-1 to validate his model. Therefore, a comparison using the Ermolin mechanism and the Korobeinichev data was undertaken in the current study. Results using Ermolin's gas-phase mechanism were poor as seen in Figure 4-5. Note that the inclusion of an area expansion did improve the solution, but an area expansion of 14 still does not give the desired results. The overall trend is inconsistent with experimental data. Therefore, this mechanism was not used in further studies of ADN combustion in the present work.

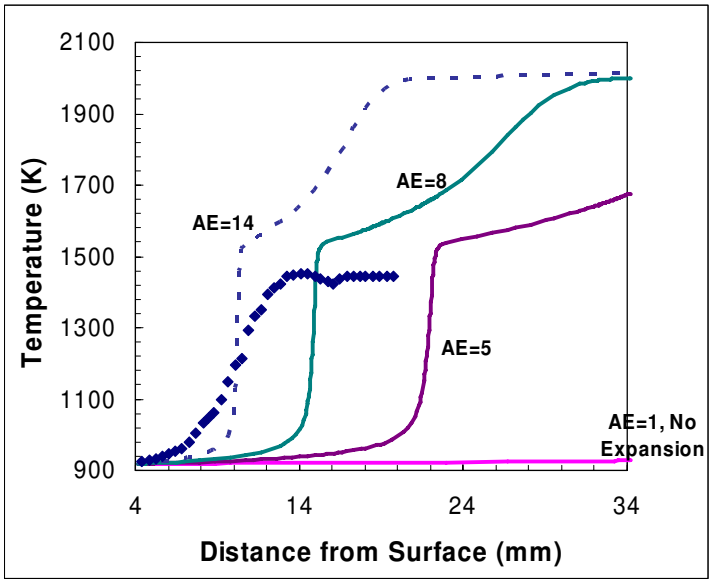

Figure 4-5: Comparison of the Ermolin mechanism (2004) to the Korobeinichev data for ADN combustion at 6 atm, including an area expansion study.

4.1.4 Evaluation of the Puduppakkam Mechanism

The Puduppakkam comprehensive mechanism[8] has been used successfully on HMX, RDX, GAP, BTTN, and combinations of these ingredients. This mechanism, using PHASE3, was used to make calculations for ADN, and the results were compared with the Korobeinichev data. The results, compared to the Korobeinichev data, were poor. The dark zone extended far beyond that measured and area expansion had little effect upon the solution. Temperature profiles are presented in Figure 4-6 with the inclusion of area expansion.

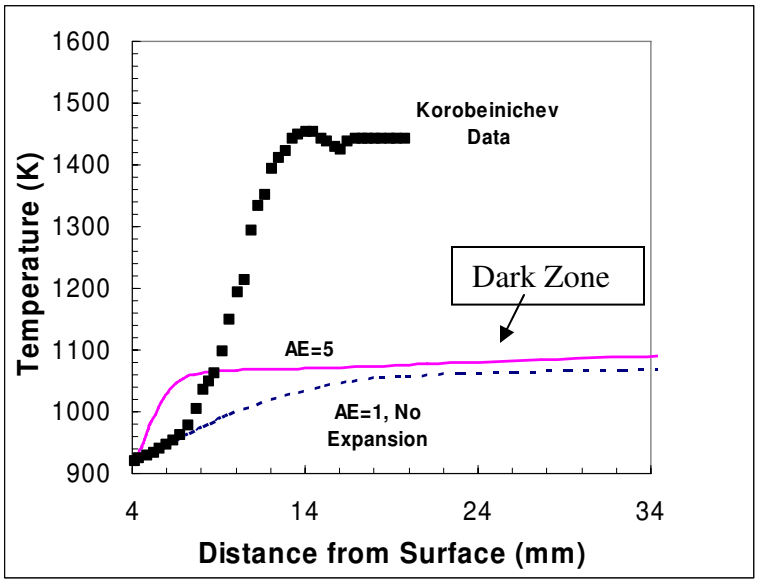

Figure 4-6: Comparison of the Puduppakkam comprehensive mechanism with the Korobeinichev data for ADN combustion at 6 atm, including an area expansion study.

A comparison was undertaken between the Liau mechanism and the Puduppakkam mechanism to determine possible reactions to include in the comprehensive mechanism for nitrogen combustion. Eight additional reactions were

added from the Liau mechanism to the comprehensive mechanism. These reactions improved the solution, but results were still not as accurate as the Liau and Korobeinichev mechanisms. Results using the comprehensive mechanism and the eight additional reactions are presented in Figure 4-7.

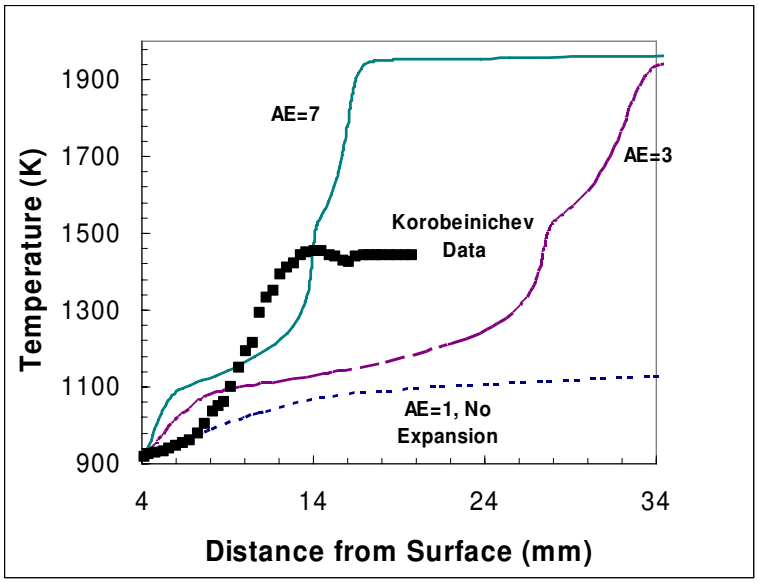

Figure 4-7: ADN area expansion study using the comprehensive mechanism and eight additional reactions from the Liau mechanism compared to the Korobeinichev data at 6 atm.

4.1.5 Summary of Mechanisms

Results from these numerical comparisons illustrate that there is a deficiency in either the gas-phase mechanisms or the experimental data used for the studies. A comparison of results obtained using the three ADN-specific mechanisms is presented in Figure 4-8. The works by both Liau and Korobeinichev were able to accurately match the experimental data, but only with the inclusion of a gas-phase area expansion. No experimental evidence for an area expansion has been noted for ADN, and therefore, the

area expansion, in effect, is a fudge factor to obtain satisfactory results. The Ermolin and Puduppakkam mechanisms were unable to obtain correct trends when compared to the experimental data, even with the inclusion of an area expansion. The Ermolin and Puduppakkam mechanisms appear to be deficient in some respect, and therefore, they were not used further in the current ADN study. The Liau mechanism required an area expansion twice the size of that for the Korobeinichev mechanism, therefore, the Korobeinichev mechanism (Appendix B) was chosen to provide the basis in the remainder of this study. Since this study was conducted, additional development has taken place on the Puduppakkam mechanism. A reevaluation of the Puduppakkam mechanism is desirable in regards to ADN combustion, but was not included in this work.

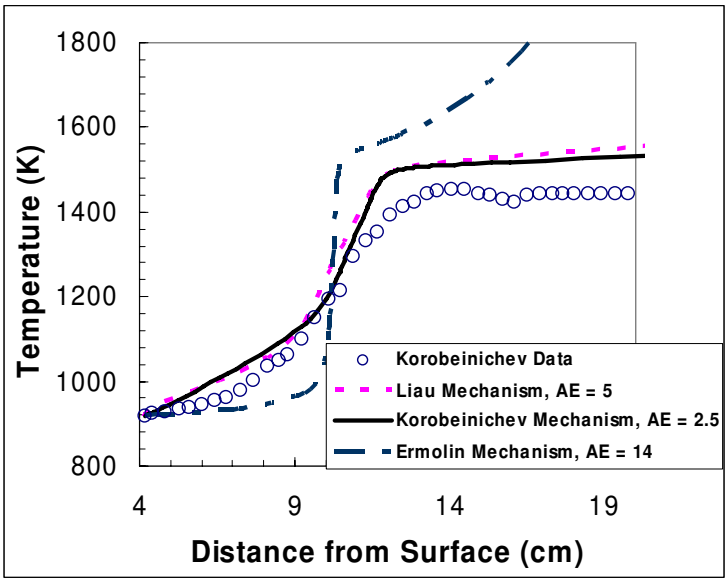

Figure 4-8: Gas-phase mechanisms compared to Korobeinichev's ADN data including area expansion values.

4.2 Calculations Using Experimental Surface Species Data

A somewhat ideal situation would be to input experimental surface species data directly into a numerical model as boundary conditions and perform gas-phase calculations. Such a methodology would eliminate the need to develop a condensed-phase mechanism. The previous mechanism evaluations used Korobeinichev experimental data, but the data were measured far into the gas phase (4.19 mm) and not at the surface. It is far more difficult to obtain accurate surface species data. Brill and Fetherolf have measured surface species data for ADN as presented in Table 2-5. These data were input into the gas-phase calculation as boundary/initial conditions to the gas phase, and calculations were performed varying area expansion and the amount of ADN(v). Predicted temperature profiles were poor for all cases when compared to the Korobeinichev data.[37] Calculations resulted in a flat temperature profile of approximately 700 K, a value about 800 K lower than experimental measurements. In most cases there was an initial decrease in temperature before it rose to the flat line temperature. Inclusion of an area expansion had virtually no effect on the solution and increasing the amount of ADN(v) in the gas phase increased the flat line temperature, but not significantly. Using the Fetherolf data as inputs into the gas-phase calculation resulted in a slightly higher temperature. This higher temperature was due to the less exothermic condensed phase reported by Fetherolf. These calculations led to the conclusion that the experimentally measured surface species contain too many final products and not the necessary radicals to sustain combustion. Therefore, it is currently infeasible to take these raw experimental data and input it into the gas phase to obtain an accurate solution. Temperature

calculations using the Brill and Fetherolf experimental data as gas-phase boundary conditions are presented in Figure 4-9.

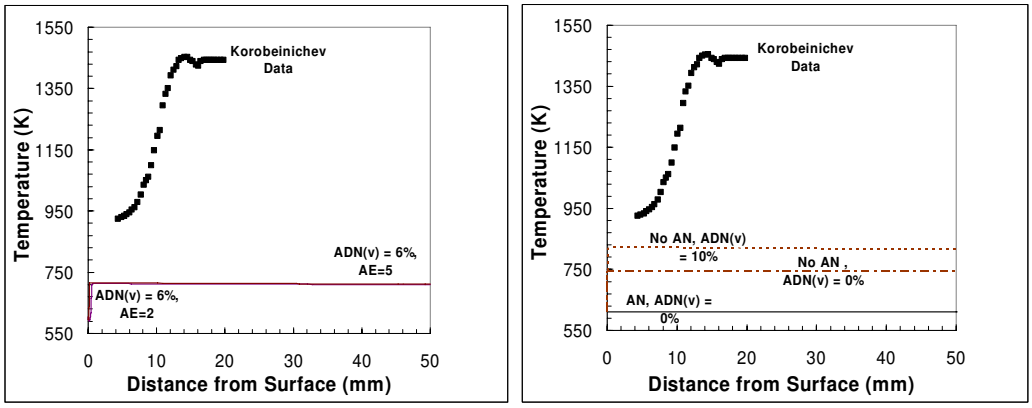

Figure 4-9: Gas-phase calculations using Brill (left) and Fetherolf (right) experimental data as gas-phase boundary conditions compared to Korobeinichev's ADN data at 6 atm.

4.3 Development of a Condensed-Phase Mechanism

4.3.1 Global Condensed-Phase Reaction

A major step in developing a combustion model for ADN is developing a global condensed-phase mechanism that can closely match the experimental species data. However, such a global reaction may be valid for only one segment of ADN's complex burning rate curve. A detailed condensed-phase mechanism is believed to be necessary to capture ADN's unique behavior over the range of pressures, but development of a global reaction will hopefully lead to a more detailed condensed-phase mechanism.

In this work, a condensed-phase global reaction was estimated based upon the surface species data of Brill[40] and Fetherolf.[51] Due to its low heat release, it is assumed that Equation (2-4) is not sufficiently exothermic to account for ADN's large heat release. However, Brill's proposed overall reaction, Equation (2-6), is too exothermic and results

in a flat gas-phase temperature profile. Therefore, it is assumed that a plausible global reaction lies somewhere between the two reactions. This assumption is further supported by conclusions drawn from Brill and Fetherolf based on their experimental observations. Brill proposed that Equation (2-5) took place at or near the surface, whereas Fetherolf proposed it took place farther into the gas phase. Based on these ideas it is assumed that part of the heat release from Equation (2-5) takes place in both phases. The condensed-phase global reaction that gives the most accurate surface species distribution compared the Brill and Fetherolf data and temperature profile compared to the Korobeinichev data is presented as Equation (4-1).

$$9ADN \rightarrow 4NH_3 + 9N_2O + 9H_2O + 4NO + 3N_2 + 4HNO_3 + 2OH \qquad (4\text{-}1)$$

Figure 4-10 compares the surface species obtained using Equation (4-1) versus the species data obtained by Brill and Fetherolf. Key differences are the absence of NO_2 in the model predictions, and the inclusion of ADN(v) and OH in the model. Reasoning for these differences is explained above and is related to having a less exothermic condensed phase. Note the reduction in the amount of the final products H_2O and N_2. Overall, the predicted mole fractions give reasonable agreement with the experimental data.

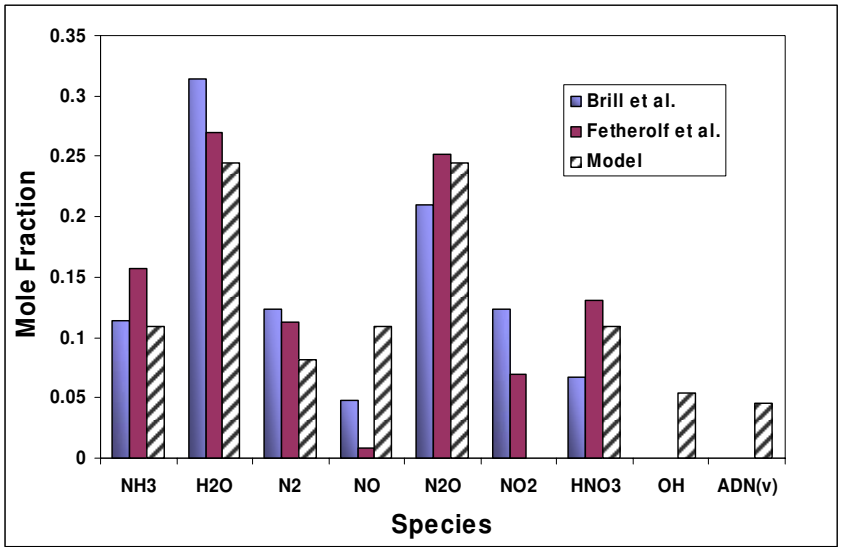

Figure 4-10: Experimental versus numerically predicted surface species for ADN decomposition.

4.3.2 Numerical Analysis of ADN Evaporation

This investigation also developed an evaporation reaction for ADN. The exact form of ADN evaporation is in debate as explained above, but all authors seem to agree that some form of ADN evaporation takes place. Korobeinichev[55] and Shmakov[45] reported vapor pressure correlations for ADN sublimation and evaporation. Using these vapor pressure correlations, temperatures were determined at various pressures and graphed against the surface temperature data for ADN in Figure 4-11. The use of these vapor pressure correlations resulted in predicted temperatures between 50 and 200 K lower than the ADN surface temperature data. It is therefore impossible to obtain reasonable surface temperatures if these vapor pressure correlations are used. Thus, the amount of evaporation could not be determined from experimental rates, and a parametric study was necessary.

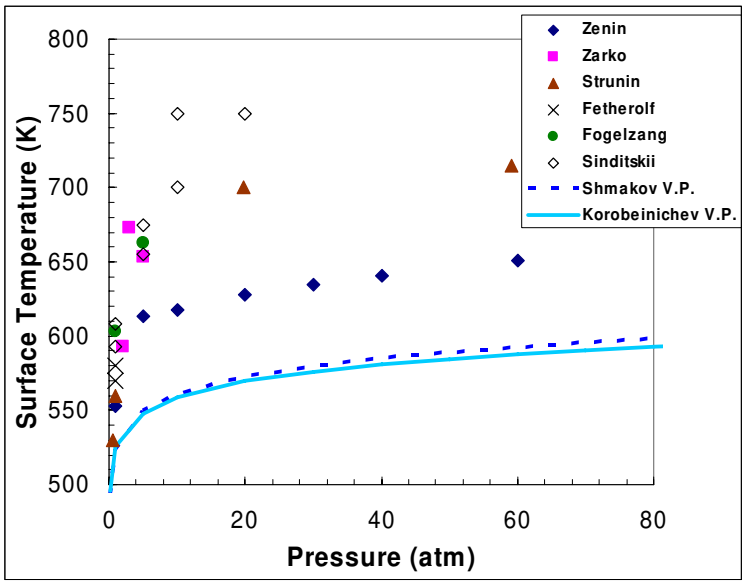

Figure 4-11: Experimental surface temperature measurements versus vapor pressure calculations for ADN.

To achieve the desired large condensed-phase heat release and a small gas-phase heat flux at the surface (as proposed by both Zenin[42] and Sinditskii[36]) it appears necessary to minimize the amount of endothermic ADN evaporation. A higher condensed-phase heat release is attainable from less evaporation because more decomposition is able to proceed via the exothermic route. Also, a lower heat flux will be generated by the condensed phase, if evaporation is minimal, because large amounts of energy are required to evaporate ADN. The gas-phase heat flux must increase as more ADN vaporizes to satisfy the surface condition; condensed-phase heat flux is equal to the gas-phase heat flux at the surface.

To examine the effects of ADN evaporation, Equation (4-1) was assumed as the condensed-phase reaction, and then the amount of ADN(v) or ADN dissociative evaporation products were systematically varied to examine their effects on the

calculated temperature profile. Eliminating ADN evaporation products resulted in a flat gas-phase temperature profile. However, as the amount of evaporation products increased, the temperature profile approached the experimental data. This is believed to be due to the importance of ADN(v) decomposition in the near-surface stages of the gas phase. Nitrogen chemistry is known to be relatively slow, and is the cause of dark zones observed during propellant combustion. By not allowing any ADN(v), a dark zone is immediately generated in the gas-phase and the reaction chemistry is so slow that the flame temperature never increases enough to initiate the nitrogen reactions. This results in a flat temperature profile. However, as the amount of ADN(v) increases, the initial energy release in the gas-phase increases.

The results of the parametric calculations indicate that the optimal amount of ADN(v) is ~5 mole% leaving the surface, as shown in Figure 4-12. If the amount is further increased, the temperature profile continues to approach the surface and overshoots the experimental data. These results agreed with the idea that ADN(v) would be minimal to generate the large condensed-phase heat release.

The assumption that ADN dissociates upon evaporation results in the release of more energy in the gas phase, and thus an increase in the temperature profile, assuming the same amount of evaporation. The reason for this is the endothermic dissociation of ADN. The assumption of evaporative dissociation places this endothermic reaction in the condensed phase, and therefore, more heat is released in the gas phase and less in the condensed phase. Whereas 5 mole% ADN(v) is necessary to match the temperature profile, only about 4 mole% of ADN is necessary to dissociative upon evaporation to match the temperature profile, as shown in Figure 4-13. Based on this numerical analysis,

the exact form of ADN evaporation appears to have little impact on the overall solution. This study, therefore, assumes that 5% ADN evaporates to form ADN(v) at 6 atm to more closely match the large heat release experimentally calculated for the condensed-phase heat release (estimated to be between 100 and 460 cal/g).[42,53]

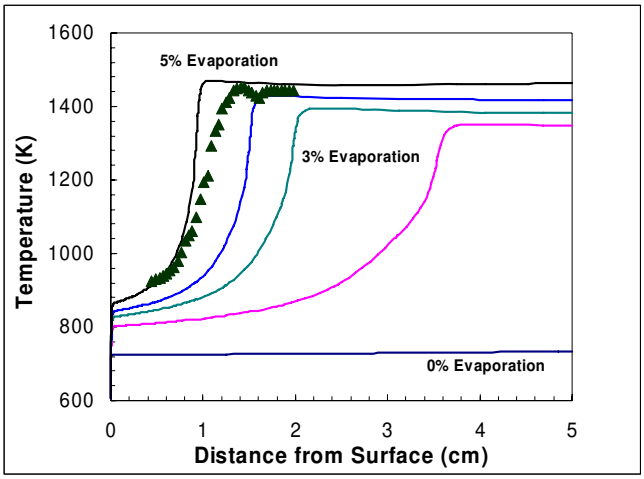

Figure 4-12: Numerical study to determine the effects of various amounts of ADN(v) on the gas-phase calculation, compared to Korobeinichev data at 6 atm.

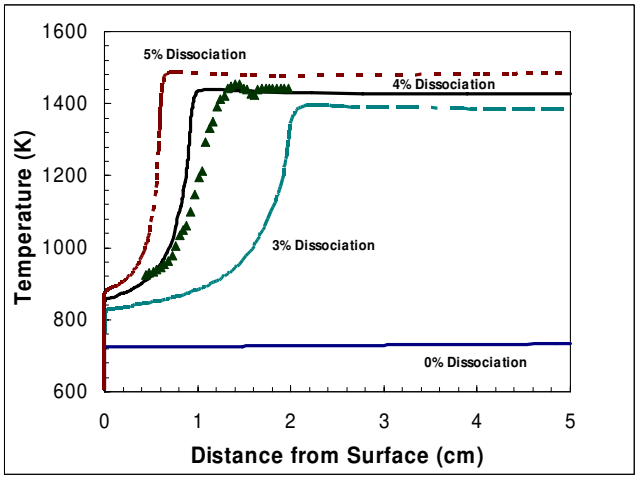

Figure 4-13: Numerical study on the effects of ADN evaporation assuming dissociative evaporation via Equation (2-2) compared to Korobeinichev data at 6 atm.

4.3.3 Area Expansion Study

An assumed area expansion was necessary to match experimentally determined gas-phase profiles when using the Korobeinichev initial conditions listed in Table 4-1. The necessity of area expansion has also been studied when linking the condensed and gas phases using Equation (4-1) and assuming ADN evaporation accounts for 5 mole% of the species leaving the surface. The parametric study determined that area expansion has a diluting effect on the flame. It spreads out the calculated heat release due to the ADN(v) decomposition and pushes the flame away from the surface, as shown in Figure 4-14. The results shown in Figure 4-14 indicate that the inclusion of area expansion to obtain accurate results is not necessary. This is encouraging because no experimental evidence exists to support the inclusion of an area expansion.

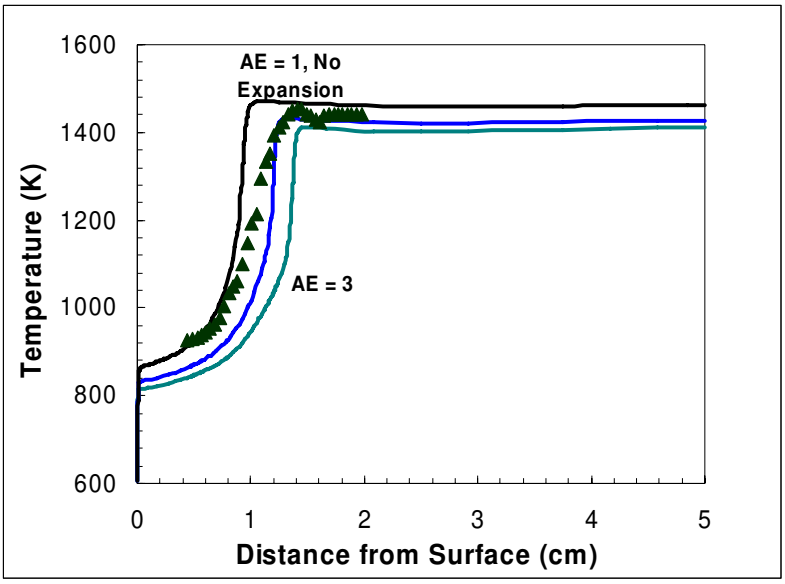

Figure 4-14: Effects of area expansion using the global reaction and assuming 5 mole% ADN(v) at the surface at 6 atm.

4.3.4 Final Condensed-Phase Mechanism

The condensed phase mechanism used for the remainder of this study consists of the global reaction, Equation (4-1), and the assumption that ADN evaporates to form ADN(v). The reaction rates used are given in Table 4-2. The global reaction rate is based on experimental reaction rates found in the literature[36,48,52,53,54] and presented in Figure 4-15. The evaporation rate uses Shamakov's activation energy and the pre-exponential factor has been reduced to slow evaporation and thus increase the surface temperature. Results are presented in the Chapter 5.

Unfortunately, this global reaction is unable to predict the combustion instability of ADN in the pressure range from 20 to 100 atm. Therefore, the activation energy of the global condensed-phase reaction was increased systematically between 20 and 90 atm. For every 5 atm increase in pressure, 100 cal/mole were added to the activation energy of the global reaction in this range. This method leads to an activation energy of 39.4 kcal/mol at 90 atm and this value was used at all higher pressures. The increase in activation energy was necessary to obtain a smooth transition between regions 1 and 3 in ADN's burning rate curve.

Table 4-2: Reaction rates used for condensed-phase mechanism.

Reaction	A	E_A (kcal/mol)
Global Reaction (s^{-1})	4.0×10^{15}	38.0
ADN=ADN(v) ($dyne/cm^2$)	5.0×10^{18}	37.0

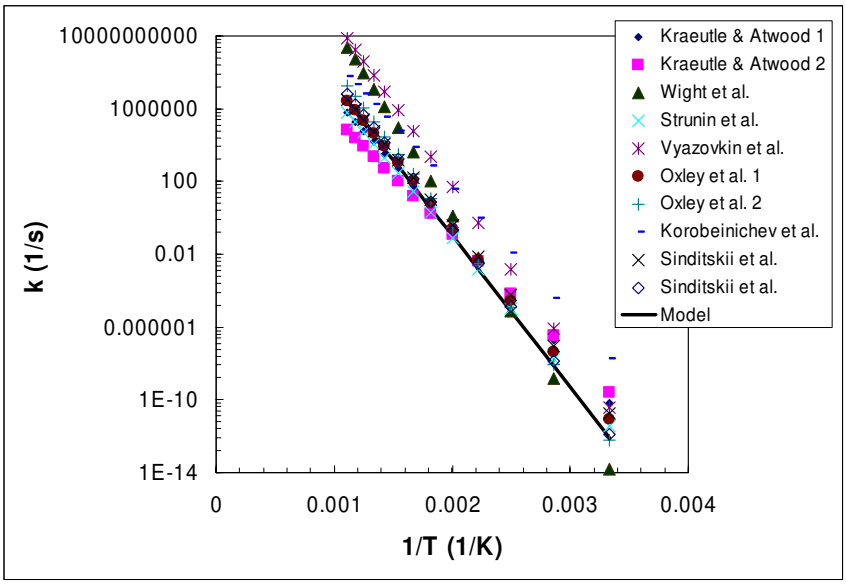

Figure 4-15: Proposed condensed-phase reaction rates.

4.4 Summary

Condensed and gas-phase mechanisms were developed for ADN monopropellant combustion. Parametric studies were performed using PHASE3 on previously published gas-phase mechanisms to evaluate their accuracy compared to experimental data obtained by Korobeinichev.[37] Results of the study indicated that the Korobeinichev mechanism most accurately matched the data. However, they used an arbitrary gas-phase area expansion.

A condensed-phase mechanism was developed based on available surface species data obtained by Brill[40] and Fetherolf.[51] The condensed-phase mechanism consists of a single global reaction and accurately predicts combustion properties of ADN in the first burning rate region. Modification to the reaction rate was necessary to create a smooth transition through the unstable combustion region between 20 and 100 atm. Such a method is not a satisfactory modeling approach and is seen as only a place holder until

future knowledge allows for a more realistic model. The current condensed-phase mechanism is seen as an initial step in the development of a more detailed mechanism. Parametric studies were then conducted to examine the path and impact of ADN evaporation. Calculations indicated that 5% ADN evaporation was an optimal value to match the data, and the inclusion of evaporation eliminated the need for the gas-phase area expansion.

5 ADN Results and Discussion

5.1 Numerical Results

The first coupled condensed-gas phase model using detailed kinetics has been developed for ADN. Very good results were obtained for ADN burning rate, species and temperature profiles, and temperature sensitivity using a single, global condensed-phase reaction for the first segment of the burning rate curve. Modifications to the condensed-phase reaction rate were necessary to obtain reasonable results for the second and third burning rate regions. Burning rate calculations are presented in Figure 5-1. As pressure decreases below 2 atm the model begins to deviate from the experimental data. However, ADN has a pdl of 2 atm;[36,39] Sinditskii reports that ADN can only burn at atmospheric pressure if it is liquefied and then heated. Therefore, the experimental data in Figure 5-1 below 2 atm are suspect. The model predicts a pressure exponent of 0.51 for the first region and 0.48 for the third region, both low compared to the experimental value of ~0.6. The second region is unstable, and therefore, not a primary focus in this study.

The ADN model was correlated to agree with the surface temperature data from Zenin. As seen in Figure 5-2, Zenin's data are on the lower end of the experimental surface temperature range. Figure 5-2 also contains a comparison of the experimental and

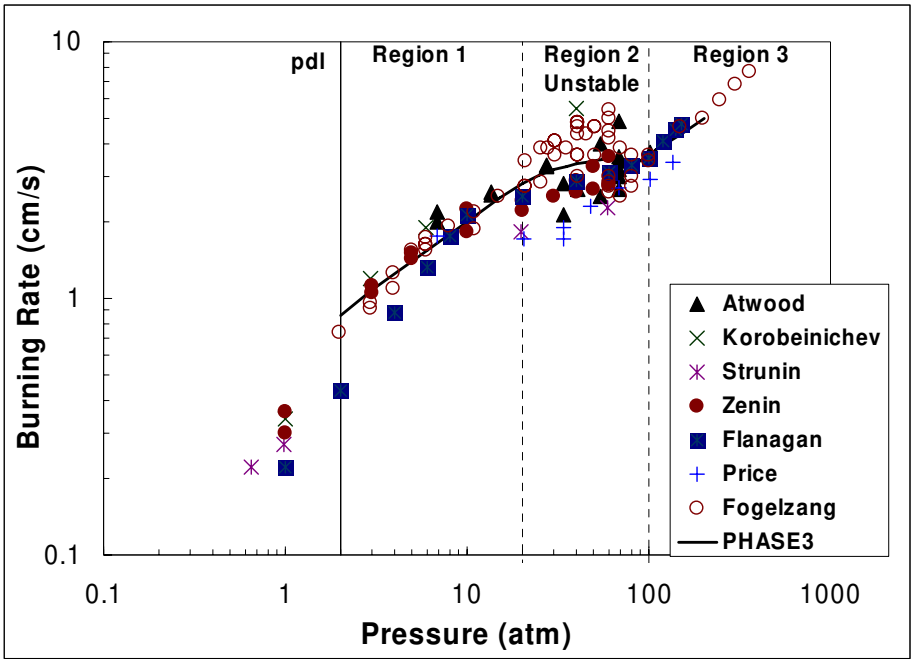

Figure 5-1: Experimental data versus numerical calculations for ADN combustion.

numerically predicted lengths of the first dark zone for various pressures. The predicted dark zone lengths follow the data fairly accurately up to approximately 20 atm. However, above 20 atm, Zenin measured the flame approaching the surface and observed the dark zone disappearing completely at 60 atm, whereas the model predicts the dark zone length stabilizing and changing slowly as pressure increases. This discrepancy is caused by the use of the single global reaction to account for condensed-phase decomposition at all pressures. It is believed that the condensed-phase mechanism should change as pressure increases, and this could result in a varying dark zone length at higher pressures.

The model provides excellent agreement when compared to the Korobeinichev temperature and species data[37] at 6 atm (see Figure 5-3). These data were used to help determine a feasible condensed-phase reaction and in the examination of ADN evaporation; therefore, the results are not surprising. The results are presented for the gas-

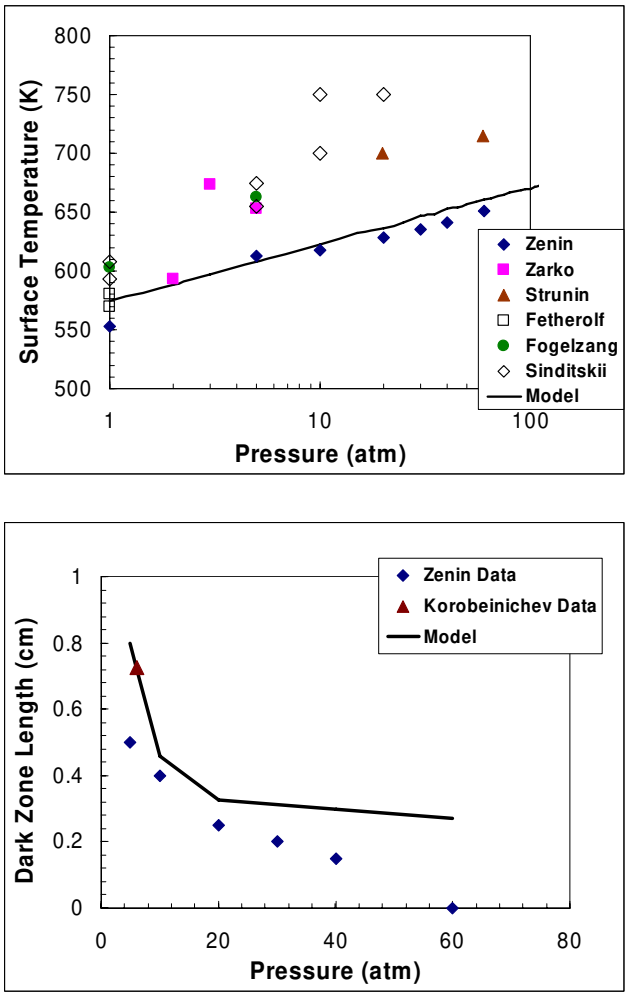

Figure 5-2: Comparison of experimental and numerical surface temperature (top) and the first dark zone length (bottom) for ADN.

phase temperature profile and a number of gas-phase species profiles. All species calculations agree with the experimental data quite accurately except for NO. In his work, Korobeinichev,[55] noted that "many other NO species (N_2O, NO_2, HNO_3, HONO, and ADN(v)) bear an input into peak 30, an error in defining NO by withdrawn sample mass-spectrum can be large in view of the analysis of NO transformations in chemical reactions zones on ADN burning at 3 atm." Therefore, the experimental species profile for NO presented by Korobeinichev is assumed to be slightly high.

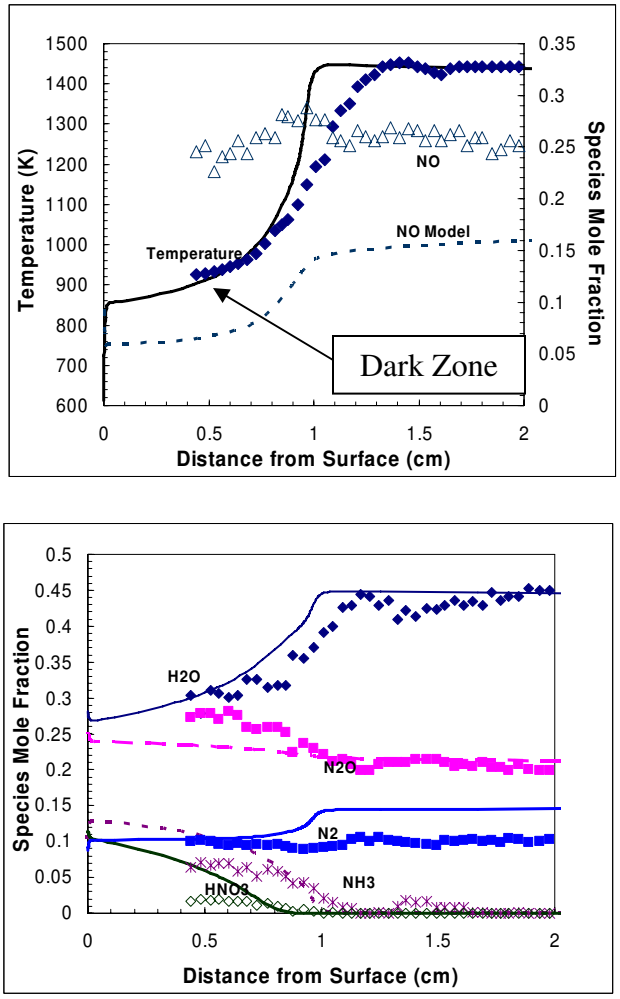

Figure 5-3: Numerical predictions compared to Korobeinichev's ADN data at 6 atm.

An interesting aspect of ADN combustion is the inability to reach its adiabatic flame temperature at low pressures. A major reason for this is assumed to be the slow kinetics of the nitrogen reactions. The flame is apparently so far from the surface that heat losses reduce the reactions before the adiabatic flame temperature can be reached. The model is able to predict the low final flame temperatures reached during ADN combustion at pressures lower than 40 atm. Figure 5-4 contains the model's predicted

final flame temperature versus experimental data for a gas-phase length of 5 cm. This length was chosen because it is around the same scale as experimental measurements.

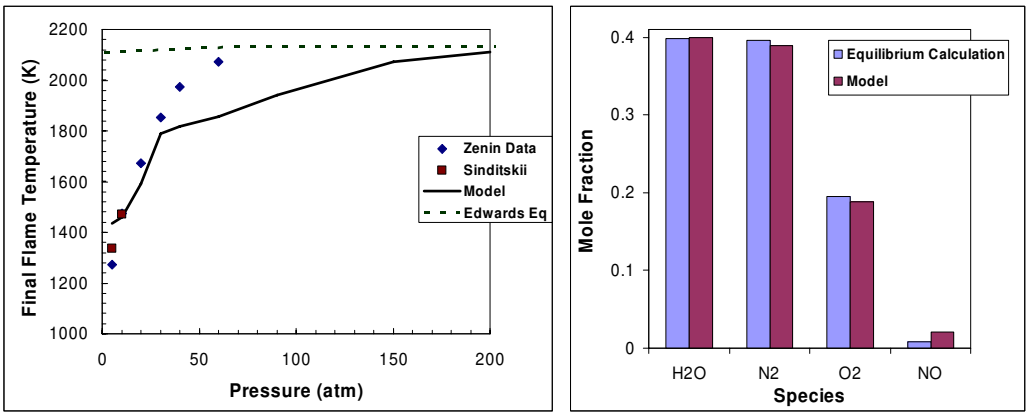

Figure 5-4: Adiabatic final flame temperature calculations compared to the current model's calculations versus experimental data (left) and adiabatic final species calculations versus current model calculations (right).

PHASE3 assumes adiabatic conditions, so it is possible to reach the adiabatic flame temperature if the numerical gas phase is extremely long (>100 cm). This is shown in Figure 5-5 where the gas-phase calculation goes out to 10 meters. In an actual experiment, the heat loss would be far too great to approach such a length. Figure 5-4 also gives the adiabatic flame temperature as calculated by the Edwards Equilibrium Code using -31.8 kcal/mol[33] for the heat of formation of ADN. The model closely matches the data up to 30 atm after which it diverges and does not approach the adiabatic flame temperature as quickly as the experimental data. Once again this is most likely due to the global condensed-phase kinetics being optimized for the first region of combustion. Figure 5-4 also shows the model's predicted final species and the final species calculated

with the Edwards Equilibrium Code at 200 atm. The final species closely match the adiabatic calculations, but with a slight excess of NO.

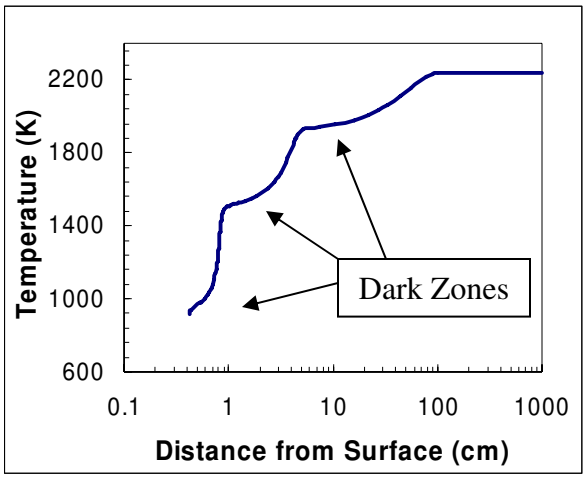

Figure 5-5: ADN gas-phase calculation using the Korobeinichev Data as initial conditions; recreation of work performed by Liau.

Figure 5-6 compares experimental data and numerical calculations for two different sets of temperature sensitivity data. The temperature sensitivity calculations follow the general trends of the experimental data for region 1, but diverge in regions 2 and 3. The poor agreement at higher pressures is attributed to the use of a global reaction in the current condensed-phase mechanism. In general, high temperature sensitivity of a monopropellant implies an exothermic condensed phase is dominating combustion. As pressure increases, the flame is typically drawn closer to the surface and the gas phase begins to dominate the combustion process. Therefore, the temperature sensitivity decreases as pressure increases. The large temperature sensitivity for ADN in region 1 is attributed to the large condensed-phase heat release (experimental values vary from 100 to 460 cal/g at atmospheric conditions). Sinditskii hypothesized that the gas phase of

ADN does not play a dominant role in combustion until region 3 (pressures above 100 atm). If correct, this hypothesis indicates that the decrease in temperature sensitivity in region 2 (20 to 100 atm) is due to a decrease in condensed-phase heat release, not an increase in gas-phase heat feedback. The use of a global reaction in the ADN condensed-phase mechanism does not allow the heat release to decrease with increasing pressure, and thus the temperature sensitivity calculations in regions 2 and 3 do not follow the data. This illustrates a shortcoming of the current condensed-phase mechanism, and therefore, a more detailed mechanism is desired.

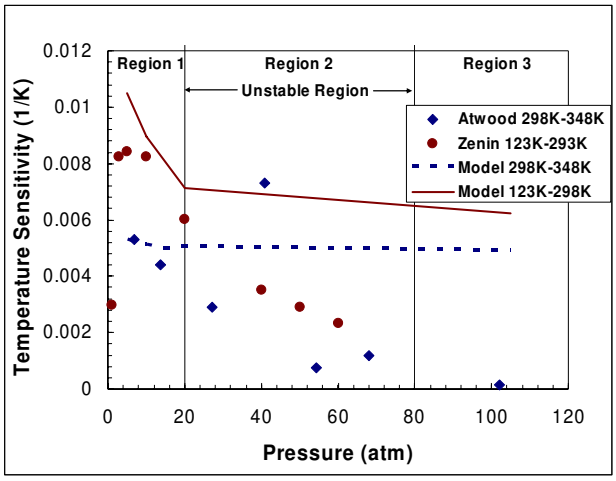

Figure 5-6: ADN temperature sensitivity.

5.2 Discussion of Results

The ADN combustion model was correlated with the Korobeinichev data at 6 atm and the Zenin surface temperature data. The model accurately predicts combustion properties of ADN in the first region of the burning rate curve including burning rate, dark zone length, final flame temperature, temperature sensitivity, and final species.

Therefore, the global condensed phase reaction is relatively accurate for this region of the burning rate curve. However, shortcomings are evident when extrapolating the global reaction to the 2nd and 3rd regions of ADN's burning rate curve. The shortcomings illustrate the need for further development of the condensed-phase model.

The major shortcoming of the current model is its inability to predict ADN's unstable combustion without modification of the condensed phase mechanism. Currently, the activation energy of the global condensed-phase reaction must be increased as pressure increases to obtain a reasonable burning rate profile through the unstable region. A second shortcoming of the model is predicting dark zone lengths. The predictions are fairly accurate in region 1, but not in regions 2 and 3. A third inaccuracy in the model is the predicted heat flux at the surface. The model predicts heat fluxes an order of magnitude higher than those calculated by Zenin.[42] A fourth inaccuracy is the poor temperature sensitivity calculations in regions 2 and 3. These deficiencies illustrate the need for a more accurate and detailed condensed-phase mechanism. The following section outlines proposed modifications to the condensed phase mechanism based on this work's numerical study and the literature review.

5.3 Proposed Condensed-Phase Modifications

Determining a global condensed phase reaction is seen as only the first step in modeling ADN combustion. It is evident from the experimental work that ADN combustion is extremely complex and cannot be represented accurately by a single global condensed-phase reaction. Sinditskii[36] proposed that ADN's instability is due to the increase of ADN's dissociation temperature with pressure, without a corresponding

increase in condensed-phase heat release. This would result in a growing deficiency of energy required to heat up and evaporate the condensed phase species. Meanwhile, the gas phase would still be unable to support combustion. Following their theory, at around 20 atm, the decomposition becomes highly unstable and results in increased dispersion of the surface layer. They proposed that this process dominates until around 100 atm, at which point the gas phase is finally able to control combustion and eliminate the instability. As an addition to this theory, it is proposed that there is a corresponding decrease in the condensed-phase heat release as the pressure increases. This can possibly be accomplished by a more detailed condensed-phase mechanism with a few modifications to Sinditskii's theory.

There are a few problems with the proposed reaction pathway given by Sinditskii[36] for ADN decomposition. The major problem being the path of AN decomposition. His proposed pathway is illustrated in Figure 5-7. According to Sinditskii, AN decomposes at a rate 10^7 to 10^8 slower than the dinitramide salt, and the large amount of water present in the initial decomposition of ADN cannot be attributed to AN. Therefore, he proposed that AN dissociates at the surface, thus using all of the energy released from forming AN in the first place. To achieve the large condensed-phase heat release observed experimentally, the conversion of ADN to NH_3 and DA must account for about 50 kcal/mol, according to their model. However, the conversion of ADN to final gas-phase products results in a heat release of 83 kcal/mol, Equation (5-1), but if it is assumed that O_2 does not form, and instead NO is formed as expressed by Equation (5-2), the heat release is only 40 kcal/mole. To obtain a heat release of 50 kcal/mol as proposed by Sinditskii, ADN decomposition must approach its final gas-

phase products in the condensed phase. It seems unlikely that final products would form by this path in the condensed phase while AN does not decompose further in the condensed phase.

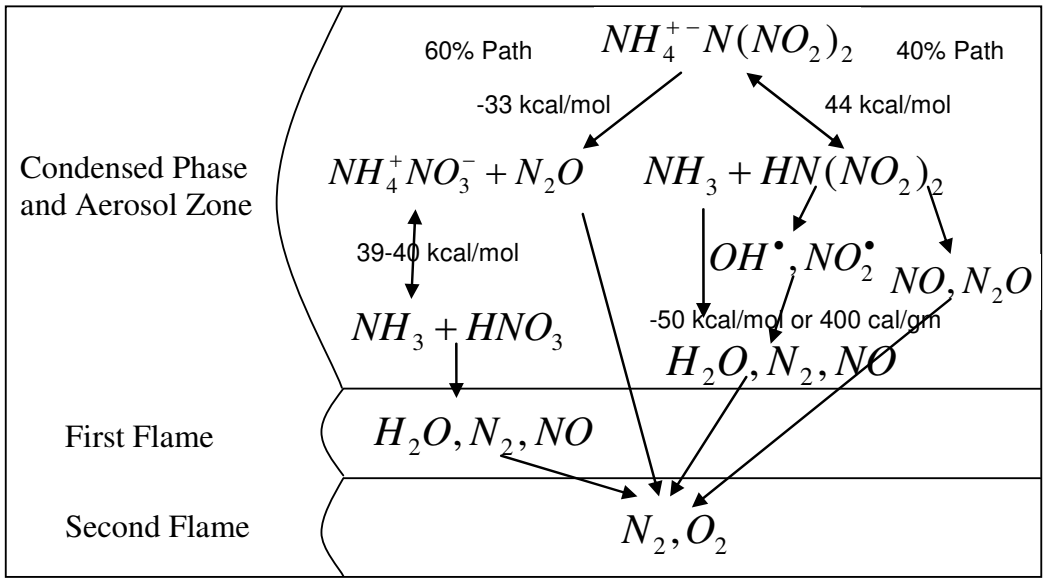

Figure 5-7: Sinditskii's proposed decomposition pathway for ADN.

$$ADN \rightarrow 2H_2O + 2N_2 + O_2 \qquad \Delta H \sim -83 \quad \text{kcal/mol} \qquad (5\text{-}1)$$

$$ADN \rightarrow 2H_2O + N_2 + 2NO \qquad \Delta H \sim -40 \quad \text{kcal/mol} \qquad (5\text{-}2)$$

Surface temperature measurements by Whittaker et al.[110] for AN do not support the idea that AN does not decompose in the condensed phase. Whittaker recorded surface temperatures for AN lower than the surface temperatures reported for ADN, see Figure 5-8. This work supports the idea that AN would decompose at lower temperatures.

Finally, Brill[40] proposed a condensed-phase reaction containing extremely large amounts of water leaving the surface of AN during decomposition, Equation (5-3), and thus AN could account for the early presence of large amounts of H_2O.

$$28AN \rightarrow 6HNO_3 + 3NO_2 + NO + 2NH_3 + 5N_2O + 13N_2 + 42H_2O + 4AN(aerosol) \quad (5\text{-}3)$$

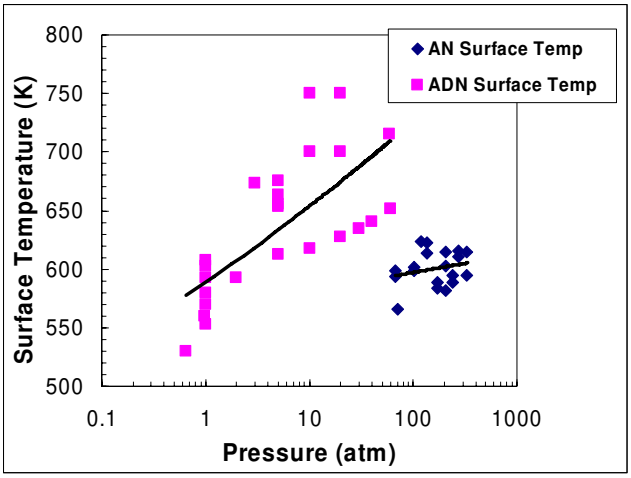

Figure 5-8: Surface temperature measurements for ADN and AN.

The author, therefore, proposes that AN decomposition does in fact take place in the condensed phase. This would allow for the large amount of heat release created from the conversion of ADN to AN to account for the large condensed phase heat release seen during ADN decomposition. The author's proposed reaction mechanism is presented in Figure 5-9.

The proposed mechanism is a parallel decomposition path in which ADN is converted to AN as one path and ADN is converted to NH_3 and DA as the second path. This is similar to that proposed by Sinditskii et al., but instead of AN entering the gas

phase, the majority of it is assumed to decompose in the condensed phase. There is a huge potential heat release if ADN converts to AN (-33 kcal/mole), but if virtually all AN dissociates upon evaporation (39-40 kcal/mol), all of the heat release is used up in the condensed phase. Decomposition of ADN via NH_3 and DA cannot produce sufficient heat to account for the large condensed phase heat release found in ADN, especially if only 40 to 50 percent of the decomposition follows this route. AN must also decompose in the condensed phase to a large extent. The exact steps after the initial decomposition are still unknown, and some type of global reaction may still be needed to represent each decomposition pathway. Due to the very low heat of formation of AN and ADN, it could be assumed that their decomposition products react with a net heat release of around 0 kcal/mol in the condensed phase. This would dictated that the majority of the heat release comes from the conversion of ADN to AN.

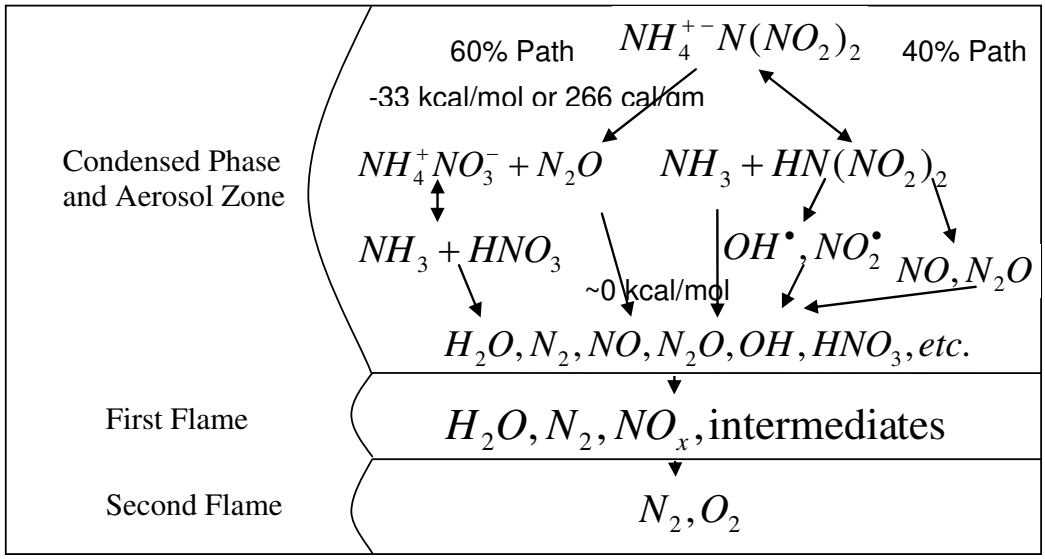

Figure 5-9: This work's proposed condensed-phase decomposition pathway for ADN.

Korobeinichev estimated the activation energy for the condensed phase reaction of ADN forming DA and NH_3 to be between 50 and 52 kcal/mol. Because the conversion to AN is assumed to dominate at low pressures, it is assumed that its activation energy would be closer to the experimentally measured values, 30 to 45 kcal/mol. Therefore, as temperature increases, the importance of the 40% pathway should also increase. This would result in a reduction of heat release in the condensed phase. A representation of the reaction rates is presented in Figure 5-10. Sinditskii[36] stated that the conversion to AN accounted for about 60% of the decomposition at low pressure with that amount decreasing with pressure, but still remaining very important. This supports the above reasoning. ADN and AN evaporation would both take place, but both would be minimal.

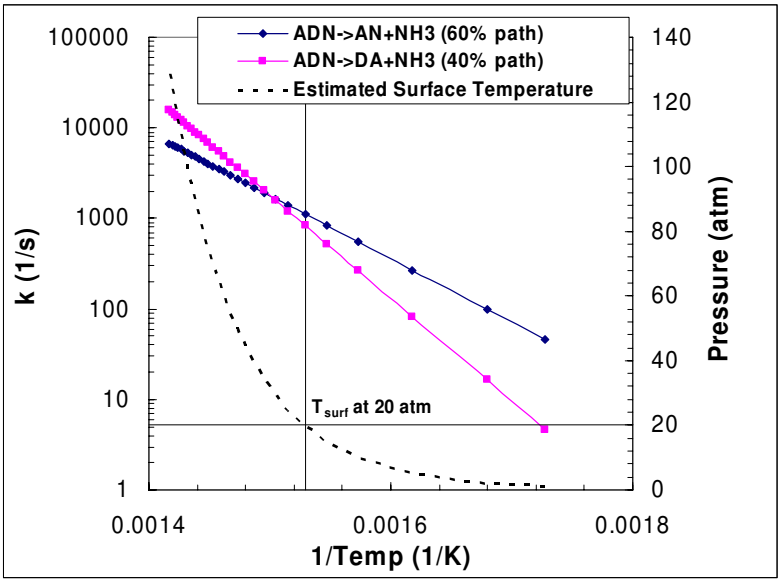

Figure 5-10: Reaction rates for pathway A (60%) and pathway B (40%) compared to assumed surface temperatures and the corresponding pressures. Note that the dominating reaction changes at ~20 atm, thus reducing the condensed-phase heat release.

An attempt to use this mechanism was performed, but due to time limitations, it was not completed. Korobeinichev's experimental data was matched correctly using the new mechanism, but the pressure exponent of the burning rate curve was only 0.3. Further work needs to be performed to analyze the reasons for a low pressure exponent, such as poor kinetics or incorrect global reactions. The results are presented in Figure 5-11. Positive aspects of this new mechanism include cutting the heat flux at the surface by more than half, and achieving a higher condensed-phase heat release at atmospheric conditions and a decrease in heat release with increasing pressure, from 200 cal/g at 6 atm to 150 cal/g at 20 atm.

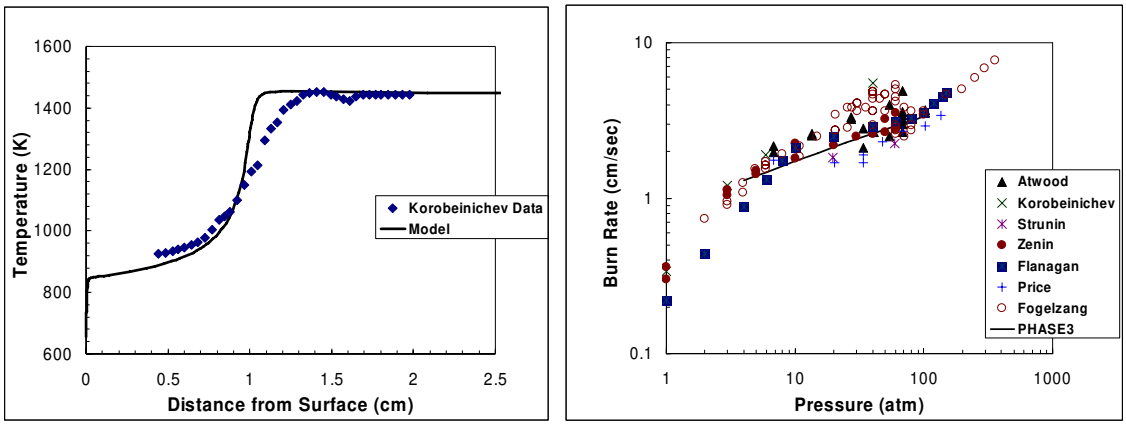

Figure 5-11: Numerical results using the proposed condensed-phase decomposition pathway for ADN.

5.4 Conclusions

A combustion model has been developed that accurately predicts experimental data for the first region of ADN combustion (2 to 20 atm). These include temperature and species profiles, burning rates, and temperature sensitivity. The model is also able to

predict burning rates over all regions and pressures, but the model uses a single global condensed-phase reaction. It is also assumed that ADN evaporates to form the molecular complex ADN(v). Shortcomings of the model include an inability to predict ADN's unstable combustion region, dark zone lengths at pressures above 20 atm, and temperature sensitivity above 20 atm. To address these shortcomings, a more detailed condensed-phase mechanism was proposed and initial results matched temperature and species data, but failed to predict an accurate pressure exponent. Further work, both experimental and theoretical, needs to be performed to analyze the reasons for a low pressure exponent, such as poor kinetics or incorrect global reactions.

6 AP/HTPB Numerical Model

To investigate the details of the flame structure produced by AP composite propellants, a two-dimensional model with detailed gas-phase chemical kinetics has been developed. The model is based largely on the work of Felt.[3] However, in the Felt model, the fully coupled conservation equations were solved. These equations resulted in a tightly coupled, nonlinear system. The system was coupled, since multiple dependent variables appear in the same equation, and nonlinear, since products of the dependent variables appear in the equations.[111] A major difficulty in solving the governing equations results from the tight coupling of pressure and velocity, a small change in pressure results in a large change in velocity.

Numerical difficulties become even more prominent at low Mach numbers ($M < 0.3$). As Mach number approaches zero, use of the fully coupled conservation equations begin to suffer in efficiency and accuracy. These numerical difficulties are due to the pressure term being on the order of $1/M^2$. Further, as M approaches zero, pressure is only a weak function of density, and therefore, of minimal importance.[112] The Felt model suffered from efficiency and accuracy problems inherent with this type of solution method. Model calculations would take weeks to converge, dozens of code crashes would be experienced due to divergence, and the final solution may have been inaccurate. Extremely small timesteps (10^{-8} to 10^{-11} sec.) had to be taken to facilitate convergence

and minimize pressure changes between steps. Even with the small timesteps, it was found that the numerical solver still frequently crashed, and thus inlet boundary condition updates also had to be minimized to ~10% or less of the actual value. This would minimize the change to the boundary conditions and help keep the code from diverging. With all the precautions, convergence was still not assured, and much user interaction was required to reach a solution. Therefore, modification of the model to a low Mach number solution technique was undertaken.

6.1 Previous Model: Pressure-Velocity Formulation

The new two-dimensional, detailed kinetic diffusion model of AP/HTPB composite propellants is based on the two-dimensional model developed by Felt.[3] The Felt diffusion model utilized the Navier-Stokes equations for momentum, in which there is a tight coupling of pressure and velocity. The mathematical equations describing reacting fluid dynamics include equations for mass continuity, species continuity, and energy. These equations are presented in vector format as Equations (6-1) to (6-5).

Mass continuity:

$$\frac{\partial \rho}{\partial t} + \left(\nabla \cdot \rho \mathbf{v}\right) = 0 \tag{6-1}$$

Momentum:

$$\frac{\partial}{\partial t}\rho \mathbf{v} + \left(\nabla \cdot \rho \mathbf{v}\mathbf{v}\right) + \nabla P + \left(\nabla \cdot \boldsymbol{\tau}\right) - \rho \mathbf{g} = 0 \tag{6-2}$$

Energy:

$$\frac{\partial}{\partial t}\left(\sum_{i=1}^{K}\rho Y_i h_i\right)+\left(\nabla\cdot\sum_{i=1}^{K}\rho Y_i h_i\left(\mathbf{v}+\hat{v}_i\right)\right)-\left(\nabla\cdot\lambda\nabla T\right)+\left(\boldsymbol{\tau}:\nabla\mathbf{v}\right)-\frac{DP}{Dt}=0 \qquad (6\text{-}3)$$

Species continuity:

$$\frac{\partial}{\partial t}\left(\rho Y_i\right)+\nabla\cdot\rho Y_i\left(\mathbf{v}+\hat{v}_i\right)-\dot{w}_i=0 \qquad (6\text{-}4)$$

Ideal gas equation of state:

$$\rho=\frac{P\overline{W}}{RT} \qquad (6\text{-}5)$$

The solution used by Felt to Equations (6-1) to (6-5) utilized a time marching technique to achieve a steady-state solution, and therefore, time derivatives had to be included. This dictates a timestep limited by the CFL criteria,[113] Equation (6-6), which dictates the timestep needed to reach a stable, steady-state solution.

$$\Delta t<\frac{\Delta x}{|v|} \qquad (6\text{-}6)$$

where Δt is the maximum timestep, Δx is the cell size, and $|v|$ is the largest velocity.

The need for a time marching technique is further dictated by the hyperbolic characteristics of the equations. The system of equations at steady-state is essentially elliptical in nature, but the presence of first-order time derivatives introduces hyperbolic characteristics to the system. These hyperbolic characteristics create a very strong

convergence dependence on initial conditions. Poor initial conditions result in difficulty obtaining a steady-state solution. Further, the pressure term is first order, and thus, also has hyperbolic characteristics. These hyperbolic characteristics, as well as the low Mach number, make accurate initial conditions all the more important.

A further difficulty associated with calculating the pressure field is the requirement of the Navier-Stokes equations to resolve a broad range of pressure scales. Both bulk pressure gradients and low-amplitude acoustic wave behavior are resolved with the Navier-Stokes equations, even though, for the current problem, pressure is essentially constant and low-amplitude acoustics are negligible (low Mach number assumption). Such resolution greatly increases the resultant CPU time. An example of the differing pressure scales is given by Kee[111] and illustrates three very different pressure scales:

> "Consider the steady flow through a pipe, where a pressure gradient is required to offset the shear drag at the walls. Assuming atmospheric pressure, the pressure variation associated with the flow is likely very small compared to atmospheric pressure. Now consider what happens if someone gently taps the pipe wall with a hammer. There are low-amplitude (acoustic) pressure variations that travel rapidly throughout the flow. While the Navier-Stokes equations are very capable of representing these pressure waves, they are essentially irrelevant to the primary pipe flow."

Resolving low-amplitude acoustics is unnecessary in the current situation and involves a large increase in computation time. Further, pressure is essentially constant during combustion despite the large variations in temperature and density, and the only pressure of interest is the operating pressure. Various methods have been devised to filter the pressure of the low-amplitude acoustic waves and such a method is desired for the current problem. For the current solving technique, a set of governing equations with mainly elliptical properties is also desired. Whereas hyperbolic equations are initial condition dependent, elliptical equations are boundary condition dependent. Therefore, if an initial guess is provided within the range of convergence, the CFL criteria can be neglected, and the steady-state form of the equations can be solved. This allows for large reductions in runtime. Therefore, to decrease runtime, it is desirable to filter the pressure and develop governing equations that are more elliptical in form than the Navier-Stokes equations.

Overall, the exact time to convergence is difficult to quantify using the Felt model because runtime varied based on the system conditions. In general, time-steps were between 10^{-8} and 10^{-11} and M << 0.05. For example, a 400 μm AP particle surrounded by binder had a maximum timestep 10^{-8}, a maximum M 0.019, and a maximum pressure variation of only 350 Pa. Over a period of months, only a handful of cases converged, and a number of them were later found to be inaccurate.

6.2 New Model: Low Mach Number Formulation

Low Mach number formulations essentially filter out the acoustics from the pressure field. A number of methods are available for low Mach flow. Such methods fall

into two categories, density-based methods and pressure-based methods.[112] Density-based methods modify the compressible equations to work in the low Mach regime, whereas pressure based methods extrapolate the corresponding incompressible equations up to the low Mach region. Density-based methods seemed most appropriate in this study because of the reactive nature of the flow. The methods investigated included the SIMPLE method,[114] projection methods such as the method used by Jackson et al.,[101] and the vorticity method used by Smooke et al.[115] Implementation of the SIMPLE or projections methods required a change to the solving technique currently used in the Felt code. Therefore, the vorticity method was chosen because it could be solved using the Newton-Rhapson method.

6.2.1 Vorticity-Velocity Formulation

The method decided upon to achieve pressure filtering and elliptical equations was the vorticity-velocity approach. Vorticity (ω) represents the angular rotation rate of a fluid and is defined as the curl of the velocity field, Equation (6-7). This results in three vorticity components for a 3-dimensional domain, Equations (6-8). However, for a two-dimensional domain only one component of the vorticity is non-zero (ω_z).[116,117]

$$\boldsymbol{\omega} = \nabla \times \mathbf{v} \tag{6-7}$$

$$\omega_x = \frac{\partial v_z}{\partial y} - \frac{\partial v_y}{\partial z}, \quad \omega_y = \frac{\partial v_x}{\partial z} - \frac{\partial v_z}{\partial x}, \quad \omega_z = \frac{\partial v_y}{\partial x} - \frac{\partial v_x}{\partial y} \tag{6-8}$$

Pressure appears in the Navier-Stokes equation in the form of a gradient and by definition, the curl of a gradient is zero. Therefore, conversion of the Navier-Stokes equations to a vorticity formulation effectively eliminates pressure. This filters the pressure and eliminates many of the numerical instabilities associated with the calculation of the pressure field.

Vorticity has been employed extensively for incompressible flow calculations. Work by Smooke in 1989[115] at Yale University resulted in the development of a vorticity-stream function formulation for use with compressible two-dimensional diffusion flame calculations. His work has been further refined to a vorticity-velocity formulation[118,119] and is the basis for the vorticity-velocity formulation employed in this study. A steady-state, ideal gas formulation of the governing equations is utilized in developing the vorticity-velocity formulation. Formulation of the vorticity equations begins with the steady-state continuity and momentum Equations (6-9) and (6-10).

Mass continuity:

$$\nabla \cdot (\rho \mathbf{v}) = 0 \tag{6-9}$$

Momentum:

$$\rho(\mathbf{v} \cdot \nabla)\mathbf{v} + \nabla P - \nabla \cdot \boldsymbol{\tau} + \rho \mathbf{g} = 0 \tag{6-10}$$

The vorticity transport equation is derived by applying Equation (6-7) to Equation (6-10) and results in Equation (6-11).

$$-\mu\nabla^2\boldsymbol{\omega}-\nabla\mu\times[2\nabla(\nabla\cdot\mathbf{v})-\nabla\times\boldsymbol{\omega}]-\nabla\times[\boldsymbol{\varepsilon}\cdot\nabla\mu]-\nabla\rho\times\mathbf{g}+\nabla\rho\times[(\mathbf{v}\cdot\nabla)\mathbf{v}]+\rho[\nabla\times(\boldsymbol{\omega}\times\mathbf{v})]=0 \tag{6-11}$$

where $\boldsymbol{\varepsilon}=\nabla\mathbf{v}+(\nabla\mathbf{v})^t$, part of the viscous stress tensor.

Elliptical velocity equations are then derived by substituting the curl of the vorticity (6-12) into the product of 1/ρ and the gradient of the continuity Equation (6-13).[119,120] The resulting velocity equation, in vector form, is presented as Equation (6-14).

$$\nabla\times\boldsymbol{\omega}=\nabla\times(\nabla\times\mathbf{v})\rightarrow\nabla(\nabla\cdot\mathbf{v})-\nabla^2\mathbf{v} \tag{6-12}$$

$$\nabla\left(\frac{\nabla\cdot\rho\mathbf{v}}{\rho}\right)=\nabla(\nabla\cdot\mathbf{v})+\nabla\left(\frac{\mathbf{v}\cdot\nabla\rho}{\rho}\right) \tag{6-13}$$

Velocity:

$$\nabla^2\mathbf{v}+\nabla\left(\frac{\mathbf{v}\cdot\nabla\rho}{\rho}\right)+\nabla\times\boldsymbol{\omega}=0 \tag{6-14}$$

Expanding the above equations, and including the ideal-gas form of the energy equation[111,120] and the continuity equation,[121] results in the governing equations for the vorticity-velocity formulation. Equations (6-15) to (6-19) present the two-dimensional equations in cylindrical form.[119]

Radial velocity:

$$\frac{\partial^2 v_r}{\partial r^2}+\frac{\partial^2 v_r}{\partial z^2}-\frac{\partial \omega}{\partial z}+\frac{\partial}{\partial r}\left(\frac{v_r}{r}\right)+\frac{\partial}{\partial r}\left(\frac{v_r}{\rho}\frac{\partial \rho}{\partial r}+\frac{v_z}{\rho}\frac{\partial \rho}{\partial z}\right)=0 \tag{6-15}$$

Axial velocity:

$$\frac{\partial^2 v_z}{\partial r^2}+\frac{\partial^2 v_z}{\partial z^2}+\frac{\partial \omega}{\partial r}+\frac{1}{r}\frac{\partial v_r}{\partial z}+\frac{\partial}{\partial z}\left(\frac{v_r}{\rho}\frac{\partial \rho}{\partial r}+\frac{v_z}{\rho}\frac{\partial \rho}{\partial z}\right)=0 \tag{6-16}$$

Vorticity:

$$\begin{aligned}\frac{\partial^2(\mu\omega)}{\partial r^2}+\frac{\partial^2(\mu\omega)}{\partial z^2}+\frac{\partial}{\partial r}\left(\frac{\mu\omega}{r}\right)-\rho v_r\frac{\partial \omega}{\partial r}-\rho v_z\frac{\partial \omega}{\partial z}+\frac{\rho v_r\omega}{r}-\overline{\nabla}\rho\cdot\nabla\left(\frac{\mathbf{v}\cdot\mathbf{v}}{2}\right)+\\ \overline{\nabla}\rho\cdot\mathbf{g}-2\left(\overline{\nabla}\left(div(\mathbf{v})\right)\cdot\nabla\mu-\nabla v_r\cdot\overline{\nabla}\frac{\partial\mu}{\partial r}-\nabla v_z\cdot\overline{\nabla}\frac{\partial\mu}{\partial z}\right)=0\end{aligned} \tag{6-17}$$

Energy:

$$\begin{aligned}\rho c_p\left(v_r\frac{\partial T}{\partial r}+v_z\frac{\partial T}{\partial z}\right)-\frac{1}{r}\frac{\partial}{\partial r}\left(r\lambda\frac{\partial T}{\partial r}\right)-\frac{\partial}{\partial z}\left(\lambda\frac{\partial T}{\partial z}\right)+\\ \rho\sum_{i=1}^{K}\left[c_{p,i}Y_i\left(\hat{v}_{i,r}\frac{\partial T}{\partial r}+\hat{v}_{i,z}\frac{\partial T}{\partial z}\right)\right]+\sum_{i=1}^{K}h_iW_i\dot{w}_i=0\end{aligned} \tag{6-18}$$

Species continuity:

$$\rho v_r\frac{\partial Y_i}{\partial r}+\rho v_z\frac{\partial Y_i}{\partial z}+\frac{1}{r}\frac{\partial}{\partial r}\left(r\rho Y_i\hat{v}_{i,r}\right)+\frac{\partial}{\partial z}\left(\rho Y_i\hat{v}_{i,z}\right)+W_i\dot{w}_i=0 \tag{6-19}$$

where $\overline{\nabla}=\hat{\mathbf{r}}\partial/\partial z-\hat{\mathbf{z}}\partial/\partial r$ and $div(\mathbf{v})=1/r\,\partial(rv_r)/\partial r+\partial v_z/\partial z$.

The following simplifying assumptions have been made in deriving Equations (6-15) to (6-19):

1. The fluid is steady, Newtonian, continuous, isotropic, and homogeneous.
2. Mixtures obey the ideal gas equation of state.
3. The Dufour effect (concentration gradients produce a heat flux) is negligible.
4. The Soret effect (temperature gradients produce species diffusion) is negligible.
5. Viscous dissipation is negligible.

6.2.2 Calculation of Thermodynamic and Transport Properties

Solution of the governing Equations (6-15) through (6-19) requires the calculation of various multi-component thermodynamic and transport properties. These properties include density, mean molecular weight, specific heat, enthalpy, chemical reaction rates, viscosity, diffusivity, and thermal conductivity. The new vorticity-velocity formulation of the equations uses the same solution approach as that used in the Felt pressure-velocity formulation and the CHEMKIN Libraries.[10,122] CHEMKIN is a problem-independent, general purpose suite of software from Sandia National Laboratories, developed by Kee in the 1980's. The CHEMKIN libraries standardize the input of chemical properties into numerical models by using a database of thermodynamic and transport properties for individual species. The thermodynamic database includes polynomial fits of specific heat (c_p/R), enthalpy ($H°/RT$), and entropy ($S°/RT$) for each species. The transport database consists of molecule geometry, Lennard-Jones potential well depth, Lennard-Jones collision diameter, dipole moment, polarizability, and rotational relaxation for each species. Input values for the thermodynamic and transport properties were taken from Jeppson.[9]

6.2.2.1 Thermodynamic Properties

The CHEMKIN subroutines[10] allow for calculation of thermodynamic properties and reactions rates. Species enthalpies and specific heats are determined directly from the thermodynamic library. The mean molecular weight is calculated as a sum of individual mass fractions and molecular weights, as seen in Equation (6-20). Density can then be calculated using the mean molecular weight and the ideal gas law.

$$\overline{W} = \frac{1}{\sum_{i=1}^{K} Y_i / W_i} \tag{6-20}$$

Chemical reaction rates for individual species are calculated by summing the forward and reverse reaction rates of all elementary reactions in which the species appears. Elementary reactions are stored in a kinetic mechanism in which the rate constants are expressed in the standard Arrhenius form. The robust CHEMKIN subroutines are able to handle dozens of species and hundreds of reactions in a very timely manner.

6.2.2.2 Transport Properties

The transport subroutines[122] are used to calculate thermal conductivity, viscosity and diffusion coefficients. Single component thermal conductivities and viscosities are calculated by the transport subroutines based on theories proposed by Warnatz and Hirschfelder respectively. A detailed outline of the methods used to calculate these values is presented in the report by Kee.[122] Mixture average thermal conductivities and

viscosities are then calculated using the single component values via Equations (6-21) and (6-22) respectively.

$$\lambda = \frac{1}{2}\left(\sum_{i=1}^{K} X_i \lambda_i + \frac{1}{\sum_{i=1}^{K} X_i / \lambda_i} \right) \tag{6-21}$$

$$\mu = \sum_{i=1}^{K} \frac{X_i \mu_i}{\sum_{j=1}^{K} X_j \Phi_{ij}} \tag{6-22}$$

where

$$\Phi_{ij} = \frac{1}{\sqrt{8}} \left(1 + \frac{W_i}{W_j} \right)^{-\frac{1}{2}} \left(1 + \left(\frac{\mu_i}{\mu_j} \right)^{\frac{1}{2}} \left(\frac{W_j}{W_i} \right)^{\frac{1}{4}} \right)^2$$

and X_k is the species mole fraction.

The transport package is used to calculate binary diffusion coefficients via Equation (6-23) which are then used in the vorticity-velocity model to calculate diffusion velocities.

$$D_{im} = \frac{\sum_{j \neq i}^{K} X_j W_j}{\overline{W} \sum_{j \neq i}^{K} X_j / D_{ij}} \tag{6-23}$$

Diffusion velocities are calculated following the procedure proposed by Coffee and Heimerl.[123] They recommended a “conservation diffusion velocity” to ensure that the

mass fractions sum to one. This procedure determines diffusion velocities $(\hat{v}_i)$ based on two parts, ordinary diffusion velocity (v_i) and a velocity correction factor (v_c), Equations (6-24) through (6-26).

$$\hat{v}_i = v_i + v_c \tag{6-24}$$

$$v_i = -D_{im} \frac{1}{X_i} \frac{dX_i}{dx} \tag{6-25}$$

$$v_c = -\sum_{i=1}^{K} Y_i v_i \tag{6-26}$$

6.2.3 Boundary Conditions

The system of equations is closed with appropriate boundary conditions for all sides of the computational domain. The inflow boundary conditions are determined through iteration with the condensed phase. To get meaningful inlet boundary conditions without dynamically modeling the condensed phase, calculations were made using the condensed phase portions of one-dimensional AP[7] and AP/HTPB[9] models. This approach necessarily neglects any two-dimensional effects in the condensed phase, but greatly simplifies the calculation of the dynamic gas-phase boundary conditions. This is the same approach used in the Felt model. The inlet boundary conditions of mass flux (ρu), species mass fractions (Y_i) and surface temperature (T_s) are calculated from curve fits of calculations performed with the one-dimensional models over a range of gas-phase heat fluxes.

Calculations were made for mixtures of AP and HTPB over a range of compositions from pure AP to 75% AP/25% HTPB. These mixtures are meant to simulate the decomposition products of large AP particles and a mixed binder containing small particles of AP. The surface temperature and burning rate were found to be simple functions of the surface heat flux and were fit to an appropriate curve. The species flux fractions were nearly constant over a large range of heat fluxes for a given bulk composition. This approach yields inlet conditions to the present two-dimensional model that are strictly a function of the gas-phase heat feedback at each inlet node. The inflow boundary conditions are presented in Equation (6-27)

$$\rho v_z, T, Y_{i\ \ condensed} = given, \quad \omega = \frac{\partial v_r}{\partial z} - \frac{\partial v_z}{\partial r}, \quad v_r = 0 \tag{6-27}$$

The particle centerline and outer radial boundary conditions were assumed to be symmetrical with no radial velocity or radial gradients, see Equation (6-28).

$$v_r = \omega = \frac{\partial v_z}{\partial r} = \frac{\partial T}{\partial r} = \frac{\partial Y_i}{\partial r} = 0 \tag{6-28}$$

The outflow boundary conditions assume a far-field in which the radial velocity vanishes as do axial gradients of the remaining variables, Equation (6-29).

$$v_r = \frac{\partial \omega}{\partial z} = \frac{\partial v_z}{\partial z} = \frac{\partial T}{\partial z} = \frac{\partial Y_i}{\partial z} = 0 \tag{6-29}$$

6.3 Numerical Methods

Solution of the governing equations presents a significant numerical challenge due to the size of the system of interest in the current problem. A total of N+4 dependent variables, where N is the number of species, must be calculated at each grid point. An exact solution to the governing equations is not possible, and therefore, the continuous information contained in the partial differential equations must be replaced by finite approximations of the equations. This requires the representation of the exact governing equations in a finite algebraic form that can then be evaluated using numerical techniques. A grid must be superimposed on the actual domain and approximations made. The method of discretization used for the current problem is a form of the control volume approach based on the work of Patankar.[114] Once the partial differential equations are approximated, the system of algebraic equations is then solved using an iterative Newton-Rhapson method that requires an initial estimate of the solution. To obtain an estimate that will lead to a converged solution, a timestepping technique can be employed.

6.3.1 Discretization

The control volume method divides the numerical domain into a series of non-overlapping volumes containing a single point at the center of the volume. The differential equations are then integrated across the control volume. Such a methodology results in the conservation of dependent variables across the control volume and the conservation of fluxes at the cell interface. The control volume method is outlined by Patankar, and was utilized by Felt in his pressure-velocity formulation. Also, both axial and radial velocities are calculated using a staggered grid to ensure accuracy.

6.3.1.1 Grid Setup

A structured grid is overlaid on the two-dimensional domain. Due to the large gradients near the surface, a successive ratio is used to allow for an increased number of nodes near the surface. Further, two successive ratios are used in the radial direction originating at the interface between the binder and the oxidizer to allow for better resolution where diffusion is of major importance. An example grid is presented in Figure 6-1 for a 200 μm particle with 40 axial and 30 radial nodes.

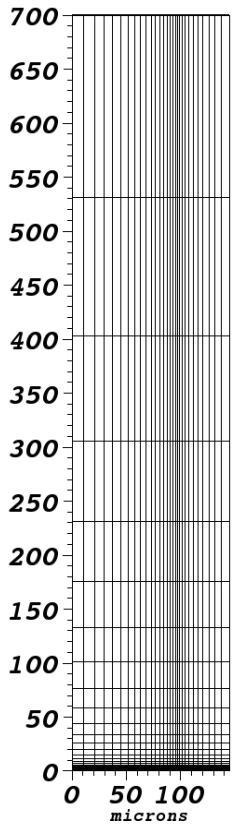

Figure 6-1: Example grid using the successive ratio with 40 axial nodes and 30 radial nodes.

6.3.1.2 Convective Terms

Convective terms are first order terms in which information is transferred between cells via convection. These terms generally involve velocity and are discretized using an upwind method. Such a method ensures that information is passed in the direction of the flow. The discretized form for convective terms is presented in Equation (6-30).

$$\frac{\partial}{\partial x}(v\phi)_i = \frac{(v\phi)_{i+\frac{1}{2}} - (v\phi)_{i-\frac{1}{2}}}{\Delta x_i} \tag{6-30}$$

where

$$\phi_{i+\frac{1}{2}} = \begin{Bmatrix} \phi_i \text{ if } v_{i+1/2} > 0 \\ \phi_{i+1} \text{ if } v_{1+1/2} < 0 \end{Bmatrix}, \qquad \phi_{i-\frac{1}{2}} = \begin{Bmatrix} \phi_{i-1} \text{ if } v_{i-1/2} > 0 \\ \phi_i \text{ if } v_{1-1/2} < 0 \end{Bmatrix}$$

6.3.1.3 Diffusive Terms

Second order diffusive terms are represented via Equation (6-31).

$$\left(\frac{\partial}{\partial x}\gamma\frac{\partial\phi}{\partial x}\right)_i = \frac{\gamma_{i+1/2}\left(\frac{\phi_{i+1}-\phi_i}{\delta x_{i+1/2}}\right) - \gamma_{i-1/2}\left(\frac{\phi_i-\phi_{i-1}}{\delta x_{i-1/2}}\right)}{\Delta x_i} \tag{6-31}$$

6.3.2 Solution Technique

The system of equations describing a burning propellant is large, tightly coupled, and highly non-linear. An equation for each of the conserved quantities must be solved

simultaneously at each node within the modeled domain. The chemical reactions, the rates of which are exponentially dependent on temperature, can consume or release large amounts of energy. These characteristics make the large set of simultaneous equations intractable to analytic methods and very difficult to solve numerically. Further, to take advantage of the elliptical nature of the vorticity formulation, an initial guess within the range of convergence must be provided. Such an initial guess is not always attainable, and therefore, a timestepping technique can be employed to bring the system within the steady-state convergence region.

6.3.2.1 Solver

The computer code makes use of the Portable Extensible Toolkit for Scientific Computation (PETSc)[124] to handle many of the difficulties of such a large and complex calculation. The libraries manage parallelization (by domain decomposition), distributed array storage, and parallel sparse matrix calculations including Krylov subspace methods, numerical Jacobian generation, preconditioners and linear and non-linear solvers.

6.3.2.2 Pseudo-Transient Terms

When a reasonable initial guess is not possible, a time marching technique is employed to progress the solution towards convergence. This introduces the stability of a time marching technique, but without low Mach flow difficulties inherent in the Navier-Stokes equations. Transient terms are added to the vorticity, energy, and species equations when a time marching technique is desired. Once the solution appears to be within range of the final solution (based on the solver residual) the transient terms can be disabled and the program rapidly converges. This technique has been used successfully by Smooke[118] for the vorticity formulation. The transient terms added to the vorticity,

energy, and species equations are presented in Equation (6-32). No transient terms are added to the velocity equations.

Vorticity:	$-\rho\frac{\partial\omega}{\partial t}$	
Energy:	$\rho c_p\frac{\partial T}{\partial t}$	(6-32)
Species:	$\rho\frac{\partial Y_i}{\partial t}$	

The form used to discretize transient terms is presented in Equation (6-33).

$$\frac{\partial\phi}{\partial t}=\frac{\phi^{t+\Delta t}-\phi^{t}}{\Delta t} \tag{6-33}$$

6.4 Model Validation

The model was validated for both diffusion and combustion capabilities against known problems, the same problems Felt used to validate his code.

6.4.1 Diffusion through a Stagnant Gas Film

The diffusion capabilities of the model were compared to diffusion through a stagnant gas film.[125] Liquid A is assumed to maintain the level $z = z_1$ in a cylinder. The concentration of A at z_1, X_{A1}, is assumed to be in equilibrium with the liquid. A gas mixture of A and B flows over the top of the cylinder to maintain the mole fraction of A

at z = z_2 constant, X_{A2}, and the temperature and pressure of the system are constant. Gases A and B are ideal. The system set up is presented in Figure 6-2.

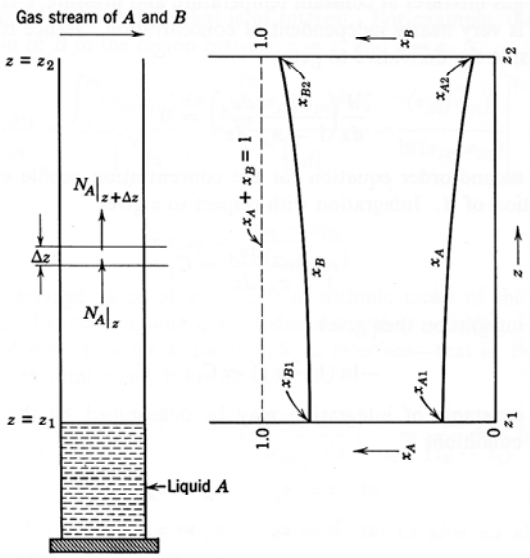

Figure 6-2: Diffusion through a stagnant gas.

An analytical solution for the concentration of A at any point in the cylinder is possible and is presented in Equation (6-34).[125]

$$\left(\frac{1-x_A}{1-x_{A1}}\right)=\left(\frac{1-x_{A2}}{1-x_{A1}}\right)^{\frac{z-z_1}{z_2-z_1}} \tag{6-34}$$

Comparison between the analytical and numerical calculations is presented in Figure 6-3 for a case assuming Ar diffusion in N_2 at 298 K, 1 atm, with an inlet mass flow rate 0.013 g/cm3 for Ar, cylinder length of 0.005 cm, and final outlet mass fraction

of Ar held constant at 0.1. The maximum error between the numerical and analytical solutions is 0.003%.

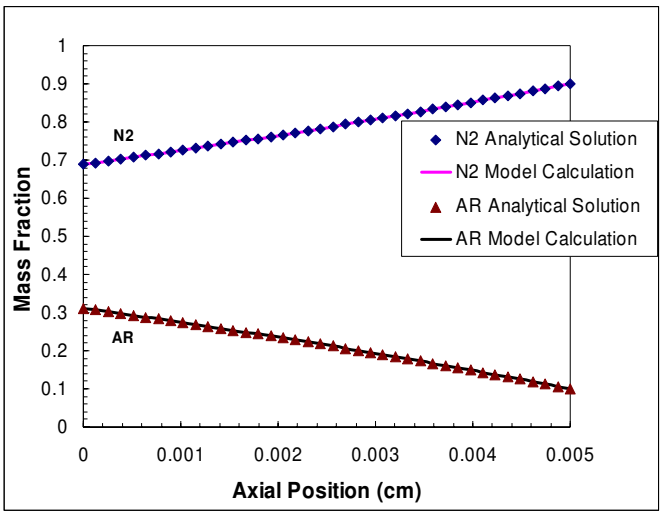

Figure 6-3: Validation of numerical model for diffusion through a stagnant gas film.

6.4.2 Combustion

Validation of the combustion properties of the numerical model were compared against work performed by Kee.[126] on an H_2/O_2 premixed flame. An 18 step kinetic mechanism had been developed to model the system. Initial conditions consisted of mass fractions of 0.28 H_2 and 0.09 O_2 in an Ar stream with a mass flow rate of 4.63×10^{-3} g/cm^2s at 373.7 K and 0.0329 atm. The diffusion flame model is able to match the calculations performed by Kee et al. within 4%. Results are presented in Figure 6-4.

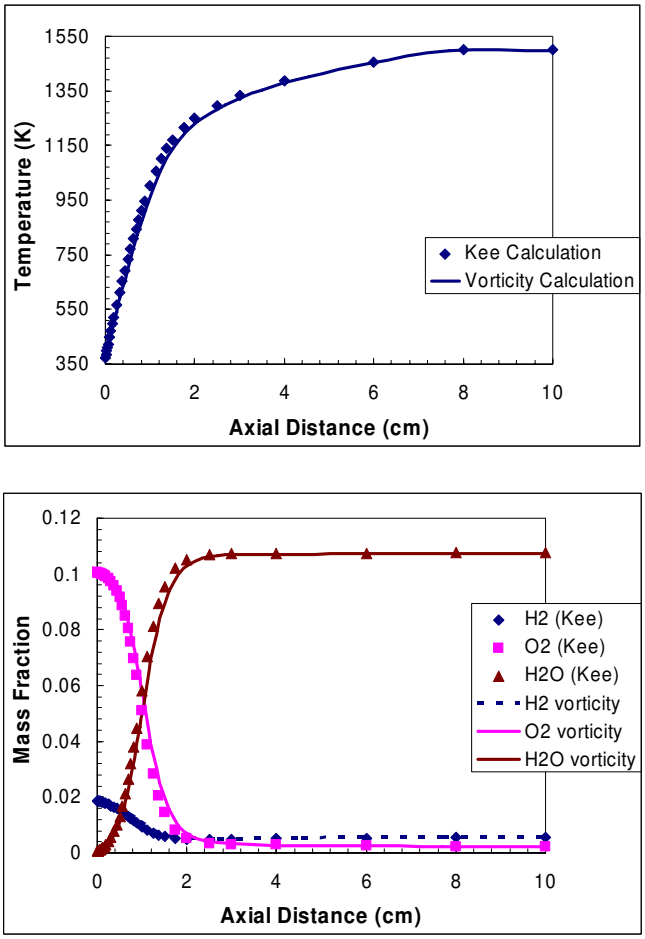

Figure 6-4: Validation for an H_2/O_2 premixed flame.

6.5 Kinetic Mechanisms

The full AP/HTPB kinetic mechanism simulating the homogeneous binder used in this model was developed by Jeppson.[95] It consists of 44 chemical species participating in 157 reaction steps and is a modified form of the smaller AP/CTPB (carboxy-terminated polybutadiene) mechanism proposed by Korobeinichev[76] with additions from Korobeinichev,[77] Ermolin,[32] Wang,[127] and Bowman.[13]

To facilitate faster calculations, the full AP/HTPB gas-phase kinetic mechanism was analyzed for species and reactions that might be removed without changing the

calculated one-dimensional burning rate. The result of this sensitivity analysis is a slightly reduced kinetic mechanism of 37 species participating in 127 reactions (Appendix C). The eliminated species are C, CH, CH_2CO, ClOO, H_2O_2, NNH and NOCl. Extensive sensitivity analysis of the gas-phase kinetic mechanism has been performed previously be Jeppson[9] and will not be repeated in the current study.

6.6 Comparison of Vorticity and Pressure Formulations

The new vorticity approach gives results consistent with the old pressure approach. Both models were applied to an 86% AP/14% HTPB propellant with 37.8% 400μm AP and 48.2% 12 μm AP. The particle size, binder composition and AP mass fraction values were chosen to correspond to a propellant formulation reported by Foster.[128] It is assumed that the 12 μm AP and the HTPB form a homogenized binder mixture. Assuming a spherical particle of AP surrounded by a shell of binder, and an overall AP mass fraction of 0.86 gave a binder thickness of 89 μm. Taking advantage of the symmetry of the system, only half of the particle diameter was modeled, and the calculations were made for a pressure of 20 atm. Figure 6-5 presents the calculated flame structures using both the pressure and vorticity formulations. Qualitatively the figures are very similar. Upon close examination, the temperature profile above the AP particle is slightly different between the two images. This is due to an inaccuracy in the condensed phase correlations used for AP in the original pressure formulation. The condensed-phase correlations used in the current study are presented in Appendix D.

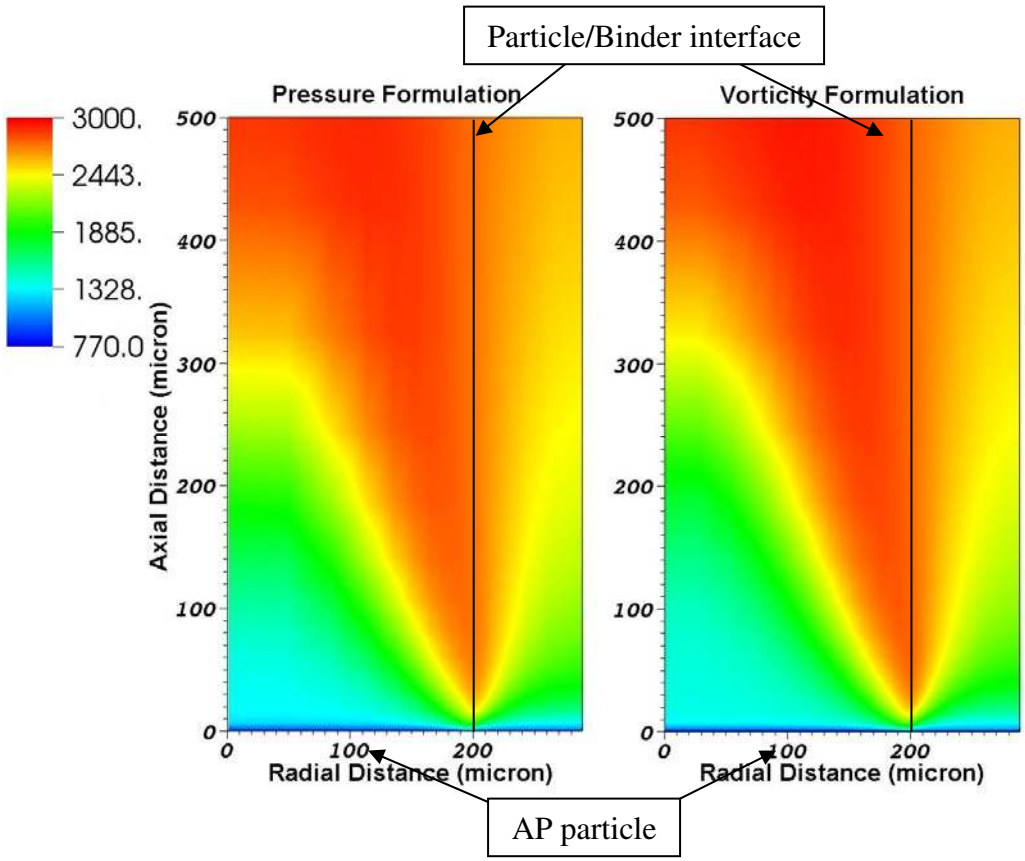

Figure 6-5: Comparison of flame structure based on the temperature (K) field for the pressure formulation (left) and the vorticity formulation (right).

An error in the AP correlation was discovered when calculations were performed for pure AP. The previous correlation predicted a slightly faster burning rate than experimentally measured. Therefore, a new correlation was created using the Jeppson model. This same model was used for the correlations for the AP containing HTPB binder. Figure 6-6 presents the calculated monopropellant AP burning rate using the old and new correlations. Unfortunately, all calculations using the pressure formulation utilized the old pure AP correlation, which results in slightly different burning rates and temperatures above the AP particle. Examination of the one-dimensional mass flux at the surface illustrates the effect of the new correlation, Figure 6-6. The mass flux above the

AP particle is higher using the old correlation, just as the burning rate is higher for the pure AP calculation.

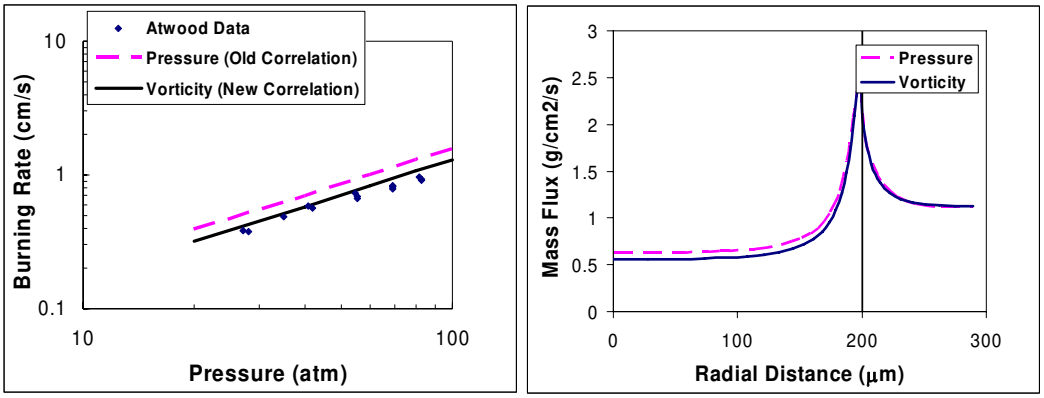

Figure 6-6: Calculated monopropellant AP burning rates (left) and inlet mass flux for a 400 μm particle at 20 atm (right) using the old and new AP condensed-phase correlations.

The goal in implementing the vorticity formulation was to increase the stability and accuracy of the numerical code, and decrease the runtime. These three objectives were met. CPU time decreased substantially, from about 1 month using the old code to around 2 days using the new code. In fact, if no timestepping is necessary, runtime decreases to about 2 hours. This was the case 30 to 40% of the time. Also, the code was run on 1/6 of the processors the pressure formulation was run on, and the vorticity version had twice the number of nodes, increasing from 600 to 1200 nodes, thus increasing accuracy.

Stability and robustness were also increased using the vorticity formulation. The previous version of the code crashed dozens of times for each case. This required substantial user interaction to diagnose the problem and restart the case. It also resulted in

large amounts of downtime. The new code rarely crashes, and if so, it generally requires the user to only turn on the timestepping algorithm to approach a reasonable solution.

Finally, the accuracy of the model was also increased. Figure 6-7 presents the effect of particle size on burning rate for a pressure of 20 atm. As seen in the image, both model formulations follow a consistent trend up to about 20 μm. The difference for smaller particles is attributed to inaccuracies in the pressure calculations. A flag was discovered in the solver that returns the reason the solver ceased calculations. At the smaller particle sizes, the solver was returning because it could not find a solution. So although the cases appeared to be working, the solver in effect was returning unconverged solutions. This was not the case using the vorticity formulation, which gives a smooth transition to an asymptotic limit.

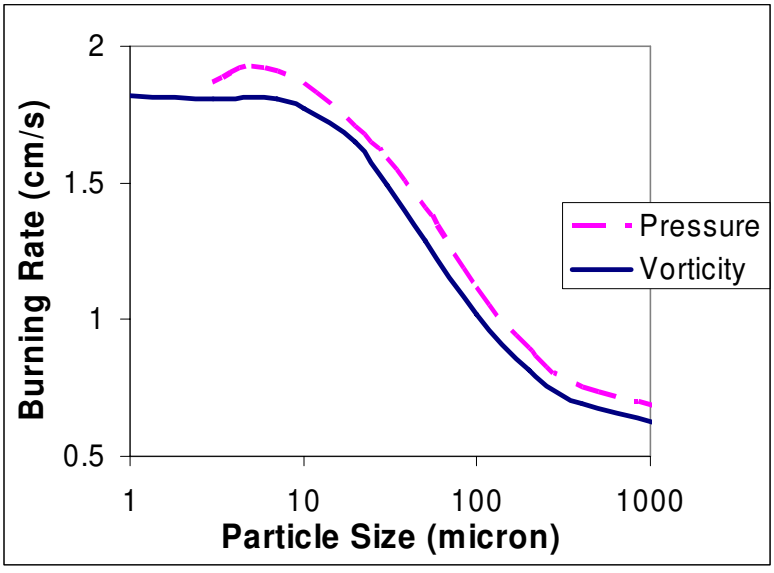

Figure 6-7: Particle size effect on burning rate using both formulations of the model.

6.7 Comparison to Premixed Models

Due to errors in the pure AP condensed-phase correlations, comparisons were made using the diffusion flame code to monopropellant AP and premixed 80% and 77.5% AP/HTPB one-dimensional calculations. Results using the diffusion flame code were able to reproduce the Jeppson calculations, the mechanism on which the current model is based, thus validating the correlations. Figure 6-8 compares the diffusion flame calculations to the Atwood data[16] for pure AP and Figure 6-9 compares premixed calculations for AP/HTPB with the Foster data. Figure 6-9 is analogous to Figure 2-13, the Jeppson calculations.

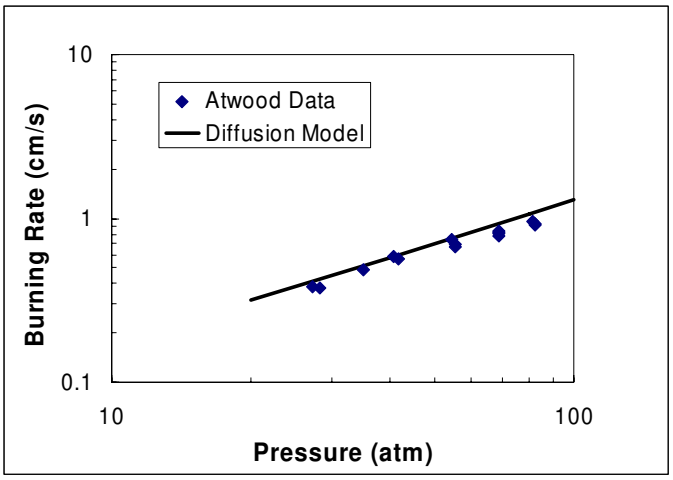

Figure 6-8: Comparison of the diffusion flame model's calculated burning rate to the Atwood data for pure AP.

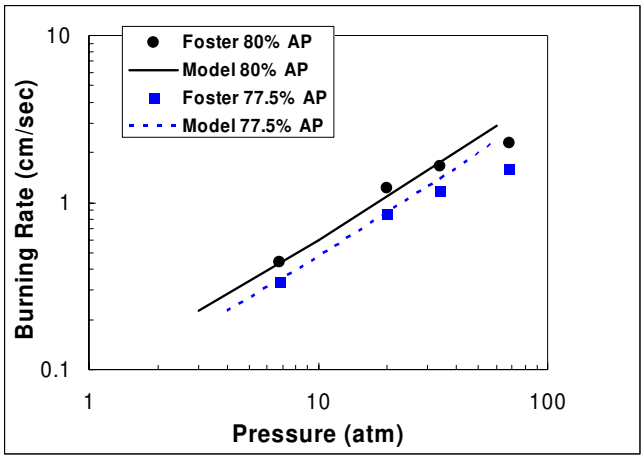

Figure 6-9: Comparison of Foster data to the diffusion flame model for 77.5% and 80% AP in HTPB.

6.8 Summary

Use of the vorticity-velocity equations for low Mach flow successfully increases accuracy, stability, and robustness of the diffusion model while also significantly decreasing runtime, from weeks to days. The vorticity formulation was validated for diffusion and combustion, through comparison with known analytical and numerical problems. Comparison to the pressure formulation results in similar results for large particle sizes. The reason for slight differences was the use of an inaccurate AP condensed-phase correlation in the pressure-velocity version. The vorticity formulation does not suffer from inaccuracies for small particles as the previous model does.

7 AP Composite Propellant Results

The vorticity formulation of the diffusion flame model has been applied to AP/HTPB composite propellants over a wide range of conditions; particle sizes ranging from 1 to 400 micron diameters and pressures ranging from 1 to 100 atm. The model was initially applied to an 86% AP/14% HTPB propellant with 37.8% 400μm AP and 48.2% 12 μm AP. The particle size, binder composition, and AP mass fraction values were chosen to correspond to a propellant formulation reported by Foster.[128] It was assumed that the 12 μm AP and the HTPB formed a homogenized binder mixture. The binder thickness was varied with particle size to give an overall AP mass fraction of 0.86. The binder thickness surrounding the AP particle was calculated based on a spherical particle of AP surrounded by a shell of homogenized binder resulting in a value of 89 μm. Taking advantage of the symmetry of the system, only half of the particle diameter was modeled. This same approach was applied to all pressure and particle size calculations. Once calculations were complete for the initial propellant formulation, variations in formulations were also investigated. The same methods were applied for different formulations to determine binder thickness and fraction of AP in the binder.

The model generates the same physical picture as the BDP Model with one variation: a premixed flame is present above the homogenized binder. The fine particles of AP in the binder are assumed to be small enough that the binder can be considered

homogeneous, and therefore, the binder decomposition products react in a premixed fourth flame zone. The calculated flame structure for AP/HTPB combustion at 20 atm is presented in Figure 7-1. The locations of the different flames, as indicated by the temperature field, are labeled. As proposed for large particles, the AP monopropellant flame, which has a final flame temperature of ~1400 K, dominates the bulk of combustion above the 400 μm AP particle. The AP monopropellant flame standoff distance is within a few microns of the surface. A primary diffusion flame is located at the interface where decomposition products from the binder and oxidizer mix in a very hot flame. Products from the premixed and primary diffusion flames react in a final diffusion flame where the adiabatic temperature is reached. The final diffusion flame is too far from the surface to have any substantial impact on the burning rate. The dynamics

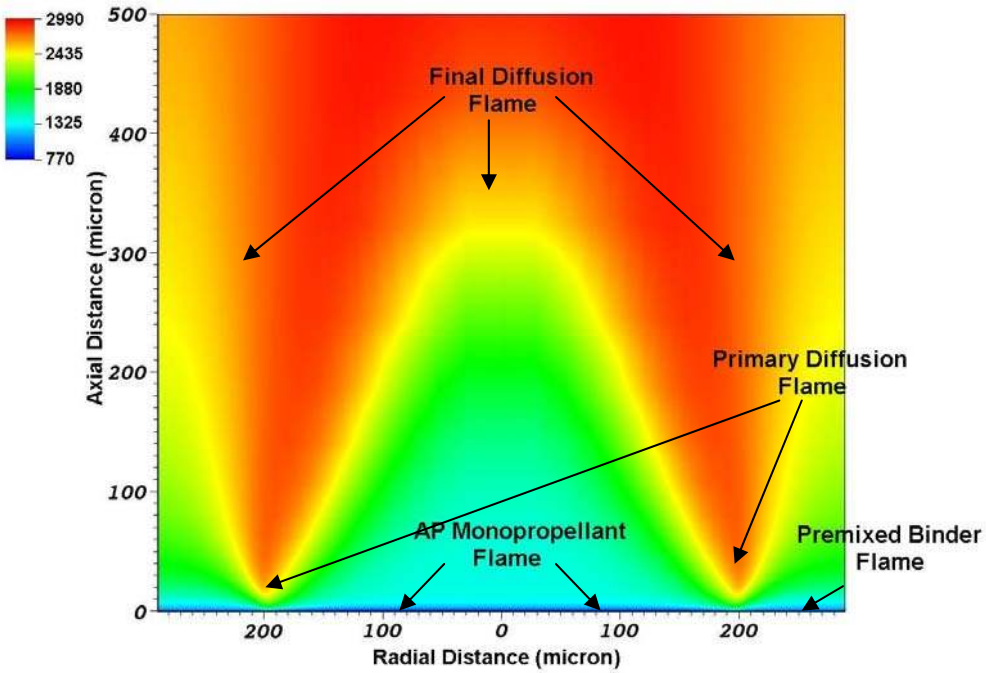

Figure 7-1: Flame structure based on temperature (K) above a 400 μm particle surrounded by 89 μm of binder at 20 atm.

of these flames will be discussed in relation to particle size and pressure in the following sections. These results give further numerical support to the validity of the BDP model concepts.

7.1 Particle Size Effects

Very distinct and important regions exist in the particle size versus burning rate curve. As outlined previously, the three regions are the AP monopropellant limit, diffusion flame, and premixed limit (see Figure 2-10). According to the BDP model, the reason for these three regions is due to variations in the composite propellant flame structure with particle size. To investigate the combustion aspects in each of these regions, a single particle size, representative of each region, was examined. Calculations were performed at 20 atm for a composite propellant consisting of 86% AP with the binder consisting of 77.5% AP in HTPB.

7.1.1 AP Monopropellant Limit: 400 μm

The 400 μm particle is representative of the region of the curve approaching the AP monopropellant burning rate. To achieve the proper AP loading, a binder thickness of 89 μm was assumed to surround the AP particle. The calculated flame structure and axial mass flux are presented in Figure 7-2. The four different flame structures are distinctly present in the temperature profile. The relatively large scale of a 400 μm particle increases the radial distance across which diffusion must take place and results in the multi-dimensional flame structure. The proximity of the monopropellant flame above the AP particle (~8 μm) controls most of the combustion above the AP particle. The

influence of the primary diffusion flame is limited to a relatively small section of the surface, and therefore, the combustion of large particles is controlled by the slower AP monopropellant rate and the premixed binder rate. The final diffusion flame also appears to "close" over the AP particle, with lower temperatures at the outlet boundary above the binder, as would be expected for a fuel-rich diffusion flame. The axial mass flux shows a peak at the interface where the primary diffusion flame is located, increasing the burning rate at that location. The mass flux then forms two distinct regions, one above the particle and one above the binder. This is an interesting result common for large particle calculations at various pressures. The exiting gases are unable to completely mix and differing mass fluxes leave the propellant surface above the AP particle compared to the binder.

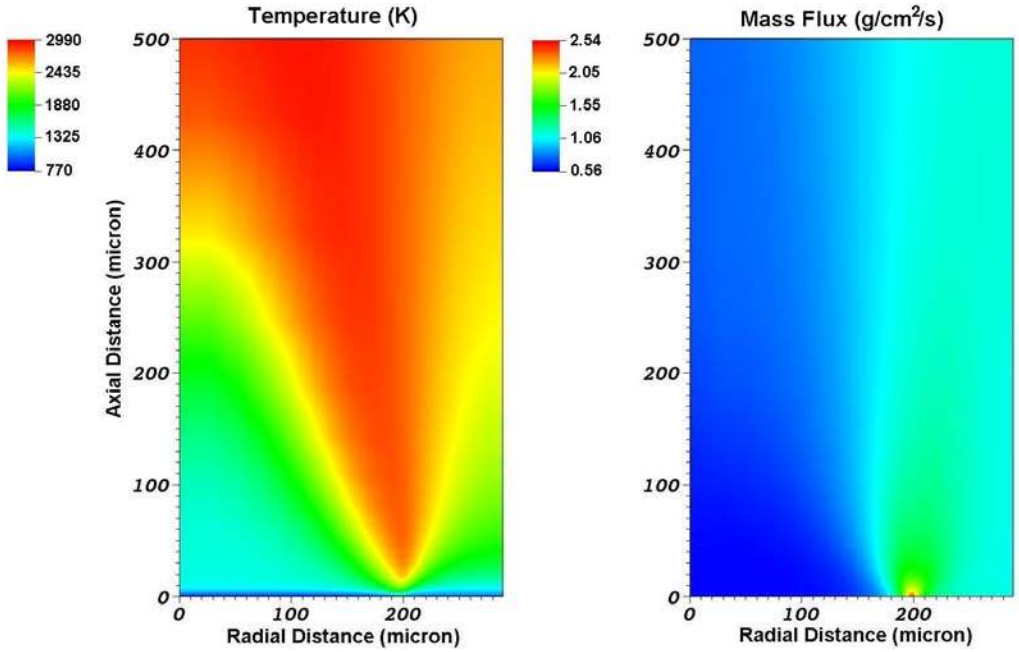

Figure 7-2: Temperature and axial mass flux profiles for a 400 μm particle at 20 atm.

To more clearly show the details of the flame structure and examine the impact of various flames on combustion, "slices" of the axial temperature profile are shown in Figure 7-3. Three radial positions are presented: at the AP particle center (r=0 µm), at the AP/binder interface (r=200 µm), and at the outer edge of the binder (r=289 µm). The resultant temperature profiles give insight into the heat feedback to the surface that drives combustion and to the controlling mechanism at each location.

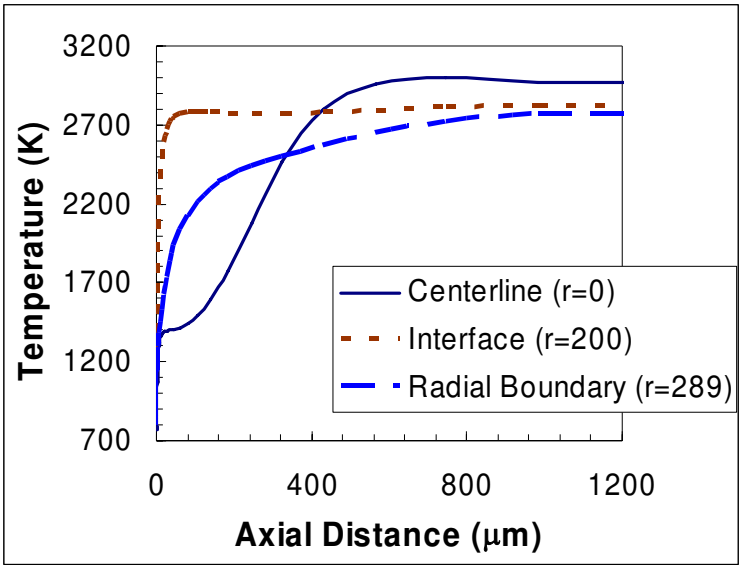

Figure 7-3: Temperature profiles for a 400 µm particle at 20 atm for three radial positions: particle centerline (r=0 µm), particle/binder interface (r=200 µm), and radial boundary (r=298 µm).

The temperature profile at the particle center (r=0 µm) rises from the surface temperature (773 K) to approximately 1350 K within 8 µm, after which it levels off before rising again to its final temperature of nearly 3000 K, relatively far from the surface. The intermediate plateau in the centerline temperature profile corresponds to the position and temperature of the AP monopropellant flame. The final temperature of

nearly 3000 K corresponds to the final diffusion flame. These trends can be seen in Figure 7-4, in which the particle centerline temperature is compared to a calculated, pure AP temperature profile at 20 atm. The calculated heat flux to the surface for the composite system (1246 W/cm^2) and for the monopropellant AP (1245 W/cm^2) are essentially identical. These calculations show that the burning rate at the particle centerline is controlled by the monopropellant decomposition rate, and not impacted by the diffusion flames.

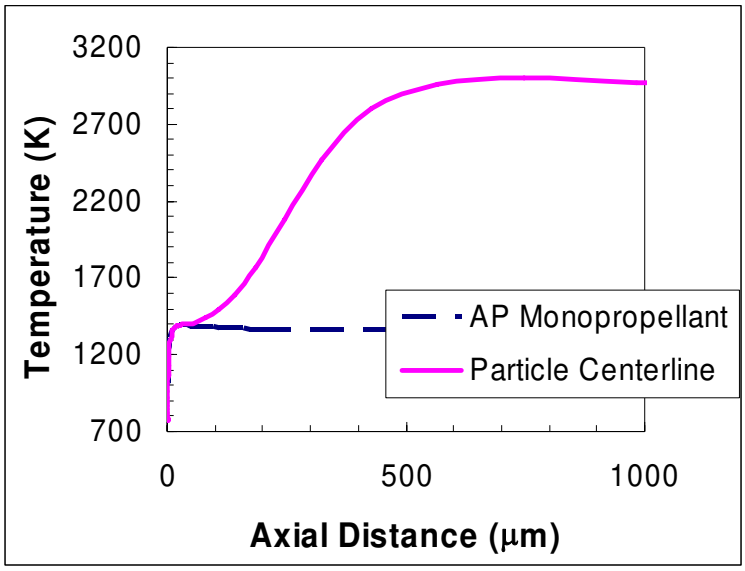

Figure 7-4: Calculated temperature profiles for a 400 μm AP particle in a composite propellant at the particle centerline (r=0 μm) and for pure AP monopropellant at 20 atm.

Calculations at 20 atm for the temperature profile at the radial boundary (r=289 μm), above the fine AP/HTPB binder, reach 95% of the premixed binder's flame temperature (2150 K) within 80 μm of the surface. The temperature then gradually approaches the final flame temperature of the system. The temperature profile above the binder corresponds to the calculated one-dimensional homogenized binder for 77.5% AP

in HTPB, as seen in Figure 7-5, before rising to the final flame temperature. The calculated heat flux above the binder was 2738 W/cm^2 compared to 3024 W/cm^2 for the premixed binder alone. There is a slight impact from the diffusion flames at 20 atm, but the impact is minimal and combustion is dominated by the premixed binder flame. Due to the higher heat flux above the binder, surface regression is faster at the binder boundary than it is at the particle centerline.

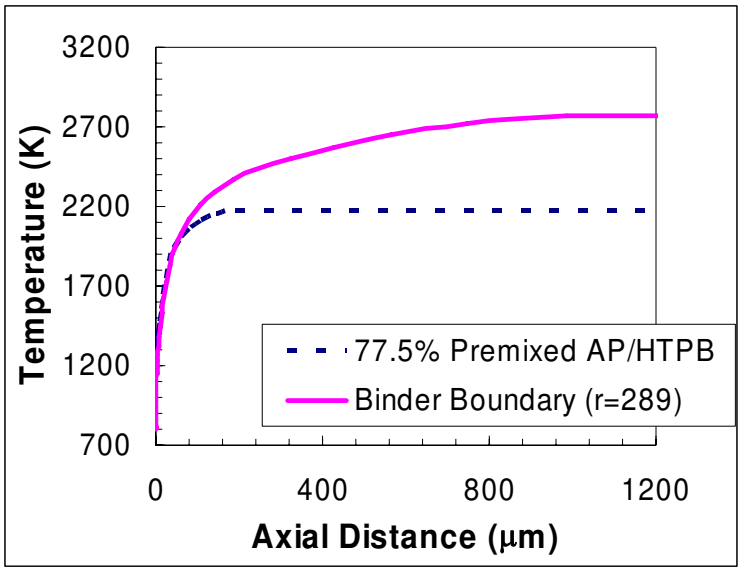

Figure 7-5: Calculated temperature profiles for a 400 µm AP particle in a composite propellant above the binder (r=298 µm) and the homogenized AP/HTPB monopropellant at 20 atm.

The primary diffusion flame above the particle/binder interface (r=200 µm) causes a much steeper temperature gradient near the surface than either the AP monopropellant flame or the premixed binder flame. The calculations show that a temperature of 2700 K is reached within approximately 35 µm of the surface, a rise of nearly 2000 K. The variation in temperature across the surface of a 400 µm particle

illustrates the scale and complexity of the flame structure above a composite propellant, demonstrating why it is so difficult to obtain detailed experimental data for such a system. The heat flux above the interface is 5736 W/cm^2, roughly 2 times higher than the heat flux above the binder and 4 times higher than at the particle centerline. Therefore, the corresponding burning rate is significantly higher at the interface compared to the rest of the surface.

The influence of the primary diffusion flame is shown graphically in Figure 7-6, where the heat flux to the surface and corresponding mass flux are plotted as a function of radial position. The heat flux to the surface is the driving force for the decomposition and gasification of the condensed-phase materials. The mass flux at the particle/binder interface (r=200 μm) is more than four times higher then the mass flux of the AP particle at its center (r=0 μm), and more than twice the mass flux of the homogenized binder (r=289 μm). This is due to the significantly higher heat feedback from the primary diffusion flame at the interface, relative to the heat flux from the AP monopropellant or binder premixed flames. The calculations indicate that the area around the edge of the particle would be regressing much faster than the rest of the surface, creating a dynamic, non-planar burning surface.

The calculated regression rate is consistent with the experimental observations for sandwich burning experiments. Korobeinichev[129] and Price[130] observed that the interfacial regions between laminae of AP and a binder were recessed with respect to the rest of the surface at moderate pressure. Also, note that the burning rates at both edges of the domain approach constant values, illustrating that the individual premixed flames control combustion at those locations. Examination of the mass flux above the particle

shows that nearly ¾ of the particle surface area is regressing at the AP monopropellant rate. Therefore, large particle regression is controlled by the monopropellant rate and thus the overall burning rate approaches the AP monopropellant limit, as expected.

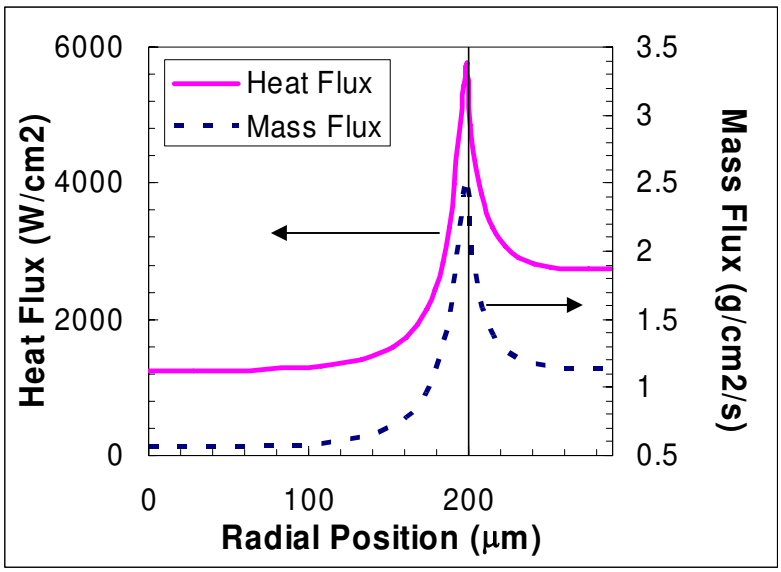

Figure 7-6: Surface heat and mass flux for a 400 μm AP particle with 77.5% AP in HTPB binder at 20 atm.

These rather dramatic heat and mass flux results point out two of the limitations of the current model, which are that the calculations are for a steady-state system and that the surface is assumed to be planar. However, even with these limitations, the understanding of the flame structure that these calculations provide is significant.

A major objective of modeling the propellant combustion is to determine an average burning rate for the propellant, which can then be compared with experimental rates. As can be seen from the highly two-dimensional surface mass flux in Figure 7-6, determining a one-dimensional average rate is not a simple exercise. An initial approach, presented here, is to average the radial rate determined by the model over the radius of

the particle and its surrounding binder. The method decided upon is presented in Equation (7-1) and assumes a cylindrical dependence on burning rate. The rates at each radial grid point are determined and are then summed over the entire radius, weighted by their corresponding cylindrical area. Thus, even though local rates are dramatically different, averaging then over their corresponding area yields what appears to be a reasonable overall rate.

$$b_{r\_average} = \frac{1}{\pi R_p{}^2} \sum b_r \left(\pi r_{i+1}^2 - \pi r_i^2 \right) \tag{7-1}$$

Use of a detailed mechanism allows for the calculation of the flame structure without any prior assumptions, aside from the inlet species, it also allows for the calculation of species profiles. Jeppson[9] performed a sensitivity analysis on the mechanism in use, and therefore, this analysis was not repeated. However, examination of species profiles above the surface is instructive. The formation of N_2 as a final product from the destruction of NO_x species follows a general paths, $NO_2 \rightarrow NO \rightarrow N_2O \rightarrow N_2$ and $NO_2 \rightarrow NO \rightarrow N_2$, where most of the NO_x species are created from the oxidation of NH_3 in the oxygen-rich environment above the AP particle. These trends are readily seen by examination of these species profiles above the surface, shown in Figure 7-7.

A major decomposition product of AP is NH_3. As seen in Figure 7-7, virtually all of the NH_3 is destroyed in the AP monopropellant flame within a few microns of the surface. The NH_3 released from the AP in the binder is not readily consumed due to the lack of oxygen in that region. Further, the NH_3 released above the binder undergoes a decomposition path that does not include NO_2 as an intermediate. This is due to the fuel-

rich nature of that region. As seen in Figure 7-7, the destruction of NH_3 above the AP particle leads to the formation of NO_2. As the concentration of NH_3 drops, the concentration of NO_2 rises. The destruction of NO_2 leads to the formation of NO, which has a longer residence time as noted by its presence at 500 μm from the surface. NO is then converted to N_2O or directly to N_2. According to Jeppson's calculations, NO is converted to N_2 instead of N_2O in a ratio of 3/1.The conversion of N_2O to N_2 is

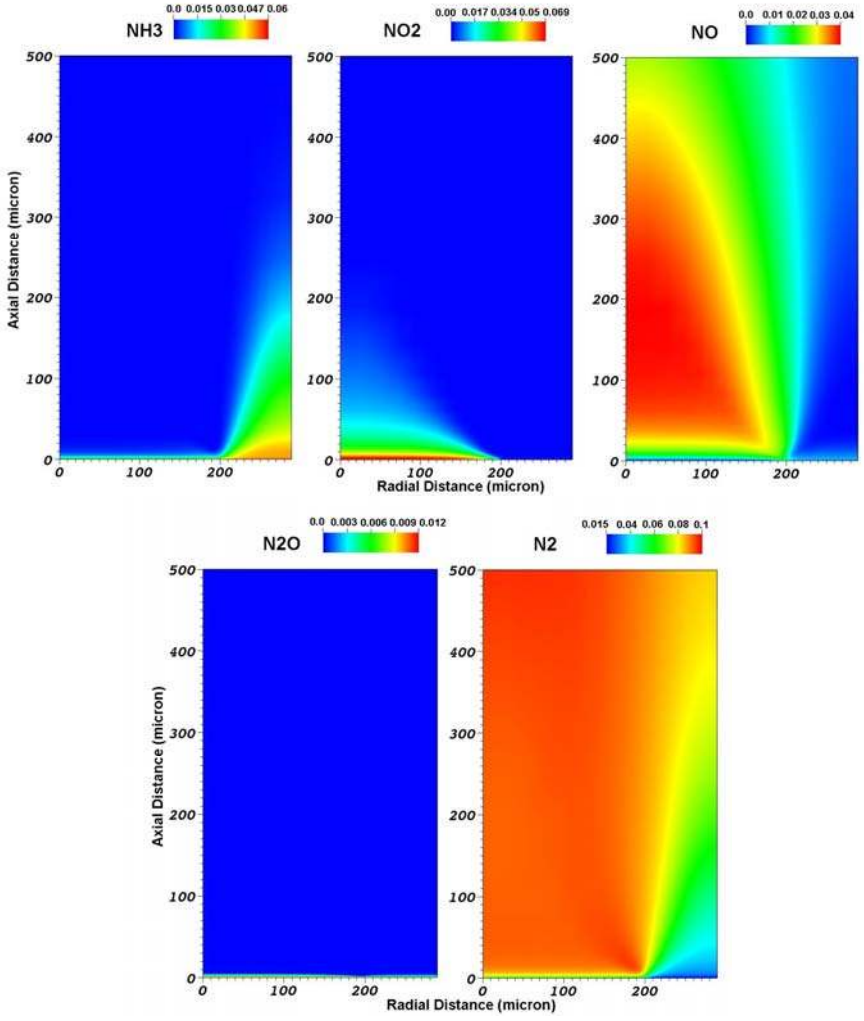

Figure 7-7: Species mass fractions for the creation of N_2 from NH_3 in an oxygen rich environment above a 400 μm AP particle at 20 atm.

apparently very rapid as noted by the essentially zero mass fraction of N_2O in the entire domain. Examination of Figure 7-7 shows that as NO is destroyed the amount of N_2 increases above the particle. It can also be seen that the lack of oxygen above the binder results in much slower production of N_2 and the equilibrium mass fraction of N_2 above the binder is not achieved within the calculated grid.

The mixture of AP/HTPB in the binder results in much of the NH_3 from the AP being converted to HCN. The lack of oxygen creates an alternative path where NH_3 is converted to N_2 by $NH_3 \rightarrow NH \rightarrow N_2$. The HCN is slowly converted to N_2, as seen in Figure 7-8. This path was outlined in the sensitivity analysis performed by Jeppson.

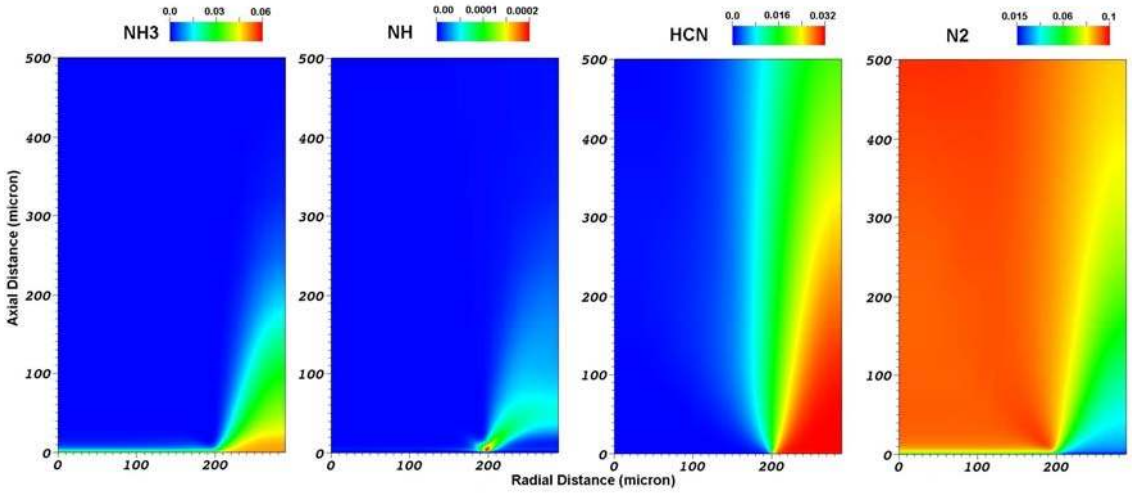

Figure 7-8: Species mass fractions for the production of N_2 in the fuel rich region above the binder for a 400 μm AP particle at 20 atm.

Another decomposition path outlined by Jeppson is the formation of HCl and Cl. The path generally follows $Cl_2 \rightarrow HCl \rightarrow Cl$ and can be seen in Figure 7-9. Large amounts of Cl_2 are generated by the monopropellant flame above the AP particle. This is then

converted into HCl. Then where large concentrations of HCl are present at high temperatures, the radical Cl is created in small amounts.

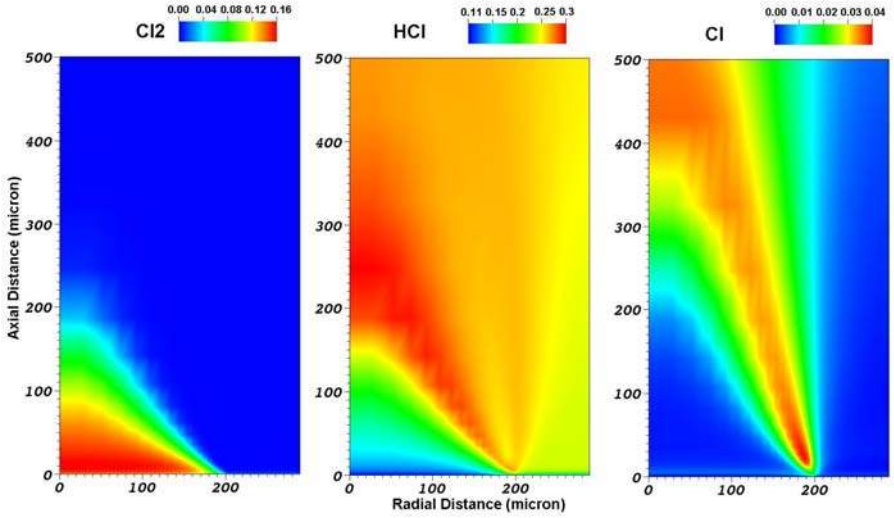

Figure 7-9: Species mass fractions for Cl2, HCl, and Cl above a 400 μm AP particle surrounded by binder.

Comparison of the O_2 concentration to some of the major final species is presented in Figure 7-10. Where O_2 exists in large concentrations, above the AP particle, many of the final species are absent, particularly carbon containing species. Oxygen and carbon must diffuse together before those species are created. Large amounts of CO_2 exit the primary diffusion flame, where oxygen is in abundance, but as CO_2 interacts with the fuel rich products, oxygen is transferred from CO_2, creating CO. Also, the lack of oxygen results in large amounts of H_2 being created in the fuel rich region of the flame as the carbon is converted to CO.

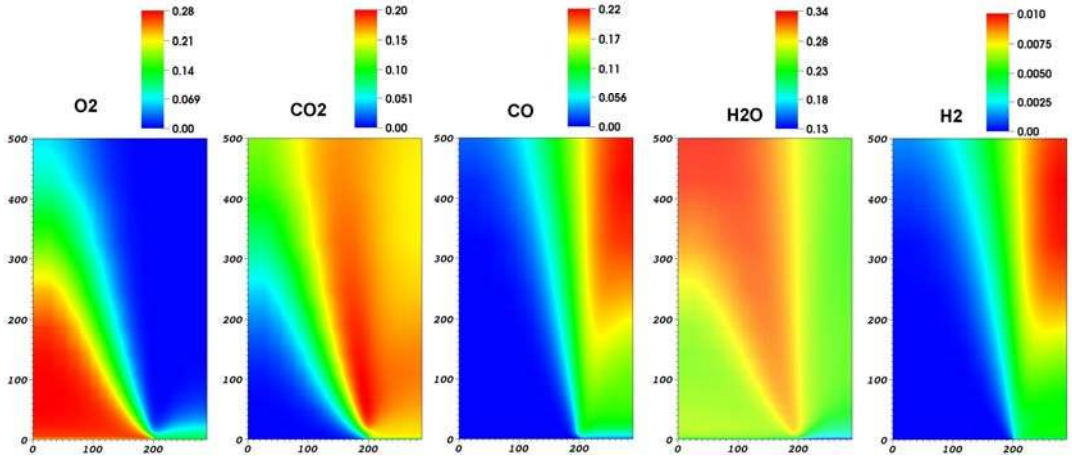

Figure 7-10: Conversion of O_2 to final species above a 400 μm AP particle at 20 atm.

7.1.2 Diffusion Flame: 50 μm

The diffusion flame region of the particle size versus burning rate curve was studied using a 50 μm particle at 20 atm. A binder thickness of 11.1 μm was calculated to

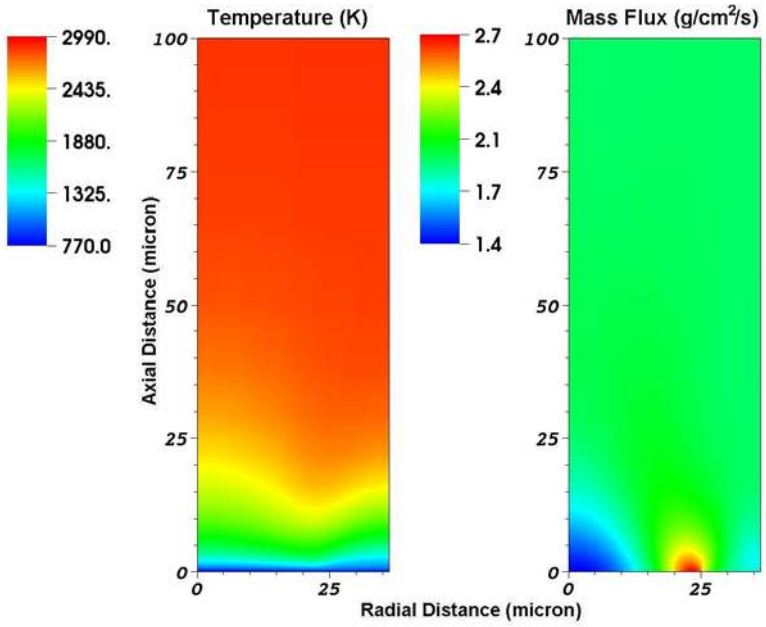

Figure 7-11: Temperature and axial mass flux profiles above a 50 μm particle at 20 atm.

achieve the proper AP loading of 86%. As with the 400 μm particle, all flames from the BDP model are present. However, the final diffusion flame is much closer to the surface, and the flame structure appears to be merging into a single flame (see Figure 7-11). Complete mixing is achieved within 30 μm of the surface, whereas the 400 μm particle was not completely mixed after 1300 μm (the entire calculated domain length). The complete mixing of the flame and proximity of the final diffusion flame is attributed to the shorter radial diffusion distances of the system.

Once again slices of the flame were taken at the particle center (r=0 μm), interface (r=25 μm), and radial boundary (r=36.1 μm) to allow for a more detailed examination of the flame structure. These one-dimensional slices are presented in Figure 7-12. Comparison of the temperature slices with those taken for a 400 μm particle, Figure 7-3, show that the 50 μm particle has a much more uniform flame structure at all locations. All three radial locations have very similar temperature profiles. Figure 7-12 also contains the temperature profiles out to a 5 μm distance, and it can be seen that slightly different heat fluxes to the surface are calculated at each location due to the different temperature slopes at the surface.

A comparison of the centerline calculation and the pure AP temperature profiles is presented in Figure 7-13. For a 50 μm particle, there is no dark zone type structure formed because of the influence of the diffusion flames. Therefore, combustion above the particle is no longer controlled by the AP monopropellant flame, but by influences of the monopropellant flame and the primary diffusion flame.

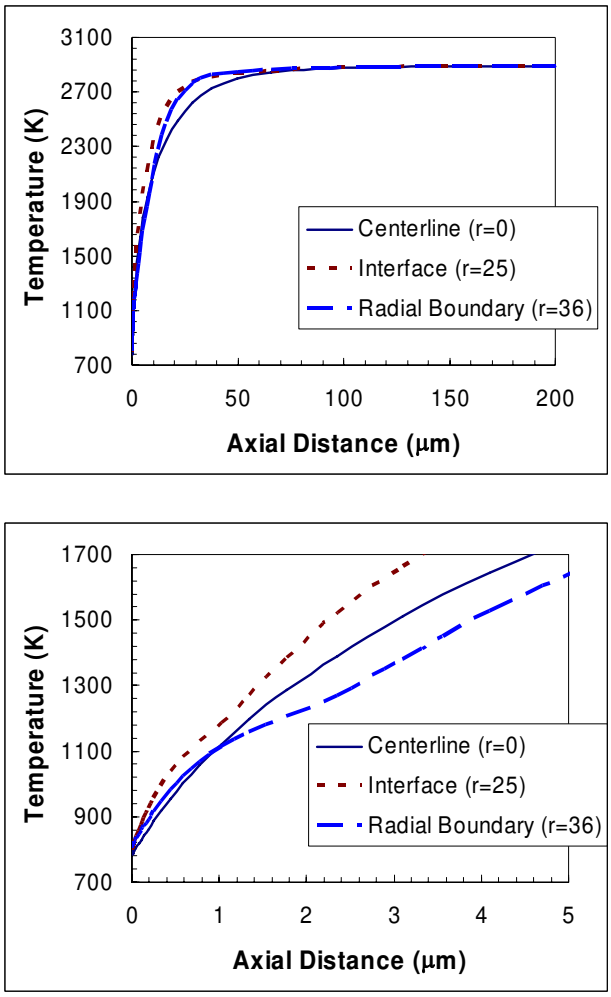

Figure 7-12: Temperature profiles for a 50 μm particle at 20 atm for three radial positions: particle centerline (r=0 μm), particle/binder interface (r=25 μm), and radial boundary (r=36.1 μm).

The heat and mass fluxes at the surface are presented in Figure 7-14 and further illustrate that the combustion is controlled by multiple flames. The heat flux above the particle center (r=0 μm) is now 3150 W/cm^2, significantly higher than the monopropellant heat flux of 1245 W/cm^2. In fact the heat fluxes at all locations are higher than the heat fluxes to the 400 μm particle. This illustrates the very definite particle size effects. As the radial diffusion distances decrease, all flames draw closer to the surface,

creating a faster burning rate. However, the diffusional distances are still too large to create a uniform burning rate.

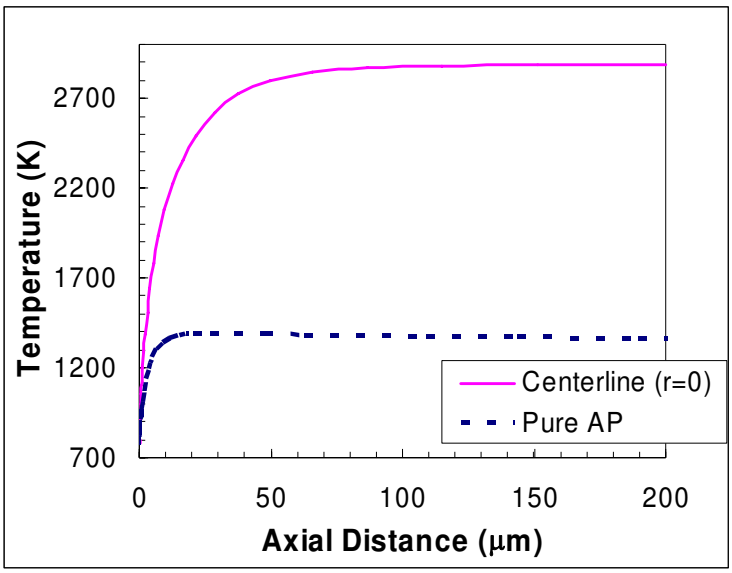

Figure 7-13: Calculated temperature profiles for a 50 μm particle in a composite propellant at the particle centerline (r=0 μm) and for pure AP monopropellant at 20 atm.

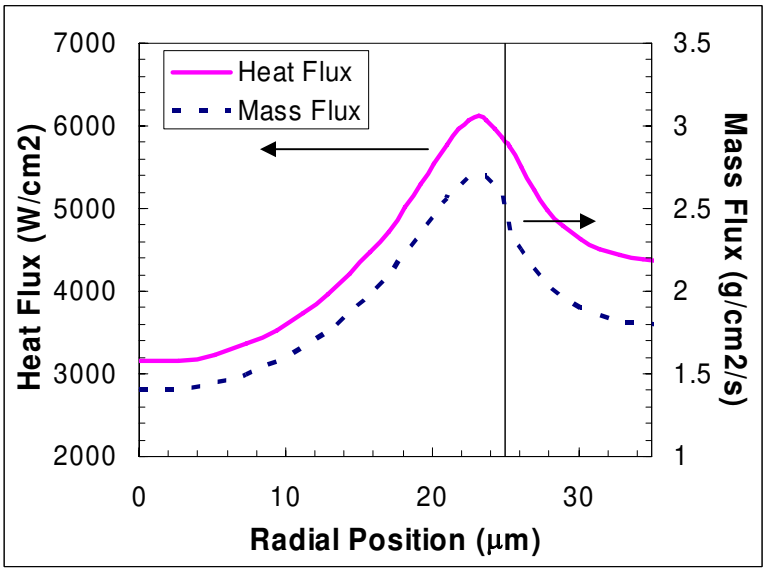

Figure 7-14: Heat flux and mass flux at the surface of a 50 μm particle at 20 atm.

In general, the same species trends are present above the 50 μm particle as were present with the 400 μm particle. Instead of taking place within the first 500 μm, the species all reach final mass fractions within 100 μm. The creation of N_2 from NH_3 in an oxygen rich environment is present in Figure 7-15. N_2O is not included due to its essentially zero mass fraction as NO → N_2. A primary difference between the calculated species fractions for the 50 μm and the 400 μm particle sizes is the ability of oxygen to diffuse above the binder for the smaller particle size. For the 400 μm particle, no NO was present above the binder, but Figure 7-15 shows that within about 8 μm NO is formed above the binder for the 50 μm particle because oxygen has diffused sufficiently above the boundary to create NO.

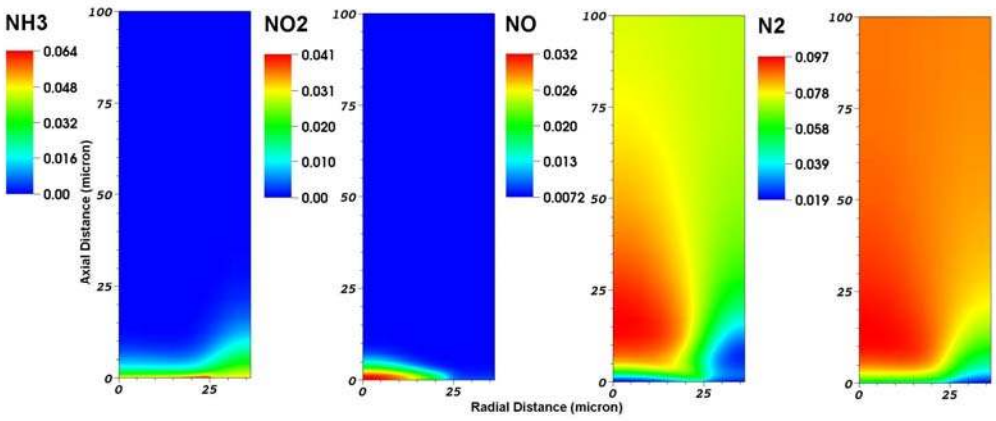

Figure 7-15: Creation of N_2 from NH_3 in the oxygen rich region of the flame, mass fractions for a 50 μm AP particle at 20 atm.

Final species mass fractions are presented in Figure 7-16. Oxygen is once again abundant above the oxidizer, but larger concentrations are also present above the binder. Water is rapidly formed and CO_2 reaches a uniform mixture within 30 μm of the surface.

For the 400 μm particle, CO_2 was reduced to create CO, whereas for the 50 μm particle it appears that the CO_2 concentration is not diminished as CO is formed. Instead, CO appears to obtain oxygen from a different path for the smaller particle size.

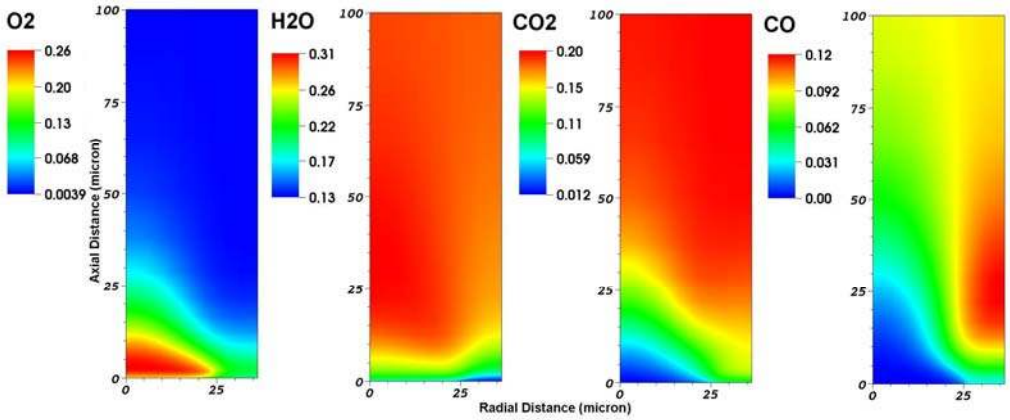

Figure 7-16: Mass fractions for some of the final species of a 50 μm AP particle at 20 atm.

7.1.3 Premixed Limit: 10 μm

Calculations using the diffusion flame model predict that the premixed limit of the burning rate versus particle size curve is reached for AP particles ~10 μm in diameter at 20 atm. This means that the primary diffusion flame has spread out to cover the entire surface, resulting in a maximum burning rate. Therefore, the 10 μm case was examined as the onset of the premixed limit. Figure 7-17 presents the calculated temperature and mass flux profiles above the surface of a 10 μm particle at 20 atm surrounded by 2.2 μm of AP/HTPB homogenized binder. The temperature profile has the appearance of a premixed flame; no BDP type flame structure is present. There is some variation in mass flux near the surface, but note that the scale on the mass flux is over a much narrower range than it was for the larger particles.

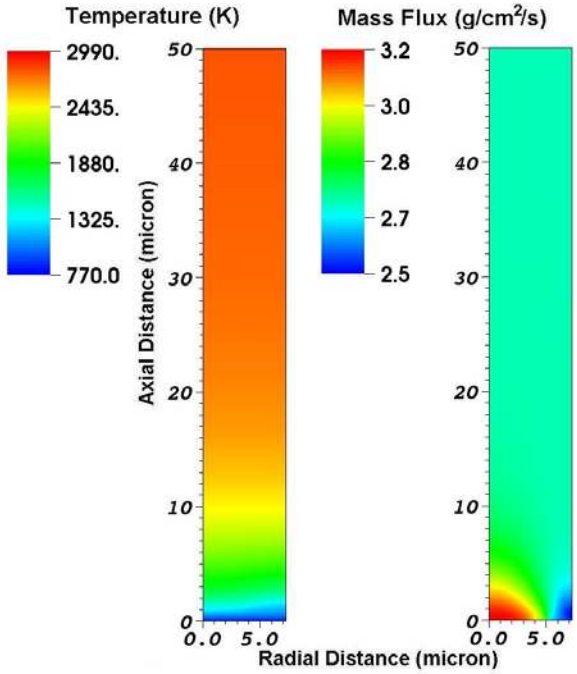

Figure 7-17: Temperature and axial mass flux profiles for combustion of a 10 μm particle at 20 atm.

Once again, one-dimensional temperature profiles were examined for three locations above the surface: the particle center (r=0 μm), the interface (r=5 μm), and the radial boundary (r=7.2 μm). The three temperature profiles are indistinguishable from each other as seen in Figure 7-18, illustrating that the flame is essentially premixed.

The heat and mass fluxes to the surface, shown in Figure 7-19, further illustrate the premixed nature of the flame. There is some slight variation across the surface, but the profiles are far more linear than they were for the larger particles. The interface/centerline heat flux ratio goes from 4.6/1 for a 400 μm particle to 1.94/1 for a 50 μm particle to 0.9/1 for the 10 μm particle. Examination of Figure 7-19 shows a slight numerical glitch at the interface. This was a continual problem for small particle sizes

(<20 μm), and its appearance is attributed to the discontinuity at the interface and possible grid spacing issues.

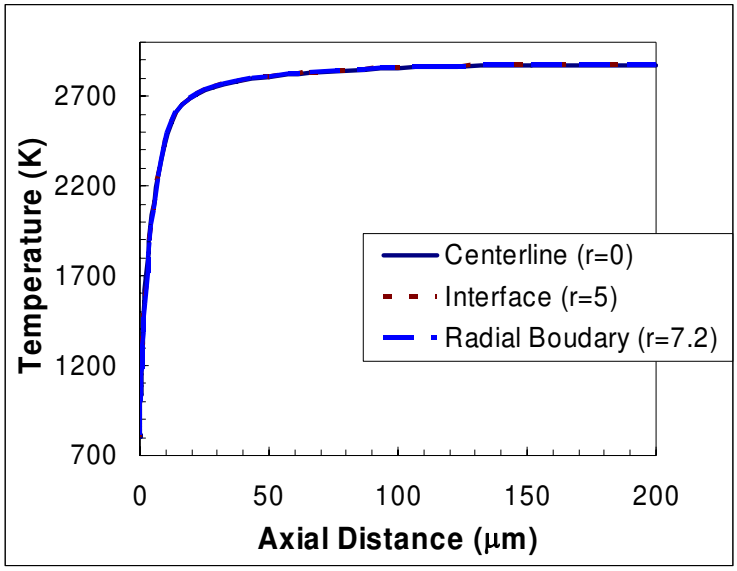

Figure 7-18: Temperature profiles for a 10 μm particle at 20 atm for three radial positions: particle centerline (r=0 μm), particle/binder interface (r=5 μm), and radial boundary (r=7.2 μm).

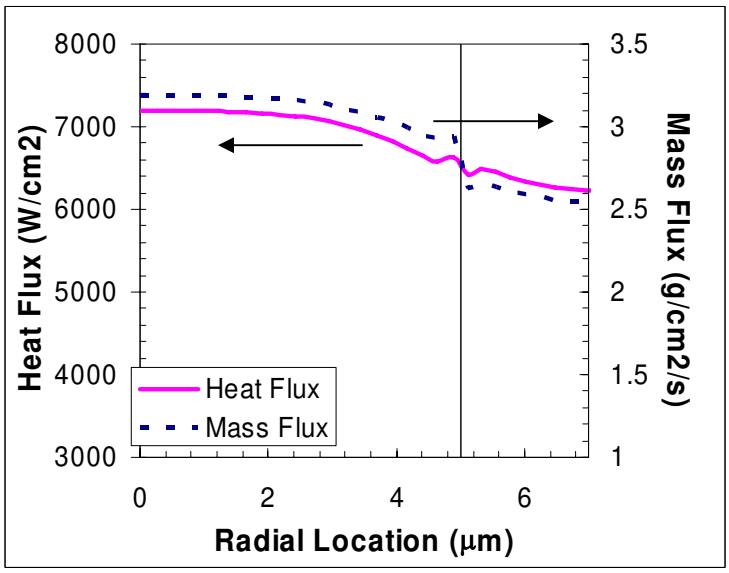

Figure 7-19: Heat and mass flux above a 10 μm particle at 20 atm.

Species profiles are consistent with the previously outlined trends. The path to convert NH_3 to N_2 in an oxygen rich environment is presented in Figure 7-20. The species reach their final concentrations within about 13 μm of the surface, and NO and N_2 appear to form a relatively premixed distribution. The NH_3 and NO_2 distributions are more heterogeneous due to the decomposition products leaving the surface.

Mass fractions are also presented for O_2, H_2O, CO_2, and CO in Figure 7-21. The O_2 mass fraction results in an interesting profile. A "sideways V" shape is formed near the surface. The short radial diffusion distance allows a higher concentration of O_2 to be reached above the binder compared to the larger particle sizes.

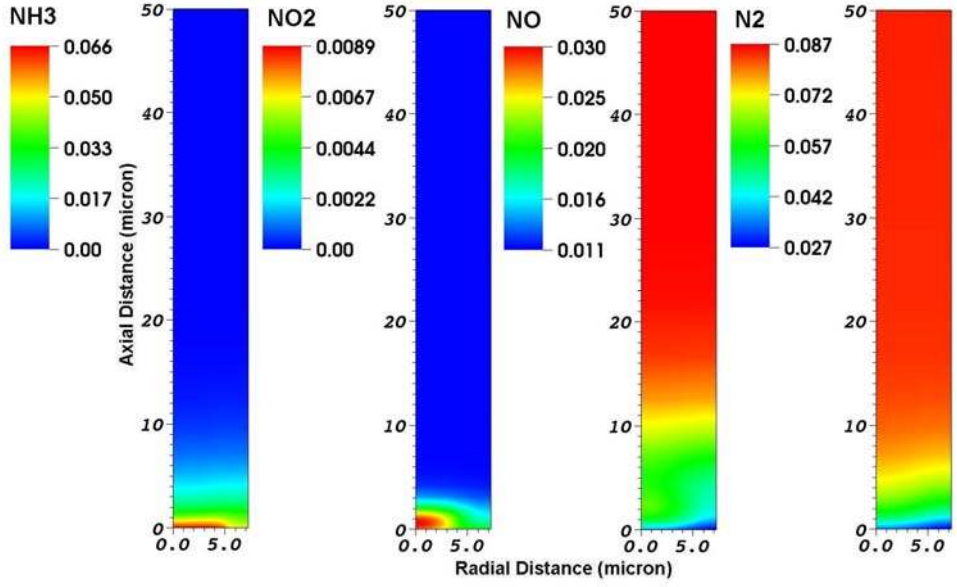

Figure 7-20: Mass fractions showing path to convert NH_3 to N_2 in an oxygen rich environment for a 10 μm particle at 20 atm.

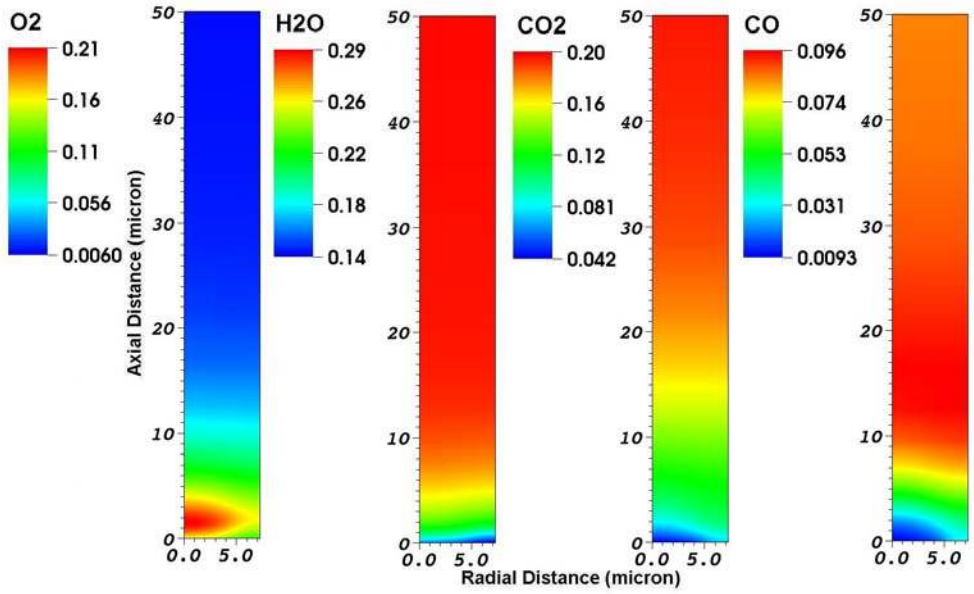

Figure 7-21: Mass fraction profiles for O_2, H_2O, CO_2, and CO above a 10 μm particle at 20 atm.

7.1.4 Particle Size Effects at 20 atm

The trends outlined above for flame structure as particle sizes change are illustrated by the surface heat flux profiles plotted in Figure 7-22 for particles from 5 to 400 μm. The radial distances were normalized by the particle radius so that the heat fluxes could be compared. The heat flux, and hence the burning rate of the system, increases with decreasing particle size, which is consistent with experimental trends. The hot primary diffusion flame increasingly controls the heat feedback to the surface as more and more of the particle surface is near the primary diffusion flame. This also causes the peak heat flux to move slightly to the particle side of the particle/binder interface as the diameter decreases. Also, as the primary flame begins to dominate, the heat flux above the AP particle approaches the heat flux above the AP/HTPB binder. By 10 μm the heat flux is roughly planar above the entire surface with the heat flux above the AP being only

slightly higher. As particle size is further decreased to 5 μm, the heat flux above the particle slightly decreases, and the heat flux above the binder slightly increases, effectively pivoting about the interface, but resulting in the same burning rate as the 10 μm particle.

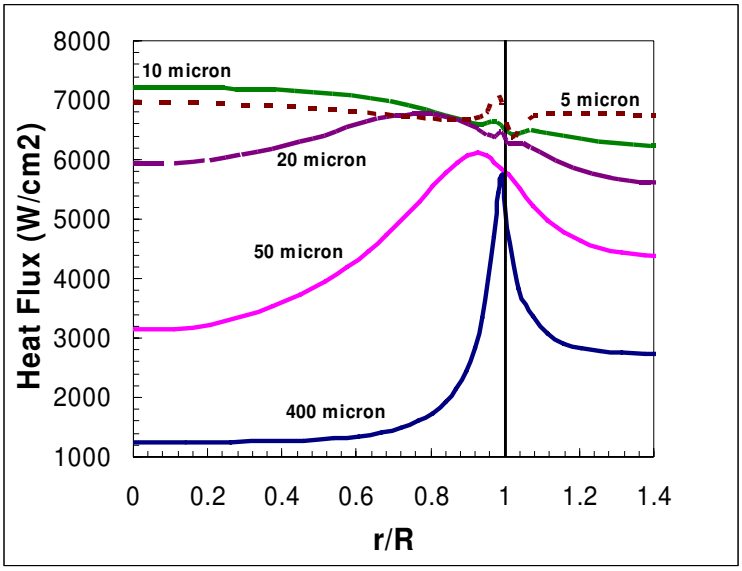

Figure 7-22: Surface heat flux profiles for various particle sizes at 20 atm.

The change in the flame structure with particle size is presented in Figure 7-23 for particle sizes ranging from 400 to 1 μm. As seen in the figure, as particle size decreases, the flame structure approaches the surface and eventually flattens out into a premixed flame. A premixed flame appears to form by 20 μm, but analysis of the heat flux gives a premixed burning rate at 10 μm.

As particle size decreases, the influence of the primary diffusion flame increases until the flame structure merges to form a premixed system. The premixed system then regresses at the rate of a premixed binder with the overall AP mass fraction (86% AP in

this case). Figure 7-24 illustrates how the calculated burning rate changes as a function of particle diameter for a simulated system of 86% AP at a pressure of 20 atm. This figure is analogous to figures generated by Beckstead[2] and Jeppson[95] showing the same trends of

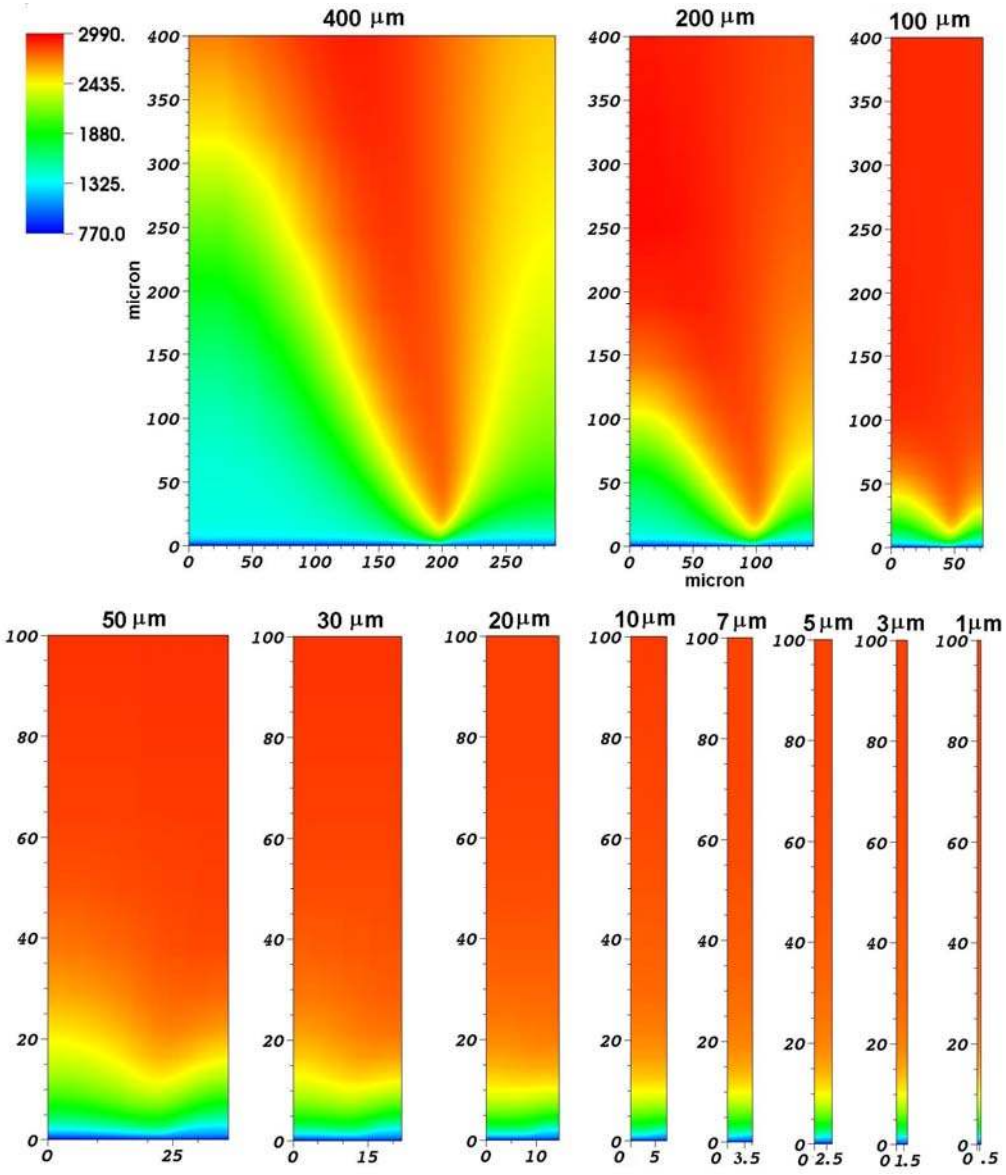

Figure 7-23: Temperature (K) profiles for particle sizes ranging form 400 μm to 1 μm at 20 atm.

burning rate with AP particle size and presented earlier in Figure 2-10. The calculations show that for this propellant formulation, all particles smaller than 10 μm can be treated as a homogenized mixture at 20 atm.

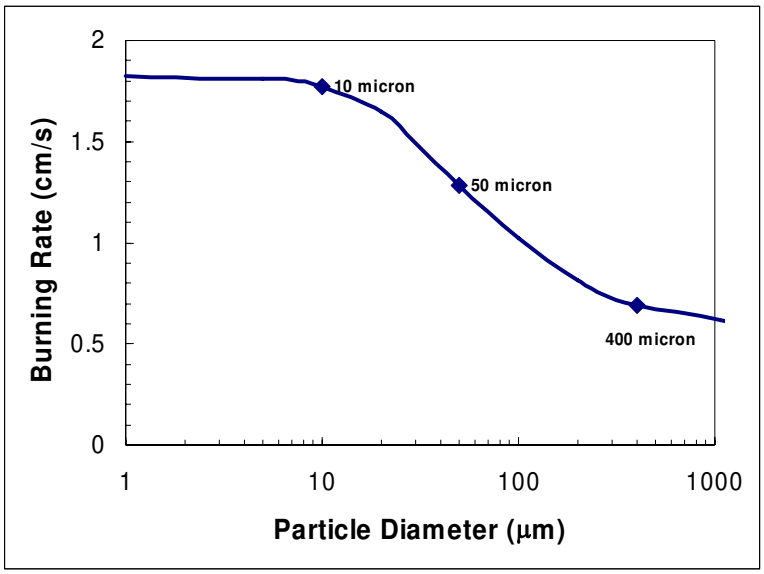

Figure 7-24: Calculated particle size effects at 20 atm for an 86% AP composite propellant.

7.2 Pressure Effects

Pressure has a strong influence on burning rate and particle size effects for a given composite propellant. Therefore, calculations were performed varying pressure from 1 to 100 atm. The influence of pressure varies based on the combustion region in which the particle size is located; therefore, a particle size from each of the three burning rate regions was examined. For consistency, particle sizes of 400 μm, 50 μm, and 10 μm were further examined.

7.2.1 AP Monopropellant Limit: 400 μm

The AP monopropellant limit is once again represented with a 400 μm particle surrounded by 89 μm of binder. The calculated temperature profiles, ranging from 1 to 100 atm are shown in Figure 7-25.

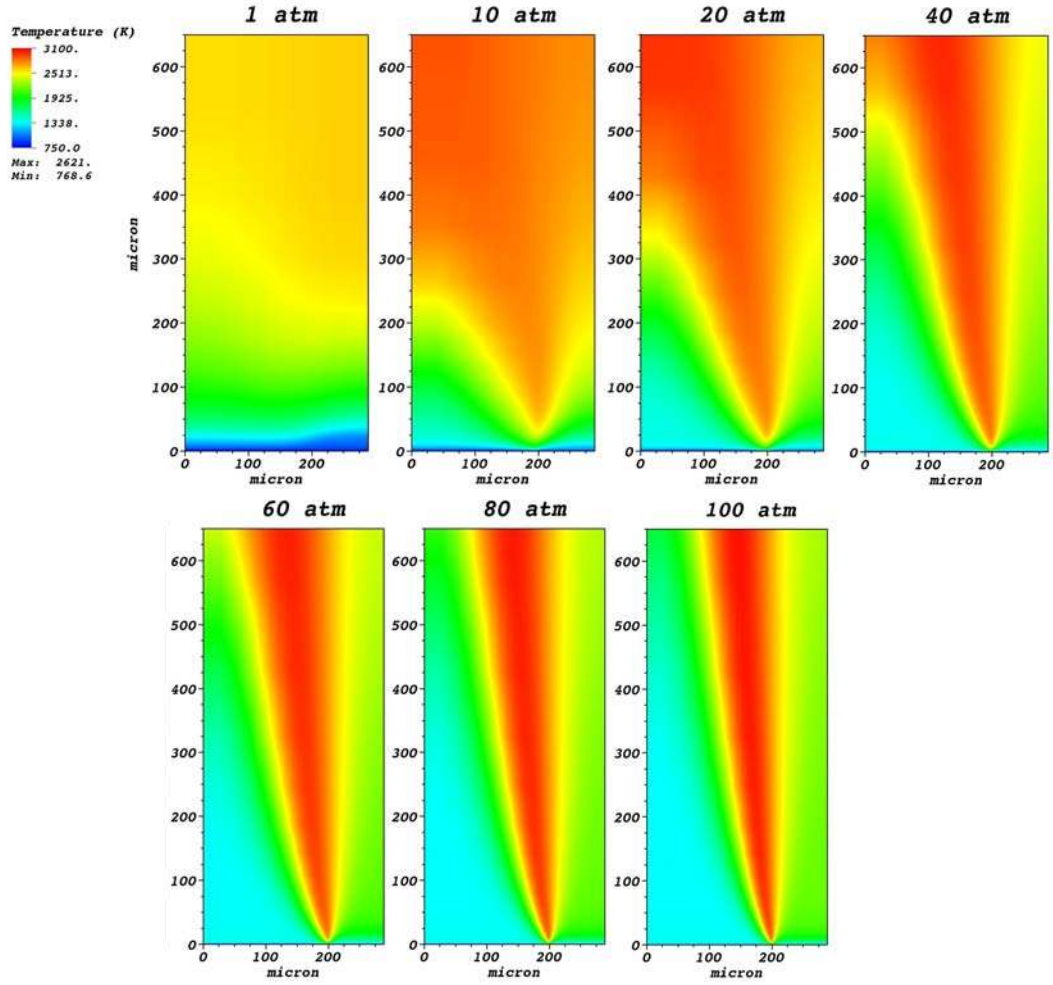

Figure 7-25: Temperature (K) profile calculations for a range of pressures above a 400 μm AP particle with an AP/HTPB binder.

The temperature profiles show very significant differences as pressure increases. At a pressure of 1 atm the flame structure is essentially uniform across the surface of the

propellant, resulting in an essentially uniform heat flux to the surface. The composite propellant is burning in a premixed fashion for a 400 μm particle at 1 atm. Particle size will not, therefore, play a significant role in combustion at atmospheric conditions. This is consistent with experimental data obtained by Miller[90,131] in which they varied particle size and pressure for an AP/HTPB containing propellant. Their results are presented in Figure 7-26. At 100 psi the burning rate is virtually linear regardless of particle size. For higher pressures the burning rate increases with decreasing particle size, forming an inverted "S" shape as previous calculated for combustion at 20 atm (see Figure 7-24). Miller's data indicate that large AP particles will react in a premixed fashion at low pressure as calculated by the current model. Even at 10 atm, there is a definite particle size impact for 400 μm AP particles, as shown in Figure 7-25. From these calculations, it is apparent that atmospheric experimental conditions will not capture the true impact of AP particle size on combustion. Also, at 1 atm, the final flame temperature is significantly lower than at higher pressures. The model predicts a value of 2610 K compared to ~2850K for higher pressures. Equilibrium calculations predict a value of 2660 K at 1 atm and 2880 K at higher pressures, both close to the values predicted by the model. The results at 1 atm are very consistent with experimental data and give significant insight into AP/HTPB combustion.

Figure 7-25 also illustrates the dynamic nature of the flame structure as pressure increases. The monopropellant AP flame, premixed binder flame, and the primary diffusion flame all draw closer to the surface as pressure increases. The final diffusion flame, on the other hand, is "blown" away from the surface with increasing system

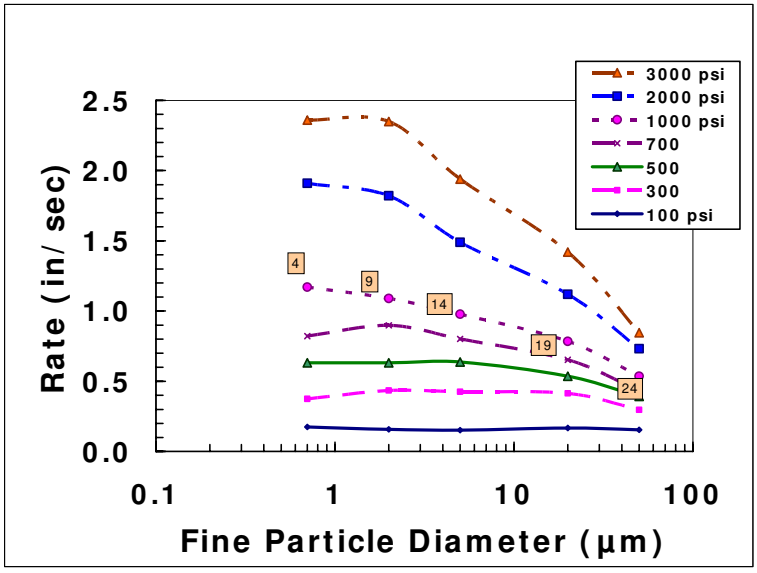

Figure 7-26: Particle size and pressure effects for AP/HTPB composite propellants consisting of 200µm/20µm/fine AP and 12% HTPB obtained by Miller.[90]

pressure. Gas-phase kinetics are proportional to pressure, and therefore, as pressure increases, reaction rates increase, drawing the flames closer to the surface and decreasing the thickness of the flames. There is also a large increase in axial mass flux. The slight increase in the radial mass flux is unable to counter the large increase in axial mass flux with increasing pressure, and the final diffusion flame is "blown" away from the surface. Gas-phase species are able to travel farther axially before they diffuse far enough radially to react, and thus the final diffusion flame moves away from the surface. The decrease in flame standoff distances can be seen more clearly in Figure 7-27, an up-close view of Figure 7-25 for pressures from 1 to 40 atm.

The transition from dark blue to light blue in Figure 7-27 is roughly the location of the AP monopropellant flame. As pressure increases, the AP flame draws nearer to the surface. Figure 7-28 presents the particle centerline calculations for various pressures. The 1 atm temperature profile is a smooth curve up to the final temperature. No plateau is

visible for the AP monopropellant flame, indicating its premixed nature at low pressure. Then, as pressure increases, the AP monopropellant flame becomes more discernible and appears as a "dark zone" with the length increasing as the pressure increases. The increase in length of the "dark zone" is due to the decrease in the monopropellant flame stand-off distance and the "blowing" effect of the higher gas-phase mass flux. Similar behavior is also calculated for the premixed binder flame, as seen in Figure 7-29. The temperature rapidly approaches the premixed binder flame temperature, but the distance necessary to reach the final flame temperature increases with pressure.

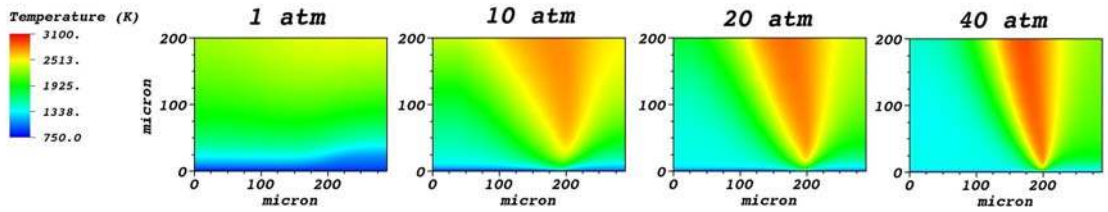

Figure 7-27: Flame stand-off distances for pressures from 1 to 40 atm.

The primary diffusion flame also changes with pressure, as was seen in Figure 7-25. As pressure increases the flame draws closer to the surface, and the width of the flame narrows. Both of these effects are seen in Figure 7-30, which presents the axial temperature profiles above the interface and the heat flux to the surface. The temperature profile is relatively far from the surface at low pressure, reaching 2400 K within 175 μm at 1 atm, and then draws very close to the surface with increasing pressure, reaching 2400 K within 4 μm at 60 atm. The heat flux to the surface increases due to the proximity of the flame, but the radial influence decreases, relatively, due to the narrowing of the primary flame. As seen in Figure 7-30, as pressure increases from 20 to 100 atm, the

width of the heat flux spike decreases at the interface. The decrease in axial flame temperature with increasing pressure (aside from the 1 atm calculation), as illustrated in Figure 7-30, is due to the "blowing" effect of the higher axial mass flux.

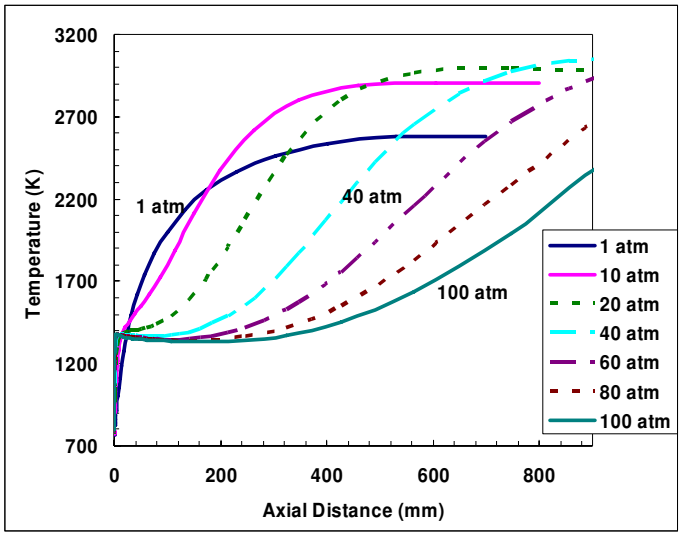

Figure 7-28: Particle centerline (r=0 μm) temperature profiles for pressures from 1 to 100 atm.

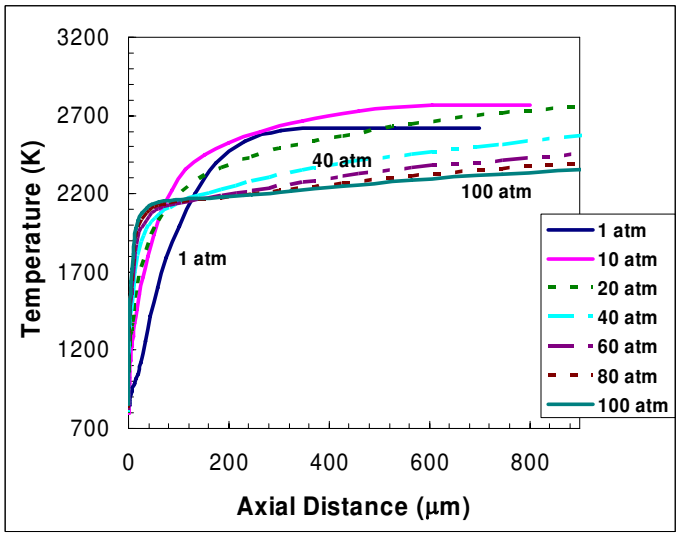

Figure 7-29: Temperature profiles above the homogeneous binder at the radial boundary (r=289 μm) for pressures from 1 to 100 atm.

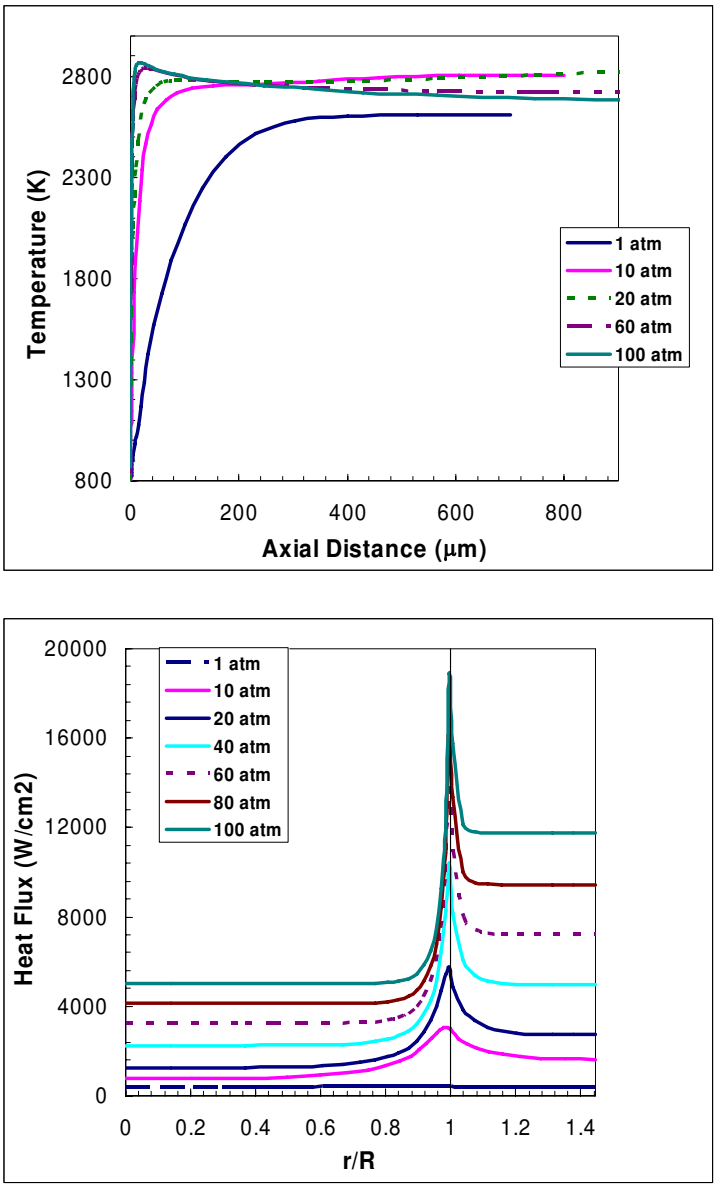

Figure 7-30: Change in axial temperature profile, the primary diffusion flame, (top) and radial surface heat flux at the particle/binder interface with pressure (bottom).

The formulation of the composite propellant used in the calculations was chosen to correspond to work performed by Foster[67] for a bimodal (400/12 μm) propellant. The 12 μm mode is assumed to be homogenized with binder resulting in a homogenized binder containing 77.5% AP. Foster obtained experimental burning rate data for this

formulation. Using Equation (7-1) to obtain an average burning rate, the current calculations are compared to the Foster data in Figure 7-31. Very good agreement is achieved, especially considering the Foster data used two particle size distributions and the model only uses a single representative particle size and a homogenized binder. In the Foster data there is a small change in slope between 15 and 20 atm. This is apparently due to the flame structure changing from premixed to the diffusion region above the 12 μm AP particles, and therefore, the 12 μm particles no longer burn as a homogenized premixed binder. As pressure increases, the primary diffusion flame has a decreasing influence across the surface and the multiple flame structure begins to dominate combustion. These experimental results are very consistent with the current numerical calculations. Assuming a 3% variation from the asymptotic premixed burning rate limit, the model predicts particle cutoff sizes to the premixed limit of 20 μm at 10 atm and 10 μm at 20 atm. This would correspond to a particle cutoff size of 12 μm at 18 atm, which

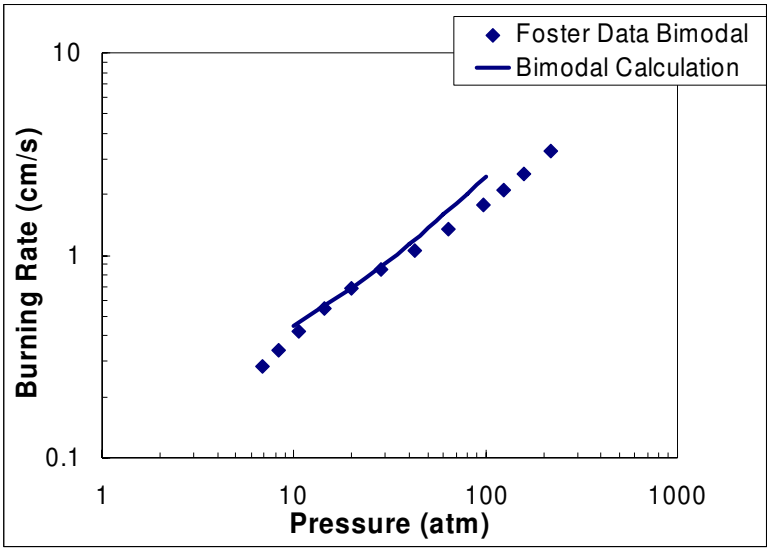

Figure 7-31: Comparison of calculated burning rate for a 400 μm particle to Foster data.

is in the region of the slope break in Foster's experimental data. Therefore, at pressures higher than 15 atm the premixed binder assumption for Foster's propellant begins to break down, and thus there is greater deviation between the calculations and the experimental data at higher pressures.

7.2.2 Diffusion Flame Zone: 50 μm

Many of the trends outlined for a 400 μm particle are consistent with the trends observed in the diffusion flame region. Calculations for a 50 μm particle surrounded by 11.1 μm of homogenized binder at pressures varying from 1 to 100 atm are presented in Figure 7-32.

A premixed flame structure is calculated at 1 atm, as expected, due to the premixed structure of a 400 μm particle at 1 atm. The domain length presented in Figure 7-32 for 1 atm is not long enough to reach the final flame temperature. An axial length of roughly 200 μm is required to reach the final flame temperature at this pressure, but to focus on the detailed flame structure at higher pressures the presented domain length was limited to 100 μm. The calculated average burning rate for a 50 μm particle at 1 atm, 0.12 cm/s, is essentially equal to the rate of a 400 μm particle, 0.11 cm/s.

By 10 atm some individual flames are beginning to appear, but the overall structure is still very much premixed. A BDP type flame structure has formed by 20 atm, as seen in Figure 7-32. As pressure continues to increases the BDP structure becomes very distinct. Also, as pressure increases, the "blowing effect" begins to move the final diffusion flame farther from the surface, but not nearly to the extent seen for the 400 μm particle.

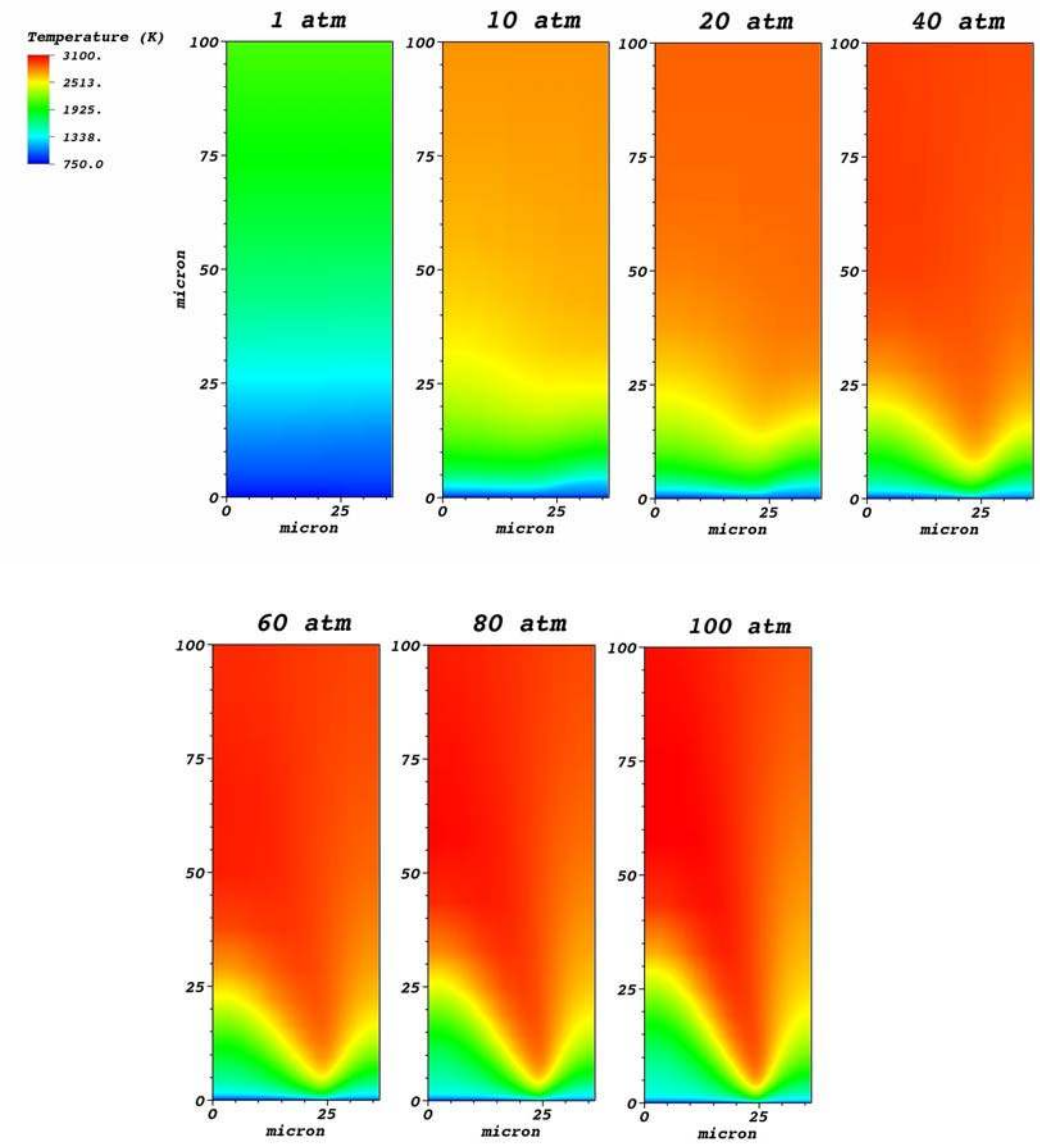

Figure 7-32: Flame structure calculations for a 50 μm particle varying pressure from 1 to 100 atm.

Figure 7-33 presents the particle centerline temperature profiles for various pressures. As pressure increases, aside from the premixed 1 atm case, the temperature profile begins to move away from the surface slightly, and by 100 atm a weak dark zone type profile is created. The dark zone type profiles illustrates that once pressure reaches 100 atm the primary diffusion flame has narrowed sufficiently to allow the

monopropellant flame to become the primary driving force for combustion at the particle center, just as it did for pressures greater than 1 atm for the 400 μm particle.

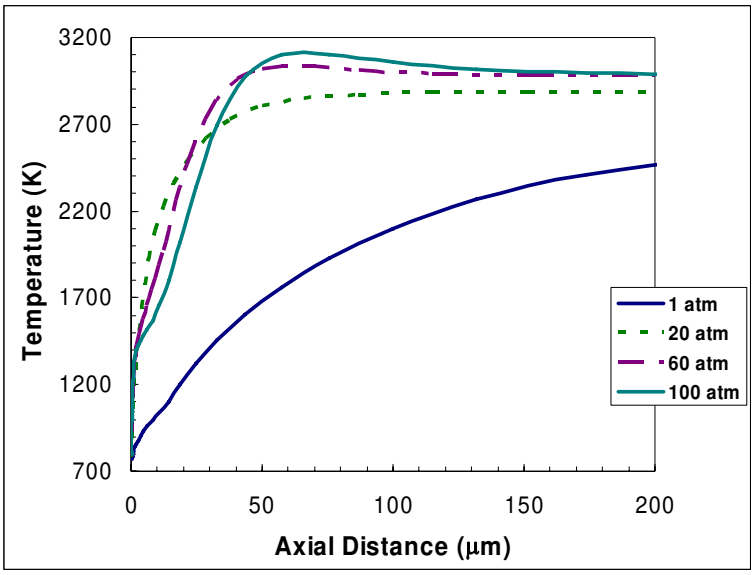

Figure 7-33: Particle centerline temperature profiles for a 50 μm particle.

The calculated heat flux to the surface is presented in Figure 7-34 for the 50 μm particle at various pressures. Note that the heat flux at 1 atm is linear, representing a premixed system. The heat flux at 10 atm is essentially linear, and therefore, the 50 μm particle is near the premixed limit. As pressure continues to increase, so does the relative size of the spike at the interface. Also, the width of the spike narrows with pressure as was observed with the 400 μm particle.

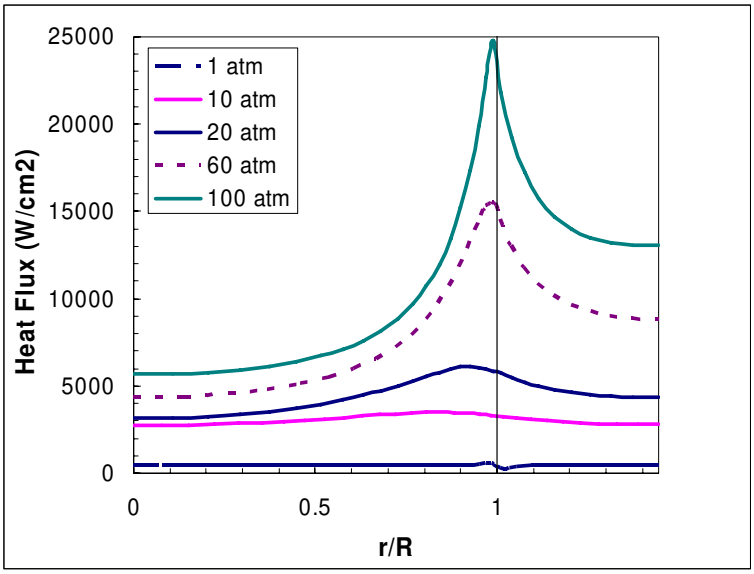

Figure 7-34: Heat flux to the surface of a 50 μm AP particle at various pressures.

7.2.3 Premixed Limit: 10 μm

The premixed limit is represented by a 10 μm particle surrounded by a 2.2 μm shell of binder. The flame structure profiles are presented in Figure 7-35. Examination of the flame structures show that a 10 μm particle transitions from the premixed limit to the diffusion flame region as pressure increases. As pressure increases from 1 to 40 atm, the premixed flame structure is drawn closer to the surface of the particle. Then as pressure continues to increase, a weak BDP type flame structure is formed, and the particle burning rate is clearly in the diffusion flame region. Just as with the 50 μm particle, the BDP structure becomes more defined with increasing pressure. These results illustrate the importance of both pressure and particle size on a composite propellants burning rate.

The calculated heat flux to the surface of a 10 μm particle is presented in Figure 7-36. The premixed nature of the flame results in virtually linear profiles from 1 to 20 atm. At 40 atm the primary diffusion flame begins to have an impact, as is evident from

the peak near the interface. At higher pressures the flame is no longer characterized by a premixed region, and there is a very definite influence of the primary diffusion flame that follows the same trends as outlined for larger particles.

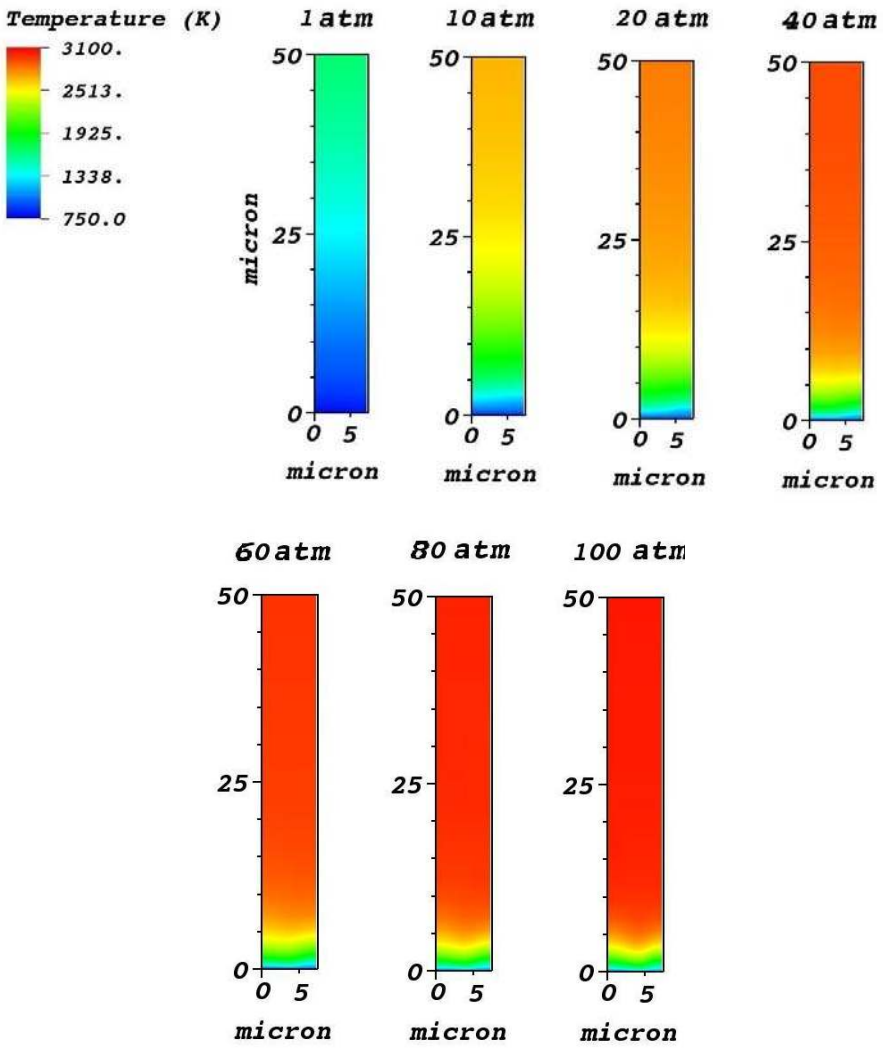

Figure 7-35: Flame structures above a 10 μm particle at pressures ranging from 1 to 100 atm.

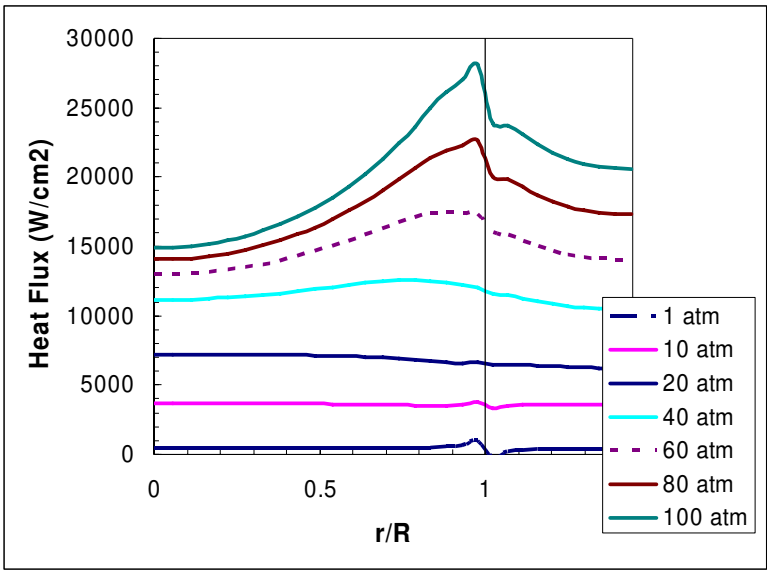

Figure 7-36: Heat flux to the surface for a 10 μm particle at pressures from 1 to 100 atm.

7.2.4 Overall Pressure Trends

At 1 atm all particle sizes result in a premixed flame. This is consistent with the experimental work performed by Foster and shows that experimental work performed at atmospheric pressures cannot capture the intricacies of composite propellant combustion. At higher pressures, the particle cutoff size for the premixed limit decreases due to the decreasing influence of the primary diffusion flame. This is attributed to the larger rise in axial mass flux when compared to radial mass flux. Species are able to travel farther downstream before they have diffused sufficiently radially to react, the "blowing effect", and thus the primary diffusion flame has less radial impact. The heat fluxes become more non-linear, and therefore, so do the burning rates as pressure increases. Also, the non-linear burning rate results in a peak burning rate near the interface where the chemistry is closest to stoichiometric conditions. A very non-linear surface results as pressure is increased.

7.3 Pressure and Particle Size Effects

A simulated composite propellant consisting of 86% AP loading and assuming the binder is made up of 77.5% AP in HTPB has been studied. Calculations have been conducted for particle sizes ranging from 1 to 400 μm and from pressures from 1 to 100 atm. The calculated particle size versus burning rate relation for all calculated pressures is presented in Figure 7-37. The calculations for 1 atm result in a constant, horizontal line, and therefore, there is no particle size effect at this pressure. As pressure is increased, the particle size effect becomes more evident. The effective premixed cutoff size, where diffusion starts to become significant, decreases with increasing pressure and by 100 atm a particle size of 1 μm appears to be in the transition region from diffusion flame to premixed limit. These calculations provide significant understanding and are important for composite propellant models, which use a particle packing code to examine combustion. A common assumption in the packing models is that the binder is homogeneous with the fine AP particles, but the question is, what is the size at which all smaller particles are homogenized. Such an assumption and its limitations now have a numerically based validation.

The relationship between pressure and burning rate is presented in Figure 7-38 for the same range of pressures and particle sizes. Note that at 1 atm, the burning rate for all particle sizes converge to the same value. The linear line at the top of the domain calculated for 1 atm represents the premixed limit. All particle sizes converge to that limit with decreasing pressure. The limit corresponds to a completely premixed composite propellant with 86% AP. This is the maximum burning rate for the given propellant formulation.

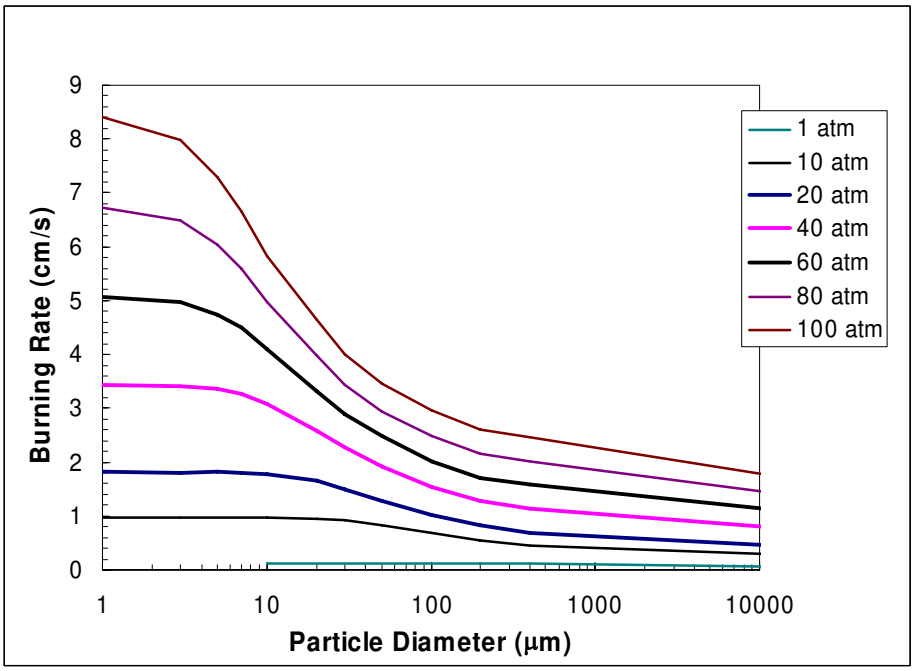

Figure 7-37: Particle size effects for pressures from 1 to 100 atm for an 86% AP propellant assuming 77.5% AP in the binder.

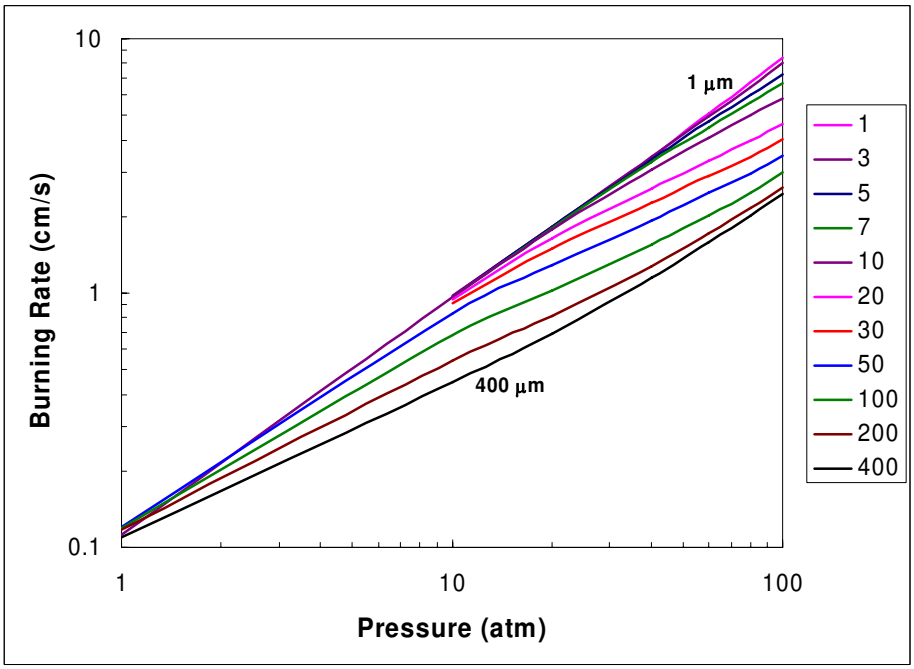

Figure 7-38: Pressure versus burning rate for various particle sizes.

7.4 Formulation Effects

The influence of a different formulation of AP/HTPB has also been investigated, utilizing another Foster propellant formulation. Foster increased the fine AP/binder ratio from 3.44 to 4.0 while maintaining the same overall AP loading of 86%. This corresponds to a binder containing 80% AP. Calculations were run using the new binder fraction for a pressure of 20 atm and all particle sizes, also calculations were performed for 400 μm particle at pressures from 1 to 100 atm. The increase in AP concentration in the binder effectively increases the amount of binder associated with each particle to achieve the same AP loading. The binder thickness for a 400 μm particle increased form 89 μm for a 77.5% AP binder to 112 μm for an 80% AP binder. Calculations were performed at a pressure of 60 atm for all particle sizes and the resulting particle size versus burning rate relation is presented in Figure 7-39.

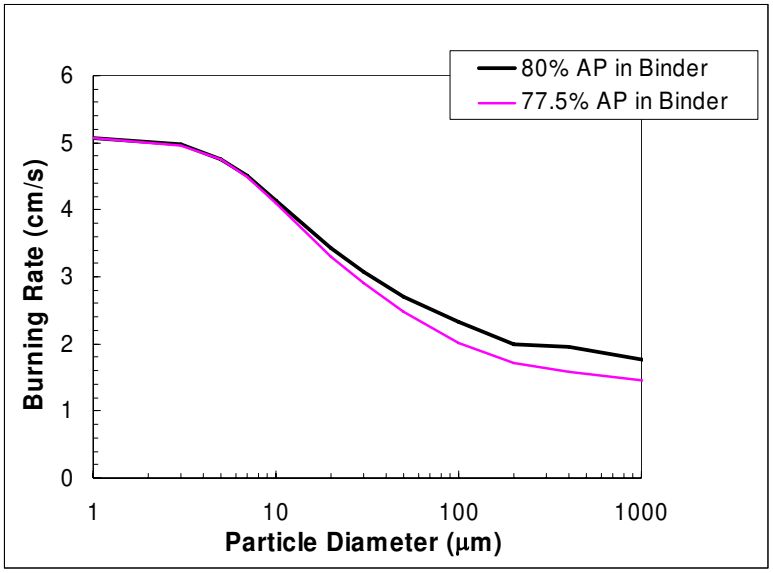

Figure 7-39: Particle size effects for 80% and 77.5% AP in binder with 86% AP overall at 60 atm.

The average burning rate for the new formulation with 80% AP in the binder is faster for the particles in the monopropellant and diffusion flame regions. The increase in burning rate is due to the increased AP content in the binder. The higher AP fraction gives the binder a faster burning rate, and thus the average burning rate is higher. This can be seen in Figure 7-40 where the mass flux to the surface of a 400 μm particle is compared for both formulations. The mass flux above the AP particle is unchanged, and the spike from the primary diffusion flame is unchanged, but the binder is regressing at a faster burning rate. However, both formulations have an overall AP loading of 86%, and therefore, both approach the same premixed limit and burning rate as seen in Figure 7-39.

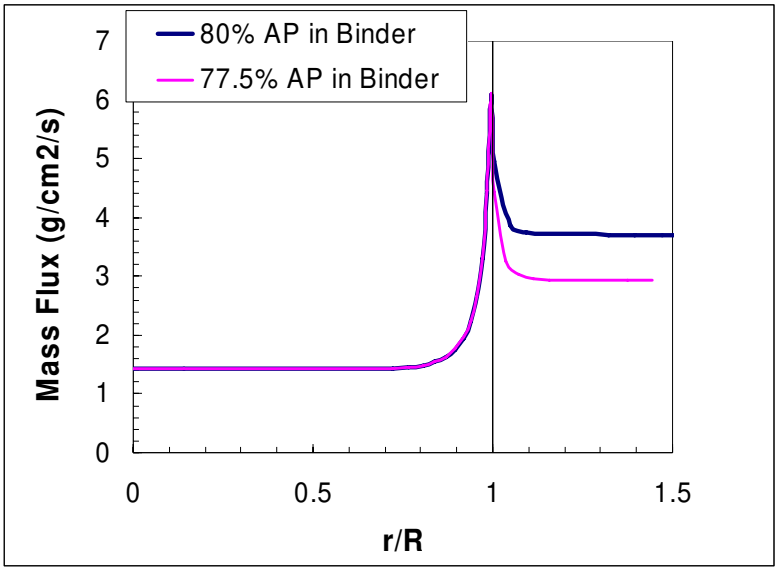

Figure 7-40: Mass flux for a 400 μm particle surrounded by 77.5% and 80% AP in HTPB at 60 atm.

Foster also collected data for the new formulation with a fine AP/binder ratio of 4.0. Comparison of the numerical calculations with the experimental data is presented in Figure 7-41, along with the comparison for the 77.5% AP binder. Once again there is a

slight slope break in the data due to the fine AP particle combustion leaving the premixed region and entering the diffusion flame region. Calculated results give excellent agreement considering the many simplifying assumptions used in the model.

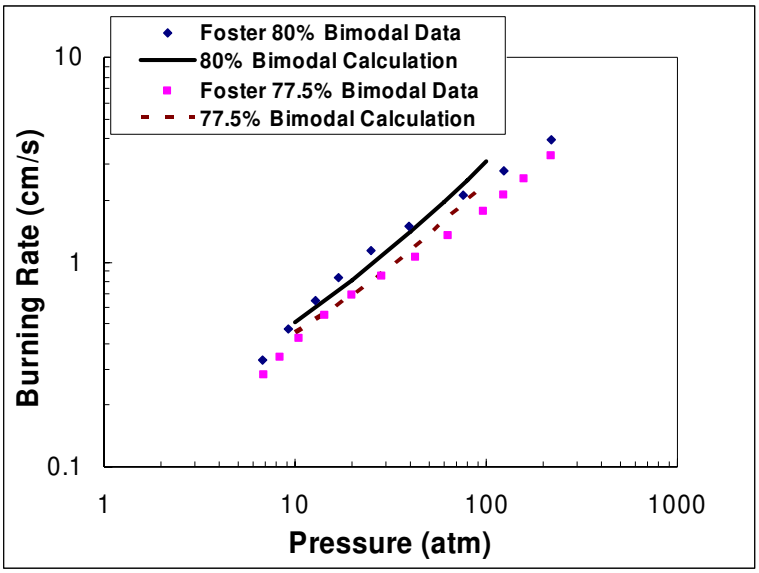

Figure 7-41: Comparison of numerical calculations to Foster data for 86% AP with different fine/binder ratios.

7.5 Summary

The diffusion flame model, utilizing the vorticity-velocity formulation of the governing equations for reacting flow, has been used to investigate the combustion of AP/HTPB. A simulated composite propellant consisting of 86% AP overall and 77.5% AP in the homogenized HTPB binder has been examined. Results illustrate the particle size and pressures effects on combustion. For AP/HTPB composite propellant combustion, the system is premixed at 1 atm and particle size does not impact the burning rate. As pressure is increased, particle size influences the combustion, and the BDP type

flame structure is formed. This results in a highly non-linear heat flux to the surface of the propellant. Comparison of numerical calculations with the experimental work of Foster gives excellent agreement, particularly at low pressures.

8 Conclusions

The unique properties of AP containing propellants, including particle size, pressure, and formulation effects, have been investigated using a two-dimensional diffusion flame model. Work was also performed to develop detailed gas-phase kinetic models for the monopropellants AP and ADN. The following sections outline the results obtained for the work performed and give recommendations for future studies.

8.1 AP Monopropellant Model

8.1.1 Summary

A comprehensive gas-phase mechanism was developed previously by Puduppakkam and has been used to successfully model HMX, RDX, GAP, BTTN, NG and combinations of these ingredients. This mechanism was expanded to include AP by adding chlorine containing reactions. Extensive theoretical work performed by Lin has identified a number of Cl-containing reactions, which have been added to the Puduppakkam gas-phase kinetic mechanism. However, results using the Puduppakkam mechanism along with the Lin Cl-containing reactions produced poor agreement with experimental data. It was therefore necessary to include an additional 4 NOCl and 7 HCl reactions proposed by Ermolin and IUPAC, as well as 1 additional reaction present in the Korobeinichev ADN gas-phase kinetic mechanism. The new expanded mechanism

yielded results that are in excellent agreement with experimental burning rate. However, the final temperature and species concentrations are still slightly off and arbitrary modifications to the reaction rate of $2NO=N_2+O_2$ had to be made to obtain correct final species. This is attributed to deficiencies in the chlorine-nitrogen chemistry of the gas-phase mechanism.

8.1.2 Future Work

The use of a global condensed-phase reaction is seen as a first step to developing a more detailed condensed-phase mechanism. Future work needs to include the addition of solid-phase decomposition and a more detailed condensed-phase reaction mechanism. This work is already underway. Along with AP monopropellant, it is also desired to model a pseudo-propellant containing AP/HTPB with the universal mechanism. Work is currently underway on this project. However, to obtain accurate models, independent theoretical work must be performed on the chlorine and nitrogen chemistry to determine more correct gas-phase reactions. The work by Lin is ongoing, and as more reactions are quantified, they need to be incorporated into the universal mechanism.

8.2 ADN Combustion Model

8.2.1 Summary

Condensed and gas-phase mechanisms were determined to model ADN monopropellant combustion. Parametric studies were performed using PHASE3 on previously published gas-phase mechanisms to evaluate their accuracy compared to experimental data obtained by Korobeinichev.[37] Results of the study indicated that the

Korobeinichev mechanism most accurately matched the data; however, use of an arbitrary gas-phase area expansion was necessary. A condensed-phase mechanism was developed based on available surface species data obtained by Brill[40] and Fetherolf.[51] The condensed-phase mechanism consists of a single global reaction and an ADN evaporation reaction. Calculations indicate that 5% ADN evaporation was an optimal value to match the data, and the inclusion of evaporation eliminated the need for the arbitrary gas-phase area expansion. Numerical results accurately predicted combustion properties of ADN in the first burning rate region. These include temperature and species profiles, burning rates, and temperature sensitivity. Modification to the condensed-phase reaction rate was necessary to create a smooth transition through the unstable combustion region between 20 and 100 atm. The current condensed-phase mechanism is seen as an initial step in the development of a more detailed mechanism.

8.2.2 Future Work

The global condensed-phase reaction needs to be examined and a more detailed mechanism developed to take its place. A methodology for developing a new mechanism was outlined and may be able to account for the erratic combustion of ADN between 20 and 100 atm. The gas-phase mechanism needs to be incorporated into the comprehensive mechanism developed by Puduppakkam.

8.3 AP/HTPB Composite Propellant Model

8.3.1 Summary

A two-dimensional model was developed to simulate the complex flame structure above an idealized ammonium perchlorate (AP)/hydroxy-terminated polybutadiene (HTPB) composite propellant. The model was changed from pressure-based equations to a vorticity formulation of the governing equations. Use of the vorticity-velocity equations for low Mach flow successfully increases accuracy, stability, and robustness of the diffusion model, while also significantly decreasing run time, from weeks to days. The vorticity formulation was validated for diffusion and combustion through comparison with known analytical and numerical problems. Comparison to the pressure formulation resulted in similar results for large particle sizes. The reason for slight differences was the use of an inaccurate AP condensed-phase correlation in the pressure-velocity version. The vorticity formulation does not suffer from inaccuracies for small particle as the previous model does.

A detailed kinetic mechanism with 37 chemical species and 127 reaction steps was utilized to describe the reactions involved. Inlet conditions to the gas phase were derived from one-dimensional model calculations. The diffusion flame model was applied to an 86% AP/14% HTPB propellant with 37.8% 400μm AP and 48.2% 12 μm AP. It was assumed that the 12 μm AP and the 14% binder make up a homogenized binder mixture that can be modeled as a premixed flame containing 77.5% AP. The calculated results showed the detailed diffusion flame structure above the idealized composite propellant surface and results agreed qualitatively with the BDP model. The AP monopropellant flame, the primary diffusion flame, and the final diffusion flame were

all apparent in the calculation, along with a premixed flame over the binder. The dominant contribution of the primary diffusion flame to the propellant's burning rate was shown.

Particle size effects were investigated for a range of pressures from 1 to 100 atm. The calculated results illustrate the changing flame structure above the propellant surface as AP particle size changes. Calculations at 1 atm predicted a premixed flame at all particle sizes, and therefore, particle size does not impact combustion at this pressure. These results are consistent with work performed by Miller on AP/HTPB propellants. An inverted "S" shaped curve is calculated at pressures greater than 1 atm as particle size varies from 400 μm to 1 μm. As the AP particle size was increased, the propellant burning rate approached the pure AP monopropellant burning rate. A particle cutoff size was calculated for the premixed limit at all pressures. Calculated particle size effects were consistent with experimentally observed trends.

Pressure effects were also investigated for pressures ranging from 1 to 100 atm. The calculated results illustrate the changing flame structure above the propellant surface as pressure increases. At 1 atm, a premixed flame structure was present above the surface, consistent with experimental results. By 10 atm a BDP type flame structure was formed with contributions from the AP monopropellant flame, the binder premixed flame, the primary flame, and the final diffusion flame. As pressure increased, the final diffusion flame was "blown" away from the surface due to increased axial mass flux. All other flames were drawn closer to the surface due to the increase of reaction rates with pressure. Insight was gained into the behavior of large AP particle containing propellants

at high pressure. Transitions from premixed limits to diffusion flame regions were predicted as pressure changed.

A second formulation was also investigated based on a second Foster propellant. The only variation was an increase in AP in the homogenized binder from 77.5% to 80%. Calculations gave consistent results. Both formulations approached the same premixed limit which corresponds to the overall AP mass fraction.

8.3.2 Future Work

Calculations need to be expanded to include a broader range of propellant formulations. This includes AP/HTPB propellants and other ingredients such as GAP/RDX propellants. Results from the diffusion model need to be parameterized to incorporate the results into an overall propellant code capable of predicting combustion properties of a number of ingredients. Also, calculations need to be performed for a non-linear surface to investigate its effects on combustion.

9 References

1. Beckstead, M.W., Derr, R.L., and Price, C.F., "A Model of Composite Solid-Propellant Combustion Based on Multiple Flames," *AIAA Journal*, Vol. 8, No. 12, 1970, pp. 2200-2207.

2. Beckstead, M.W., "Combustion Calculations for Composite Solid Propellants," *13th JANNAF Combustion Meeting*, Vol. II, CPIA No. 281, 1976, pp. 299-312.

3. Felt, S.A., "Two-Dimensional Modeling of AP Composite Propellant Flame Structure with Detailed Kinetics," Ph. D. Dissertation, Department of Chemical Engineering, Brigham Young University, Provo, UT, 2004.

4. Beckstead, M. W., Puduppakkam, K. V., and Gross, M. L., "Modern Approaches to Modeling Solid Propellant Combustion," *HEMCE-07 Conference*, Chennai, India, Dec. 2007.

5. Davidson, J.E., "Combustion Modeling of RDX, HMX, and GAP with Detailed Kinetics," Ph. D. Dissertation, Department of Chemical Engineering, Brigham Young University, Provo, UT, 1997.

6. Washburn, E., "Modeling Multi-Phase Effects in the Combustion of HMX and RDX," Ph. D. Dissertation, Department of Chemical Engineering, Brigham Young University, Provo, UT, 2004.

7. Jing, Q., Beckstead, M.W., and Jeppson, M., "Influence of AP Solid Phase Decomposition on Temperature Profile and Sensitivity," *AIAA 36th Aerospace Sciences Meeting & Exhibit,* AIAA-98-0448, 1998.

8. Beckstead, M.W., Puduppakkam, K.V., and Yang, V., "Modeling and Simulation of Combustion of Solid Propellant Ingredients Using Detailed Chemical Kinetics," *49th AIAA Joint Propulsion Conference and Exhibit*, AIAA-2004-4036, 2004.

9. Jeppson, M.B., "A Kinetics model for the Premixed Combustion of a Fine AP/HTPB Composite Propellant," M.S. Thesis, Department of Chemical Engineering, Brigham Young University, Provo, UT, 1998.

10. Kee, R.J., Rupley, F.M., and Miller, J.A., "CHEMKIN-II: A FORTRAN Chemical Kinetics Package for the Analysis of Gas-Phase Chemical Kinetics," Report SAND89-8009B, Sandia National Lab, Albuquerque, NM, 1991.

11. Beckstead, M.W., Puduppakkam, K., and Yang, V., "Modeling and Simulation of Combustion of Solid Propellant Ingredients Using Detailed Chemical Kinetics," *40th AIAA Joint Propulsion Conference and Exhibit*, Ft. Lauderdale, FL, AIAA-2004-4036, July 2004.

12. Yetter, R.A., Dryer, F.L., Allen, M.T., and Gatto, J.L., "Development of Gas-Phase Reaction Mechanism for Nitramine Combustion," *Journal of Propulsion and Power*, Vol. 11, No. 4, 1995, pp. 683-697.

13. Frenklach, M., Bowman, T., Smith, G., and Gardiner, B., "GRI-MECH 3.0," [http://www.me.berkeley.edu/gri_mech/]

14. Miller, M.S. and Anderson, W.R., "Energetic-Material Combustion Modeling with Elementary Gas-Phase Reactions: a Practical Approach," *Solid Propellant Chemistry, Combustion, and Motor Interior Ballistics*, Vol. 185, 2000, pp. 501-531.

15. Lin, M.C., "M.C. Lin's Chemical Kinetics Research Group," Oct. 2002. [http://mc2.chem.emory.edu/]

16. Atwood, A.I., Boggs, T.L., Curran, P.O., Parr, T.P., Hanson-Parr, D.M., Price, C.F., and Wiknich, J., "Burning Rate of Solid Propellant Ingredients, Part1: Pressure and Initial Temperature Effects," *Journal of Propulsion and Power*, Vol. 15, No. 6, Nov-Dec 1999, pp 740-747.

17. Boggs, T.L., "Deflagration Rate, Surface Structure, and Subsurface Profile of Self-Deflagrating Single Crystals of Ammonium Perchlorate," *AIAA Journal*, Vol. 8, No. 5, 1970, pp. 867-873.

18. Boggs, T.L., Price, E.W., and Zurn, D.E. "The Deflagration of Pure and Isomorphously Doped Ammonium Perchlorate," *Proceedings of the Combustion Institute*, Vol. 13, 1971, pp. 995-1008.

19. Friedman, R., Nugent, R.G., Rumbel, K.E., and Scurlock, A.C., "Deflagration of Ammonium Perchlorate," *Proceedings of the Combustion Institute,* Vol. 6, 1956, pp. 612-618.

20. Behrens, R. and Minier, L., "The Thermal Decomposition Behavior of Ammonium Perchlorate and of an Ammonium-Perchlorate-Based Composite Propellant," *33rd JANNAF Combustion Subcommittee Meeting*, Vol. II, CPIA No. 653, 1996, pp.1-19.

21. Ermolin, N.E., Korobeinichev, O.P., Tereshchenko, A.G., and Fomin, V.M., "Measurement of the Concentration Profiles of Reacting Components and Temperature in an Ammonium Perchlorate Flame," *Combustion, Explosion, and Shock Waves*, Vol. 18, 1982, pp. 36-38.

22. Brill, T.B., Brush, P.J., and Patil, D.G., "Thermal Decomposition of Energetic Materials 60, Major Reaction Stages of a Simulated Burning Surface of NH_4CLO_4," *Combustion and Flame*, Vol. 94, 1993, pp. 70-76.

23. Kraeutle, K.J., "The Response of Ammonium Perchlorate to Thermal Stimulus," NWC TP 7053, China Lake, CA, 1990, pp. 9-42.

24. Brill, T.B., Beckstead, M.W., Flanagan, J.E., Lin, M.C., Litzinger, T.A., Waesche, R.H.W., and Wight, C.A., "Chemical Speciation and Dynamics in the Surface Combustion Zone of Energetic Materials," *Journal of Propulsion and Power*, Vol. 18, No. 4, 2002, pp. 824-834.

25. Manelis, G.B. and Strunin, V.A., "The Mechanism of Ammonium Perchlorate Burning," *Combustion and Flame*, Vol. 17, 1971, pp. 69-77.

26. Miller, M.S., "In Search of an Idealized Model of Homogeneous Solid Propellant Combustion," *Combustion and Flame*, Vol. 46, 1982, pp.51-73.

27. Merzhanov, A.G., "The Theory of Stable Homogeneous Combustion of Condensed Substances," *Combustion and Flame*, Vol. 13, No. 2, 1969, pp.143-156.

28. Guirao, C. and Williams, F.A., "A Model for Ammonium Perchlorate Deflagration between 20 and 100 atm," *AIAA Journal*, Vol. 9, No. 7, 1971, pp. 1345-1356.

29. Beckstead, M.W., Derr, R.L., and Price, C.F., "The Combustion of Solid Monopropellants and Composite Propellants," *Proceedings of the Combustion Institute*, Vol. 13, 1971, pp. 1047-1056.

30. Ermolin, N.E., Korobeinichev, O.P., Tereshchenko, A.G., and Fomin, V.M., "Kinetic Calculations and Mechanism Definitions for Reactions in an Ammonium Perchlorate Flame," *Combustion, Explosion, and Shock Waves*, Vol. 18, 1982, pp. 180-188.

31. Nahari, H.K., Mukunda, H.S., and Jain, V.K. "A Model of Combustion Monopropellants (AP) with Complex Gas Phase Kinetics," *Proceedings of the Combustion Institute*, Vol. 20, 1984, pp.2073-2082.

32. Ermolin, N.E., "Model for Chemical Reaction Kinetics in Perchloric Acid – Ammonia Flames," *Combustion, Explosion, and Shock Waves*, Vol. 31, No. 5, 1995, pp. 555-565.

33. Pak, Z., "Some Ways to Higher Environmental Safety of Solid Rocket Propellant Application," *AIAA 29th Joint Propulsion Conference and Exhibit*, AIAA-93-1755, 1993.

34. BYU DIPPR Thermophyscial Properties Laboratory, Brigham Young University, Provo, UT, 2007. [http://dippr.byu.edu]

35. Beckstead, M.W., "Modeling AN, AP, HMX, and Double Base Monopropellants," *26th JANNAF Combustion Meeting*, Vol. IV, CPIA No. 529, 1989, pp. 255-268.

36. Sinditskii, V.P., Egorshev, V.Y., Levshenkov, A.I., and Serushlin, V.V., "Combustion of Ammonium Dinitramide, part 2: Combustion Mechanism," *Journal of Propulsion and Power,* Vol. 22, No. 4, 2006, pp. 777-785.

37. Korobeinichev, O.P., Kuibida, L.V., Paletsky, A.A., and Schmakov, A.G., "Development and Application of Molecular Beam Mass-Spectrometry to the Study of ADN Combustion Chemistry," *AIAA 36th Aerospace Sciences Meeting and Exhibit*, Reno, NV, AIAA-98-0445, 1998.

38. Strunin, V.A., D'Yakov, A.P., and Manelis, G.B., "Combustion of Ammonium Dinitramide," *Combustion and Flame*, Vol. 117, 1999, pp. 429-434.

39. Fogelzang, A.E., Sinditskii, V.P., Serushkin, V.V., Egorshev, V.Y., Kolesov, V.I., and Levshenkov, A.I. "Combustion Behavior of Ammonium Dinitramide," Mendeleev Univ. of Chemical Technology, Russia, F61708-96-W0278, 1997.

40. Brill, T.B., Brush, P.J., and Patil, D.G., "Thermal Decomposition of Energetic Materials 58. Chemistry of Ammonium Nitrate and Ammonium Dinitramide Near the Burning Surface Temperature," *Combustion and Flame*, Vol. 92, 1993, pp. 178-186.

41. Wight, C.A. and Vyazovkin, S., "Kinetics and Mechanism of Thermal Decomposition of ADN," *33rd JANNAF Combustion Meeting*, Vol. II, CPIA No. 653, 1996, pp. 127-133.

42. Zenin, A.A., Puchkov, V.M., and Finjakov, S.V. "Physics of ADN Combustion,"*37th AIAA Aerospace Sciences Meeting and Exhibit*, Reno, NV, AIAA-99-0595, 1999.

43. Ostmark, H., Helte, A., Karlsson, S., Hahma, A., and Edvinsson, H., "Detonation Properties and Reaction Rate Modeling of Melt Cast Ammonium Dinitramide (ADN)," 2002. [www.intdetsymp.org/detsymp2002/PaperSubmit/FinalManuscript/pdf/Ostmark-164.pdf – Accessed 05/29/2007]

44. Velardez, G.F., Alavi, S., and Thompson, D.L., "Molecular Dynamics Studies of Melting and Liquid Properties of Ammonium Dinitramide," *Journal of Chemical Physics*, Vol. 119, No. 13, 2003, pp. 6698-6708.

45. Shmakov, A.G., Korobeinichev, O.P, and Bol'shova, T.A., "Thermal Decomposition of Ammonium Dinitramide Vapor in a Two-Temperature Flow Reactor," *Combustion, Explosion, and Shock Waves*, Vol. 38, No. 3, 2002, pp. 284-294.

46. Sinditskii, V.P., Egorshev, V.Y., Serushkin, V.V., and Levshenkov, A.I., "Chemical Peculiarities of Combustion of Solid Propellant Oxidizers," *8th International Workshop on Combustion and Propulsion*, Naples, Italy, 2002.

47. Sinditskii, V.P., Fogelzang, A.E., Levshenkov, A.I., Egorshev, V.Y., and Serushkin, V.V. "Combustion Behavior of Dinitramide Salts," *AIAA 36th Aerospace Sciences Meeting and Exhibit*, Reno, NV, AIAA-98-0808, 1998.

48. Strunin, D.R. and Manelis, G.B., "Analysis of Elementary Models for the Steady-State Combustion of Solid Propellants," *Journal of Propulsion and Power*, Vol. 11, No. 4, 1995, pp. 666-675.

49. Parr, T. P. and Hanson-Parr D. M., "The Application of Imaging Laser Induced Fluorescence to the Measurement of HMX and Aluminized Propellant Ignition and Deflagration Flame Structure", *23rd JANNAF Combustion Meeting*, Vol. I, CPIA No. 457, 1986, pp. 249-267.

50. Wight, C.A. and Vyazovkin, S., "Kinetics and Mechanism of Thermal Decomposition of ADN," *33rd JANNAF Combustion Meeting*, Vol. II, CPIA No. 653, 1996, pp. 127-133.

51. Fetherolf, B.L. and Litzinger, T.A., "Physical and Chemical Processes Governing the CO2 Laser-Induced Deflagration of Ammonium Dinitramide," *29th JANNAF Combustion Meeting*, Vol. II, CPIA No. 593, 1992, pp. 329-338.

52. Oxley, J.C., Smith, J.L., Zheng, W., Rogers, E., and Coburn, M.D., "Thermal Decomposition Studies on Ammonium Dinitramide (ADN) and 15N and 2H Isotopomers," *Journal of Physical Chemistry A,* Vol. 101, No. 31, 1997, pp. 5646-5652.

53. Vyazovkin, S. and Wight, C.A., "Ammonium Dinitramide: Kinetics and Mechanism of Thermal Decomposition," *Journal of Physical Chemistry A*, Vol. 101, 1997, pp. 5653-5658.

54. Kraeulte, K.J. and Atwood, A.I. "The Reaction of Ammonium Dinitramide Under Thermal Load," *29th JANNAF Combustion Meeting*, Vol. II, CPIA No. 593, 1993, pp. 157-170.

55. Korobeinichev, O.P, Kuibida, L.V., Paletsky, A.A., and Shmakov, A.G. "Molecular-Beam Mass-Spectrometry to Ammonium Dinitramide Combustion Chemistry Studies," *Journal of Propulsion and Power*, Vol. 14, No. 6, 1998, pp. 991-1000.

56. Russell, T.P., Stern, A.G., Koppes, W.M., and Bedford, C.D., "Thermal Decomposition and Stabilization of Ammonium Dinitramide," *29th JANNAF Combustion Meeting*, Vol. II, CPIA No. 593, 1992, pp. 339-345.

57. Fetherolf, B.L. and Litzinger, T.A., "CO2 Laser-Induced Combustion of Ammonium Dinitramide (ADN)," *Combustion and Flame*, Vol. 114, No. 3-4, 1998, pp. 515-530.

58. Sinditskii, V.P., Egorshev, V.Y., Levshenkiv, A.I., and Serushlin, V.V., "Combustion of Ammonium Dinitramide, part 1. Burning Behavior," *Journal of Propulsion and Power*, Vol. 22, No. 4, July-August 2006, pp. 769-776.

59. Feick, G., "The Dissociation Pressure and Free Energy of Formation of Ammonium Nitrate," *Nature*, Vol. 76, 1954, pp. 5858-5860.

60. Mebel, A.M., Lin, M.C., Morokuma, K., and Melius, C.F., "Theoretical Study of the Gas-Phase Structure, Thermochemistry, and Decomposition Mechanism of NH4NO2 and NH4N(NO2)2," *Journal of Physical Chemistry*, Vol. 99, 1995, pp. 6842-6848.

61. Ermolin, N.E., "Modeling of Pyrolysis of Ammonium Dinitramide Sublimation Products under Low-Pressure Conditions," *Combustion, Explosion, and Shock Wave*, Vol. 40, No. 1, 2004, pp. 92-109.

62. Ermolin, N.E., "Interim (annual) Report on the Study of the Chemical Structure of ADN Flame," 1996.

63. Park, J., Chakraborty, D., and Lin, M.C., "Thermal Decomposition of Gaseous Ammonium Dinitramide at Low Pressure: Kinetic Modeling of Product Formation with *Ab Initio* MO/cVRRKM Calculations," *27th Symposium (International) on Combustion,* The Combustion Institute, 1998, pp. 2351-2357.

64. Liau, Y.C., Yang, V., Lin, M.C., and Park, J., "Analysis of Ammonium Dinitramide (ADN) Combustion with Detailed Chemistry," *35th JANNAF Combustion Meeting*, CPIA No. 685, 1998, pp.13-30.

65. Liau, Y.C. and Yang, V., "An Improved Model of Ammonium Dinitramide (ADN) Combustion with Detailed Chemistry," *36th JANNAF Combustion Meeting*, Vol. I, CPIA No. 691, 1999, pp. 369-377.

66. Korobeinichev, O.P., Bolshova, T.A., and Paletsky, A.A., "Modeling the Chemical Reaction of Ammonium Dinitramide (ADN) in a Flame," *Combustion and Flame*, Vol. 126, 2001, pp. 1516-1523

67. Foster, R.L., Condon, J.A., and Miller, R.R., "Low Exponent Technology," Report AFRPL-TR-81-95, Hercules Inc. prepared for Air Force Rocket Propulsion Laboratory, Edwards AFB, CA, 1982.

68. Miller, R.R., Donohue, M.T., and Martin, J.R., "Control of Solids Distribution: I-Ballistics of Non-Aluminized HTPB Propellants," *12th JANNAF Combustion Meeting*, Vol. II, CPIA-No. 273, 1975, pp. 371-387.

69. Miller, R.R., Donohue, M.T., and Peterson, J.P., "Ammonium Perchlorate Size Effects on Burn Rate – Possible Modification by Binder Type," *13th JANNAF Combustion Meeting*, Vol. II, CPIA-No. 281, 1976, pp. 1-18.

70. Boggs, T.L. and Zurn, D.E., "The Deflagration of Ammonium Perchlorate-Polymeric Binder Sandwich Models," *Combustion Science and Technology*, Vol. 4, 1972, pp. 279-292.

71. Price, E.W., Handley, J.C., Panyam, R.R., Sigman, R.K., and Ghosh, A. "Combustion of Ammonium Perchlorate-Polymer Sandwiches," *AIAA Journal*, Vol. 19, No. 3, 1981, pp. 380-386.

72. Price, E.W., Sambamurthi, J.K., Sigman, R.K., and Panyam, R.R., "Combustion of Ammonium Perchlorate-Polymer Sandwiches," *Combustion and Flame*, Vol. 63, 1986, pp. 381-413.

73. Chorpening, B.T., Knott, G.M., and Brewster, M.Q., "Flame Structure and Burning Rate of Ammonium Perchlorate/Hydroxyl-Terminated Polybutadiene Propellant Sandwiches," *Proceedings of the Combustion Institute*, Vol. 28, 2000, pp. 847-853.

74. Boggs, T.L., Derr, R.L., and Beckstead, M.W., "Surface Structure of Ammonium Perchlorate Composite Propellants," *AIAA Journal*, Vol. 8, No. 2, 1970.

75. Lee, T, Kim, I., and Park, Y.K., "A Study on the Low Pressure Burning Characteristics of the Composite Propellants," *AIAA 31st Joint Propulsion Conference and Exhibit,* San Diego, CA, AIAA-95-2712, 1995.

76. Korobeinichev, O.P., Ermolin, N.E., Chernov, A.A., and Emel'yanov, I.D., "Flame Structure, Kinetics and Mechanism of Chemical Reactions in Flames of Mixed Composition Based on Ammonium Perchlorate and Polybutadiene Rubber," *Combustion, Explosion, and Shock Waves*, Vol. 28, No. 4, 1992, pp. 53-59.

77. Korobeinichev, O.P., Chernov, A.A., Emel'yanov, I.D., Ermolin, N.E., and Trofimycheva, T.V. "Investigation of the Kinetics and the Chemical Reaction Mechanism in the Flame of a Mixed Compound, Based on Ammonium Perchlorate and Polybutadiene Rubber," *Combustion, Explosion, and Shock Waves*, Vol. 26, 1990, pp.292-300.

78. Williams, F.A., *Combustion Theory*, Benjamin/Cummings, Menlo Park, CA, 1985.

79. Burke, S.P. and Schumann, T.E.W., "Diffusion Flames," *Industrial & Engineering Chemistry*, Vol. 20, No. 10, 1928, pp. 998-1004.

80. Hermance, C.E., "A Model of Composite Propellant Combustion Including Surface Heterogeneity and Heat Generation," *AIAA Journal*, Vol. 4, No. 9, 1966, pp. 1629-1637.

81. Cohen, N.S. and Strand, L.D., "An Improved Model for the Combustion of AP Composite Propellants," *AIAA Journal*, Vol. 20, No. 12, 1982, pp. 1739-1746.

82. Ermolin, N.E., "Kinetic Parameters of Overall Gas-Phase Reactions for Propellants Based on Ammonium Perchlorate and Polybutadiene Binder," *Fizika Goreniya I Vzryva*, Vol. 29, No. 4, 1993, pp. 97-104.

83. Beckstead, M.W., "A Model for Solid Propellant Combustion," *18th Symposium International on Combustion,* 1981, pp. 175-185.

84. Beckstead, M.W. "An Overview of Combustion Mechanisms and Flame Structures for Advanced Solid Propellants," 36th *AIAA Joint Propulsion Conference and Exhibit*, Huntsville, AL, AIAA-2000-3325, 2000.

85. Kishore, K., "Comprehensive View of the Combustion Models of Composite Solid Propellants," *AIAA Journal*, Vol. 17, No. 11, 1979, pp. 1216-1224.

86. Cohen, N.S. "Review of Composite Propellant Burn Rate Modeling," *AIAA Journal*, Vol. 18, No. 3, 1980, pp. 277-293.

87. Cohen, N.S. and Flanagan, D.A. "Mechanisms and Models of Solid-Propellant Burn Rate Temperature Sensitivity: A Review," *AIAA Journal*, Vol. 23, No. 10, 1985, pp. 1538-1547.

88. Strunin, V.A. and Manelis, G.B. "Analysis of Elementary Models for the Steady-State Combustion of Solid Propellants," *Journal of Propulsion and Power*, Vol. 11, No. 4, 1995, pp. 666-676.

89. Miller, R.R. "A Framework for a Totally Statistical Composite Propellant Combustion Model," *19th JANNAF Meeting*, Vol. II, CPIA No. 366, 1982, pp. 81-92.

90. Miller, R.R. and Freeman, J.M. "A Semi-Empirical Model for Plateau Propellant Burn Rates: Effects of AP Size Distribution," *36th JANNAF Meeting*, Vol. I, CPIA No. 701, 1999, pp. 355-370.

91. Tanner, M.W., Beckstead, M.W., Gross, M.L., and Davis, I.L., "Heterogeneous Propellant Combustion Modeling Using a Particle Packing Model," *40th JANNAF Combustion Meeting*, 2005.

92. Ermolin, N. E., Korbeinichev, O.P., Tereshchenko, A.G., and Fomin, V.M., "Kinetic Calculations and Mechanism Definition for Reactions in an Ammonium Perchlorate Flame," *Combustion, Explosion & Shock Waves*, Vol. 18, No. 2, 1982, pp. 61-70.

93. Ermolin, N. E., Korbeinichev, O.P., Tereshchenko, A.G., and Fomin, V.M., "Simulation of Kinetics and Chemical Reaction Mechanism of Ammonium Perchlorate Burning," *Soviet Journal of Chemistry*, Vol. 1, No. 12, 1984, pp. 2872-2883.

94. Beckstead, M. W., Tanaka, M., Jing, Q., and Jeppson, M.B., "An Ammonium Perchlorate Model Based on a Detailed Kinetic Mechanism," *33rd JANNAF Combustion Meeting*, Vol. II, CPIA # 653, 1996, pp. 21-34.

95. Jeppson, M. B., Beckstead, M. W. and Jing, Q., "A Kinetic Model for the Premixed Combustion of a Fine AP/HTPB Composite Propellant," *36th Aerospace Sciences Meeting & Exhibit*, AIAA-98-0447, 1998.

96. Tanoff, M. A., Illincic, N., et al., "Computational and Experimental Study of Ammonium Perchlorate Combustion in a Counterflow Geometry," *Proceedings of the Combustion Institute*, Vol. 27, 1998, pp. 2397-2404.

97. Smooke, M. D., Yetter, R.A., Parr, T.P., et al.., "Computational and Experimental Study of Ammonium Perchlorate/Ethylene Counterflow Diffusion Flames," *Proceedings of the Combustion Institute*, Vol. 28, 2000, pp. 2013-2020.

98. Smooke, M. D., Yetter, R.A., Parr, T.P., and Hanson-Parr, D.M., "Modeling Two-Dimensional Ammonium Perchlorate Diffusion Flames," *36th JANNAF Combustion Subcommittee Meeting*, 1999.

99. Smooke, M. D., Yetter, R.A., Parr, T.P., and Hanson-Parr, D.M., "Experimental and Modeling Studies of Two-Dimensional Ammonium Perchlorate Diffusion Flames," *Proceedings of the Combustion Institute*, Vol. 28, 2000, pp. 839-846.

100. Parr, T., Hanson-Parr, D.M., Smooke, M.D., and Yetter, R.A., "AP/Gaseous Fuel Co-Flow Diffusion Flame Studies," 36th JANNAF Combustion Subcommittee Meeting, Vol. II, CPIA #662, 1999, pp. 351-358.

101. Jackson, T.L. and Buckmaster, J., "Heterogeneous Propellant Combustion," *AIAA Journal*, Vol. 40, No. 6, 2002, pp. 1122-1130.

102. Massa, L., Jackson, T.L., Buckmaster, J., and Campbell, M., "Three-Dimensional Heterogeneous Propellant Combustion," *Proceedings of the Combustion Institute*, Vol. 29, 2002, pp. 2975-2983.

103. Massa, L., Jackson, T.L., and Short, M., "Numerical Solution of Three-Dimensional Heterogeneous Solid Propellants," *Combustion Theory and Modeling*, Vol. 7, 2003, pp. 579-602.

104. Buckmaster, J., Jackson, T. L., Yao, J., "An Elementary Discussion of Propellant Flame Geometry," *Combustion and Flame*, Vol. 117, 1999, pp. 541-552.

105. Kochevets, S., Buckmaster, J., and Jackson, T. L., "Random Propellant Packs and the Flames They Support," *36th AIAA Joint Propulsion Conference*, AIAA 2000-3461, 2000.

106. Sethian, J.A. and Smereka, P., "Level Set Methods for Fluid Interfaces," *Annual Review of Fluid Mechanics*, Vol. 35, 2003, pp. 341-372.

107. Wang, X., Jackson, T.L., and Massa, L., "Numerical Simulation of Heterogeneous Propellant Combustion by a Level Set Method," *Combustion Theory and Modeling*, Vol. 8, 2004, pp. 227-254.

108. International Union of Pure and Applied Chemistry, "IUPAC Subcommittee for Gas Kinetic Data Evaluation," June 2006. [http://www.iupac-kinetic.ch.cam.ac.uk/]

109. National Institute of Standards and Technology, Standard Reference Database 17, Version 7.0, Release 1.4, 2000. [http://kinetics.nist.gov/]

110. Whittaker, A.G. and Barham, D.C., "Surface Temperature Measurements on Burning Solids," *Journal of Physical Chemistry*, Vol. 86, No. 1, 1964, pp.196-199.

111. Kee, R.J., M.E. Coltrin, and P. Glarborg, *Chemically Reacting Flow: Theory & Practice*, Wiley-Interscience: A John Wiley & Sons Publication, Hoboken, NJ, 2003.

112. Keshtiban, I.J., Belblidia, F., and Webster, M.F., "Compressible Flow Solvers for Low Mach Number Flows – a review," Institute of Non-Newtonian Fluid Mechanics, University of Wales, UK, 2004. [http://www.cs.swan.ac.uk/reports/yr2004/CSR2-2004.pdf]

113. Oran, E.S. and J.P. Boris, *Numerical Simulation of Reactive Flow*, Cambridge University Press, Cambridge, United Kingdom, 2001.

114. Patankar, S.V., *Numerical Heat Transfer and Fluid Flow*, Taylor & Fracis, Bristol, PA, 1980.

115. Smooke, M.D., R.E. Mitchell, and D.E. Keyes, "Numerical Solution of Two-Dimensional Axisymmetric Laminar Diffusion Flames," *Combustion Science and Technology*, Vol. 67, 1989, pp. 85-122.

116. Cottet, G, and P.D. Koumoutsakos, *Vortex Methods: Theory and Practice*, Cambridge University Press, Cambridge, UK, 2000.

117. Hoffman, K.A., and Chiang, S.T., *Computational Fluid Dynamics for Engineers – Volume I*, Engineering Education System, Wichita, KS,1995.

118. Bennett, B.A.V and M.D. Smooke, "Local Rectangular Refinement with Application to Axisymmetric Laminar Flames," *Combustion Theory Modeling,* Vol. 2, No. 3, 1998, pp. 221-258.

119. Dworkin, S.B., B.A.V. Bennett, and M.D. Smooke, "A Mass-Conserving Vorticity-Velocity Formulation with Application to Nonreacting and Reacting Flows," *Journal of Computational Physics*, Vol. 215, 2006, pp.430-447.

120. Pozrikidis, C., *Introduction to Theoretical and Computational Fluid Dynamics*, Oxford University Press, New York, NY, 1997.

121. Kuo, K.K., *Principles of Combustion*, John Wiley & Sons, Hoboken, NJ, 2005.

122. Kee, R.J., D. Dixon-Lewis, J. Warnatz, M.E. Coltrin, and J.A. Miller, "A Fortran Computer Code Package for the Evaluation of Gas-Phase Mulitcomponent Transport Properties," SAND86-8246, Sandia National Laboratories, Albuquerque, NM, 1992.

123. Coffee, T.P. and T.G. Heimerl, "Transport Algorithms for Premised Laminar, Steady-State Flames," *Combustion and Flame*, Vol. 43, 1981, pp 273.

124. Balay, S, Buschelman, K., Eijkhout, V., et al. "PETSc Users Manual," ANL-95/11 - Revision 2.2.1, Argonne National Laboratory, 2004. [http://www.mcs.anl.gov/petsc/]

125. Bird, R., Stewart, W, and Lightfoot, E., *Transport Phenomena*, John Wiley & Sons, New York, NY, 2002.

126. Kee, R.J., Grcar, J.F., Smooke, M.D., and Miller, J.A., "A Fortran Program for Modeling Steady Laminar One-Dimensional Premixed Flames," Sandia Report, SAND85-8240, Albuquerque, NM, 1992.

127. Wang, H., Sung, C. J. and Law, C. K., "On Mild and Vigorous Oxidation of Mixtures of Chlorinated Hydrocarbons in Droplet Burning," *Combustion and Flame*, No. 110, 1997, pp 222-238.

128. Miller, R. R. and Foster R. L., "The Influence of the Fine AP/Binder Matrix on Composite Propellant Ballistic Properties," *17th JANNAF Combustion Meeting*, Vol. III, CPIA #329, 1980, pp. 91-104.

129. Korobeinichev, O.P, Tereschenko, A.G., et al., "A Study of Flame Structure of Sandwich Systems Based on Ammonium Perchlorate, HMX, and Polybutadiene Binder," *Flame Structure*, Vol. 1(Nauka, Novosibirsk), 1991, pp. 262-267.

130. Price, E.W., Handley, J.C., Panyam, R.R., Sigman, R.K., and Ghosh, A., "Combustion of Ammonium Perchlorate-Polymer Sandwiches," *AIAA Journal*, Vol. 19, No. 3, 1981, pp. 380-386.

131. Miller, R.R., Donohue, M.T., and Martin, J.R., "Control of Solids Distribution 1 – Ballistics of Non-Aluminized HTPB Propellants," *12th JANAF Meeting*, Vol. II, CPIA # 273, 1975, pp. 371-387.

Appendix A. Universal Gas-Phase Mechanism

The following is the universal gas-phase mechanism including the Puduppakkam comprehensive mechanism, Lin's Cl-containing reactions, and the 12 additional reactions outlined in Chapter 3 added to model AP monopropellant combustion.

```
CHEMKIN INTERPRETER OUTPUT: CHEMKIN-II Version 3.1 Feb. 1993
                            DOUBLEPRECISION

                           --------------------
                           ELEMENTS     ATOMIC
                           CONSIDERED   WEIGHT
                           --------------------
                            1. AR      39.9480
                            2. C       12.0112
                            3. H       1.00797
                            4. N       14.0067
                            5. O       15.9994
                            6. CL      35.4530
                           --------------------

-------------------------------------------------------------------------------
                         C
                       P H
                       H A
                       A R
SPECIES                S G MOLECULAR TEMPERATURE   ELEMENT COUNT
CONSIDERED             E E WEIGHT    LOW    HIGH   AR C  H  N  O  CL
-------------------------------------------------------------------------------
  1. AR                G 0  39.94800  300.0 5000.0  1  0  0  0  0  0
  2. H2                G 0   2.01594  300.0 5000.0  0  0  2  0  0  0
  3. O2                G 0  31.99880  300.0 5000.0  0  0  0  0  2  0
  4. H2O               G 0  18.01534  300.0 5000.0  0  0  2  0  1  0
  5. O                 G 0  15.99940  300.0 5000.0  0  0  0  0  1  0
  6. HNOH              G 0  32.02204  300.0 4000.0  0  0  2  1  1  0
  7. H                 G 0   1.00797  300.0 5000.0  0  0  1  0  0  0
  8. OH                G 0  17.00737  300.0 5000.0  0  0  1  0  1  0
  9. HO2               G 0  33.00677  200.0 3500.0  0  0  1  0  2  0
 10. H2O2              G 0  34.01474  300.0 5000.0  0  0  2  0  2  0
 11. CH2O              G 0  30.02649  300.0 5000.0  0  1  2  0  1  0
 12. HCO               G 0  29.01852  300.0 5000.0  0  1  1  0  1  0
 13. CO                G 0  28.01055  300.0 5000.0  0  1  0  0  1  0
 14. CO2               G 0  44.00995  300.0 5000.0  0  1  0  0  2  0
 15. N                 G 0  14.00670  200.0 6000.0  0  0  0  1  0  0
 16. N2                G 0  28.01340  300.0 5000.0  0  0  0  2  0  0
 17. NO                G 0  30.00610  200.0 6000.0  0  0  0  1  1  0
 18. NO2               G 0  46.00550  200.0 6000.0  0  0  0  1  2  0
```

19. NH	G	0	15.01467	200.0	6000.0	0	0	1	1	0	0
20. NH2	G	0	16.02264	200.0	6000.0	0	0	2	1	0	0
21. NH3	G	0	17.03061	200.0	6000.0	0	0	3	1	0	0
22. NNH	G	0	29.02137	200.0	6000.0	0	0	1	2	0	0
23. HNO	G	0	31.01407	200.0	6000.0	0	0	1	1	1	0
24. HONO	G	0	47.01347	300.0	5000.0	0	0	1	1	2	0
25. HCN	G	0	27.02582	200.0	6000.0	0	1	1	1	0	0
26. N2O	G	0	44.01280	200.0	6000.0	0	0	0	2	1	0
27. CN	G	0	26.01785	200.0	6000.0	0	1	0	1	0	0
28. C2N2	G	0	52.03570	300.0	5000.0	0	2	0	2	0	0
29. NCN	G	0	40.02455	300.0	4000.0	0	1	0	2	0	0
30. NCO	G	0	42.01725	200.0	6000.0	0	1	0	1	1	0
31. CNO	G	0	42.01725	300.0	4000.0	0	1	0	1	1	0
32. HNCO	G	0	43.02522	300.0	5000.0	0	1	1	1	1	0
33. HOCN	G	0	43.02522	300.0	5000.0	0	1	1	1	1	0
34. HCNO	G	0	43.02522	300.0	5000.0	0	1	1	1	1	0
35. NO3	G	0	62.00490	300.0	5000.0	0	0	0	1	3	0
36. HNO3	G	0	63.01287	300.0	5000.0	0	0	1	1	3	0
37. H2CN	G	0	28.03379	300.0	4000.0	0	1	2	1	0	0
38. H2CNH	G	0	29.04176	300.0	4000.0	0	1	3	1	0	0
39. H2CNO	G	0	44.03319	300.0	4000.0	0	1	2	1	1	0
40. H2CNNO	G	0	58.03989	300.0	4000.0	0	1	2	2	1	0
41. H2CNNO2	G	0	74.03929	300.0	4000.0	0	1	2	2	2	0
42. RDX	G	0	222.11787	300.0	4000.0	0	3	6	6	6	0
43. RDXR	G	0	176.11237	300.0	4000.0	0	3	6	5	4	0
44. RDXRO	G	0	176.11237	300.0	4000.0	0	3	6	5	4	0
45. HNC	G	0	27.02582	300.0	5000.0	0	1	1	1	0	0
46. H2COHNNO2	G	0	91.04666	300.0	4000.0	0	1	3	2	3	0
47. C	G	0	12.01115	300.0	5000.0	0	1	0	0	0	0
48. CH	G	0	13.01912	300.0	5000.0	0	1	1	0	0	0
49. CH2	G	0	14.02709	250.0	4000.0	0	1	2	0	0	0
50. CH2(S)	G	0	14.02709	300.0	4000.0	0	1	2	0	0	0
51. CH3	G	0	15.03506	300.0	5000.0	0	1	3	0	0	0
52. CH4	G	0	16.04303	300.0	5000.0	0	1	4	0	0	0
53. CH2OH	G	0	31.03446	250.0	4000.0	0	1	3	0	1	0
54. CH3O	G	0	31.03446	300.0	3000.0	0	1	3	0	1	0
55. CH3OH	G	0	32.04243	300.0	5000.0	0	1	4	0	1	0
56. C2H3	G	0	27.04621	300.0	5000.0	0	2	3	0	0	0
57. C2H2	G	0	26.03824	300.0	5000.0	0	2	2	0	0	0
58. C2H	G	0	25.03027	300.0	5000.0	0	2	1	0	0	0
59. C2H4	G	0	28.05418	300.0	5000.0	0	2	4	0	0	0
60. C2H5	G	0	29.06215	300.0	5000.0	0	2	5	0	0	0
61. C2H6	G	0	30.07012	300.0	4000.0	0	2	6	0	0	0
62. HCCO	G	0	41.02967	300.0	4000.0	0	2	1	0	1	0
63. CH2CO	G	0	42.03764	300.0	5000.0	0	2	2	0	1	0
64. HCCOH	G	0	42.03764	300.0	4000.0	0	2	2	0	1	0
65. HCNN	G	0	41.03252	300.0	5000.0	0	1	1	2	0	0
66. C3H7	G	0	43.08924	300.0	5000.0	0	3	7	0	0	0
67. C3H8	G	0	44.09721	300.0	5000.0	0	3	8	0	0	0
68. CH2CHO	G	0	43.04561	300.0	5000.0	0	2	3	0	1	0
69. CH3CHO	G	0	44.05358	200.0	6000.0	0	2	4	0	1	0
70. C(S)	S	0	12.01115	300.0	5000.0	0	1	0	0	0	0
71. C4H6	G	0	54.09242	300.0	5000.0	0	4	6	0	0	0
72. N2H2	G	0	30.02934	300.0	5000.0	0	0	2	2	0	0
73. N2H3	G	0	31.03731	300.0	5000.0	0	0	3	2	0	0
74. N2H4	G	0	32.04528	300.0	5000.0	0	0	4	2	0	0
75. BTTN	G	0	241.11509	200.0	6000.0	0	4	7	3	9	0
76. HOCO	G	0	45.01792	300.0	4000.0	0	1	1	0	2	0
77. HNNO	G	0	45.02077	300.0	4000.0	0	0	1	2	1	0
78. ADN(G)	G	0	124.05628	300.0	5000.0	0	0	4	4	4	0
79. HN3O4	G	0	107.02567	300.0	5000.0	0	0	1	3	4	0
80. HNNO2	G	0	61.02017	300.0	5000.0	0	0	1	2	2	0
81. H2NNO	G	0	46.02874	300.0	4000.0	0	0	2	2	1	0

```
 82. H2NO             G 0  32.02204  300.0 4000.0  0  0  2  1  1  0
 83. HNNH             G 0  30.02934  300.0 6000.0  0  0  2  2  0  0
 84. H2NOH            G 0  33.03001  300.0 4000.0  0  0  3  1  1  0
 85. CLO              G 0  51.45240  300.0 5000.0  0  0  0  0  1  1
 86. CLO2             G 0  67.45180  300.0 5000.0  0  0  0  0  2  1
 87. CLO3             G 0  83.45120  300.0 4000.0  0  0  0  0  3  1
 88. CLO4             G 0  99.45060  300.0 4000.0  0  0  0  0  4  1
 89. CL               G 0  35.45300  300.0 5000.0  0  0  0  0  0  1
 90. CLOH             G 0  52.46037  300.0 5000.0  0  0  1  0  1  1
 91. HCL              G 0  36.46097  300.0 5000.0  0  0  1  0  0  1
 92. HCLO4            G 0 100.45857  300.0 4000.0  0  0  1  0  4  1
 93. NOCL             G 0  65.45910  300.0 5000.0  0  0  0  1  1  1
 94. CL2              G 0  70.90600  300.0 5000.0  0  0  0  0  0  2
 95. CLOO             G 0  67.45180  300.0 4000.0  0  0  0  0  2  1
 96. CL2O             G 0  86.90540  300.0 5000.0  0  0  0  0  1  2
 97. HCLO2            G 0  68.45977  300.0 4000.0  0  0  1  0  2  1
 98. HCLO3            G 0  84.45917  300.0 4000.0  0  0  1  0  3  1
 99. HOOCLO2          G 0 100.45857  300.0 4000.0  0  0  1  0  4  1
100. CLNO2            G 0  81.45850  300.0 5000.0  0  0  0  1  2  1
101. CLONO2           G 0  97.45790  300.0 5000.0  0  0  0  1  3  1
102. CLOCL            G 0  86.90540  300.0 5000.0  0  0  0  0  1  2
103. CLOOCL           G 0 102.90480  300.0 5000.0  0  0  0  0  2  2
104. CLOCLO           G 0 102.90480  300.0 5000.0  0  0  0  0  2  2
105. CLOCLOO          G 0 118.90420  300.0 5000.0  0  0  0  0  3  2
106. O3               G 0  47.99820  300.0 5000.0  0  0  0  0  3  0
--------------------------------------------------------------------------------
```

```
                                                        (k = A T**b exp(-E/RT))
   REACTIONS CONSIDERED                                   A        b        E

  1. H2+M=H+H+M                                      4.57E+19   -1.4   104000.0
       H2              Enhanced by    2.500E+00
       H2O             Enhanced by    1.200E+01
       CO              Enhanced by    1.900E+00
       CO2             Enhanced by    3.800E+00
  2. O+H2O=OH+OH                                     2.97E+06    2.0    13400.0
  3. O+H2=H+OH                                       5.06E+04    2.7     6290.0
  4. O+O+M=O2+M                                      6.17E+15   -0.5     0.0
       H2              Enhanced by    2.500E+00
       H2O             Enhanced by    1.200E+01
       CO              Enhanced by    1.900E+00
       CO2             Enhanced by    3.800E+00
  5. H+O2=O+OH                                       1.94E+14    0.0    16440.0
  6. H+O2(+M)=HO2(+M)                                4.52E+13    0.0        0.0
     Low pressure limit:  0.67000E+20 -0.14200E+01  0.00000E+00
     TROE centering:      0.10000E+01  0.10000E-89  0.10000E+91
       H2              Enhanced by    2.500E+00
       H2O             Enhanced by    1.200E+01
       CO              Enhanced by    1.900E+00
       CO2             Enhanced by    3.800E+00
  7. H+O+M=OH+M                                      4.72E+18   -1.0        0.0
       H2              Enhanced by    2.500E+00
       H2O             Enhanced by    1.200E+01
       CO              Enhanced by    1.900E+00
       CO2             Enhanced by    3.800E+00
  8. OH+H2=H2O+H                                     2.16E+08    1.5     3430.0
  9. OH+H+M=H2O+M                                    2.21E+22   -2.0        0.0
       H2              Enhanced by    2.500E+00
       H2O             Enhanced by    1.200E+01
       CO              Enhanced by    1.900E+00
       CO2             Enhanced by    3.800E+00
```

```
10. HO2+O=O2+OH                                   1.75E+13    0.0     -397.0
11. HO2+H=H2+O2                                   6.62E+13    0.0     2130.0
12. HO2+H=OH+OH                                   1.69E+14    0.0      874.0
13. HO2+OH=H2O+O2                                 1.90E+16   -1.0        0.0
14. HO2+HO2=H2O2+O2                               4.20E+14    0.0    11980.0
    Declared duplicate reaction...
15. HO2+HO2=H2O2+O2                               1.30E+11    0.0    -1629.0
    Declared duplicate reaction...
16. H2O2(+M)=OH+OH(+M)                            2.95E+14    0.0    48460.0
    Low pressure limit:  0.12000E+18  0.00000E+00  0.45500E+05
    TROE centering:      0.50000E+00  0.10000E-89  0.10000E+91
17. H2O2+O=OH+HO2                                 9.64E+06    2.0     3970.0
18. H2O2+H=H2O+OH                                 1.00E+13    0.0     3590.0
19. H2O2+H=HO2+H2                                 4.82E+13    0.0     7950.0
20. H2O2+OH=H2O+HO2                               1.00E+12    0.0        0.0
    Declared duplicate reaction...
21. H2O2+OH=H2O+HO2                               5.80E+14    0.0     9557.0
    Declared duplicate reaction...
22. CH2O+O2=HCO+HO2                               2.05E+13    0.0    38920.0
23. CH2O+O=HCO+OH                                 1.81E+13    0.0     3078.0
24. CH2O+H=HCO+H2                                 1.26E+08    1.6     2163.0
25. CH2O+OH=HCO+H2O                               3.43E+09    1.2     -447.0
26. CH2O+HO2=HCO+H2O2                             1.99E+12    0.0    11660.0
27. HCO+M=H+CO+M                                  1.85E+17   -1.0    17000.0
       H2               Enhanced by    1.890E+00
       H2O              Enhanced by    1.200E+01
       CO               Enhanced by    1.900E+00
       CO2              Enhanced by    3.800E+00
28. HCO+O2=CO+HO2                                 7.58E+12    0.0      406.0
29. HCO+O=CO+OH                                   3.00E+13    0.0        0.0
30. HCO+O=CO2+H                                   3.00E+13    0.0        0.0
31. HCO+H=CO+H2                                   7.23E+13    0.0        0.0
32. HCO+OH=CO+H2O                                 3.00E+13    0.0        0.0
33. HCO+HO2=CO2+OH+H                              3.00E+13    0.0        0.0
34. CO+O(+M)=CO2(+M)                              1.80E+10    0.0     2380.0
    Low pressure limit:  0.13500E+25 -0.27880E+01  0.41910E+04
    TROE centering:      0.10000E+01  0.10000E-89  0.10000E+91
       N2               Enhanced by    1.330E+00
       H2               Enhanced by    2.500E+00
       H2O              Enhanced by    1.200E+01
       CO               Enhanced by    1.900E+00
       CO2              Enhanced by    3.800E+00
35. CO+O2=CO2+O                                   2.53E+12    0.0    47700.0
36. CO+OH=CO2+H                                   1.50E+07    1.3     -765.0
37. CO+HO2=CO2+OH                                 5.80E+13    0.0    22930.0
38. N+H2=H+NH                                     1.60E+14    0.0    25140.0
39. N+O2=NO+O                                     6.40E+09    1.0     6280.0
40. N+OH=NO+H                                     3.80E+13    0.0        0.0
41. N+HO2=NH+O2                                   1.00E+13    0.0     2000.0
42. N+HO2=NO+OH                                   1.00E+13    0.0     2000.0
43. N+NO=N2+O                                     3.27E+12    0.3        0.0
44. N+NO2=NO+NO                                   4.00E+12    0.0        0.0
45. N+NO2=N2O+O                                   5.00E+12    0.0        0.0
46. N+NO2=N2+O2                                   1.00E+12    0.0        0.0
47. N+HNO=NH+NO                                   1.00E+13    0.0     2000.0
48. N+HNO=N2O+H                                   5.00E+10    0.5     3000.0
49. N+N2O=N2+NO                                   1.00E+13    0.0    19870.0
50. NO+M=N+O+M                                    9.64E+14    0.0   148400.0
       N2               Enhanced by    1.500E+00
       CO2              Enhanced by    2.500E+00
51. NO+O(+M)=NO2(+M)                              1.30E+15   -0.8        0.0
    Low pressure limit:  0.47200E+25 -0.28700E+01  0.15510E+04
    TROE centering:      0.95700E+00  0.10000E-89  0.83320E+04
```

```
 52. NO+H(+M)=HNO(+M)                                1.52E+15   -0.4        0.0
     Low pressure limit:  0.89600E+20 -0.13200E+01  0.73520E+03
     TROE centering:      0.82000E+00  0.10000E-89  0.10000E+91
 53. NO+OH(+M)=HONO(+M)                              1.99E+12   -0.1     -721.0
     Low pressure limit:  0.50800E+24 -0.25100E+01 -0.67560E+02
     TROE centering:      0.62000E+00  0.10000E-89  0.10000E+91
        H2O              Enhanced by    5.000E+00
 54. HO2+NO=NO2+OH                                   2.11E+12    0.0     -479.0
 55. NO+HCO=HNO+CO                                   7.23E+12    0.0        0.0
 56. NO2+O=O2+NO                                     3.91E+12    0.0     -238.0
 57. NO2+O(+M)=NO3(+M)                               1.33E+13    0.0        0.0
     Low pressure limit:  0.14900E+29 -0.40800E+01  0.24670E+04
     TROE centering:      0.82600E+00  0.10000E-89  0.31910E+04
 58. NO2+H=NO+OH                                     1.32E+14    0.0      361.6
 59. NO2+OH(+M)=HNO3(+M)                             2.41E+13    0.0        0.0
     Low pressure limit:  0.64200E+33 -0.54900E+01  0.23500E+04
     TROE centering:      0.83700E+00  0.10000E-89  0.16570E+04
 60. NO2+HCO=CO+HONO                                 1.24E+23   -3.3     2354.0
 61. NO2+HCO=H+CO2+NO                                8.39E+15   -0.8     1927.0
 62. NO2+CO=CO2+NO                                   9.03E+13    0.0    33780.0
 63. NO2+NO2=NO3+NO                                  9.64E+09    0.7    20920.0
 64. NO2+NO2=2NO+O2                                  1.63E+12    0.0    26120.0
 65. NH+M=N+H+M                                      2.65E+14    0.0    75510.0
 66. NH+O2=HNO+O                                     3.89E+13    0.0    17890.0
 67. NH+O2=NO+OH                                     7.60E+10    0.0     1530.0
 68. NH+O=NO+H                                       5.50E+13    0.0        0.0
 69. NH+O=N+OH                                       3.72E+13    0.0        0.0
 70. NH+OH=HNO+H                                     2.00E+13    0.0        0.0
 71. NH+OH=N+H2O                                     5.00E+11    0.5     2000.0
 72. NH+N=N2+H                                       3.00E+13    0.0        0.0
 73. NH+NO=N2O+H                                     2.94E+14   -0.4        0.0
     Declared duplicate reaction...
 74. NH+NO=N2O+H                                     ********   -0.2        0.0
     Declared duplicate reaction...
 75. NH+NO=N2+OH                                     2.16E+13   -0.2        0.0
 76. NH+NO2=NO+HNO                                   1.00E+11    0.5     4000.0
 77. NH+NO2=N2O+OH                                   1.00E+13    0.0        0.0
 78. NH+NH=N2+H+H                                    5.10E+13    0.0        0.0
 79. NH2+O2=HNO+OH                                   1.78E+12    0.0    14900.0
 80. NH2+O=HNO+H                                     6.63E+14   -0.5        0.0
 81. NH2+O=NH+OH                                     6.75E+12    0.0        0.0
 82. NH2+H=NH+H2                                     6.92E+13    0.0     3650.0
 83. NH2+OH=NH+H2O                                   4.00E+06    2.0     1000.0
 84. NH2+N=N2+2H                                     7.20E+13    0.0        0.0
 85. NH2+NO=NNH+OH                                   2.80E+13   -0.6        0.0
 86. NH2+NO=N2+H2O                                   1.30E+16   -1.2        0.0
     Declared duplicate reaction...
 87. NH2+NO=N2+H2O                                   ********   -0.6        0.0
     Declared duplicate reaction...
 88. NH2+NO=N2O+H2                                   5.00E+13    0.0    24640.0
 89. NH2+NO=HNO+NH                                   1.00E+13    0.0    40000.0
 90. NH2+NO2=N2O+H2O                                 3.28E+18   -2.2        0.0
 91. NH3+M=NH2+H+M                                   2.20E+16    0.0    93470.0
 92. NH3+O=NH2+OH                                    9.40E+06    1.9     6460.0
 93. NH3+H=NH2+H2                                    6.40E+05    2.4    10170.0
 94. NH3+OH=NH2+H2O                                  2.04E+06    2.0      566.0
 95. NH3+HO2=NH2+H2O2                                3.00E+11    0.0    22000.0
 96. NH2+HO2=NH3+O2                                  1.00E+13    0.0        0.0
 97. NH2+NH2=NH3+NH                                  5.00E+13    0.0    10000.0
 98. NNH+M=N2+H+M                                    1.00E+14    0.0     3000.0
 99. NNH+O=N2O+H                                     1.00E+14    0.0        0.0
100. NNH+H=N2+H2                                     1.00E+14    0.0        0.0
101. NNH+OH=N2+H2O                                   5.00E+13    0.0        0.0
```

```
102. NNH+NO=N2+HNO                                    5.00E+13    0.0        0.0
103. NNH+NH=N2+NH2                                    5.00E+13    0.0        0.0
104. NNH+NH2=N2+NH3                                   5.00E+13    0.0        0.0
105. HNO+O2=NO+HO2                                    1.00E+13    0.0    25000.0
106. HNO+O=OH+NO                                      1.81E+13    0.0        0.0
107. HNO+H=H2+NO                                      1.81E+13    0.0      993.5
108. HNO+OH=H2O+NO                                    1.00E+13    0.0      993.5
109. HNO+NO=N2O+OH                                    2.00E+12    0.0    26000.0
110. HNO+NO2=HONO+NO                                  6.02E+11    0.0     1987.0
111. HNO+NH2=NO+NH3                                   2.00E+13    0.0     1000.0
112. HNO+HNO=H2O+N2O                                  8.51E+08    0.0     3080.0
113. HONO+O=OH+NO2                                    1.20E+13    0.0     5961.0
114. HONO+H=H2+NO2                                    1.20E+13    0.0     7352.0
115. HONO+OH=H2O+NO2                                  1.26E+10    1.0      135.1
116. HCN(+M)=H+CN(+M)                                 8.30E+17   -0.9   123800.0
     Low pressure limit:  0.35700E+27 -0.26000E+01  0.12490E+06
     TROE centering:      0.95700E+00  0.10000E-89  0.83320E+04
117. HCN+O=CN+OH                                      2.70E+09    1.6    29200.0
118. HCN+O=NH+CO                                      3.45E+03    2.6     4980.0
119. HCN+O=NCO+H                                      1.38E+04    2.6     4980.0
120. HCN+OH=H2O+CN                                    3.90E+06    1.8    10290.0
121. HCN+OH=H+HOCN                                    5.85E+04    2.4    12500.0
122. HCN+OH=H+HNCO                                    1.98E-03    4.0     1000.0
123. HCN+OH=NH2+CO                                    7.83E-04    4.0     4000.0
124. HCN=HNC                                          2.06E+14   -1.1    43710.0
125. HNC+O=NH+CO                                      2.89E+12    0.0        0.0
126. HNC+O=H+NCO                                      1.60E+01    3.1     -224.0
127. HNC+OH=HNCO+H                                    2.80E+13    0.0     3700.0
128. HNC+OH=CN+H2O                                    1.50E+12    0.0     7680.0
129. HNC+NO2=HNCO+NO                                  1.00E+12    0.0    32000.0
130. HNC+CN=C2N2+H                                    1.00E+13    0.0        0.0
131. N2O(+M)=N2+O(+M)                                 7.91E+10    0.0    56020.0
     Low pressure limit:  0.91300E+15  0.00000E+00  0.57690E+05
        H2O              Enhanced by    7.500E+00
        NO               Enhanced by    2.000E+00
        CO               Enhanced by    2.000E+00
        CO2              Enhanced by    3.000E+00
        HCN              Enhanced by    3.000E+00
132. N2O+O=O2+N2                                      1.00E+14    0.0    28000.0
133. N2O+O=2NO                                        1.00E+14    0.0    28000.0
134. N2O+H=N2+OH                                      2.53E+10    0.0     4550.0
     Declared duplicate reaction...
135. N2O+H=N2+OH                                      2.23E+14    0.0    16750.0
     Declared duplicate reaction...
136. N2O+OH=HO2+N2                                    2.00E+12    0.0    40000.0
137. N2O+CO=N2+CO2                                    5.01E+13    0.0    44000.0
138. CN+H2=H+HCN                                      5.50E+02    3.2     -223.0
139. CN+O2=NCO+O                                      7.50E+12    0.0     -389.0
140. CN+O=CO+N                                        1.80E+13    0.0        0.0
141. CN+OH=NCO+H                                      4.22E+13    0.0        0.0
142. CN+CH2O=HCN+HCO                                  4.22E+13    0.0        0.0
143. CN+HCO=HCN+CO                                    6.02E+13    0.0        0.0
144. CN+CO2=CO+NCO                                    3.67E+06    2.2    26900.0
145. CN+NO=NCO+N                                      9.64E+13    0.0    42120.0
146. CN+NO2=NCO+NO                                    1.59E+13    0.0    -1133.0
147. CN+HNO=HCN+NO                                    1.81E+13    0.0        0.0
148. CN+HONO=HCN+NO2                                  1.20E+13    0.0        0.0
149. CN+HCN=H+C2N2                                    1.21E+07    1.7     1530.0
150. CN+N2O=NCN+NO                                    3.85E+03    2.6     3696.0
151. CN+CN(+M)=C2N2(+M)                               5.66E+12    0.0        0.0
     Low pressure limit:  0.34200E+26 -0.26100E+01  0.00000E+00
     TROE centering:      0.50000E+00  0.10000E-89  0.10000E+91
152. C2N2+O=NCO+CN                                    4.57E+12    0.0     8880.0
```

```
153. C2N2+OH=HOCN+CN                                  1.86E+11    0.0     2900.0
154. NCN+O2=NO+NCO                                    1.00E+14    0.0        0.0
155. NCN+O=CN+NO                                      1.00E+14    0.0        0.0
156. NCN+H=HCN+N                                      1.00E+14    0.0        0.0
157. NCN+OH=HCN+NO                                    5.00E+13    0.0        0.0
158. NCO+M=N+CO+M                                     3.10E+16   -0.5    48300.0
       N2               Enhanced by    1.500E+00
159. NCO+H2=HNCO+H                                    7.60E+02    3.0     4000.0
160. NCO+O2=NO+CO2                                    2.00E+12    0.0    20000.0
161. NCO+O=CO+NO                                      2.00E+13    0.0        0.0
162. NCO+H=NH+CO                                      5.36E+13    0.0        0.0
163. NCO+OH=NO+CO+H                                   1.00E+13    0.0        0.0
164. NCO+OH=NO+HCO                                    5.00E+12    0.0    15000.0
165. NCO+CH2O=HNCO+HCO                                6.02E+12    0.0        0.0
166. NCO+HCO=HNCO+CO                                  3.61E+13    0.0        0.0
167. NCO+N=N2+CO                                      2.00E+13    0.0        0.0
168. NCO+NO=N2O+CO                                    6.20E+17   -1.7      763.0
169. NCO+NO=CO2+N2                                    7.80E+17   -1.7      763.0
170. NCO+NO2=CO+2NO                                   1.39E+13    0.0        0.0
171. NCO+NO2=CO2+N2O                                  4.17E+12    0.0        0.0
172. NCO+HNO=HNCO+NO                                  1.81E+13    0.0        0.0
173. NCO+HONO=HNCO+NO2                                3.61E+12    0.0        0.0
174. NCO+N2O=N2+NO+CO                                 9.03E+13    0.0    27820.0
175. NCO+CN=NCN+CO                                    1.81E+13    0.0        0.0
176. NCO+NCO=N2+2CO                                   1.00E+13    0.0        0.0
177. CNO+O=CO+NO                                      1.00E+13    0.0        0.0
178. CNO+NO2=CO+2NO                                   1.00E+13    0.0        0.0
179. CNO+N2O=N2+CO+NO                                 1.00E+12    0.0    15000.0
180. HNCO(+M)=NH+CO(+M)                               6.00E+13    0.0    99800.0
     Low pressure limit:  0.21700E+29 -0.31000E+01  0.10190E+06
     TROE centering:      0.93800E+00  0.10000E-89  0.33040E+04
181. HNCO+O2=HNO+CO2                                  1.00E+12    0.0    35000.0
182. HNCO+O=CO2+NH                                    9.64E+07    1.4     8524.0
183. HNCO+O=OH+NCO                                    6.67E-04    4.5     1780.0
184. HNCO+O=HNO+CO                                    1.58E+08    1.6    44300.0
185. HNCO+H=NH2+CO                                    2.20E+07    1.7     3800.0
186. HNCO+OH=H2O+NCO                                  6.38E+05    2.0     2563.0
187. HNCO+HO2=NCO+H2O2                                3.00E+11    0.0    29000.0
188. HNCO+NH=NH2+NCO                                  3.00E+13    0.0    23700.0
189. HNCO+NH2=NH3+NCO                                 5.00E+12    0.0     6200.0
190. HNCO+CN=HCN+NCO                                  1.51E+13    0.0        0.0
191. HCNO+O=HCO+NO                                    1.00E+12    0.0     9000.0
192. HCNO+OH=HCO+HNO                                  1.00E+13    0.0     5000.0
193. HCNO+OH=CNO+H2O                                  1.00E+12    0.0     2000.0
194. HCNO+CN=HCN+CNO                                  1.00E+12    0.0     2000.0
195. HOCN+O=NCO+OH                                    1.50E+04    2.6     4000.0
196. HOCN+H=HNCO+H                                    2.00E+07    2.0     2000.0
197. HOCN+OH=NCO+H2O                                  6.40E+05    2.0     2560.0
198. H2CN+M=HCN+H+M                                   5.30E+16    0.0    29000.0
199. H2CN+CH2O=H2CNH+HCO                              1.00E+11    0.0    14000.0
200. H2CN+NO=HCN+HNO                                  1.00E+11    0.0     3000.0
201. H2CN+NO2=HCN+HONO                                1.00E+11    0.0     1000.0
202. H2CN+NO2=H2CNO+NO                                1.00E+11    0.0     3000.0
203. H2CN+HNO=H2CNH+NO                                1.00E+11    0.0     4000.0
204. H2CN+HONO=H2CNH+NO2                              1.00E+11    0.0    12000.0
205. H2CN+N2O=H2CNO+N2                                1.00E+11    0.0     3000.0
206. H2CNH+OH=H2CN+H2O                                1.00E+13    0.0        0.0
207. H2CNH+CN=H2CN+HCN                                1.00E+13    0.0        0.0
208. H2CNO+M=HCNO+H                                   1.00E+16    0.0    50000.0
209. H2CNO+OH=HCNO+H2O                                1.00E+13    0.0        0.0
210. H2CNO+NO=HCNO+HNO                                1.00E+12    0.0    25000.0
211. H2CNO+NO2=HCNO+HONO                              1.00E+12    0.0     2000.0
212. H2CNO+NO2=CH2O+NO+NO                             1.00E+12    0.0        0.0
```

```
213. H2CNO+HNO=H2CN+HONO                              1.00E+12    0.0     2000.0
214. H2CNNO(+M)=H2CN+NO(+M)                           1.00E+16    0.0     2000.0
     Low pressure limit:  0.76900E+17  0.00000E+00  0.15000E+05
215. H2CNNO2(+M)=H2CN+NO2(+M)                         2.46E+15    0.0    34200.0
     Low pressure limit:  0.23500E+57 -0.13260E+02  0.24550E+05
216. H2CNNO2(+M)=HONO+HCN(+M)                         6.21E+12    0.0    32500.0
     Low pressure limit:  0.28700E+40 -0.93700E+01  0.17800E+05
217. H2CNNO2(+M)=CH2O+N2O(+M)                         4.52E+11    0.0    38400.0
     Low pressure limit:  0.13800E+05  0.00000E+00  0.12100E+05
218. RDX(+M)=RDXR+NO2(+M)                             2.00E+16    0.0    45000.0
     Low pressure limit:  0.15700E+18  0.00000E+00  0.28000E+05
219. RDX+H=RDXR+HONO                                  1.00E+13    0.0     5000.0
220. RDX+OH=>2H2CNNO2+H2COHNNO2                       1.00E+13    0.0     5000.0
221. H2COHNNO2=>HCN+NO2+H2O                           1.00E+16    0.0        0.0
222. RDXR(+M)=>RDXRO(+M)                              1.00E+16    0.0    23000.0
     Low pressure limit:  0.76900E+17  0.00000E+00  0.18000E+05
223. RDXRO(+M)=>2H2CNNO2+H2CN(+M)                     1.00E+16    0.0    23000.0
     Low pressure limit:  0.76900E+17  0.00000E+00  0.18000E+05
224. O+CH<=>H+CO                                      5.70E+13    0.0        0.0
225. O+CH2<=>H+HCO                                    8.00E+13    0.0        0.0
226. O+CH2(S)<=>H2+CO                                 1.50E+13    0.0        0.0
227. O+CH2(S)<=>H+HCO                                 1.50E+13    0.0        0.0
228. O+CH3<=>H+CH2O                                   5.06E+13    0.0        0.0
229. O+CH4<=>OH+CH3                                   1.02E+09    1.5     8600.0
230. O+CH2OH<=>OH+CH2O                                1.00E+13    0.0        0.0
231. O+CH3O<=>OH+CH2O                                 1.00E+13    0.0        0.0
232. O+CH3OH<=>OH+CH2OH                               3.88E+05    2.5     3100.0
233. O+CH3OH<=>OH+CH3O                                1.30E+05    2.5     5000.0
234. O+C2H<=>CH+CO                                    5.00E+13    0.0        0.0
235. O+C2H2<=>H+HCCO                                  1.35E+07    2.0     1900.0
236. O+C2H2<=>OH+C2H                                  4.60E+19   -1.4    28950.0
237. O+C2H2<=>CO+CH2                                  6.94E+06    2.0     1900.0
238. O+C2H3<=>H+CH2CO                                 3.00E+13    0.0        0.0
239. O+C2H4<=>CH3+HCO                                 1.25E+07    1.8      220.0
240. O+C2H5<=>CH3+CH2O                                2.24E+13    0.0        0.0
241. O+C2H6<=>OH+C2H5                                 8.98E+07    1.9     5690.0
242. O+HCCO<=>H+2CO                                   1.00E+14    0.0        0.0
243. O+CH2CO<=>OH+HCCO                                1.00E+13    0.0     8000.0
244. O+CH2CO<=>CH2+CO2                                1.75E+12    0.0     1350.0
245. H+2O2<=>HO2+O2                                   2.08E+19   -1.2        0.0
246. 2H+H2<=>2H2                                      9.00E+16   -0.6        0.0
247. 2H+H2O<=>H2+H2O                                  6.00E+19   -1.2        0.0
248. 2H+CO2<=>H2+CO2                                  5.50E+20   -2.0        0.0
249. H+HO2<=>O+H2O                                    3.97E+12    0.0      671.0
250. H+CH<=>C+H2                                      1.65E+14    0.0        0.0
251. H+CH2(+M)<=>CH3(+M)                              6.00E+14    0.0        0.0
     Low pressure limit:  0.10400E+27 -0.27600E+01  0.16000E+04
     TROE centering:      0.56200E+00  0.91000E+02  0.58360E+04  0.85520E+04
        H2               Enhanced by    2.000E+00
        H2O              Enhanced by    6.000E+00
        CH4              Enhanced by    2.000E+00
        CO               Enhanced by    1.500E+00
        CO2              Enhanced by    2.000E+00
        C2H6             Enhanced by    3.000E+00
        AR               Enhanced by    7.000E-01
252. H+CH2(S)<=>CH+H2                                 3.00E+13    0.0        0.0
253. H+CH3(+M)<=>CH4(+M)                              1.39E+16   -0.5      536.0
     Low pressure limit:  0.26200E+34 -0.47600E+01  0.24400E+04
     TROE centering:      0.78300E+00  0.74000E+02  0.29410E+04  0.69640E+04
        H2               Enhanced by    2.000E+00
        H2O              Enhanced by    6.000E+00
        CH4              Enhanced by    3.000E+00
        CO               Enhanced by    1.500E+00
```

```
        CO2              Enhanced by    2.000E+00
        C2H6             Enhanced by    3.000E+00
        AR               Enhanced by    7.000E-01
254. H+CH4<=>CH3+H2                                 6.60E+08    1.6    10840.0
255. H+CH2O(+M)<=>CH2OH(+M)                         5.40E+11    0.5     3600.0
     Low pressure limit:  0.12700E+33 -0.48200E+01  0.65300E+04
     TROE centering:      0.71870E+00  0.10300E+03  0.12910E+04  0.41600E+04
        H2               Enhanced by    2.000E+00
        H2O              Enhanced by    6.000E+00
        CH4              Enhanced by    2.000E+00
        CO               Enhanced by    1.500E+00
        CO2              Enhanced by    2.000E+00
        C2H6             Enhanced by    3.000E+00
256. H+CH2O(+M)<=>CH3O(+M)                          5.40E+11    0.5     2600.0
     Low pressure limit:  0.22000E+31 -0.48000E+01  0.55600E+04
     TROE centering:      0.75800E+00  0.94000E+02  0.15550E+04  0.42000E+04
        H2               Enhanced by    2.000E+00
        H2O              Enhanced by    6.000E+00
        CH4              Enhanced by    2.000E+00
        CO               Enhanced by    1.500E+00
        CO2              Enhanced by    2.000E+00
        C2H6             Enhanced by    3.000E+00
257. H+CH2OH(+M)<=>CH3OH(+M)                        1.06E+12    0.5       86.0
     Low pressure limit:  0.43600E+32 -0.46500E+01  0.50800E+04
     TROE centering:      0.60000E+00  0.10000E+03  0.90000E+05  0.10000E+05
        H2               Enhanced by    2.000E+00
        H2O              Enhanced by    6.000E+00
        CH4              Enhanced by    2.000E+00
        CO               Enhanced by    1.500E+00
        CO2              Enhanced by    2.000E+00
        C2H6             Enhanced by    3.000E+00
258. H+CH2OH<=>H2+CH2O                              2.00E+13    0.0        0.0
259. H+CH2OH<=>OH+CH3                               1.65E+11    0.7     -284.0
260. H+CH2OH<=>CH2(S)+H2O                           3.28E+13   -0.1      610.0
261. H+CH3O(+M)<=>CH3OH(+M)                         2.43E+12    0.5       50.0
     Low pressure limit:  0.46600E+42 -0.74400E+01  0.14080E+05
     TROE centering:      0.70000E+00  0.10000E+03  0.90000E+05  0.10000E+05
        H2               Enhanced by    2.000E+00
        H2O              Enhanced by    6.000E+00
        CH4              Enhanced by    2.000E+00
        CO               Enhanced by    1.500E+00
        CO2              Enhanced by    2.000E+00
        C2H6             Enhanced by    3.000E+00
262. H+CH3O<=>H+CH2OH                               4.15E+07    1.6     1924.0
263. H+CH3O<=>H2+CH2O                               2.00E+13    0.0        0.0
264. H+CH3O<=>OH+CH3                                1.50E+12    0.5     -110.0
265. H+CH3O<=>CH2(S)+H2O                            2.62E+14   -0.2     1070.0
266. H+CH3OH<=>CH2OH+H2                             1.70E+07    2.1     4870.0
267. H+CH3OH<=>CH3O+H2                              4.20E+06    2.1     4870.0
268. H+C2H(+M)<=>C2H2(+M)                           1.00E+17   -1.0        0.0
     Low pressure limit:  0.37500E+34 -0.48000E+01  0.19000E+04
     TROE centering:      0.64640E+00  0.13200E+03  0.13150E+04  0.55660E+04
        H2               Enhanced by    2.000E+00
        H2O              Enhanced by    6.000E+00
        CH4              Enhanced by    2.000E+00
        CO               Enhanced by    1.500E+00
        CO2              Enhanced by    2.000E+00
        C2H6             Enhanced by    3.000E+00
        AR               Enhanced by    7.000E-01
269. H+C2H2(+M)<=>C2H3(+M)                          5.60E+12    0.0     2400.0
     Low pressure limit:  0.38000E+41 -0.72700E+01  0.72200E+04
     TROE centering:      0.75070E+00  0.98500E+02  0.13020E+04  0.41670E+04
        H2               Enhanced by    2.000E+00
```

```
        H2O              Enhanced by    6.000E+00
        CH4              Enhanced by    2.000E+00
        CO               Enhanced by    1.500E+00
        CO2              Enhanced by    2.000E+00
        C2H6             Enhanced by    3.000E+00
        AR               Enhanced by    7.000E-01
270. H+C2H3(+M)<=>C2H4(+M)                          6.08E+12    0.3      280.0
     Low pressure limit:  0.14000E+31 -0.38600E+01  0.33200E+04
     TROE centering:      0.78200E+00  0.20750E+03  0.26630E+04  0.60950E+04
        H2               Enhanced by    2.000E+00
        H2O              Enhanced by    6.000E+00
        CH4              Enhanced by    2.000E+00
        CO               Enhanced by    1.500E+00
        CO2              Enhanced by    2.000E+00
        C2H6             Enhanced by    3.000E+00
        AR               Enhanced by    7.000E-01
271. H+C2H3<=>H2+C2H2                               3.00E+13    0.0        0.0
272. H+C2H4(+M)<=>C2H5(+M)                          5.40E+11    0.5     1820.0
     Low pressure limit:  0.60000E+42 -0.76200E+01  0.69700E+04
     TROE centering:      0.97530E+00  0.21000E+03  0.98400E+03  0.43740E+04
        H2               Enhanced by    2.000E+00
        H2O              Enhanced by    6.000E+00
        CH4              Enhanced by    2.000E+00
        CO               Enhanced by    1.500E+00
        CO2              Enhanced by    2.000E+00
        C2H6             Enhanced by    3.000E+00
        AR               Enhanced by    7.000E-01
273. H+C2H4<=>C2H3+H2                               1.32E+06    2.5    12240.0
274. H+C2H5(+M)<=>C2H6(+M)                          5.21E+17   -1.0     1580.0
     Low pressure limit:  0.19900E+42 -0.70800E+01  0.66850E+04
     TROE centering:      0.84220E+00  0.12500E+03  0.22190E+04  0.68820E+04
        H2               Enhanced by    2.000E+00
        H2O              Enhanced by    6.000E+00
        CH4              Enhanced by    2.000E+00
        CO               Enhanced by    1.500E+00
        CO2              Enhanced by    2.000E+00
        C2H6             Enhanced by    3.000E+00
        AR               Enhanced by    7.000E-01
275. H+C2H5<=>H2+C2H4                               2.00E+12    0.0        0.0
276. H+C2H6<=>C2H5+H2                               1.15E+08    1.9     7530.0
277. H+HCCO<=>CH2(S)+CO                             1.00E+14    0.0        0.0
278. H+CH2CO<=>HCCO+H2                              5.00E+13    0.0     8000.0
279. H+CH2CO<=>CH3+CO                               1.13E+13    0.0     3428.0
280. H+HCCOH<=>H+CH2CO                              1.00E+13    0.0        0.0
281. OH+C<=>H+CO                                    5.00E+13    0.0        0.0
282. OH+CH<=>H+HCO                                  3.00E+13    0.0        0.0
283. OH+CH2<=>H+CH2O                                2.00E+13    0.0        0.0
284. OH+CH2<=>CH+H2O                                1.13E+07    2.0     3000.0
285. OH+CH2(S)<=>H+CH2O                             3.00E+13    0.0        0.0
286. OH+CH3(+M)<=>CH3OH(+M)                         2.79E+18   -1.4     1330.0
     Low pressure limit:  0.40000E+37 -0.59200E+01  0.31400E+04
     TROE centering:      0.41200E+00  0.19500E+03  0.59000E+04  0.63940E+04
        H2               Enhanced by    2.000E+00
        H2O              Enhanced by    6.000E+00
        CH4              Enhanced by    2.000E+00
        CO               Enhanced by    1.500E+00
        CO2              Enhanced by    2.000E+00
        C2H6             Enhanced by    3.000E+00
287. OH+CH3<=>CH2+H2O                               5.60E+07    1.6     5420.0
288. OH+CH3<=>CH2(S)+H2O                            6.44E+17   -1.3     1417.0
289. OH+CH4<=>CH3+H2O                               1.00E+08    1.6     3120.0
290. OH+CH2OH<=>H2O+CH2O                            5.00E+12    0.0        0.0
291. OH+CH3O<=>H2O+CH2O                             5.00E+12    0.0        0.0
```

```
292. OH+CH3OH<=>CH2OH+H2O                          1.44E+06    2.0     -840.0
293. OH+CH3OH<=>CH3O+H2O                           6.30E+06    2.0     1500.0
294. OH+C2H<=>H+HCCO                               2.00E+13    0.0        0.0
295. OH+C2H2<=>H+CH2CO                             2.18E-04    4.5    -1000.0
296. OH+C2H2<=>H+HCCOH                             5.04E+05    2.3    13500.0
297. OH+C2H2<=>C2H+H2O                             3.37E+07    2.0    14000.0
298. OH+C2H2<=>CH3+CO                              4.83E-04    4.0    -2000.0
299. OH+C2H3<=>H2O+C2H2                            5.00E+12    0.0        0.0
300. OH+C2H4<=>C2H3+H2O                            3.60E+06    2.0     2500.0
301. OH+C2H6<=>C2H5+H2O                            3.54E+06    2.1      870.0
302. OH+CH2CO<=>HCCO+H2O                           7.50E+12    0.0     2000.0
303. HO2+CH2<=>OH+CH2O                             2.00E+13    0.0        0.0
304. HO2+CH3<=>O2+CH4                              1.00E+12    0.0        0.0
305. HO2+CH3<=>OH+CH3O                             3.78E+13    0.0        0.0
306. C+O2<=>O+CO                                   5.80E+13    0.0      576.0
307. C+CH2<=>H+C2H                                 5.00E+13    0.0        0.0
308. C+CH3<=>H+C2H2                                5.00E+13    0.0        0.0
309. CH+O2<=>O+HCO                                 6.71E+13    0.0        0.0
310. CH+H2<=>H+CH2                                 1.08E+14    0.0     3110.0
311. CH+H2O<=>H+CH2O                               5.71E+12    0.0     -755.0
312. CH+CH2<=>H+C2H2                               4.00E+13    0.0        0.0
313. CH+CH3<=>H+C2H3                               3.00E+13    0.0        0.0
314. CH+CH4<=>H+C2H4                               6.00E+13    0.0        0.0
315. CH+CO(+M)<=>HCCO(+M)                          5.00E+13    0.0        0.0
     Low pressure limit:  0.26900E+29 -0.37400E+01  0.19360E+04
     TROE centering:      0.57570E+00  0.23700E+03  0.16520E+04  0.50690E+04
        H2               Enhanced by    2.000E+00
        H2O              Enhanced by    6.000E+00
        CH4              Enhanced by    2.000E+00
        CO               Enhanced by    1.500E+00
        CO2              Enhanced by    2.000E+00
        C2H6             Enhanced by    3.000E+00
        AR               Enhanced by    7.000E-01
316. CH+CO2<=>HCO+CO                               1.90E+14    0.0    15792.0
317. CH+CH2O<=>H+CH2CO                             9.46E+13    0.0     -515.0
318. CH+HCCO<=>CO+C2H2                             5.00E+13    0.0        0.0
319. CH2+O2=>OH+H+CO                               5.00E+12    0.0     1500.0
320. CH2+H2<=>H+CH3                                5.00E+05    2.0     7230.0
321. 2CH2<=>H2+C2H2                                1.60E+15    0.0    11944.0
322. CH2+CH3<=>H+C2H4                              4.00E+13    0.0        0.0
323. CH2+CH4<=>2CH3                                2.46E+06    2.0     8270.0
324. CH2+CO(+M)<=>CH2CO(+M)                        8.10E+11    0.5     4510.0
     Low pressure limit:  0.26900E+34 -0.51100E+01  0.70950E+04
     TROE centering:      0.59070E+00  0.27500E+03  0.12260E+04  0.51850E+04
        H2               Enhanced by    2.000E+00
        H2O              Enhanced by    6.000E+00
        CH4              Enhanced by    2.000E+00
        CO               Enhanced by    1.500E+00
        CO2              Enhanced by    2.000E+00
        C2H6             Enhanced by    3.000E+00
        AR               Enhanced by    7.000E-01
325. CH2+HCCO<=>C2H3+CO                            3.00E+13    0.0        0.0
326. CH2(S)+N2<=>CH2+N2                            1.50E+13    0.0      600.0
327. CH2(S)+AR<=>CH2+AR                            9.00E+12    0.0      600.0
328. CH2(S)+O2<=>H+OH+CO                           2.80E+13    0.0        0.0
329. CH2(S)+O2<=>CO+H2O                            1.20E+13    0.0        0.0
330. CH2(S)+H2<=>CH3+H                             7.00E+13    0.0        0.0
331. CH2(S)+H2O(+M)<=>CH3OH(+M)                    4.82E+17   -1.2     1145.0
     Low pressure limit:  0.18800E+39 -0.63600E+01  0.50400E+04
     TROE centering:      0.60270E+00  0.20800E+03  0.39220E+04  0.10180E+05
        H2               Enhanced by    2.000E+00
        H2O              Enhanced by    6.000E+00
        CH4              Enhanced by    2.000E+00
```

```
        CO               Enhanced by    1.500E+00
        CO2              Enhanced by    2.000E+00
        C2H6             Enhanced by    3.000E+00
332. CH2(S)+H2O<=>CH2+H2O                          3.00E+13    0.0        0.0
333. CH2(S)+CH3<=>H+C2H4                           1.20E+13    0.0     -570.0
334. CH2(S)+CH4<=>2CH3                             1.60E+13    0.0     -570.0
335. CH2(S)+CO<=>CH2+CO                            9.00E+12    0.0        0.0
336. CH2(S)+CO2<=>CH2+CO2                          7.00E+12    0.0        0.0
337. CH2(S)+CO2<=>CO+CH2O                          1.40E+13    0.0        0.0
338. CH2(S)+C2H6<=>CH3+C2H5                        4.00E+13    0.0     -550.0
339. CH3+O2<=>O+CH3O                               3.56E+13    0.0    30480.0
340. CH3+O2<=>OH+CH2O                              2.31E+12    0.0    20315.0
341. CH3+H2O2<=>HO2+CH4                            2.45E+04    2.5     5180.0
342. 2CH3(+M)<=>C2H6(+M)                           6.77E+16   -1.2      654.0
     Low pressure limit:  0.34000E+42 -0.70300E+01  0.27620E+04
     TROE centering:      0.61900E+00  0.73200E+02  0.11800E+04  0.99990E+04
        H2               Enhanced by    2.000E+00
        H2O              Enhanced by    6.000E+00
        CH4              Enhanced by    2.000E+00
        CO               Enhanced by    1.500E+00
        CO2              Enhanced by    2.000E+00
        C2H6             Enhanced by    3.000E+00
        AR               Enhanced by    7.000E-01
343. 2CH3<=>H+C2H5                                 6.84E+12    0.1    10600.0
344. CH3+HCO<=>CH4+CO                              2.65E+13    0.0        0.0
345. CH3+CH2O<=>HCO+CH4                            3.32E+03    2.8     5860.0
346. CH3+CH3OH<=>CH2OH+CH4                         3.00E+07    1.5     9940.0
347. CH3+CH3OH<=>CH3O+CH4                          1.00E+07    1.5     9940.0
348. CH3+C2H4<=>C2H3+CH4                           2.27E+05    2.0     9200.0
349. CH3+C2H6<=>C2H5+CH4                           6.14E+06    1.7    10450.0
350. HCO+H2O<=>H+CO+H2O                            1.50E+18   -1.0    17000.0
351. CH2OH+O2<=>HO2+CH2O                           1.80E+13    0.0      900.0
352. CH3O+O2<=>HO2+CH2O                            4.28E-13    7.6    -3530.0
353. C2H+O2<=>HCO+CO                               1.00E+13    0.0     -755.0
354. C2H+H2<=>H+C2H2                               5.68E+10    0.9     1993.0
355. C2H3+O2<=>HCO+CH2O                            4.58E+16   -1.4     1015.0
356. C2H4(+M)<=>H2+C2H2(+M)                        8.00E+12    0.4    86770.0
     Low pressure limit:  0.15800E+52 -0.93000E+01  0.97800E+05
     TROE centering:      0.73450E+00  0.18000E+03  0.10350E+04  0.54170E+04
        H2               Enhanced by    2.000E+00
        H2O              Enhanced by    6.000E+00
        CH4              Enhanced by    2.000E+00
        CO               Enhanced by    1.500E+00
        CO2              Enhanced by    2.000E+00
        C2H6             Enhanced by    3.000E+00
        AR               Enhanced by    7.000E-01
357. C2H5+O2<=>HO2+C2H4                            8.40E+11    0.0     3875.0
358. HCCO+O2<=>OH+2CO                              3.20E+12    0.0      854.0
359. 2HCCO<=>2CO+C2H2                              1.00E+13    0.0        0.0
360. NNH<=>N2+H                                    3.30E+08    0.0        0.0
361. NNH+O2<=>HO2+N2                               5.00E+12    0.0        0.0
362. NNH+O<=>OH+N2                                 2.50E+13    0.0        0.0
363. NNH+O<=>NH+NO                                 7.00E+13    0.0        0.0
364. NNH+CH3<=>CH4+N2                              2.50E+13    0.0        0.0
365. H2CN+N<=>N2+CH2                               6.00E+13    0.0      400.0
366. C+N2<=>CN+N                                   6.30E+13    0.0    46020.0
367. CH+N2<=>HCN+N                                 3.12E+09    0.9    20130.0
368. CH+N2(+M)<=>HCNN(+M)                          3.10E+12    0.1        0.0
     Low pressure limit:  0.13000E+26 -0.31600E+01  0.74000E+03
     TROE centering:      0.66700E+00  0.23500E+03  0.21170E+04  0.45360E+04
        H2               Enhanced by    2.000E+00
        H2O              Enhanced by    6.000E+00
        CH4              Enhanced by    2.000E+00
```

```
        CO                Enhanced by    1.500E+00
        CO2               Enhanced by    2.000E+00
        C2H6              Enhanced by    3.000E+00
        AR                Enhanced by    1.000E+00
369. CH2+N2<=>HCN+NH                                  1.00E+13    0.0    74000.0
370. CH2(S)+N2<=>NH+HCN                               1.00E+11    0.0    65000.0
371. C+NO<=>CN+O                                      1.90E+13    0.0        0.0
372. C+NO<=>CO+N                                      2.90E+13    0.0        0.0
373. CH+NO<=>HCN+O                                    4.10E+13    0.0        0.0
374. CH+NO<=>H+NCO                                    1.62E+13    0.0        0.0
375. CH+NO<=>N+HCO                                    2.46E+13    0.0        0.0
376. CH2+NO<=>H+HNCO                                  3.10E+17   -1.4     1270.0
377. CH2+NO<=>OH+HCN                                  2.90E+14   -0.7      760.0
378. CH2+NO<=>H+HCNO                                  3.80E+13   -0.4      580.0
379. CH2(S)+NO<=>H+HNCO                               3.10E+17   -1.4     1270.0
380. CH2(S)+NO<=>OH+HCN                               2.90E+14   -0.7      760.0
381. CH2(S)+NO<=>H+HCNO                               3.80E+13   -0.4      580.0
382. CH3+NO<=>HCN+H2O                                 9.60E+13    0.0    28800.0
383. CH3+NO<=>H2CN+OH                                 1.00E+12    0.0    21750.0
384. HCNN+O<=>CO+H+N2                                 2.20E+13    0.0        0.0
385. HCNN+O<=>HCN+NO                                  2.00E+12    0.0        0.0
386. HCNN+O2<=>O+HCO+N2                               1.20E+13    0.0        0.0
387. HCNN+OH<=>H+HCO+N2                               1.20E+13    0.0        0.0
388. HCNN+H<=>CH2+N2                                  1.00E+14    0.0        0.0
389. HNCO+OH<=>NH2+CO2                                3.30E+06    1.5     3600.0
390. HCNO+H<=>H+HNCO                                  2.10E+15   -0.7     2850.0
391. HCNO+H<=>OH+HCN                                  2.70E+11    0.2     2120.0
392. HCNO+H<=>NH2+CO                                  1.70E+14   -0.8     2890.0
393. HCCO+NO<=>HCNO+CO                                9.00E+12    0.0        0.0
394. CH3+N<=>H2CN+H                                   6.10E+14   -0.3      290.0
395. CH3+N<=>HCN+H2                                   3.70E+12    0.1      -90.0
396. O+CH3=>H+H2+CO                                   3.37E+13    0.0        0.0
397. O+C2H4<=>H+CH2CHO                                6.70E+06    1.8      220.0
398. O+C2H5<=>H+CH3CHO                                1.10E+14    0.0        0.0
399. OH+CH3=>H2+CH2O                                  8.00E+09    0.5    -1755.0
400. CH+H2(+M)<=>CH3(+M)                              1.97E+12    0.4     -370.0
     Low pressure limit:  0.48200E+26 -0.28000E+01  0.59000E+03
     TROE centering:      0.57800E+00  0.12200E+03  0.25350E+04  0.93650E+04
        H2                Enhanced by    2.000E+00
        H2O               Enhanced by    6.000E+00
        CH4               Enhanced by    2.000E+00
        CO                Enhanced by    1.500E+00
        CO2               Enhanced by    2.000E+00
        C2H6              Enhanced by    3.000E+00
        AR                Enhanced by    7.000E-01
401. CH2+O2=>2H+CO2                                   5.80E+12    0.0     1500.0
402. CH2+O2<=>O+CH2O                                  2.40E+12    0.0     1500.0
403. CH2+CH2=>2H+C2H2                                 2.00E+14    0.0    10989.0
404. CH2(S)+H2O=>H2+CH2O                              6.82E+10    0.2     -935.0
405. C2H3+O2<=>O+CH2CHO                               3.03E+11    0.3       11.0
406. C2H3+O2<=>HO2+C2H2                               1.34E+06    1.6     -384.0
407. O+CH3CHO<=>OH+CH2CHO                             2.92E+12    0.0     1808.0
408. O+CH3CHO=>OH+CH3+CO                              2.92E+12    0.0     1808.0
409. O2+CH3CHO=>HO2+CH3+CO                            3.01E+13    0.0    39150.0
410. H+CH3CHO<=>CH2CHO+H2                             2.05E+09    1.2     2405.0
411. H+CH3CHO=>CH3+H2+CO                              2.05E+09    1.2     2405.0
412. OH+CH3CHO=>CH3+H2O+CO                            2.34E+10    0.7    -1113.0
413. HO2+CH3CHO=>CH3+H2O2+CO                          3.01E+12    0.0    11923.0
414. CH3+CH3CHO=>CH3+CH4+CO                           2.72E+06    1.8     5920.0
415. H+CH2CO(+M)<=>CH2CHO(+M)                         4.86E+11    0.4    -1755.0
     Low pressure limit:  0.10120E+43 -0.76300E+01  0.38540E+04
     TROE centering:      0.46500E+00  0.20100E+03  0.17730E+04  0.53330E+04
        H2                Enhanced by    2.000E+00
```

```
        H2O              Enhanced by    6.000E+00
        CH4              Enhanced by    2.000E+00
        CO               Enhanced by    1.500E+00
        CO2              Enhanced by    2.000E+00
        C2H6             Enhanced by    3.000E+00
        AR               Enhanced by    7.000E-01
416. O+CH2CHO=>H+CH2+CO2                          1.50E+14    0.0        0.0
417. O2+CH2CHO=>OH+CO+CH2O                        1.81E+10    0.0        0.0
418. O2+CH2CHO=>OH+2HCO                           2.35E+10    0.0        0.0
419. H+CH2CHO<=>CH3+HCO                           2.20E+13    0.0        0.0
420. H+CH2CHO<=>CH2CO+H2                          1.10E+13    0.0        0.0
421. OH+CH2CHO<=>H2O+CH2CO                        1.20E+13    0.0        0.0
422. OH+CH2CHO<=>HCO+CH2OH                        3.01E+13    0.0        0.0
423. CH3+C2H5(+M)<=>C3H8(+M)                      9.43E+12    0.0        0.0
     Low pressure limit:  0.27100E+75 -0.16820E+02  0.13065E+05
     TROE centering:      0.15270E+00  0.29100E+03  0.27420E+04  0.77480E+04
        H2               Enhanced by    2.000E+00
        H2O              Enhanced by    6.000E+00
        CH4              Enhanced by    2.000E+00
        CO               Enhanced by    1.500E+00
        CO2              Enhanced by    2.000E+00
        C2H6             Enhanced by    3.000E+00
        AR               Enhanced by    7.000E-01
424. O+C3H8<=>OH+C3H7                             1.93E+05    2.7     3716.0
425. H+C3H8<=>C3H7+H2                             1.32E+06    2.5     6756.0
426. OH+C3H8<=>C3H7+H2O                           3.16E+07    1.8      934.0
427. C3H7+H2O2<=>HO2+C3H8                         3.78E+02    2.7     1500.0
428. CH3+C3H8<=>C3H7+CH4                          9.03E-01    3.6     7154.0
429. CH3+C2H4(+M)<=>C3H7(+M)                      2.55E+06    1.6     5700.0
     Low pressure limit:  0.30000E+64 -0.14600E+02  0.18170E+05
     TROE centering:      0.18940E+00  0.27700E+03  0.87480E+04  0.78910E+04
        H2               Enhanced by    2.000E+00
        H2O              Enhanced by    6.000E+00
        CH4              Enhanced by    2.000E+00
        CO               Enhanced by    1.500E+00
        CO2              Enhanced by    2.000E+00
        C2H6             Enhanced by    3.000E+00
        AR               Enhanced by    7.000E-01
430. O+C3H7<=>C2H5+CH2O                           9.64E+13    0.0        0.0
431. H+C3H7(+M)<=>C3H8(+M)                        3.61E+13    0.0        0.0
     Low pressure limit:  0.44200E+62 -0.13545E+02  0.11357E+05
     TROE centering:      0.31500E+00  0.36900E+03  0.32850E+04  0.66670E+04
        H2               Enhanced by    2.000E+00
        H2O              Enhanced by    6.000E+00
        CH4              Enhanced by    2.000E+00
        CO               Enhanced by    1.500E+00
        CO2              Enhanced by    2.000E+00
        C2H6             Enhanced by    3.000E+00
        AR               Enhanced by    7.000E-01
432. H+C3H7<=>CH3+C2H5                            4.06E+06    2.2      890.0
433. OH+C3H7<=>C2H5+CH2OH                         2.41E+13    0.0        0.0
434. HO2+C3H7<=>O2+C3H8                           2.55E+10    0.3     -943.0
435. HO2+C3H7=>OH+C2H5+CH2O                       2.41E+13    0.0        0.0
436. CH3+C3H7<=>2C2H5                             1.93E+13   -0.3        0.0
437. H+O2+H2O<=>HO2+H2O                           1.13E+19   -0.8        0.0
438. H+O2+N2<=>HO2+N2                             2.60E+19   -1.2        0.0
439. H+O2+AR<=>HO2+AR                             7.00E+17   -0.8        0.0
440. BTTN=>2NO2+3CH2O+HCO+NO                      5.00E+16    0.0    40000.0
441. BTTN=>3CH2O+NO2+NO+CO+HONO                   5.00E+16    0.0    40000.0
442. N2+M=N+N+M                                   3.71E+21   -1.6   225000.0
443. NO2+NO3=NO+NO2+O2                            1.40E+11    0.0     3180.0
444. H2+O2=2OH                                    1.70E+13    0.0    47780.0
445. N2O+H=N2+OH                                  2.53E+10    0.0     4550.0
```

```
     Declared duplicate reaction...
446. N2O+H=N2+OH                                       2.23E+14    0.0    16750.0
     Declared duplicate reaction...
447. NH2+NH=N2H2+H                                     1.50E+15   -0.5        0.0
448. NH2+NH2=N2H2+H2                                   5.00E+11    0.0        0.0
449. NH2+NH2=N2H3+H                                    1.79E+13   -0.3    11320.0
450. NH2+NH2+M=N2H4+M                                  2.98E+47   -9.4     9680.0
451. N2H4+H=N2H3+H2                                    1.00E+12    0.5     2000.0
452. N2H4+OH=N2H3+H2O                                  3.00E+10    0.7     1290.0
453. N2H4+O=N2H3+OH                                    2.00E+13    0.0     1000.0
454. N2H3=N2H2+H                                       1.20E+13    0.0    58000.0
455. N2H3+H=N2H2+H2                                    1.00E+12    0.5     2000.0
456. N2H3+OH=N2H2+H2O                                  3.00E+10    0.7     1290.0
457. N2H3+O=N2H2+OH                                    2.00E+13    0.0     1000.0
458. N2H2+M=NNH+H+M                                    5.00E+16    0.0    50000.0
        H2O              Enhanced by    1.500E+01
        O2               Enhanced by    2.000E+00
        N2               Enhanced by    2.000E+00
        H2               Enhanced by    2.000E+00
459. N2H2+H=NNH+H2                                     5.00E+13    0.0     1000.0
460. N2H2+O=NH2+NO                                     1.00E+13    0.0        0.0
461. N2H2+O=NNH+OH                                     2.00E+13    0.0     1000.0
462. N2H2+OH=NNH+H2O                                   1.00E+13    0.0     1000.0
463. N2H2+NH=NNH+NH2                                   1.00E+13    0.0     1000.0
464. N2H2+NH2=NH3+NNH                                  1.00E+13    0.0     1000.0
465. N2O+NO=N2+NO2                                     4.29E+13    0.0    47130.0
466. NO+NO+NO=N2O+NO2                                  1.07E+10    0.0    26800.0
467. HOCO+M=OH+CO+M                                    2.19E+23   -1.9    35270.0
468. CH+NO2=HCO+NO                                     1.01E+14    0.0        0.0
469. NNH=N2+H                                          3.00E+08    0.0        0.0
470. HNO+NO+NO=HNNO+NO2                                1.70E+11    0.0     2100.0
471. HNNO+NO=NNH+NO2                                   3.20E+12    0.0      270.0
472. HNNO+NO=N2+HONO                                   2.60E+11    0.0      810.0
473. HNNO+M=H+N2O+M                                    2.20E+15    0.0    21600.0
474. HNNO+M=N2+OH+M                                    1.00E+15    0.0    25600.0
475. H+HCO(+M)<=>CH2O(+M)                              1.09E+12    0.5     -260.0
     Low pressure limit:  0.13500E+25 -0.25700E+01  0.14250E+04
     TROE centering:      0.78240E+00  0.27100E+03  0.27550E+04  0.65700E+04
        H2               Enhanced by    2.000E+00
        H2O              Enhanced by    6.000E+00
        CO               Enhanced by    1.500E+00
        CO2              Enhanced by    2.000E+00
476. H2+CO(+M)<=>CH2O(+M)                              4.30E+07    1.5    79600.0
     Low pressure limit:  0.50700E+28 -0.34200E+01  0.84350E+05
     TROE centering:      0.93200E+00  0.19700E+03  0.15400E+04  0.10300E+05
        H2               Enhanced by    2.000E+00
        H2O              Enhanced by    6.000E+00
        CO               Enhanced by    1.500E+00
        CO2              Enhanced by    2.000E+00
477. HCO+HCO=CH2O+CO                                   3.00E+13    0.0        0.0
478. HCO+HCO=H2+CO+CO                                  5.20E+12    0.0        0.0
479. ADN(G)+M=>NH3+HN3O4+M                             3.00E+12    0.0    12040.0
480. HN3O4=HNNO2+NO2                                   2.01E+48  -10.9    42214.0
481. HNNO2+M<=>N2O+OH+M                                7.53E+24   -2.9    25150.0
482. HNNO2+M<=>NH+NO2+M                                6.35E+18   -1.1    39397.0
483. HNNO2+NO2<=>HNO+NO+NO2                            3.00E+12    0.0        0.0
484. HNNO2+OH<=>H2O+2NO                                5.00E+12    0.0        0.0
485. HNNO2+OH<=>HNO+HONO                               5.00E+12    0.0        0.0
486. NH2+NO2<=>H2NO+NO                                 6.56E+16   -1.5      268.0
487. H2NO+H<=>HNO+H2                                   3.00E+07    2.0     2000.0
488. H2NO+H<=>NH2+OH                                   5.00E+13    0.0        0.0
489. H2NO+M<=>H2+NO+M                                  7.83E+27   -4.3    60306.0
490. H2NO+M<=>HNO+H+M                                  1.69E+32   -5.0    62312.0
```

```
491. H2NO+M<=>HNOH+M                                  4.46E+30   -3.8    56888.0
492. H2NO+NH2<=>HNO+NH3                              3.00E+12    0.0     1000.0
493. H2NO+NO<=>HNO+HNO                               2.00E+07    2.0    13000.0
494. H2NO+NO2<=>HONO+HNO                             6.00E+11    0.0     2000.0
495. H2NO+O<=>HNO+OH                                 3.00E+07    2.0     2000.0
496. H2NO+O<=>NH2+O2                                 4.00E+13    0.0        0.0
497. HNNH+OH<=>H2O+N2+H                              2.50E+12    0.0        0.0
498. HNNO2+NH2<=>HNNH+HONO                           2.50E+12    0.0        0.0
499. HNNO2+NO<=>HNNO+NO2                             2.50E+12    0.0        0.0
500. HNNO2+NO<=>HONO+N2O                             2.50E+12    0.0        0.0
501. HNOH+M<=>H+HNO+M                                1.03E+04   -4.8    59527.0
502. HONO+H<=>HNO+OH                                 5.64E+10    0.9     4969.0
503. HONO+H<=>NO+H2O                                 8.13E+06    1.9     3846.0
504. HONO+HONO<=>NO+NO2+H2O                          9.69E+10    0.0    14132.0
505. HONO+NH<=>NH2+NO2                               1.00E+13    0.0        0.0
506. N2H2+NO<=>N2O+NH2                               3.00E+12    0.0        0.0
507. N2H3+M<=>N2H2+H+M                               3.50E+16    0.0    46000.0
508. N2H3+NH<=>N2H2+NH2                              2.00E+13    0.0        0.0
509. N2H3+O<=>NH2+HNO                                1.00E+13    0.0        0.0
510. N2H3+OH<=>NH3+HNO                               1.00E+12    0.0    15000.0
511. N2H4+NH2<=>N2H3+NH3                             3.90E+12    0.0     1500.0
512. N2H4+O<=>N2H2+H2O                               8.50E+13    0.0     1200.0
513. NH2+HO2<=>H2NO+OH                               2.50E+13    0.0        0.0
514. NH3+HNO3<=>H2NO+H2O+NO                          2.32E+01    3.5    44926.0
515. NNH<=>N2+H                                      1.00E+06    0.0        0.0
516. NO3+H<=>NO2+OH                                  6.00E+13    0.0        0.0
517. NO3+HO2<=>NO2+O2+OH                             1.50E+12    0.0        0.0
518. NO3+O<=>NO2+O2                                  1.00E+13    0.0        0.0
519. NO3+OH<=>NO2+HO2                                1.00E+13    0.0        0.0
520. HCO+HONO=CH2O+NO2                               2.39E-03    4.3     4370.0
521. HCO+HONO=H2O+CO+NO                              1.90E-08    6.1     9190.0
522. HCO+HNOH=HNO+CO+H2                              1.71E+03    2.3    -9424.0
523. HCO+HNOH=CH2O+HNO                               3.10E-01    3.5     -854.0
524. HCO+HNOH=H2NOH+CO                               2.15E+03    2.4    -8446.0
525. HCO+HNO=CH2O+NO                                 5.83E-01    3.8      115.0
526. HCO+HNO=CO+H2NO                                 4.89E+01    3.3     1754.5
527. HCO+HNO=HNOH+CO                                 1.31E+13   -0.2     3646.0
528. C4H6+OH=2C2H2+H2+OH                             5.00E+12    0.7     1100.0
529. C4H6+CLO=2C2H2+CLOH+H                           5.00E+12    0.5     6400.0
530. C4H6+CL=2C2H2+HCL+H                             6.75E+12    0.5      100.0
531. C4H6=2C2H3                                      2.50E+18    0.0   100000.0
532. C4H6+H=C2H3+C2H2+H2                             2.30E+12    0.0    20000.0
533. C4H6+O=C2H4+CH2CO                               1.00E+12    0.0        0.0
534. NH3+NO2=NH2+HONO                                2.45E+11    0.0    25075.9
535. H2NO+OH=HNO+H2O                                 2.00E+07    2.0     1000.0
536. NH2+OH+M=H2NOH+M                                5.00E+17    0.0        0.0
537. HNO3+OH=H2O+NO3                                 1.03E+10    0.0    -1240.0
538. HCLO4(+M)=>OH+CLO3(+M)                          1.45E+17    0.0    52655.0
     Low pressure limit:  0.20400E+55 -0.10900E+02  0.58477E+05
539. OH+CLO3=>HCLO4                                  1.17E+60  -15.3    11012.0
540. OH+CLO3=HO2+CLO2                                1.26E+14    0.1       35.8
541. OH+CLO=HO2+CL                                   2.05E+11    0.3    -1440.6
542. OH+CLO=HCL+O2                                   3.52E+05    1.7    -3827.0
543. CLO3(+M)=>O+CLO2(+M)                            1.50E+20   -1.1    36481.3
     Low pressure limit:  0.37600E+26 -0.32800E+01  0.27599E+05
544. O+CLO2=>CLO3                                    2.41E+25   -6.2      800.8
545. O+CLO2=CLO+O2                                   5.23E+07    1.4      876.3
546. OH+CLO2=>HO2+CLO                                7.35E+01    2.8    -3342.1
547. OH+CLO2=CLOH+O2                                 3.29E+04    2.1    -4101.2
548. OH+CLO2=HCLO3                                   3.01E+58  -22.4    19486.5
549. OH+CLO2(+M)=>HCLO3(+M)                          1.95E+13    0.3       35.8
     Low pressure limit:  0.10600E+36 -0.84200E+01  0.22850E+05
550. CLO+CLO(+M)=>CLOOCL(+M)                         9.64E+14   -0.7      127.2
```

```
     Low pressure limit:  0.30100E+29 -0.49600E+01  0.66760E+03
551. CLO+CLO(+M)=>CLOCLO(+M)                        3.85E+15   -0.8      151.0
     Low pressure limit:  0.62400E+34 -0.69900E+01  0.18400E+04
552. CLOOCL(+M)=>CLO+CLO(+M)                        6.30E+19   -1.3    19868.0
     Low pressure limit:  0.27900E+33 -0.52000E+01  0.20186E+05
553. CLOCLO(+M)=>CLO+CLO(+M)                        5.99E+20   -1.6    12863.8
     Low pressure limit:  0.41000E+31 -0.49000E+01  0.12892E+05
554. CLO+CLO=CL2+O2                                 6.56E+10    0.7     3759.4
555. CLO+CLO=CL+CLOO                                8.19E+10    0.8     4307.8
556. CLO+CLO=CLO2+CL                                3.77E+13    0.0     5754.4
557. CL+CLOOCL=CL2+CLOO                             9.21E+10    1.1     -234.5
     Declared duplicate reaction...
558. CL+CLOOCL=CL2+CLOO                             4.30E+12    0.9     4709.2
     Declared duplicate reaction...
559. CL+CLOOCL=CL2O+CLO                             1.32E+10    0.7     2205.6
560. HO2+CLO=CLOH+O2                                9.88E+13   -0.6     -212.6
     Declared duplicate reaction...
561. HO2+CLO=CLOH+O2                                7.83E+03    2.4     5110.6
     Declared duplicate reaction...
562. HO2+CLO=CLOH+O2                                8.37E+02    2.3     -449.1
     Declared duplicate reaction...
563. HO2+CLO=OH+CLOO                                4.58E+05    1.8     2116.2
564. HO2+CLO=>CLO2+OH                               1.34E+03    2.3     5098.6
565. HO2+CLO=HCL+O3                                 4.58E+03    2.0     1698.9
566. CLO+CLO2(+M)=CLOCLOO(+M)                       9.21E+14   -0.2      262.3
     Low pressure limit:  0.39900E+31 -0.55000E+01  0.79080E+03
567. CLO+CLO2=CLOO+CLO                              6.20E+01    2.8      155.0
568. CL+O2(+M)=>CLOO(+M)                            1.08E+14    0.0        0.0
     Low pressure limit:  0.45700E+32 -0.62200E+01  0.18737E+04
569. O+CLO(+M)=>CLO2(+M)                            2.61E+13    0.0      -85.5
     Low pressure limit:  0.31200E+28 -0.41000E+01  0.83450E+03
570. CLO2(+M)=>CLO+O(+M)                            1.11E+16   -0.3    58749.6
     Low pressure limit:  0.98800E-23  0.11000E+02  0.33080E+05
571. O+CLO=CL+O2                                    2.48E+13   -0.1      -83.5
572. CLOO(+M)=>CL+O2(+M)                            4.87E+15   -0.6     5136.4
     Low pressure limit:  0.28100E+40 -0.41000E+00  0.37694E+04
573. CLO+CLO3=CLOO+CLO2                             1.11E+06    2.3     4802.6
574. CLO+CLO3=2CLO2                                 8.55E+05    2.1     5702.7
575. CL+NH3=NH2+HCL                                 5.49E+05    2.5     1442.6
576. CLO+NH3=NH2+CLOH                               1.13E+00    3.9     8631.5
577. CLO2+NH3=NH2+HCLO2                             8.91E+03    3.0    31110.5
578. CLO3+NH3=NH2+HCLO3                             8.19E+09    1.0     4480.7
579. CLO4+NH3=NH2+HCLO4                             1.41E+04    2.8    -8726.9
580. CLO+NH2=HCL+HNO                                2.83E+16   -1.1      256.3
581. CLO+NH2=CL+H2NO                                1.02E+15   -0.6       47.7
582. CLO+NH2=CLOH+NH                                2.89E-05    5.1     2056.5
583. HCLO3(+M)=>CLO2+OH(+M)                         4.07E+21   -1.6    34540.0
     Low pressure limit:  0.75900E+41 -0.76000E+01  0.35245E+05
584. H+HCLO4=H2+CLO4                                8.85E+05    2.0    15815.0
585. H+HCLO4=OH+HCLO3                               2.00E+06    2.0    13667.0
586. CLO4(+M)=CLO3+O(+M)                            5.20E+20   -1.3    46128.2
     Low pressure limit:  0.95800E+47 -0.90000E+01  0.48216E+05
587. HO2+CLO2(+M)=HOOCLO2(+M)                       2.10E+14    0.0        0.0
     Low pressure limit:  0.52200E+49 -0.13100E+02  0.19130E+04
588. HO2+CLO2=HCLO2+O2                              6.02E-03    3.6     2098.0
589. CLO+NO=CL+NO2                                  3.12E+11    0.4     -761.0
590. CLNO2(+M)=CL+NO2(+M)                           1.65E+19   -1.0    33450.0
     Low pressure limit:  0.18900E+56 -0.12100E+02  0.41890E+05
591. CLO+NO2(+M)=>CLONO2(+M)                        1.39E+14    0.0        0.0
     Low pressure limit:  0.74000E+44 -0.10990E+02 -0.88450E+04
592. CLONO2(+M)=>CLO+NO2(+M)                        1.44E+23   -1.8    27175.0
     Low pressure limit:  0.79500E+15 -0.28000E+00  0.98300E+04
593. CL+NH2=HCL+NH                                  8.23E+10    0.9    -1671.1
```

594.	CLO2+NH2=CLOH+HNO	2.14E-01	3.0	-1746.6
595.	CLO2+NH2=CLO+H2NO	1.70E+03	2.5	-1478.3
596.	CLO3+NH2=HCLO2+HNO	3.48E+07	1.0	-1250.0
597.	CLO3+NH2=CLO2+H2NO	5.96E+15	-0.5	47.7
598.	CLO4+NH2=CLO3+H2NO	8.90E+17	-1.1	1260.0
599.	NO+NO=N2+O2	5.00E+20	0.0	75506.0
600.	NOCL+M=CL+NO+M	2.00E+17	0.0	37700.0
601.	CL2+NO=CL+NOCL	2.70E+12	0.0	19900.0
602.	CLOH+HNO=H2O+NOCL	3.00E+12	0.0	0.0
603.	CLO+NOCL=CL2+NO2	1.50E+12	0.0	0.0
604.	OH+HCL=H2O+CL	1.08E+12	0.0	477.0
605.	CL+H2=HCL+H	2.35E+13	0.0	4590.0
606.	CL+H2O2=HCL+HO2	6.62E+12	0.0	1947.0
607.	CL+HO2=HCL+O2	2.47E+13	0.0	894.0
608.	CLOH+O=HCL+O2	1.20E+14	0.0	0.0
609.	CLOH+HCL=CL2+H2O	4.00E+12	0.0	10000.0
610.	CL2+H=HCL+CL	8.40E+13	0.0	1150.0
611.	HCL+O=CL+OH	2.30E+11	0.6	900.0

NOTE: A units mole-cm-sec-K, E units cal/mole

Appendix B. ADN Gas-Phase Mechanism

The following is the Korobeinichev ADN gas-phase mechanism utilized in the current work to simulate ADN combustion.

ELEMENTS CONSIDERED	ATOMIC WEIGHT
1. H	1.00797
2. N	14.0067
3. O	15.9994

SPECIES CONSIDERED	PHASE	CHARGE	MOLECULAR WEIGHT	TEMPERATURE LOW	TEMPERATURE HIGH	ELEMENT COUNT H	N	O
1. H2	G	0	2.01594	300.0	5000.0	2	0	0
2. O2	G	0	31.99880	300.0	5000.0	0	0	2
3. H2O	G	0	18.01534	300.0	5000.0	2	0	1
4. O	G	0	15.99940	300.0	5000.0	0	0	1
5. HNOH	G	0	32.02204	300.0	4000.0	2	1	1
6. H	G	0	1.00797	300.0	5000.0	1	0	0
7. OH	G	0	17.00737	300.0	5000.0	1	0	1
8. HO2	G	0	33.00677	300.0	5000.0	1	0	2
9. H2O2	G	0	34.01474	300.0	5000.0	2	0	2
10. N	G	0	14.00670	300.0	5000.0	0	1	0
11. N2	G	0	28.01340	300.0	5000.0	0	2	0
12. NO	G	0	30.00610	300.0	5000.0	0	1	1
13. NO2	G	0	46.00550	300.0	5000.0	0	1	2
14. NH	G	0	15.01467	300.0	5000.0	1	1	0
15. NH2	G	0	16.02264	300.0	5000.0	2	1	0
16. NH3	G	0	17.03061	300.0	5000.0	3	1	0
17. NNH	G	0	29.02137	250.0	4000.0	1	2	0
18. HNO	G	0	31.01407	300.0	5000.0	1	1	1
19. HONO	G	0	47.01347	300.0	5000.0	1	1	2
20. N2O	G	0	44.01280	300.0	5000.0	0	2	1
21. NO3	G	0	62.00490	300.0	5000.0	0	1	3
22. HNO3	G	0	63.01287	300.0	5000.0	1	1	3
23. N2H2	G	0	30.02934	300.0	5000.0	2	2	0
24. N2H3	G	0	31.03731	300.0	5000.0	3	2	0
25. N2H4	G	0	32.04528	300.0	5000.0	4	2	0
26. HNNO	G	0	45.02077	300.0	4000.0	1	2	1
27. ADN(G)	G	0	124.05628	300.0	3000.0	4	4	4

```
28. AN(G)            G 0  80.04348  300.0 2000.0  4  2  3
29. HN3O4            G 0 107.02567  300.0 5000.0  1  3  4
30. HNNO2            G 0  61.02017  300.0 5000.0  1  2  2
31. H2NO             G 0  32.02204  300.0 4000.0  2  1  1
32. HNNH             G 0  30.02934  300.0 5000.0  2  2  0
33. H2NOH            G 0  33.03001  300.0 4000.0  3  1  1
--------------------------------------------------------------------------------
```

	REACTIONS CONSIDERED		(k = A T**b exp(-E/RT)) A	b	E
1.	H2+M=H+H+M		4.57E+19	-1.4	104000.0
	H2	Enhanced by 2.500E+00			
	H2O	Enhanced by 1.200E+01			
2.	O+H2O=OH+OH		2.97E+06	2.0	13400.0
3.	O+H2=H+OH		5.06E+04	2.7	6290.0
4.	O+O+M=O2+M		6.17E+15	-0.5	0.0
	H2	Enhanced by 2.500E+00			
	H2O	Enhanced by 1.200E+01			
5.	H+O2=O+OH		1.94E+14	0.0	16440.0
6.	H+O2(+M)=HO2(+M)		4.52E+13	0.0	0.0
	Low pressure limit:	0.67000E+20 -0.14200E+01	0.00000E+00		
	TROE centering:	0.10000E+01 0.10000E-89	0.10000E+91		
	H2	Enhanced by 2.500E+00			
	H2O	Enhanced by 1.200E+01			
7.	H+O+M=OH+M		4.72E+18	-1.0	0.0
	H2	Enhanced by 2.500E+00			
	H2O	Enhanced by 1.200E+01			
8.	OH+H2=H2O+H		2.16E+08	1.5	3430.0
9.	OH+H+M=H2O+M		2.21E+22	-2.0	0.0
	H2	Enhanced by 2.500E+00			
	H2O	Enhanced by 1.200E+01			
10.	HO2+O=O2+OH		1.75E+13	0.0	-397.0
11.	HO2+H=H2+O2		6.62E+13	0.0	2130.0
12.	HO2+H=OH+OH		1.69E+14	0.0	874.0
13.	HO2+OH=H2O+O2		1.90E+16	-1.0	0.0
14.	HO2+HO2=H2O2+O2		4.20E+14	0.0	11980.0
	Declared duplicate reaction...				
15.	HO2+HO2=H2O2+O2		1.30E+11	0.0	-1629.0
	Declared duplicate reaction...				
16.	H2O2(+M)=OH+OH(+M)		2.95E+14	0.0	48460.0
	Low pressure limit:	0.12000E+18 0.00000E+00	0.45500E+05		
	TROE centering:	0.50000E+00 0.10000E-89	0.10000E+91		
17.	H2O2+O=OH+HO2		9.64E+06	2.0	3970.0
18.	H2O2+H=H2O+OH		1.00E+13	0.0	3590.0
19.	H2O2+H=HO2+H2		4.82E+13	0.0	7950.0
20.	H2O2+OH=H2O+HO2		1.00E+12	0.0	0.0
	Declared duplicate reaction...				
21.	H2O2+OH=H2O+HO2		5.80E+14	0.0	9557.0
	Declared duplicate reaction...				
22.	N+H2=H+NH		1.60E+14	0.0	25140.0
23.	N+O2=NO+O		6.40E+09	1.0	6280.0
24.	N+OH=NO+H		3.80E+13	0.0	0.0
25.	N+HO2=NH+O2		1.00E+13	0.0	2000.0
26.	N+HO2=NO+OH		1.00E+13	0.0	2000.0
27.	N+NO=N2+O		3.27E+12	0.3	0.0
28.	N+NO2=NO+NO		4.00E+12	0.0	0.0
29.	N+NO2=N2O+O		5.00E+12	0.0	0.0
30.	N+NO2=N2+O2		1.00E+12	0.0	0.0
31.	N+HNO=NH+NO		1.00E+13	0.0	2000.0
32.	N+HNO=N2O+H		5.00E+10	0.5	3000.0

```
33. N+N2O=N2+NO                                     1.00E+13    0.0    19870.0
34. NO+M=N+O+M                                      9.64E+14    0.0   148400.0
       N2               Enhanced by    1.500E+00
35. NO+H(+M)=HNO(+M)                                1.52E+15   -0.4        0.0
    Low pressure limit:  0.89600E+20 -0.13200E+01  0.73510E+03
    TROE centering:      0.82000E+00  0.10000E-89  0.10000E+91
       N2O              Enhanced by    5.000E+00
       H2O              Enhanced by    5.000E+00
       N2               Enhanced by    1.000E+00
36. NO+OH(+M)=HONO(+M)                              1.99E+12   -0.1     -721.0
    Low pressure limit:  0.50800E+24 -0.25100E+01 -0.67560E+02
    TROE centering:      0.62000E+00  0.10000E-89  0.10000E+91
       N2O              Enhanced by    5.000E+00
       H2O              Enhanced by    8.300E+00
       N2               Enhanced by    1.000E+00
37. HO2+NO=NO2+OH                                   2.11E+12    0.0     -479.0
38. NO2(+M)=NO+O(+M)                                7.60E+18   -1.3    73290.0
    Low pressure limit:  0.25000E+29 -0.32700E+01  0.74800E+05
    TROE centering:      0.95700E+00  0.10000E-89  0.83320E+04
       N2O              Enhanced by    1.500E+00
       H2O              Enhanced by    4.400E+00
       N2               Enhanced by    1.000E+00
39. NO2+O=O2+NO                                     3.91E+12    0.0     -238.0
40. NO2+O(+M)=NO3(+M)                               1.33E+13    0.0        0.0
    Low pressure limit:  0.14900E+29 -0.40800E+01  0.24670E+04
    TROE centering:      0.82600E+00  0.10000E-89  0.31910E+04
41. NO2+H=NO+OH                                     1.32E+14    0.0      361.6
42. NO2+OH(+M)=HNO3(+M)                             2.41E+13    0.0        0.0
    Low pressure limit:  0.64200E+33 -0.54900E+01  0.23500E+04
    TROE centering:      0.83700E+00  0.10000E-89  0.16570E+04
43. NO2+NO2=NO3+NO                                  9.64E+09    0.7    20920.0
44. NO2+NO2=2NO+O2                                  1.63E+12    0.0    26120.0
45. NH+M=N+H+M                                      2.65E+14    0.0    75510.0
46. NH+O2=HNO+O                                     3.89E+13    0.0    17890.0
47. NH+O2=NO+OH                                     7.60E+10    0.0     1530.0
48. NH+O=NO+H                                       5.50E+13    0.0        0.0
49. NH+O=N+OH                                       3.72E+13    0.0        0.0
50. NH+OH=HNO+H                                     2.00E+13    0.0        0.0
51. NH+OH=N+H2O                                     5.00E+11    0.5     2000.0
52. NH+N=N2+H                                       3.00E+13    0.0        0.0
53. NH+NO=N2O+H                                     2.94E+14   -0.4        0.0
    Declared duplicate reaction...
54. NH+NO=N2O+H                                     2.16E+13   -0.2        0.0
    Declared duplicate reaction...
55. NH+NO=N2+OH                                     2.16E+13   -0.2        0.0
56. NH+NO2=NO+HNO                                   1.00E+11    0.5     4000.0
57. NH+NO2=N2O+OH                                   1.00E+13    0.0        0.0
58. NH+NH=N2+H+H                                    5.10E+13    0.0        0.0
59. NH2+O2=HNO+OH                                   1.78E+12    0.0    14900.0
60. NH2+O=HNO+H                                     6.63E+14   -0.5        0.0
61. NH2+O=NH+OH                                     6.75E+12    0.0        0.0
62. NH2+H=NH+H2                                     6.92E+13    0.0     3650.0
63. NH2+OH=NH+H2O                                   4.00E+06    2.0     1000.0
64. NH2+N=N2+2H                                     7.20E+13    0.0        0.0
65. NH2+NO=NNH+OH                                   9.19E+22   -3.0     9575.0
66. NH2+NO=N2+H2O                                   3.40E+14   -1.0    -2600.0
67. NH2+NO=N2O+H2                                   5.00E+13    0.0    24640.0
68. NH2+NO=HNO+NH                                   1.00E+13    0.0    40000.0
69. NH2+NO2=N2O+H2O                                 3.28E+18   -2.2        0.0
70. NH3+M=NH2+H+M                                   2.20E+16    0.0    93470.0
71. NH3+O=NH2+OH                                    9.40E+06    1.9     6460.0
72. NH3+H=NH2+H2                                    6.40E+05    2.4    10170.0
73. NH3+OH=NH2+H2O                                  2.04E+06    2.0      566.0
```

74.	NH3+HO2=NH2+H2O2	3.00E+11	0.0	22000.0
75.	NH2+HO2=NH3+O2	1.00E+13	0.0	0.0
76.	NH2+NH2=NH3+NH	5.00E+13	0.0	10000.0
77.	NNH+M=N2+H+M	1.00E+14	0.0	3000.0
78.	NNH+O=N2O+H	1.00E+14	0.0	0.0
79.	NNH+H=N2+H2	1.00E+14	0.0	0.0
80.	NNH+OH=N2+H2O	5.00E+13	0.0	0.0
81.	NNH+NO=N2+HNO	5.00E+13	0.0	0.0
82.	NNH+NH=N2+NH2	5.00E+13	0.0	0.0
83.	NNH+NH2=N2+NH3	5.00E+13	0.0	0.0
84.	HNO+O2=NO+HO2	1.00E+13	0.0	25000.0
85.	HNO+O=OH+NO	1.81E+13	0.0	0.0
86.	HNO+H=H2+NO	1.81E+13	0.0	993.5
87.	HNO+OH=H2O+NO	1.00E+13	0.0	993.5
88.	HNO+NO=N2O+OH	2.00E+12	0.0	26000.0
89.	HNO+NO2=HONO+NO	6.02E+11	0.0	1987.0
90.	HNO+NH2=NO+NH3	2.00E+13	0.0	1000.0
91.	HNO+HNO=H2O+N2O	8.51E+08	0.0	3080.0
92.	HONO+O=OH+NO2	1.20E+13	0.0	5961.0
93.	HONO+H=H2+NO2	1.20E+13	0.0	7352.0
94.	HONO+OH=H2O+NO2	1.26E+10	1.0	135.1
95.	N2O+M=N2+O+M	1.30E+11	0.0	59610.0
96.	N2O+O=O2+N2	1.00E+14	0.0	28000.0
97.	N2O+O=2NO	1.00E+14	0.0	28000.0
98.	N2O+H=N2+OH	2.53E+10	0.0	4550.0
	Declared duplicate reaction...			
99.	N2O+H=N2+OH	2.23E+14	0.0	16750.0
	Declared duplicate reaction...			
100.	N2O+OH=HO2+N2	2.00E+12	0.0	40000.0
101.	N2O+NO=NO2+N2	1.00E+14	0.0	50000.0
102.	HNO3+OH=NO3+H2O	1.03E+10	0.0	-1240.0
103.	NO2+HO2=HONO+O2	4.64E+11	0.0	479.0
104.	NH3+NO2=NH2+HONO	2.45E+11	0.0	25029.0
105.	NO+NO=N2+O2	1.30E+14	0.0	75506.0
106.	NH3+O=H2+HNO	1.10E+10	0.0	500.0
107.	NH2+NO=N2+OH+H	1.08E+11	0.0	-1300.0
108.	NH+H2O=HNO+H2	1.00E+11	0.5	3000.0
109.	NH+NO=NNH+O	3.00E+13	0.0	17000.0
110.	NO+N2H2=HNO+NNH	5.00E+12	0.0	10000.0
111.	HN3O4=HNNO2+NO2	9.50E+41	-8.1	42515.0
112.	HNNO2+M=NH+NO2+M	6.35E+18	-1.1	39397.0
113.	HNNO2+M=N2O+OH+M	7.53E+24	-2.9	25150.0
114.	HNNO2+NO2=HNO+NO+NO2	3.00E+12	0.0	0.0
115.	HNNO2+OH=H2O+2NO	5.00E+12	0.0	0.0
116.	HNNO2+OH=HNO+HONO	5.00E+12	0.0	0.0
117.	NH2+NO2=H2NO+NO	6.56E+16	-1.5	268.0
118.	H2NO+H=HNO+H2	3.00E+07	2.0	2000.0
119.	H2NO+H=NH2+OH	5.00E+13	0.0	0.0
120.	H2NO+M=H2+NO+M	7.83E+27	-4.3	60306.0
121.	H2NO+M=HNO+H+M	1.69E+32	-5.0	62312.0
122.	H2NO+M=HNOH+M	4.46E+30	-3.8	56888.0
123.	H2NO+NH2=HNO+NH3	3.00E+12	0.0	1000.0
124.	H2NO+NO=HNO+HNO	2.00E+07	2.0	13000.0
125.	H2NO+NO2=HONO+HNO	6.00E+11	0.0	2000.0
126.	H2NO+O=HNO+OH	3.00E+07	2.0	2000.0
127.	H2NO+O=NH2+O2	4.00E+13	0.0	0.0
128.	H2NO+OH=HNO+H2O	2.00E+07	2.0	1000.0
129.	N2H2+OH=>H2O+N2+H	2.50E+12	0.0	0.0
130.	HNNO+M=>H+N2O+M	5.00E+15	0.0	20000.0
131.	HNNO+NO=N2+HONO	2.60E+11	0.0	1620.0
132.	HNNO+NO=NNH+NO2	3.20E+12	0.0	540.0
133.	HNNO2+NH2=>N2H2+HONO	2.50E+12	0.0	0.0
134.	HNNO2+NO=HNNO+NO2	4.00E+12	0.0	0.0

135.	HNNO2+NO=HONO+N2O	2.00E+12	0.0	0.0
136.	HNOH+M=H+HNO+M	1.03E+04	-4.8	59527.0
137.	HO2+H=O+H2O	3.00E+13	0.0	1721.0
138.	HONO+H=HNO+OH	5.64E+10	0.9	4969.0
139.	HONO+H=NO+H2O	8.13E+06	1.9	3846.0
140.	HONO+HONO=NO+NO2+H2O	9.69E+10	0.0	14132.0
141.	HONO+NH=NH2+NO2	1.00E+13	0.0	0.0
142.	N2H2+H=NNH+H2	5.00E+13	0.0	1000.0
143.	N2H2+M=NNH+H+M	5.00E+16	0.0	50000.0
144.	N2H2+NH=NNH+NH2	1.00E+13	0.0	1000.0
145.	N2H2+NH2=NNH+NH3	1.00E+13	0.0	1000.0
146.	N2H2+OH=NNH+H2O	1.00E+13	0.0	1000.0
147.	N2H2+NO=N2O+NH2	3.00E+12	0.0	0.0
148.	N2H2+O=NH2+NO	1.00E+13	0.0	1000.0
149.	N2H2+O=NNH+OH	2.00E+13	0.0	1000.0
150.	N2H3+H=NH2+NH2	1.60E+12	0.0	0.0
151.	N2H3+M=N2H2+H+M	3.50E+16	0.0	46000.0
152.	N2H3+NH=N2H2+NH2	2.00E+13	0.0	0.0
153.	N2H3+O=N2H2+OH	5.00E+12	0.0	5000.0
154.	N2H3+O=NH2+HNO	1.00E+13	0.0	0.0
155.	N2H3+OH=N2H2+H2O	1.00E+13	0.0	1000.0
156.	N2H3+OH=NH3+HNO	1.00E+12	0.0	15000.0
157.	N2H4+H=N2H3+H2	1.30E+13	0.0	2500.0
158.	N2H4+NH2=N2H3+NH3	3.90E+12	0.0	1500.0
159.	N2H4+O=N2H2+H2O	8.50E+13	0.0	1200.0
160.	N2H4+OH=N2H3+H2O	4.00E+13	0.0	0.0
161.	NH2+HO2=H2NO+OH	2.50E+13	0.0	0.0
162.	NH2+NH=N2H2+H	5.00E+13	0.0	0.0
163.	NH2+NH2=N2H2+H2	8.50E+11	0.0	0.0
164.	NH2+OH+M=H2NOH+M	5.00E+17	0.0	0.0
165.	NH3+HNO3=H2NO+H2O+NO	2.32E+01	3.5	44926.0
166.	NNH=N2+H	1.00E+06	0.0	0.0
167.	NO3+H=NO2+OH	6.00E+13	0.0	0.0
168.	NO3+HO2=NO2+O2+OH	1.50E+12	0.0	0.0
169.	NO3+NO2=NO+NO2+O2	4.90E+10	0.0	2940.0
170.	NO3+O=NO2+O2	1.00E+13	0.0	0.0
171.	NO3+OH=NO2+HO2	1.00E+13	0.0	0.0
172.	ADN(G)+M=>NH3+HN3O4+M	3.00E+12	0.0	11481.0
173.	AN(G)+M=>NH3+HNO3	3.00E+10	0.0	8000.0

NOTE: A units mole-cm-sec-K, E units cal/mole

Appendix C. AP/HTPB Gas-Phase Mechanism

The following is the AP/HTPB mechanism utilized in the current work to simulate two-dimensional combustion. This mechanism is a reduced form of the Jeppson AP/HTPB mechanism.

ELEMENTS CONSIDERED	ATOMIC WEIGHT
1. C	12.0112
2. CL	35.4530
3. H	1.00797
4. N	14.0067
5. O	15.9994

SPECIES CONSIDERED	PHASE	CHARGE	MOLECULAR WEIGHT	TEMPERATURE LOW	TEMPERATURE HIGH	ELEMENT COUNT C	CL	H	N	O
1. C2H2	G	0	26.03824	300.0	5000.0	2	0	2	0	0
2. C2H3	G	0	27.04621	300.0	5000.0	2	0	3	0	0
3. C2H4	G	0	28.05418	300.0	5000.0	2	0	4	0	0
4. C4H6	G	0	54.09242	300.0	5000.0	4	0	6	0	0
5. CH2O	G	0	30.02649	300.0	5000.0	1	0	2	0	1
6. CH2	G	0	14.02709	250.0	4000.0	1	0	2	0	0
7. CH3	G	0	15.03506	300.0	5000.0	1	0	3	0	0
8. CH4	G	0	16.04303	300.0	5000.0	1	0	4	0	0
9. CO	G	0	28.01055	300.0	5000.0	1	0	0	0	1
10. CO2	G	0	44.00995	300.0	5000.0	1	0	0	0	2
11. CL	G	0	35.45300	300.0	5000.0	0	1	0	0	0
12. CL2	G	0	70.90600	300.0	5000.0	0	2	0	0	0
13. CLO	G	0	51.45240	300.0	5000.0	0	1	0	0	1
14. CLO2	G	0	67.45180	300.0	5000.0	0	1	0	0	2
15. CLO3	G	0	83.45120	300.0	4000.0	0	1	0	0	3
16. CLOH	G	0	52.46037	300.0	5000.0	0	1	1	0	1
17. H	G	0	1.00797	300.0	5000.0	0	0	1	0	0
18. H2	G	0	2.01594	300.0	5000.0	0	0	2	0	0
19. H2O	G	0	18.01534	300.0	5000.0	0	0	2	0	1
20. HCN	G	0	27.02582	300.0	5000.0	1	0	1	1	0
21. HCO	G	0	29.01852	300.0	5000.0	1	0	1	0	1
22. HCL	G	0	36.46097	300.0	5000.0	0	1	1	0	0

23. HCLO4	G	0	100.45857	300.0	4000.0	0	1	1	0	4
24. HNO	G	0	31.01407	300.0	5000.0	0	0	1	1	1
25. HO2	G	0	33.00677	300.0	5000.0	0	0	1	0	2
26. N	G	0	14.00670	300.0	5000.0	0	0	0	1	0
27. N2	G	0	28.01340	300.0	5000.0	0	0	0	2	0
28. N2H2	G	0	30.02934	300.0	5000.0	0	0	2	2	0
29. N2O	G	0	44.01280	300.0	5000.0	0	0	0	2	1
30. NH	G	0	15.01467	300.0	5000.0	0	0	1	1	0
31. NH2	G	0	16.02264	300.0	5000.0	0	0	2	1	0
32. NH3	G	0	17.03061	300.0	5000.0	0	0	3	1	0
33. NO	G	0	30.00610	300.0	5000.0	0	0	0	1	1
34. NO2	G	0	46.00550	300.0	5000.0	0	0	0	1	2
35. O	G	0	15.99940	300.0	5000.0	0	0	0	0	1
36. O2	G	0	31.99880	300.0	5000.0	0	0	0	0	2
37. OH	G	0	17.00737	300.0	5000.0	0	0	1	0	1

REACTIONS CONSIDERED	(k = A T**b exp(-E/RT)) A	b	E

REACTIONS CONSIDERED	(k = A T**b exp(-E/RT)) A	b	E

1. HCLO4=CLO3+OH				1.00E+14	0.0	39100.0
2. HCLO4+HNO=CLO3+H2O+NO				1.50E+13	0.0	6000.0
3. HCLO4+HCO=CLO3+CO+H2O				5.00E+13	0.0	0.0
4. HCLO4+HCO=CLO2+CO2+H2O				1.50E+12	0.0	0.0
5. CLO3=CLO+O2				1.70E+13	0.5	0.0
6. CL2+O2+M=CLO2+CL+M				6.00E+08	0.0	11200.0
N2	Enhanced by	1.000E+00				
H2	Enhanced by	2.000E+00				
H2O	Enhanced by	6.000E+00				
CH4	Enhanced by	2.000E+00				
CO	Enhanced by	1.500E+00				
CO2	Enhanced by	2.000E+00				
7. CLO+NO=CL+NO2				6.78E+12	0.0	311.0
8. CLO+CLOH=CL2+HO2				1.00E+11	0.0	10000.0
9. CLOH+OH=CLO+H2O				1.80E+13	0.0	0.0
10. HCL+OH=CL+H2O				5.00E+11	0.0	750.0
11. CL2+H=HCL+CL				8.40E+13	0.0	1150.0
12. CLO+NH3=CLOH+NH2				6.00E+11	0.5	6400.0
13. NH3+CL=NH2+HCL				4.50E+11	0.5	100.0
14. NH3+OH=NH2+H2O				5.00E+07	1.6	955.0
15. NH2+O2=HNO+OH				3.00E+09	0.0	0.0
16. NH2+NO=H2O+N2				6.20E+15	-1.3	0.0
17. HNO+OH=NO+H2O				1.30E+07	1.9	-950.0
18. HNO+O2=NO2+OH				1.50E+13	0.0	10000.0
19. HNO+H=H2+NO				4.50E+11	0.7	660.0
20. NO+H+M=HNO+M				8.90E+19	-1.3	740.0
H2	Enhanced by	2.000E+00				
H2O	Enhanced by	6.000E+00				
CH4	Enhanced by	2.000E+00				
CO	Enhanced by	1.500E+00				
CO2	Enhanced by	2.000E+00				
21. HO2+N2=HNO+NO				2.70E+10	0.5	41800.0
22. NO+HO2=NO2+OH				2.11E+12	0.0	480.0
23. H+NO2=NO+OH				3.47E+14	0.0	1480.0
24. H2+OH=H2O+H				2.16E+08	1.5	3430.0

```
25. C2H3+O2=CH2O+HCO                                3.98E+12    0.0     -240.0
26. C2H2+H(+M)=C2H3(+M)                             5.60E+12    0.0     2400.0
       CH4              Enhanced by    2.000E+00
       CO               Enhanced by    1.500E+00
       CO2              Enhanced by    2.000E+00
       H2               Enhanced by    2.000E+00
       H2O              Enhanced by    6.000E+00
    Low pressure limit:  0.38000E+41 -0.72700E+01  0.72200E+04
    TROE centering:      0.75070E+00  0.98500E+02  0.13020E+04  0.41670E+04
27. C2H2+OH=CH3+CO                                  4.84E-04    4.0    -2000.0
28. H2+CO(+M)<=>CH2O(+M)                            4.30E+07    1.5    79600.0
       H2               Enhanced by    2.000E+00
       H2O              Enhanced by    6.000E+00
       CH4              Enhanced by    2.000E+00
       CO               Enhanced by    1.500E+00
       CO2              Enhanced by    2.000E+00
    Low pressure limit:  0.50700E+28 -0.34200E+01  0.84350E+05
    TROE centering:      0.93200E+00  0.19700E+03  0.15400E+04  0.10300E+05
29. CH4+CL=CH3+HCL                                  2.50E+13    0.0     3830.0
30. CH4+CLO=CH3+CLOH                                6.00E+11    0.5     5700.0
31. CH4+H=CH3+H2                                    6.60E+08    1.6    10840.0
32. CH4+OH=CH3+H2O                                  1.00E+08    1.6     3120.0
33. CH3+H(+M)=CH4(+M)                               1.27E+16   -0.6      383.0
       CH4              Enhanced by    2.000E+00
       CO               Enhanced by    1.500E+00
       CO2              Enhanced by    2.000E+00
       H2               Enhanced by    2.000E+00
       H2O              Enhanced by    6.000E+00
    Low pressure limit:  0.24800E+34 -0.47600E+01  0.24400E+04
    TROE centering:      0.78300E+00  0.74000E+02  0.29410E+04  0.69640E+04
34. HCO+M=CO+H+M                                    1.87E+17   -1.0    17000.0
       H2               Enhanced by    2.000E+00
       H2O              Enhanced by    0.000E+00
       CH4              Enhanced by    2.000E+00
       CO               Enhanced by    1.500E+00
       CO2              Enhanced by    2.000E+00
35. HCN+OH=NH2+CO                                   1.62E+02    2.6     9000.0
36. CO+OH=CO2+H                                     4.76E+07    1.2       70.0
37. CO+CLO=CO2+CL                                   3.00E+12    0.0     1000.0
38. CO+CLO2=CO2+CLO                                 1.00E+10    0.0        0.0
39. C2H4+OH=H2O+C2H3                                3.60E+06    2.0     2500.0
40. C4H6+OH=2C2H2+H2+OH                             5.00E+12    0.7     1100.0
41. C4H6+CLO=2C2H2+CLOH+H                           5.00E+12    0.5     6400.0
42. C4H6+CL=2C2H2+HCL+H                             6.75E+12    0.5      100.0
43. C4H6=2C2H3                                      2.50E+18    0.0   100000.0
44. C4H6+H=C2H3+C2H2+H2                             2.30E+12    0.0    20000.0
45. H+O2=O+OH                                       8.30E+13    0.0    14413.0
46. C2H2+O=CH2+CO                                   1.02E+07    2.0     1900.0
47. CH2+H2=CH3+H                                    5.00E+05    2.0     7230.0
48. CH2+H(+M)=CH3(+M)                               2.50E+16   -0.8        0.0
       CH4              Enhanced by    2.000E+00
       CO               Enhanced by    1.500E+00
       CO2              Enhanced by    2.000E+00
       H2               Enhanced by    2.000E+00
       H2O              Enhanced by    6.000E+00
    Low pressure limit:  0.32000E+28 -0.31400E+01  0.12300E+04
    TROE centering:      0.68000E+00  0.78000E+02  0.19950E+04  0.55900E+04
49. CH4+O=CH3+OH                                    1.02E+09    1.5      600.0
50. CH3+O=CH2O+H                                    8.43E+13    0.0        0.0
51. CH2+O=H+HCO                                     8.00E+13    0.0        0.0
52. CH3+O2=OH+CH2O                                  3.60E+10    0.0     8940.0
53. OH+CH3=CH2+H2O                                  5.60E+07    1.6     5420.0
54. OH+CH2=H+CH2O                                   2.00E+13    0.0        0.0
```

```
55. CH2+O2=OH+HCO                                   1.32E+13    0.0     1500.0
56. C2H4+O2=2CO+2H2                                 1.80E+14    0.0    35500.0
57. NH2+NO2=2HNO                                    1.40E+12    0.0        0.0
58. NH2+CLO=HNO+HCL                                 2.50E+12    0.0        0.0
59. O2+HNO=NO+HO2                                   1.00E+13    0.0    13000.0
60. H+CL+M=HCL+M                                    5.30E+21   -2.0    -2000.0
       H2               Enhanced by    2.000E+00
       CH4              Enhanced by    2.000E+00
       CO               Enhanced by    1.500E+00
       CO2              Enhanced by    2.000E+00
61. CL+CL+M=CL2+M                                   3.34E+14    0.0    -1800.0
       H2               Enhanced by    2.000E+00
       CH4              Enhanced by    2.000E+00
       CO               Enhanced by    1.500E+00
       CO2              Enhanced by    2.000E+00
62. CL+HO2=CLO+OH                                   2.47E+13    0.0      894.0
63. CL+CH2O=HCO+HCL                                 5.00E+13    0.0      500.0
64. CLO+O=CL+O2                                     6.60E+13    0.0      440.0
65. CLO+CH3=>CH2O+H+CL                              3.33E+11    0.5       30.0
66. CLO+CH3=CH2O+HCL                                3.47E+18   -1.8     2070.0
67. H+HCL=CL+H2                                     7.94E+12    0.0     3400.0
68. HCL+O=CL+OH                                     2.30E+11    0.6      900.0
69. CL2+O=CL+CLO                                    2.51E+12    0.0     2720.0
70. N2O(+M)=N2+O(+M)                                6.20E+14    0.0    56100.0
       CH4              Enhanced by    2.000E+00
       CO               Enhanced by    1.500E+00
       CO2              Enhanced by    2.000E+00
       H2               Enhanced by    2.000E+00
       H2O              Enhanced by    6.000E+00
    Low pressure limit:  0.62000E+15  0.10000E-03  0.56100E+05
    TROE centering:      0.13000E+12  0.10000E-03  0.59620E+05
71. N2O+OH=N2+HO2                                   2.00E+12    0.0    21060.0
72. N2O+O=NO+NO                                     2.90E+13    0.0    23150.0
73. N2O+O=N2+O2                                     1.40E+12    0.0    10810.0
74. N2O+H=N2+OH                                     4.40E+14    0.0    18880.0
75. 2H+M<=>H2+M                                     1.00E+18   -1.0        0.0
       CH4              Enhanced by    2.000E+00
76. 2H+H2<=>2H2                                     9.00E+16   -0.6        0.0
77. 2H+H2O<=>H2+H2O                                 6.00E+19   -1.3        0.0
78. 2H+CO2<=>H2+CO2                                 5.50E+20   -2.0        0.0
79. H+HCO<=>H2+CO                                   7.34E+13    0.0        0.0
80. H+CH2O<=>HCO+H2                                 2.30E+10    1.1     3275.0
81. H+C2H3<=>H2+C2H2                                3.00E+13    0.0        0.0
82. H+C2H4<=>C2H3+H2                                1.33E+06    2.5    12240.0
83. C2H4(+M)<=>H2+C2H2(+M)                          8.00E+12    0.4    88770.0
       H2               Enhanced by    2.000E+00
       H2O              Enhanced by    6.000E+00
       CH4              Enhanced by    2.000E+00
       CO               Enhanced by    1.500E+00
       CO2              Enhanced by    2.000E+00
    Low pressure limit:  0.70000E+51 -0.93100E+01  0.99860E+05
    TROE centering:      0.73450E+00  0.18000E+03  0.10350E+04  0.54170E+04
84. CLO2+NO=CLO+NO2                                 1.00E+11    0.0        0.0
85. CL+CLO2=CLO+CLO                                 5.00E+13    0.0     6000.0
86. CLO+CLO=CL2+O2                                  1.00E+11    0.0        0.0
87. CL+HO2=HCL+O2                                   1.80E+13    0.0        0.0
88. CL+O2+M=CLO2+M                                  8.00E+06    0.0     5200.0
89. CLOH+O=HCL+O2                                   1.20E+14    0.0        0.0
90. NO2+O=NO+O2                                     1.00E+13    0.0      600.0
91. HNO+HNO=H2O+N2O                                 3.95E+12    0.0     5000.0
92. NO2+NO2=NO+NO+O2                                1.00E+14    0.0    25000.0
93. CL+N2O=CLO+N2                                   1.20E+14    0.0    33500.0
94. HCLO4+HNO=CLO2+H2O+NO2                          2.00E+13    0.0     6000.0
```

95.	OH+OH=H2O+O	6.00E+08	1.3	0.0
96.	NH2+NO2=H2O+N2O	4.50E+11	0.0	0.0
97.	HNO+NH2=NH3+NO	5.00E+11	0.5	1000.0
98.	CLOH+HCL=CL2+H2O	4.00E+12	0.0	10000.0
99.	HCLO4+NH2=CLO2+H2O+HNO	1.00E+12	0.0	0.0
100.	HCLO4+NH2=CLOH+HNO+HO2	1.00E+11	0.0	0.0
101.	HCLO4+NO=CLO+HO2+NO2	1.00E+13	0.0	10000.0
102.	CLO2+CLO2=CLO+CLO3	1.80E+13	0.0	18000.0
103.	CLO+HNO=HCL+NO2	3.00E+12	0.0	0.0
104.	HCL+HO2=CLO+H2O	3.00E+12	0.0	0.0
105.	NH2+NO=H+N2+OH	6.30E+19	-2.5	1900.0
106.	NH2+OH=H2O+NH	4.00E+06	2.0	1000.0
107.	NH2+NH2=NH+NH3	5.00E+13	0.0	10000.0
108.	NH+NO=N2+OH	1.00E+13	0.0	0.0
109.	NH+NO=H+N2+O	2.30E+13	0.0	0.0
110.	CL+NH2=HCL+NH	5.00E+10	0.5	0.0
111.	CLO2+NH=CLO+HNO	1.00E+14	0.0	0.0
112.	HCLO4+NH=CLO2+HNO+OH	1.00E+14	0.0	0.0
113.	N+NO2=NO+NO	1.00E+14	0.0	0.0
114.	N+N2O=N2+NO	5.00E+13	0.0	0.0
115.	NH+OH=H2O+N	5.00E+11	0.5	2000.0
116.	NH+OH=H2+NO	1.60E+12	0.6	1500.0
117.	NH+NH2=N+NH3	1.00E+13	0.0	2000.0
118.	NH+NH2=H+N2H2	5.00E+13	0.0	0.0
119.	NH2+NH2=H2+N2H2	5.00E+11	0.0	0.0
120.	N2H2+NO=N2O+NH2	3.00E+12	0.0	0.0
121.	CLOH+H=CLO+H2	6.00E+12	0.0	0.0
122.	HCLO4+NH=CLO3+H2O+N	1.00E+14	0.0	11000.0
123.	HO2+CH3<=>O2+CH4	1.00E+12	0.0	0.0
124.	CH2+CH4<=>2CH3	2.46E+06	2.0	8270.0
125.	CH3+HCO<=>CH4+CO	2.65E+13	0.0	0.0
126.	CH3+CH2O<=>HCO+CH4	3.32E+03	2.8	5860.0
127.	CH3+C2H4<=>C2H3+CH4	2.27E+05	2.0	9200.0

NOTE: A units mole-cm-sec-K, E units cal/mole

Appendix D. AP/HTPB Condensed-Phase Correlations

The following are the condensed-phase correlations used in the two-dimensional AP/HTPB diffusion flame calculations. Burning rate and surface temperature are functions of the heat flux to the surface. Species mass fractions are constant for all heat fluxes.

100% AP

```
1.0             * mass fraction oxidizer in ingredient
1.756   * density of ingredient (g/cm^3)
4.94414E-03     2.51608E-04     0.000000000     * rb = a + bx + cx^2
7.66761E+02     5.31216E-03     0.000000000     * Ts = a + bx + cx^2
12              * number of inlet species mass fractions
3.69503E-02     'O2'
1.54293E-03     'OH'
2.95769E-02     'H2O'
2.23600E-02     'N2O'
2.81363E-04     'HNO'
1.27439E-01     'NH3'
2.08684E-04     'NO2'
7.57079E-03     'CLO3'
1.60817E-04     'CL'
3.30908E-02     'HCL'
7.33409E-01     'HCLO4'
7.41000E-03     'CL2'
```

75% AP Binder

```
0.75    * fraction oxidizer
1.408   * density of ingredient
9.95428E-03   2.86270E-04   0.000000000   * rb = a + bx + cx^2
7.99710E+02   4.23588E-04   3.43097E-07   * Ts = a + bx + cx^2
24.0            * # of inlet mass fractions
```

1.69040E-02 'C2H2'
2.49448E-02 'C2H4'
1.39990E-01 'C4H6'
1.24557E-02 'CH4'
3.73590E-02 'CO'
3.99997E-02 'CO2'
7.64838E-05 'CL'
5.55691E-03 'CL2'
5.99758E-02 'CLO2'
3.60063E-03 'CLO3'
3.40572E-02 'CLOH'
6.54373E-05 'H'
9.90975E-03 'H2'
2.68962E-02 'H2O'
3.50150E-02 'HCN'
2.47247E-02 'HCL'
3.98322E-01 'HCLO4'
1.33815E-04 'HNO'
1.67682E-02 'N2O'
6.94317E-02 'NH3'
5.33608E-03 'NO'
3.08592E-03 'NO2'
2.76301E-02 'O2'
7.76016E-03 'OH'

77.5% AP Binder

0.775 * fraction oxidizer
1.437 * density of ingredient
1.58154E-02 2.81568E-04 0.000000000 * rb = a + bx + cx^2
7.99872E+02 3.72526E-04 3.39249E-07 * Ts = a + bx + cx^2
24 * # of inlet mass fractions
1.55010E-02 'C2H2'
2.28822E-02 'C2H4'
1.24528E-01 'C4H6'
1.10844E-02 'CH4'
3.42709E-02 'CO'
3.66863E-02 'CO2'
8.25397E-05 'CL'
5.70766E-03 'CL2'
5.50067E-02 'CLO2'
3.88576E-03 'CLO3'
3.12367E-02 'CLOH'
6.00127E-05 'H'
9.08893E-03 'H2'
2.70980E-02 'H2O'

3.21140E-02 'HCN'
2.53965E-02 'HCL'
4.29903E-01 'HCLO4'
1.44490E-04 'HNO'
1.72123E-02 'N2O'
7.48835E-02 'NH3'
4.89380E-03 'NO'
2.84710E-03 'NO2'
2.83838E-02 'O2'
7.10774E-03 'OH'

80% AP Binder

0.80 * fraction oxidizer
1.467 * density of ingredient
2.94389E-03 2.81544E-04 0.000000000 * rb = a + bx + cx^2
7.94260E+02 3.23500E-03 0.000000000 * Ts = a + bx + cx^2
24.0 * # of inlet mass fractions
1.40106E-02 'C2H2'
2.06750E-02 'C2H4'
1.09538E-01 'C4H6'
9.74620E-03 'CH4'
3.09643E-02 'CO'
3.31530E-02 'CO2'
8.85463E-05 'CL'
5.92812E-03 'CL2'
4.97098E-02 'CLO2'
4.16850E-03 'CLO3'
2.82277E-02 'CLOH'
5.42365E-05 'H'
8.21351E-03 'H2'
2.75635E-02 'H2O'
2.90215E-02 'HCN'
2.63906E-02 'HCL'
4.61247E-01 'HCLO4'
1.54919E-04 'HNO'
1.78883E-02 'N2O'
8.02934E-02 'NH3'
4.42271E-03 'NO'
2.59035E-03 'NO2'
2.94884E-02 'O2'
6.46197E-03 'OH'

86% AP Binder

0.86 * fraction oxidizer

```
1.544   * density of ingredient
2.19789E-01   2.37370E-04   0.000000000   * rb = a + bx + cx^2
7.92472E+02   3.80818E-03   0.000000000   * Ts = a + bx + cx^2
24.0          * # of inlet mass fractions
1.01541E-02   'C2H2'
1.49841E-02   'C2H4'
7.49681E-02   'C4H6'
6.67034E-03   'CH4'
2.24411E-02   'CO'
2.40274E-02   'CO2'
1.03491E-04   'CL'
6.37261E-03   'CL2'
3.60268E-02   'CLO2'
4.87204E-03   'CLO3'
2.04578E-02   'CLOH'
3.93075E-05   'H'
5.95268E-03   'H2'
2.82520E-02   'H2O'
2.10331E-02   'HCN'
2.83865E-02   'HCL'
5.40168E-01   'HCLO4'
1.81066E-04   'HNO'
1.92296E-02   'N2O'
9.39099E-02   'NH3'
3.20532E-03   'NO'
1.92836E-03   'NO2'
3.17144E-02   'O2'
4.92162E-03   'OH'
```